Universidad de Oviedo
Universidá d'Uviéu
University of Oviedo

Advanced power electronics for the aircraft electrification challenge

Tania Cuesta Cano

Programa de Doctorado en Ingeniería Eléctrica y Electrónica Departamento de Ingeniería Eléctrica, Electrónica, de Computadores y Sistemas.
2024

Universidad de Oviedo
Universidá d'Uviéu
University of Oviedo

Advanced power electronics for the aircraft electrification challenge

Tania Cuesta Cano

Supervisors:
Dr. Ignacio Castro Álvarez
Dr. Alberto Rodríguez Alonso

Programa de Doctorado en Ingeniería Eléctrica y Electrónica Departamento de Ingeniería Eléctrica, Electrónica, de Computadores y Sistemas.

Year 2024

Created at ART-Ireland - This document Contains technical data: UNCTD(EU) CLS45360480

Universidad de Oviedo

RESUMEN DEL CONTENIDO DE TESIS DOCTORAL

1.- Título de la Tesis	
Español/Otro Idioma: Electrónica de potencia avanzada para el reto de la electrificación de aeronaves	Inglés: Advanced power electronics for the aircraft electrification challenge.

2.- Autor	
Nombre: Tania Cuesta Cano	
Programa de Doctorado: Ingeniería eléctrica y electrónica.	
Órgano responsable: Centro Internacional de Postgrado.	

RESUMEN (en español)

La electrificación del sector aeroespacial se ha identificado como un hito principal en la reducción de las emisiones de CO_2 para limitar el impacto ambiental. Esta tesis doctoral se centra en el contexto de un avión de fuselaje estrecho, uno de los mayores contribuyentes de las emisiones totales del transporte aéreo. La electrificación de este tipo de aeronaves requiere un rediseño del sistema eléctrico de potencia del avión (on-board electric power system, EPS), esto se debe a que la potencia manejada pasa de unos cientos de kW a decenas de MW. Esta tesis doctoral presenta un amplio debate sobre los cambios fundamentales que implica la electrificación de los aviones comerciales y las principales estrategias y pilares en los que está basada su transición. En el documento se abarcan tres áreas de actuación: evaluación de las principales arquitecturas de propulsión, convertidores de potencia a través de la propuesta de una nueva topología de convertidor, así como nuevas soluciones activas para la supresión de interferencias electromagnéticas o *EMI,* siglas del término anglosajón. El documento de doctorado está organizado de la siguiente manera:

Capítulo 1 – El papel de la aviación en el calentamiento global: Este primer capítulo ofrece una evaluación general de la contribución de la aviación al calentamiento global y una introducción a la estrategia de descarbonización del sector, así como los principales conceptos de propulsión electrificada para aeronaves. Los principales cambios necesarios para la adaptación del sistema eléctrico original a los conceptos de avión-más-eléctrico (more-electric aircraft, *MEA*) y avión-eléctrico o híbrido-eléctrico (all-electric/ hybrid electric aircraft, *AEA/HEA*), son identificados. El *EPS* se divide en cuatro secciones principales, de las cuales se destacan las áreas más importantes de desarrollo tecnológico, haciendo hincapié en el requisito de reducción de peso.

Capítulo 2 - Arquitecturas de sistemas de propulsión eléctrica para la aviación comercial: Este capítulo se centra en el análisis a alto nivel del sistema eléctrico de potencia, lo cual es fundamental para definir los requisitos de diseño de los diferentes componentes. Guiando así el esfuerzo de desarrollo tecnológico. Este estudio aspira poder estimar cual es la configuración más prometedora a aplicar en aeronaves con propulsión eléctrica o híbrida-eléctrica. Se realiza para el contexto de un tipo de avión bi-motor, equivalente a un Airbus A320. Inicialmente, el documento ofrece una introducción detallada a las diferentes arquitecturas del *EPS* para los distintos conceptos de propulsión eléctrica o híbrida-eléctrica. Identificando los principales componentes implicados y requisitos técnicos necesarios estimados, como por ejemplo, la potencia específica, la eficiencia y la tasa de fallos. Además, se presenta una revisión de la normativa de seguridad a aplicar. En el análisis se evalúan tanto casos con distribución en corriente continua (CC) como en corriente alterna (CA), realizándose un estudio comparativo basado en el estudio de tres figuras de mérito: fiabilidad, eficiencia y potencia específica.

Capítulo 3 – Evaluación de convertidores modulares y multinivel para el uso en el avión eléctrico del futuro: En este capítulo se propone una solución de convertidor de potencia, basada en una topología modular y multinivel o *MMC*, siglas del término anglosajón. Su aplicación se orienta al tren de potencia de un avión eléctrico o híbrido-eléctrico. La idea se sustenta en el uso de un sistema de generación multifásico. Esta nueva topología demuestra una reducción del valor del condensador de celda y una mejor capacidad de tolerancia al cortocircuito en comparación con un MMC clásico. Lo cual se ha verificado mediante

simulaciones. El estudio demuestra que, con un diseño adecuado del rectificador de potencia conectado a cada celda, se reduce el valor de condensador necesario para mantener la tensión dentro de un rango de variación máxima. Del mismo modo, se ha demostrado que esta nueva topología permite bloquear la corriente de cortocircuito, causada por un fallo en el puerto de alta tensión continua, mediante la apertura de todos los interruptores. Lo cual no es posible en un MMC clásico.

Capítulo 4 – Supresión de *EMI*: En primer lugar, se ofrece una introducción a los límites de *EMI* establecidos en los nuevos esquemas de propulsión de los aviones del futuro. El capítulo introduce el concepto de interferencia electromagnética de tipo conducido y la metodología convencional de diseño de filtros pasivos, o filtro *EMI*, para su supresión. Seguidamente, se investigan soluciones activas para ayudar a minimizar el tamaño del filtro *EMI*. La incorporación de circuitos activos para modificar la impedancia de cualquiera de los elementos del filtro *EMI* se denominará en el contexto de esta tesis como filtro *EMI* híbrido. En este capítulo se proponen y verifican dos soluciones de circuitos activos para la amplificación del valor del condensador conectado a tierra (*shunt capacitor,* en inglés). Aplicables a cualquier tipo de filtro de EMI conducido. Ambas soluciones se basan en un sistema de medida de tensión e inyección de corriente.

Capítulo 5 - Conclusiones y trabajo futuro: El capítulo final resume los principales resultados del trabajo de investigación, el trabajo futuro y la lista de publicaciones y patentes elaboradas.

RESUMEN (en Inglés)

Electrification of the aerospace sector has been identified as a main milestone in the reduction of CO_2 emissions to limit the climate change impact. The scope of this PhD thesis is focused on the narrowbody aircraft type, a significant contributor of the total emissions of the air transport sector. In this context, the on-board electric power system (EPS) needs to be redesigned as the power requirement scales from hundreds of kW to tens of MW. This PhD thesis presents an extensive discussion about the fundamental changes the electrification of commercial aircraft implies, and the main strategies and pillars in which this transition is based on. Three areas of action are covered: propulsion architecture evaluation, power conversion through the proposal of a new topology and new solutions for EMI mitigation. The PhD document is organised as follows:

Chapter 1 - Aviation contribution to global warming: This first chapter provides a general evaluation of the aviation contribution to the global warming and an introduction to the aviation decarbonization strategy and the main aircraft electrification concepts. The main changes for the evolution of the original electric power system towards the more-electric aircraft (MEA) and all-electric/ hybrid electric aircraft (AEA/HEA) concepts are identified. The key technological development areas of the four main sections of the EPS are covered. Emphasis is given to the weight reduction requirement.

Chapter 2 - Electric propulsion system architectures for commercial aviation: This chapter focuses on a high-level system analysis, crucial to set the requirements of the different building blocks, which guide the technology development effort. The high-level study aims to estimate the most promising configuration for future electric aircraft in the context of a twin-engine aircraft type, equivalent to an Airbus A320. A detailed introduction of the different EPS schemes of the different electric propulsion concepts is provided, identifying the main building blocks involved and presenting their estimated specific power, efficiency and failure rate required specifications. Additionally, safety regulation is reviewed. Both direct current (DC) and alternating current (AC) distribution cases are evaluated and the comparison among all the cases is done based on three different figures of merit: reliability, efficiency, and specific power.

Chapter 3 - Evaluation of modular multilevel converters for the future electric aircraft: A power converter solution based on a modular multilevel topology, to be used at the power train of a hybrid or electric aircraft, is proposed in this chapter. The idea is based on using multiple multi-phase generation systems. The new topology demonstrates an output capacitance reduction of the needed cell capacitor and better short-circuit tolerance capability when comparing with the classical MMC. The previous mentioned features have been verified by simulation. It has been demonstrated, that with a proper design of the power rectifier, the capacitance at the cell required to keep the voltage within a maximum variation requirement is reduced. Similarly, it has been shown that this new topology makes possible to fade the short-circuit current caused by a high voltage direct current (HVDC) port fault by opening all the switches.

Chapter 4 - EMI mitigation: EMI mitigation requirements for the new propulsion schemes of

the future aircraft, particularly for a twin-engine aircraft, are covered. The chapter introduces the concept of conducted EMI noise and the conventional design methodology of passive filters. Active solutions are investigated to help on the minimization of the EMI filter size. Particularly, the combination of active circuits to modify the impedance of any of the EMI filter elements is named as hybrid EMI filter in the PhD thesis. Two active circuit solutions are proposed and verified to enhance the shunt capacitance of any common mode filter by using a voltage measure and current injection active solution.
Chapter 5 - Conclusions and future work: The final chapter summarizes the main outputs of the research work, the future work and list of publications and patents.

SR. PRESIDENTE DE LA COMISIÓN ACADÉMICA DEL PROGRAMA DE DOCTORADO EN _____

Universidad de Oviedo
Universidá d'Uviéu
University of Oviedo

Advanced power electronics for the aircraft electrification challenge

Tania Cuesta Cano

Supervisors:
Dr. Ignacio Castro Álvarez
Dr. Alberto Rodríguez Alonso

Programa de Doctorado en Ingeniería Eléctrica y Electrónica Departamento de Ingeniería Eléctrica, Electrónica, de Computadores y Sistemas.

Year 2024

Acknowledgments

Completing this PhD thesis has been a challenging journey, and it would not have been possible without the support, guidance, and encouragement of many individuals.

First, I would like to thank Dr. Diego González Lamar who, back in 2019, considered me as a good candidate for taking this PhD opportunity. Secondly, I would like to thank my supervisors, Dr. Ignacio Castro Álvarez and Dr. Alberto Rodríguez Alonso, for their advice, support and time throughout this journey. I really appreciate the countless hours they dedicated to guidance, reviewing drafts, and providing feedback.

I would like to make an special mention here to my colleagues from the University of Oviedo, who contributed to create a good atmosphere during my time there and with who I shared numerous good moments and conversations. Special thanks to Abraham, who, even after moving to work at the company, has made a special effort to keep me posted about any important matter, JR who encouraged me during our catch-ups, and Miguel Costales who taught us that there is always a second chance to an old shoe if you have a drill. For their helpful and meaningful discussions during lunch breaks.

Acknowledge to my discipline leader at Collins Aerospace, Laura Albiol-Tendillo, whose understanding and flexibility allowed me to balance my professional responsibilities with my academic pursuits. Special thanks to my great collages at Collins Aerospace, specially to my group peers Douglas, Andrei, Sarbani and George. I need to make here a dedicated acknowledge to George, for his really good advice and en-

courage in all those moments I felt I was failing and I was about to give up. I think your support this last year has made a real difference.

Finally, I would like to dedicate this to my family. Specially to my mum that in many occasions has suffered more than me and that has made all possible to give me the opportunity to reach where I am today. To my dad and brother, thanks for your support.

Resumen

La electrificación del sector aeroespacial ha sido definida como una de las principales objetivos para la reducción de emisiones de CO_2, cuyo fin es frenar el cambio climático. Este proceso de transformación abarca todos los sectores de la aviación e industria relacionada. El contexto de esta tesis doctoral se centra en el tipo de aeronaves de fuselaje estrecho, el cuál ha sido identificado como uno de los contribuyente más significativos en las emisiones totales del transporte aéreo. En este ámbito, el sistema de energía eléctrica a bordo (EPS, siglas en inglés) necesita ser rediseñado. Esto se debe a que los requisitos de potencia pasan de ser de unos cientos de kW a decenas de MW. La electrificación de la propulsión constituye el cambio más revolucionario, pero este desafío afecta a todos los elementos que forman parte del EPS. La tecnología disponible actualmente presenta varias limitaciones a superar, lo cual impulsa un gran esfuerzo en la investigación y identificación de nuevas soluciones clave. En la tesis doctoral se presenta una discusión exhaustiva sobre los cambios fundamentales que implica la electrificación de aeronaves comerciales, así como las principales estrategias y pilares en los que esta se basa. Tres áreas de acción son abarcadas: evaluación de las arquitecturas de propulsión, propuesta de una nueva topología de convertidor, así cómo, propuesta de nuevas soluciones relacionadas con la supresión de EMI. Cada una de estas áreas se cubrirá en un capítulo de forma independiente, el documento está organizado de la siguiente manera:

- **Capítulo 1 - El papel de la aviación en el calentamiento global:** Este primer capítulo tiene como objetivo proporcionar una visión general de la contribución de la aviación al calentamiento global e introducir cual es la estrategia de descarbonización actualmente en Europa. De igual modo, se presentan los

principales conceptos de electrificación para aeronaves. Los principales cambios implicados en la transición del sistema eléctrico original hacia conceptos como el avión más eléctrico (MEA, siglas en inglés) y los aviones eléctricos o híbridos eléctricos (AEA/HEA, siglas en inglés) son identificados. En la sección final, las áreas clave de desarrollo tecnológico de las cuatro secciones principales del EPS son desglosadas y evaluadas. El EPS se divide en las siguientes secciones: fuentes de energía, conversión de energía, distribución y propulsión. A lo largo del capítulo, y la tesis en general, se hace especial hincapié en la necesidad de reducción de peso. Esto se debe a su influencia directa en el rendimiento aerodinámico de la aeronave y, en consecuencia, en el rango de vuelo. El propósito principal de este capítulo es proporcionar al lector una visión general de las principales barreras tecnológicas a superar en cada una de las secciones mencionadas.

- **Capítulo 2 - Arquitecturas de propulsión eléctrica aplicables en la avión comercial:** Este capítulo proporciona un análisis del sistema a alto nivel, el cual es crucial para establecer requisitos de diseño de los diferentes componentes. Esto guia el esfuerzo de desarrollo tecnológico. El estudio tiene como objetivo estimar cual es la arquitectura más prometedora. Este se centra en el caso de un avión bi-motor, equivalente a un Airbus A320. La primera parte del capítulo proporciona una introducción detallada de los diferentes esquemas de EPS para los distintos conceptos de propulsión eléctrica. Los principales componentes involucrados y estimación de sus características son proporcionados. El análisis se centra en la evaluación de la potencia específica, la eficiencia y la fiabilidad. Además, se proporciona una revisión de la regulación de fiabilidad aplicable. A continuación, se presenta un análisis comparativo de las

arquitecturas de propulsión más comunes. Se evalúan tanto casos de distribución en DC, como de AC. La comparativa entre todos los casos se realiza en base a tres criterios: fiabilidad, eficiencia y potencia específica.

- **Capítulo 3 - Evaluación de convertidores modulares y mutinivel para el futuro avión eléctrico:** En este capítulo se propone una solución de convertidor de potencia basado en una topología de convertidor modular multinivel (MMC, siglas en inglés). La propuesta tiene el fin de ser usada en el tren de potencia de un avión híbrido eléctrico o totalmente eléctrico. Esta idea se basa en el potencial uso de escenarios con sistemas de generación multifásicos. La nueva topología demuestra una reducción del condensador de celda y una mejor tolerancia a cortocircuitos en comparación con un MMC clásico. Dichas ventajas han sido verificadas mediante simulación. Se ha demostrado que con un diseño adecuado del rectificador de potencia conectada a cada celda, el valor del condensador necesario para mantener su tensión dentro de un rango máximo de variación es menor que para un MMC. Del mismo modo, se ha demostrado que esta nueva topología permite bloquear la corriente de cortocircuito resultante de un fallo en el bus de alta tensión y corriente directa (HVDC, siglas en inglés) mediante la apertura de todos los interruptores.

- **Capítulo 4 - Supresión de EMI:** En este capítulo, los límites de interferencia electromagnética o EMI, considerados actualmente en los nuevos esquemas de propulsión de las futuras aeronaves son identificados. Particularizándose en aviones bi-motor. El capítulo introduce el concepto de ruido EMI conducido y la metodología de diseño convencional de filtros pasivos. La maximización de la potencia específica de los filtros pasivos de EMI, está limitada tecnológicamente por los materiales disponible y los requisitos de impedancia mínima a tierra que

imponen ls regulaciones de seguridad. En consecuencia, soluciones activas son investigadas para ayudar en la minimización del tamaño del filtro EMI. En particular, la integración de circuitos activos para modificar la impedancia de uno de los elementos del filtro EMI pasivo se denominará filtro EMI híbrido en esta tesis doctoral. En este contexto, se han propuesto dos soluciones de circuitos activos para incrementar el valor del condensador conectado a tierra (conocido en inglés como "shunt capacitor"). Dichas soluciones son aplicables a cualquier tipo de filtro de EMI. Las soluciones activas se basan en medida de tensión e inyección de corriente. Para la primera solución, se ofrece una validación experimetal de la respuesta en frecuencia entre el filtro EMI híbrido y un equivalente pasivo. Demostrándose un incremento del valor de capacidad del condensador conectado a tierra de forma activa. La validación de la segunda solución se realiza mediante simulación.

- **Capítulo 5 - Conclusiones y trabajo futuro:** El capítulo final resume los principales resultados del trabajo de investigación y propone ideas de trabajo futuro. Además, incluye la lista de publicaciones y patentes resultado de la tesis doctoral.

Abstract

Electrification of the aerospace sector has been identified as one of the main milestones in the reduction of CO_2 emissions to limit the climate change impact. The paradigm change covers all aviation sectors and related businesses. The scope of this PhD thesis is focused on the narrowbody aircraft type, as it has been identified as a significant contributor of the total emissions of the air transport sector. In this context, the on-board electric power system (EPS) needs to be redesigned as the power requirement scales from hundreds of kW to tens of MW. Propulsion electrification prompts the biggest disruptive change, but the challenge affects all the elements that are part of the EPS. The current available technology has several gaps, so a significant innovation effort drives the pursuit of the enhancement of the identified key technologies enablers. This PhD thesis presents an extensive discussion about the fundamental changes the electrification of commercial aircraft implies, and the main strategies and pillars in which this transition is based on. The document covers three areas of action: propulsion architecture evaluation, power converters through a new topology proposal and new proposed solutions for EMI mitigation. Each of them is covered in one chapter and the PhD document is organised as follows:

- **Chapter 1 - Aviation contribution to global warming:** This first chapter aims to provide a general evaluation of the aviation contribution to the global warming and an introduction to the aviation decarbonization strategy and the main aircraft electrification concepts. The main changes for the evolution of the original electric power system towards the more-electric aircraft (MEA) and all-electric/ hybrid electric aircraft (AEA/HEA) concepts are identified. The final section covers the key technological development areas of the four

main sections of the EPS, which are broken down and evaluated. The areas considered are power sources, power conversion, distribution, and propulsion. Emphasis is given to the weight reduction requirement, as the weight directly influences the aerodynamic performance of the aircraft and consequently the flight range. The purpose is to provide the reader with an overview of the main technology barriers at each of the mentioned areas.

- **Chapter 2 - Electric propulsion system architectures for commercial aviation:** This chapter focuses on the high-level system analysis, crucial to set the requirements of the different building blocks, which guide the technology development effort. The high-level study aims to estimate the most promising configuration for future electric aircraft in the context of a twin-engine aircraft type, equivalent to an Airbus A320. The first part of the chapter provides a more detailed introduction of the different EPS schemes of the different electric propulsion concepts, identifying the main building blocks involved and presenting their estimated specific power, efficiency and failure rate required specifications. Additionally, safety regulation is reviewed. The rest of the chapter presents the architectures trade-off analysis. Both DC and AC distribution cases are evaluated and the comparison among all the cases is done based on three different figures of merit: reliability, efficiency and specific power.

- **Chapter 3 - Evaluation of modular multilevel converters for the future electric aircraft:** A power converter solution based on a modular multilevel converter (MMC) topology to be used at the power train of a hybrid or electric aircraft is proposed in this chapter. The idea is based on using multiple multi-phase generation systems. The new topology demonstrates an output capacitance reduction of the needed cell capacitor and better short-circuit

tolerance capability when comparing with the classical MMC. The previous mentioned features have been verified by simulation. It has been demonstrated that with a proper design of the power rectifier, the capacitance at the cell required to keep the voltage within a maximum variation requirement, is reduced. Similarly, it has been shown that this new topology makes possible to fade the short-circuit current caused by a HVDC port fault by opening all the switches.

- **Chapter 4 - EMI mitigation:** In this chapter, EMI mitigation requirements for the new propulsion schemes of the future aircraft, particularly for a twin-engine aircraft, are covered. The chapter introduces the concept of conducted EMI noise and the conventional design methodology of passive filters. Regarding power density increase, passive EMI filters are limited by the material technology available and safety minimum impedance to ground requirements. Consequently, active solutions are investigated to help on the minimization of the EMI filter size. Particularly, the combination of active circuits to modify the impedance of any of the EMI filter elements is named as hybrid EMI filter in the PhD thesis. In this context, two active circuit solutions are proposed to enhance the shunt capacitance of any common mode filter by using a voltage measure and current injection active solution. The frequency response of a hybrid EMI filter, where the shunt effective capacitance value is increased actively, is successfully compared with an equivalent full passive solution for one of the proposals. The verification of the performance of the second approach is done by simulation.

- **Chapter 5 - Conclusions and future work:** The final chapter summarizes the main outcomes of the research work, the future work. Including the list of

publications and patents which output from this PhD thesis.

Contents

List of Figures

List of Tables

Chapter 1

Aviation contribution to global warming

Global warming is a present reality, its effects manifest in various forms depending on the region, such as: widespread drought, heatwaves,below-average precipitations, and consequently wildfires, loss of biodiversity, crop production declining,etc., [1]. 2022 marked the hottest summer and the second warmest year. The average global temperature in 2023 was 0.95 to 1.2°C higher than in the 19^{th} century, with greenhouse gases (GHG) emissions identified as the main cause. Furthermore, global warming impacts renewable energy sources. In most parts of Europe, anomalies in precipitation have directly affected water resources and river flows. Additionally, wind speed irregularities has reduced the wind farms power generation potential [2].

Some key actions to reduce GHG emissions are increasing the renewable energy source power generation contribution and pursuing new transportation solutions with

lower or null CO_2 emissions. This leads to a new paradigm in which power electronics become one of the key enablers. Huge development in the state of the art (SoA) of power converters can be already appreciated driven by the road transport electrification and the increasing integration of renewable power generation.

This thesis focuses on aviation electrification, a critical domain with a profound impact on the evolution of CO_2 emissions owing to its significant current contribution and rapid growth projection. Moreover, aircraft electrification presents an immense technological development challenge that exceeds the capabilities of existing technology, including solutions adopted in electric vehicles (EVs). This technological disparity is catalyzing an impressive wave of innovation, to which this thesis aspires to contribute. As the reader will be able to conclude at the end of this document, the main complexity on delivering satisfactory solutions in the context of aircraft electrification stems from the intricate interaction of every element to reach the optimal system design, the rigorous operational conditions and application requirements, and the heightened vulnerability to malfunctions.

1.1 The impact of aviation

According to 2019 records, aviation accounts for 3% of total CO_2 emissions [3]. While this percentage may be relative low, addressing CO_2 reduction strategies is crucial do to its significant impact on the overall transport emissions. The number of flights is increasing continuously. Despite aviation was the transportation sector most affected by COVID-19 pandemic, by 2022 aviation had nearly reached 80% of pre-pandemic levels. Projections indicate that the return to pre-COVID traffic levels is expected to

occur between 2023 and 2025 [4–6], and the trend is to expect it continues increasing due to the constant growth of the sector.Furthermore, commercial aviation is the main contributor to CO_2 emissions in aviation. Figure 1-1 , provides a classification by operation and aircraft class subdivisions [7].

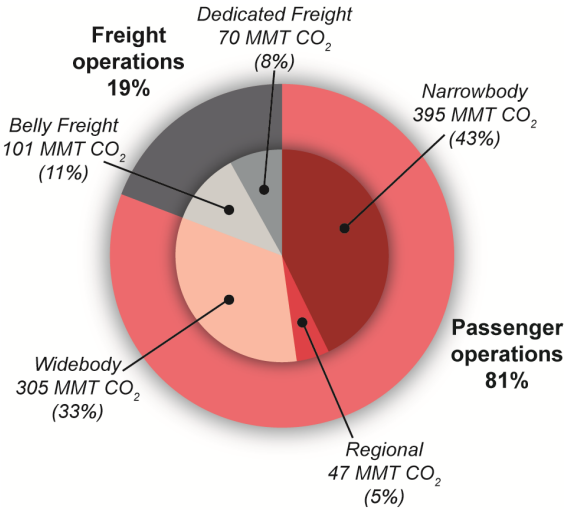

Figure 1-1. CO2 emissions generation by the aerospace sector and classified by operations and aircraft classes (2018 data). CO_2 is expressed in million metric tons (MMT)

Upon closer examination of Figure 1-1, it becomes evident that passenger operations account for the majority of CO_2 emissions (i.e.,81%). This category is further subdivided into three aircraft classes: narrowbody or single-aisle aircraft, which accommodate up to 295 passengers; widebody or two-aisle aircraft, catering to between 250 and 600 passengers; and regional aircraft, designated for short-haul flights of up to 100 passengers. Freight operations encompass two aircraft classes: dedicated freight or cargo aircraft, specifically designed for cargo transportation, and belly freight, which involves utilizing the deck of passenger aircraft for air cargo. Notably, narrowbody (as well know as single-aisle) and widebody passenger aircraft classes together contribute to 76% of the total CO_2 emissions. Consequently, they are desired

aircraft classes to address.

It should be mention notice that CO_2 is the largest element present in the plane exhaust, although it is not the only component with negative climate impact. Research on the contrail effect on climate change is currently ongoing. For instance, water vapour produced during combustion does not have a direct warming impact, but under certain meteorological conditions it can persist in the atmosphere and contribute to the formation of cirrus clouds—high-altitude clouds. They are composed of ice crystals that trap infrared rays. They have a relatively short lifespan of a few hours. Nonetheless, the collective influence of thousands of flights can have a significant warming effect [8]. This phenomena drive to take special attention when exploring some of the solutions proposed for CO_2 emission reduction. Their impact on increasing the contrails presence, such as those which imply direct or indirect H_2 combustion, should be analysed. Additionally, the net effect of nitrous gases is under investigation, as they chemically form ozone (O_3), a greenhouse gas, while also working to eliminate methane. Similarly, soot can influence the formation of cirrus clouds, as it can serve as ice crystal nuclei. It is important to note that non-CO_2 emissions carry significant scientific uncertainty but should not be overlooked. Some researchers have proposed multiplying aviation emissions by a factor of 1.9 based on the best available scientific knowledge [9].

Concluding, there is a clear necessity to aim new aviation propulsion solutions that will reduce the CO_2 emissions.There are some other co-benefits to human health through addressing this concern, such as nitrogen oxides (NO_x) and noise reduction. Definition of strategies and identification of key enablers are crucial to manage this issue. In the following lines, an assessment of these two topics is presented with the aim of providing a general understanding of the decarbonization paradigm, enabling

the reader to identify the contributions of this thesis easier.

1.2 The aviation decarbonisation strategy

The fight against climate change is a top priority for the European Parliament. In 2008, the European Union (EU) established a target to reduce emissions by 20% compared to 1990 levels by 2020. In 2015, as part of the Paris Agreement, the EU committed to reducing greenhouse gas emissions by at least 40% below 1990 levels by 2030. The result is that emissions decreased by 24% by 2019 and by 31% by 2020. Although the COVID-19 pandemic partially contributed to this decline, ongoing strategies appear to have positive effects. In 2021, with new targets outlined in The European Green Deal, the goal is to achieve zero net emissions by 2050 [10]. In the same year, the Air Transport Action Group embraced the same commitment [11] and defined a plan for achieving this challenging and ambitious decarbonization target, the Waypoint 2050 [12]. Additionally, long-term roadmaps such as the Advisory Council for Aeronautics Research in Europe (ACARE) Flightpath 2050 set specific goals, such as a 75% reduction in CO_2 emissions per passenger kilometer and a 90% reduction in NOx emissions [13].

The decarbonization of the aviation sector presents a significant challenge. Over the past 30 years, aviation has made efforts to halve CO_2 emissions compared to the first commercial service. Aircraft design has undergone constant improvement since its inception, achieving significant efficiency gains in recent decades. This progress has been primarily driven by enhancements in gas turbine design, fuel composition, and air traffic management strategies. As a result, fuel consumption per passenger

decreased by 24% between 2005 and 2017 [14]. However, the growth in air traffic has overshadowed these achievements. To meaningfully reduce CO_2 emissions, the commercial aviation sector must undertake drastic measures. The capability and investment capacity needed is well beyond the private sector bandwidth, therefore institutional leadership and support is needed to pull together resources and commitments.

In Europe, the transformation towards a sustainable air transport is mainly led by the EU program, Clean Aviation Joint Undertaking . Through its Strategic Research and Innovation Agenda (SRIA) it defines the research roadmap to define and mature new and disruptive technologies to meet the Green Deal objectives in 2030 and 2050. Currently,three key " thrust" or pillars are defined to guide the research and innovation efforts: Hybrid electric and full electric architectures, ultra-efficient aircraft architectures and disruptive technologies to enable hydrogen-powered aircraft. Each of them, target research, innovation and maturation of technologies at demonstration level of potential transformation enablers. The first "thrust" is focused in the definition and demonstration of novel full electric architectures for small/commuter planes and hybrid electric propulsion and ultra-efficient structures for regional and short-range applications. The second one, is oriented to short and medium range applications, focusing on efficiency improvement of gas turbines, enhancement of the thermal propulsion system and airframe integration. Finally, the last one addresses novel concepts with hydrogen direct combustion and fuel cell based propulsion [15]. In addition, transversal collaboration among the three pillars is embrace to work on the definition of new certification methods, aircraft architecture and technology integration.

Table 1.1 summarizes the main projects launched under the different "thrust" on

date of this document. In addition to them there are HERA, CONCERTO and and SMR ACAP that are the transversal projects mentioned. At the United States the research and innovation effort towards more sustainable aviation is carried by a partnership among NASA, Federal Aviation Administration (FAA) and industry. NASA Glenn's research in Electrified Aircraft Propulsion (EAP) is running projects that covers a big portfolio of technologies and conceptual aircraft design studies [16]. Aircraft electrification is in centre of the definition of a new aviation paradigm. However, nowadays the way towards a climate neutral aviation is not clear because of the complexity of the application. A huge researching effort is essential at this point to develop the technology that enable the decarbonization of sector.

TABLE 1.1. Clean Aviation Program main projects

Thrust	Project	Definition
Hybrid Electric	**HE-ART**	2.150-2.850 MW Multi Hybrid Electric porpulsion system for regional AiRcrafT
	AMBER	2.250 MW Multi Power train Innovative for Hybrid Electric Regional Application
	TheMa4HERA	Thermal Management Solutions for Hybrid Electric Regional Aircraft
	HECATE	Electric Distribution Solutions for Hybrid Electric Regional Aircraft
	HERWINGT	Hybrid Electric Regional Wing Integration Novel Green Technologies
Ultra Efficient/ Short-Medium Range	**HEAVEN**	Ultrafan -Hydrogen and Hybrid gas turbine design
	SWITCH	Sustainable Water-Enhanced-Turbofan (WET) Comprising Hybrid Electric
	OFELIA	Open fan engine demostrator
	UP WING	Ultra Performance wing
	FASTER-H2	Fuselage H2 integration and Ultra efficient empennage.
Hydrogen Powered Aircraft	**CAVENDISH**	Consortium for the Advent of Aero-engine Demonstration and Aircraft integration
	HYDEA	Hydrogen Demonstrator for Aviation
	NEWBORN	Next Generation High Power Fuel Cells for Airborne application
	H2ELIOS	Hydrogen Lightweight and Innovation Tank for Zero-emissions
	FLHYing Tank	Flight demonstration of a Liquid Hydrogen tank in an unmanned cargo platform
	HYPoTrade	Hydrogen Fuel Cell Electric Power Train Demostration

1.3 Technology innovation as a decarbonization enabler

Airframers have initiated action by electrifying some subsystems of the aircraft, a concept known as MEA, which is presented with more detail in Section 1.3.2. MEA technologies have delivered operational and environmental benefits. Nonetheless, drastic measures imply the transitioning from conventional propulsion systems to AEA/HEA.

This section offers an overview of conventional aircraft energy systems, with special focus on the electric power system. This introduction covers the main changes applied to a conventional system to achieve the two different electrification grades, MEA and AEA/HEA. For the MEA concept the main electrified subsystems are enumerated and the impact on the design of the electric power network is analysed. Following, the under study concepts of AEA/HEA explained and some platforms examples are presented to illustrate the power levels expected. Additionally, this information will help the reader to follow the trade-off architecture analysis covered in Chapter 2. The conceptual understanding of the electric propulsion will help to understand the more detailed EPS study cases that have been considered during the analysis.

1.3.1 Conventional aircraft electric system

Conventional aircraft rely on fuel combustion as their primary power source. Gas turbine engines generate the thrust necessary for flight and supply power to all on-board systems during flight. Non-propulsive power, which includes power consumed by secondary systems, accounts for approximately 5% of total power usage. Figure 1-2, as illustrated in [17] , provides a comprehensive overview of the engine power output utilization in an A-330 aircraft.

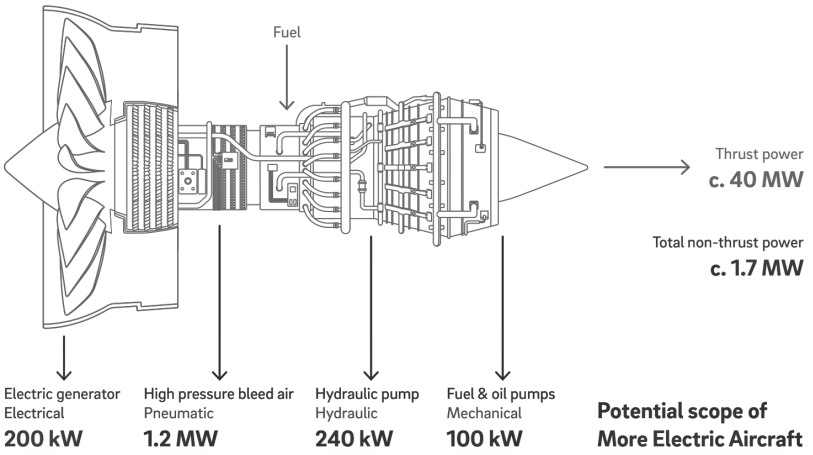

Figure 1-2. Aircraft turbine engine output power sharing. A330 sized aircraft

From Figure 1-2 it can be seen that current on board energy system is based on four different power source subsystems. They are:

- **Pneumatic power:** the main engine is connected to a compressor that produces the compression power. This feeds the Environmental Control System (ECS) and the Wing Anti-Icing (WAI).
- **Mechanical power:** a gearbox is connected to the turbine engines which

drives hydraulic pumps and other mechanically driven systems, such as the electric generators.

- **Hydraulic power:** this is mainly used to the actuation of primary and secondary flight control, the landing gear and the engine actuation.
- **Electrical power:** the main generator driven by the gearbox connected to the turbine engine provides electric power to the avionics, lights, galleys and other minor loads.

The conventional architecture of the electric power system relies on a centralized distribution system. In a twin-engine aircraft, this typically involves a split-bus configuration where each electric generator, driven by an engine, supplies power to one of two independent microgrids under normal conditions. Galley loads are powered by both feeders, forming an independent nanogrid. In case of a fault detection, circuit breakers facilitate system reconfiguration to ensure uninterrupted operation of all main loads. Figure 1-3 illustrates the fundamental architecture utilized in conventional aircraft.

It features two main 115 VAC buses operating at a fixed frequency of 400 Hz and a low-voltage 28 VDC distribution bus. This last one is formed by the ac-dc conversion units seen in the scheme. They are traditionally based on transformer rectifier units (TRU), Figure 1-4. During normal opreation of the aircraft, the 115 VAC buses are formed by tow generators driven at constant speed by two engines connected to a Constant Speed Drive (CSD), which stabilizes the variable speed of the engine. When the aircraft is at the airport, the distribution system is powered by an external source, the Ground Power Unit (GPU). Additionally, all commercial aircraft count with an Auxiliary Power Unit (APU). APU is a small gas-turbine

engine that commonly is place in the tail cone of the aircraft. It provides power to all the aircraft system in absence of a GPU and support engine starting. In case of main engine failure, APU can provide power to guarantee continuous operation of essential systems, such as the pressurization system.

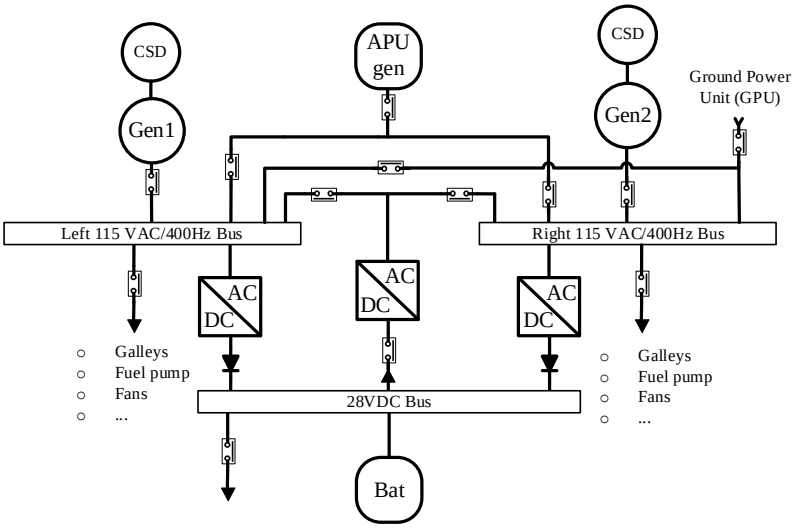

Figure 1-3. EPS architecture in conventional twin-engine airplanes.

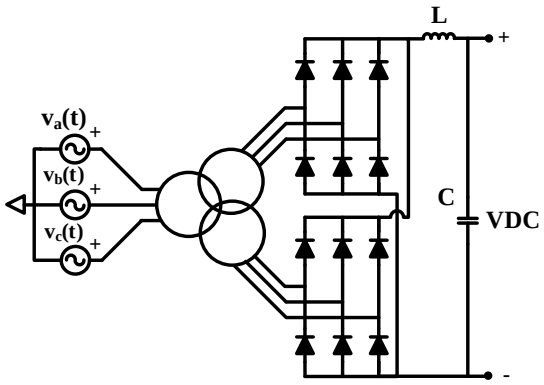

Figure 1-4. 12-pulse transformer rectifier simplified scheme.

1.3.2 The More Electric Aircraft

In recent decades, research efforts have been concentrated on exploring electric alternatives to existing non-electric onboard subsystems. This is known as MEA concept. The goal is to reduce the fuel usage and increase the operational efficiency of the aircraft. The coexistence of multiple power systems introduces complexity and diminishes overall efficiency. Furthermore, hydraulic and pneumatic systems are prone to leaks that are challenging to detect and repair, necessitating regular maintenance to ensure optimal operation. These factors underscore the importance of transitioning towards solutions with greater integration of electric systems [18].

Replacing traditional mechanical, hydraulic, and pneumatic energy-powered aircraft subsystems with electric alternatives enhances energy management flexibility and reduces power extraction from the propulsion engine (as depicted in Figure 1-2). Consequently, gas turbine design can be optimized for propulsion power, leading to higher efficiency and reduced weight. Substituting conventional bleed air systems with an electric compressor can decrease fuel consumption by 2%, while eliminating the pneumatic network at the gas turbine results in significant weight reduction [19]. In [20], it is claim a 200 kg weight reduction of the ECS.

Figure 1-4 illustrates the contrast between the current conventional energy dispatch and the desired approach for MEA solution.

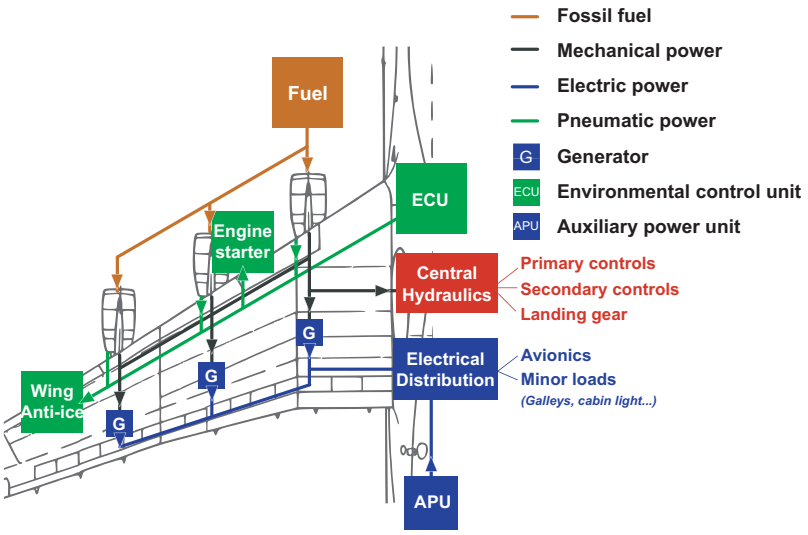

(a)

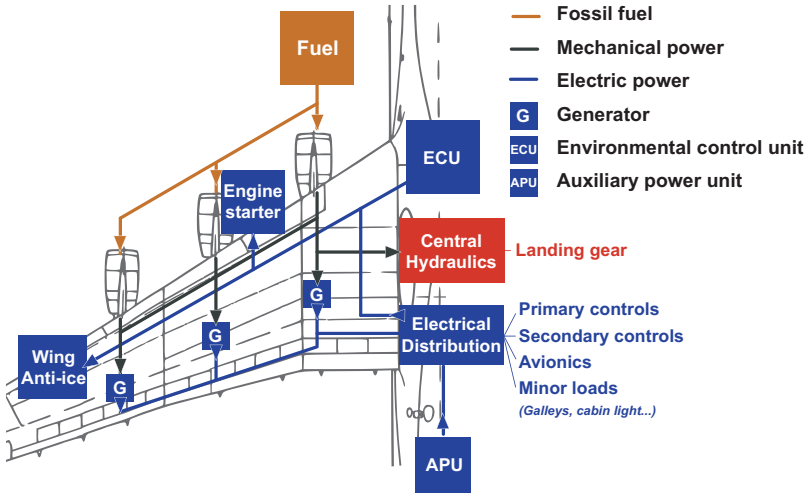

(b)

Figure 1-4. On board power systems. (a) Current commercial aircraft and (b) MEA.

The electrification of traditionally non-electric systems increases power consump-

tion from a few kilowatts to hundreds of kilowatts, with the potential to reach the megawatt range. Consequently, the original electric power supply system, depicted in Figure 1-3, requires a thorough redesign. This new distribution system must be highly reliable, fault-tolerant, and fully controllable, capable of delivering different voltage levels. Initially, new distribution designs may follow a centralized scheme similar to the traditional one, as this steady approach is more conducive to airworthiness certification. However, the trend toward integrating new high-power loads favours dividing the system into several power sections, leading to decentralized approaches, as outlined in [21] and [22]. Figure 1-5 illustrates an example of a possible decentralized network using distributed power center units (DPCUs). DPCUs are modular power units with features such as bidirectionality, self-reconfiguration, and redundancy.

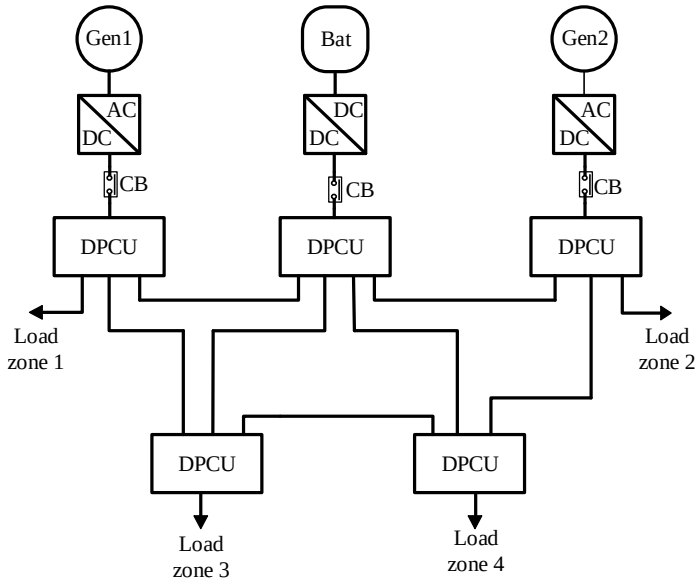

Figure 1-5. Decentralized EPS approach

Because of the higher power and voltage levels compare to the conventional ones,

new EPS solutions cannot follow the current standard regulated specifications, so the leading proposals are driven by industry requirements in terms of reliability, performance and feasibility. The new synthesis of MEA architectures need a deep examination and new standards should be populated.

The most promising MEA EPS architectures that have emerged in recent years are analyzed in [23]. Examples include the Airbus A380, Boeing 787, A350 XWB, and Embraer-E2. The A380, which could be considered the first example of MEA in flight since 2005, replaced its original hydraulic flight control actuators with electric solutions. A notable feature of the A380 EPS, compared to the conventional electric system shown in Figure 1-3, is that its two 115 VAC buses have variable frequency (360 - 800 Hz). The Boeing 787 and A350XWB, launched later (with first flights in 2009 and 2013, respectively), exhibit a higher level of electrification. In addition to electric flight control actuators, these aircraft incorporate various modifications:

- **WAI protection:** instead of using bleed-air, the new de-icing protection system presents an electric heater net made of conductive materials. Additionally, this is operated as independent zones and it uses a control algorithm that ensures the power optimization.
- **Engine starting:** Traditionally, APU and engine turbines were started using external bleed-air sources. Boeing 787 uses the synchronous generators operated as motors to star the engine and the APU .
- **Cabin ECS:** instead of using the engine bleed air, here the compressed air is produced by adjustable speed electric motor-compressors.

The power distribution architecture of the Boeing 787 is presented in more detail,

as this aircraft has the highest electric consumption thus far. Figure 1-6 illustrates a simplified scheme of its electrical system. The EPS of this plane consists of a hybrid voltage system with a main AC and variable frequency bus of 230 VAC/400 Hz and three types of secondary buses: $\pm$ 270VDC, 115 VAC/400 Hz, and 28 VDC. The $\pm$ 270VDC bus is generated by auto-transformer units (ATRU), the 115 VAC/400 Hz by auto-transformers (ATU) and the 28 VDC by TRUs.

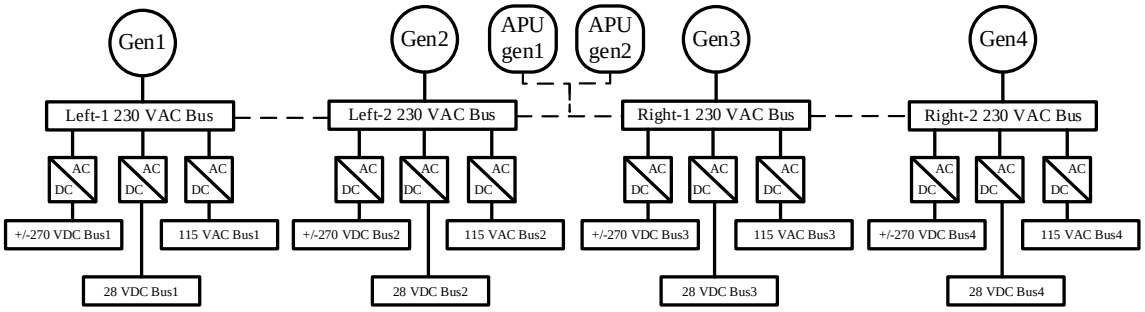

Figure 1-6. Simplified Boeing 787 electrical distribution system.

The system features a total of six generators (two per engine and two per APU), with an operating voltage of 230 VAC. This voltage level was not used in traditional designs before, it reduces the feeder weight. Further weight reduction was achieved by removing the CSD, allowing the generators to be directly connected to the engine gearboxes. This change also increased the reliability of the generators, reduced maintenance requirements, and lowered spare costs. Additionally, the Boeing 787 has two electric bays and several remote power distribution units (RPDUs), which reduce the length of the power feeders and consequently the total wiring weight. The RPUs are based on solid-state power controllers (SSPCs) that replace traditional thermal circuit breakers (CB) and relays, significantly reducing volume and weight [24, 25].

Lastly, some operational peculiarities of this distribution architecture include that only one generator can be connected to one of the main AC buses with variable frequency at any given time, and the secondary bus should be connected to only one main bus simultaneously. Therefore, one generator with its auxiliaries and supplied loads can be separated as an independent unit. Weight reduction can be identified in the Boeing 787 EPS as the main re-design target and it is the main challenge of the new electric aviation solutions.

1.3.3 Aircraft propulsion electrification

As previously mentioned, while MEA solutions presented have successfully demonstrated the feasibility and benefits of electrifying certain subsystems in aircraft, achieving the ACARE emission reduction targets, coupled with the projected growth in aircraft, demands further action from the aviation industry. Additionally, in section 1.2 AEA/HEA approach has been identified as one of the "thrust" the European Union has identified to decarbonized the air transport. The main AEA/HEA propulsion architectures are extensively covered in the literature [26–29], and simplified diagrams are presented in Figure 1-7.

There are six main electrified propulsion categories: parallel hybrid, series hybrid, series/parallel hybrid, all turboelectric, partial turboelectric, and all-electric. Figure 1-7 (a) illustrates a parallel hybrid architecture, where an electric motor is connected to the low-pressure spool of the turbine, allowing either the gas turbine or the motor-driven fan, or both, to provide propulsive thrust independently [28, 30]. In a series hybrid configuration, as represented in Figure 1-7 (b), a turboshaft drives an electric generator, and the generated power is used either to drive the propulsion engines

directly or to charge an energy storage system (ESS). The ESS also supports power demand when required [31]. Series/parallel propulsion, as depicted in Figure 1-7 (c), combines conventional fuel-based turbines with electrically driven ones to produce the required thrust. The electrically driven turbines can be powered by either a battery or a generator driven by the gas turbines. All-turboelectric propulsion, shown in Figure 1-7 (d), involves optimizing turboshafts to drive an electric generator, which then powers electric motor fans [32]. If there is a turbofan instead of a turboshaft (i.e., providing both thrust and shaft power), the total thrust is divided between the turbofan and the electric motor fans, as shown in Figure 1-7 (e) [33]. Finally, an all-electric propulsion scheme, depicted in Figure 1-7 (f), employs an ESS to drive the propulsion engines electrically [34, 35].

Depending on the aircraft type, some schemes are more suitable that others, due to the power levels required and the actual technology gap. Figure 1-8, developed by Airbus, provides an overview of the propulsion electric power levels handled in different aircraft platforms as well as the potential enabling technology [36]. Additionally, Airbus current demonstrator projects are cited. Initial developments have predominantly focused on small aircraft but are now transitioning to larger commercial aircraft, which will have greater environmental impact in terms of reducing CO_2 and NO_x emissions for future air transport systems. Notice that urban mobility or light aircrafts are identified as platforms where the all electric scheme can be adopted. For platforms where higher levels of power or flight range are required, hybrid electric propulsion schemes are suggested, where batteries are replaced by fuel cells as the main energy storage unit. Furthermore, superconductivity is highlighted as a requirement for implementing an all electric 10 MW power range platform.

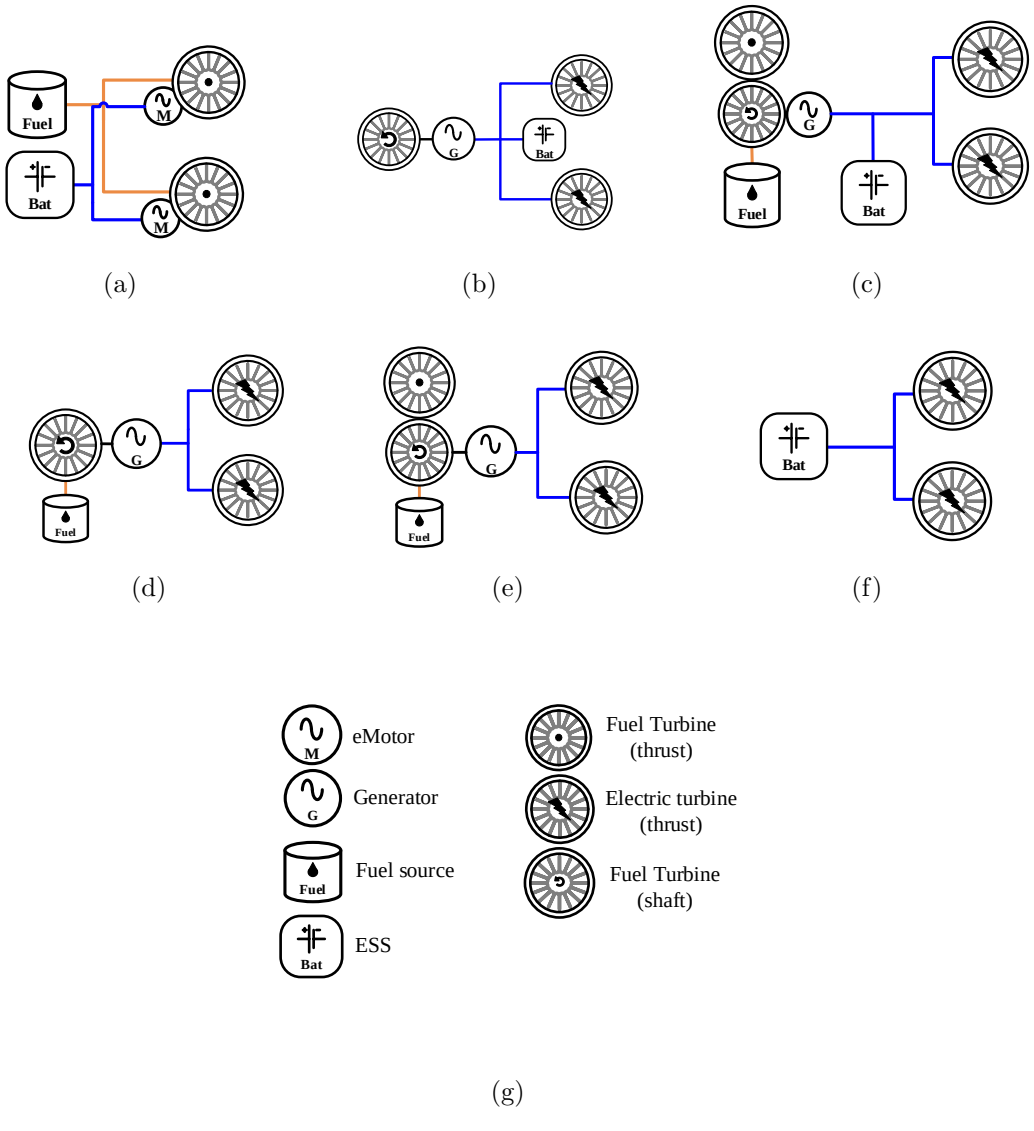

Figure 1-7. High Level AEA/HEA propulsion architecture diagrams (a) Parallel hybrid. (b) Series hybrid. (c) Series/Parallel hybrid. (d) All turboelectric. (e) Partial turboelectric. (f) All electric. (g) Legend

A review of the most significant electrified aircraft demonstrators investigated overall are listed in Table 1.2. Some of them have already performed a first flight, and

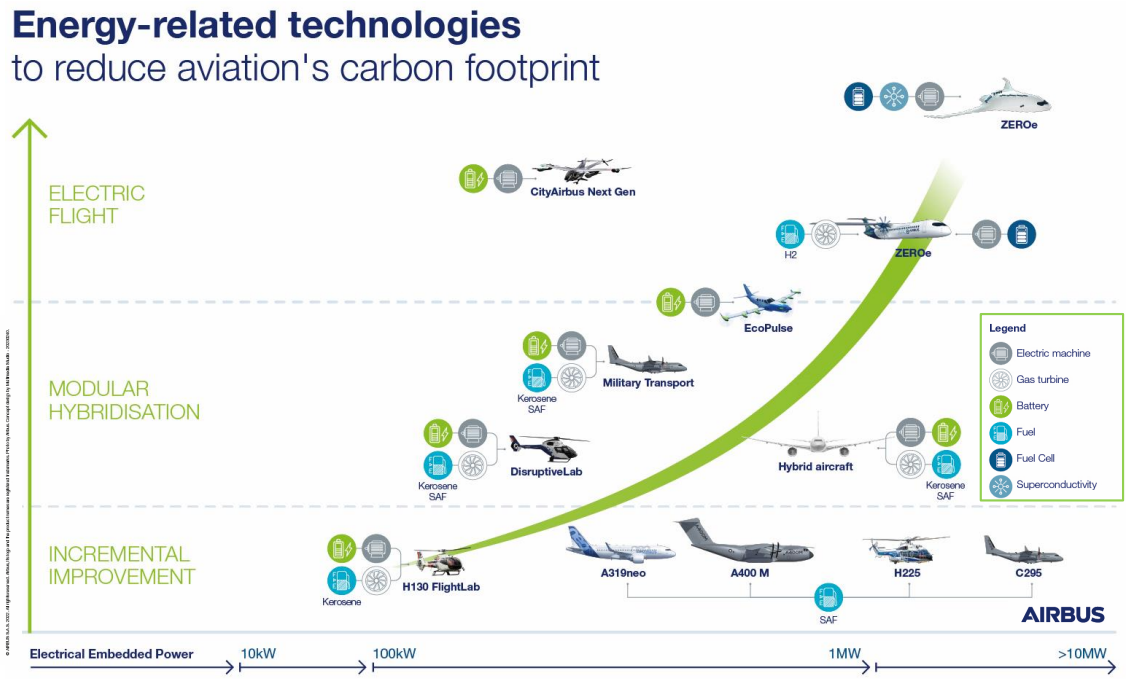

Figure 1-8. AEA/HEA power ratings and enabling technology. Airbus Roadmap

others are planning to reach demonstration mature in the future. A few of them are still concept designs. It can be seen that as the power is increasing turboelectric and hybrid propulsion configurations have been preferred. In fact, numerous studies discuss the utilization of hybrid propulsion systems in both regional and large commercial aircraft applications. Gas turbines employed in hybrid propulsion systems are designed to operate at nearly constant speeds throughout the entire flight envelope, as the electric system assists in managing peaks and troughs. Which creates new opportunities for optimization, and cost savings for operators. In Chapter 2 further analysis will be provided.

TABLE 1.2. AEA/HEA demonstrators review

Demonstrator/Team	Platform	AEA/HEA concept	Peak Power	First flight
CityAirbus	eVOLT 4 seats	All Electric	8x100kW	2019
E-FanX	Regional 70-seats	Hybrid electric 1 eMotor	2 MW	2021 (Cancelled)
ALICE **Eviation**	Regional 9 seats	All Electric	2x634 kW	2022
Tech TP Engine **Safran**	Regional Turbopropeller	Parallel Hybrid Electric	25-kVA motor-generator	2023
eDA40 **Diamond Aircraft/Safran**	Light Aircraft Single Engine Aircraft 2 seats	All Electric	130 kW	2023
EcoPulse **Airbus/Daher/Safran**	Regional Distributed propulsion EcoPulse : 5 seats	Hybrid distributed 6 eMotors	6 x 50 kW	2023
CASSIO **Voltaero/Safran**	Regional Single Engine Cassio 330 : 5-seats Cassio 480: 6-seats Cassio 600: 12-seats	Parallel Hybrid Electric	Cassio 330: 330 kW Cassio 480: 480 kW Cassio 600: 600 kW	2024 (Cassio 330)
ZeroAvia	Regional Twin-propeller Short-term: 19 seats Long-term: 90 seats	All-Electric (Fuel Cell)	Short-term: 600 kW Long-term: 2.5MW	2025 (short-term)
ERA **Aura Aero/Safran**	Regional Distributed propulsion ERA: 19 seats	Partial-turboelectric	8 x 50 / 100 kW	2026
STARC-ABL **NASA**	Single-aisle Medium range >100 seats	Partial Turboelectric (BLI)	2-3 MW	2035
SUGAR-volt **Boeing/NASA**	Regional Single aisle 150 seats	Parallel Hybrid Electric	1.3 / 5.3 MW	2030-2050
PEGASUS Concept **NASA**	Regional Distributed propulsion 70-90 seats	Partial Turboelectric (BLI)	˜ 300 kW 20% hybridization	Conceptual design
SUSAN **NASA**	Single-aisle Medium range >100 seats	Partial Turboelectric (BLI)	20 MW	Conceptual design
CHEETA **University of Illinois**	no specified	Hybrid centrilized-distirbuted	25 MW	Conceptual design
IZEA	Medium-large range >100 seats	Hybrid distrubuted Wing-body	24 MW	Conceptual design

1.4 Electric propulsion main barriers

Aircraft propulsion electrification offers the potential for a more sustainable future in aviation, yet its widespread adoption is impeded by several barriers. These obstacles include technological immaturity, such as limitations in energy storage systems and the need for higher power density and effective high voltage management. Addition-

ally, regulatory hurdles related to certification, safety standards, and integration into existing airspace systems pose significant challenges. Market demand also presents obstacles, as operators require assurance of lifecycle cost reductions to justify the higher initial investment costs compared to traditional aircraft. Demonstrating and guaranteeing these features and benefits is essential for overcoming electric propulsion barriers.

In this section the main technological barriers that aircraft electrification faces are overviewed. The main potential technology solutions, currently under study, are cited. Consequently, the section identifies the main technology development requirements.

1.4.1 Technological development

The design of MW EPS faces numerous challenges mainly related with adapting high-power electric systems to aerospace application. Primary focus on achieving lossless, compact, and lightweight systems is identified to enable zero fuel dependency or substantial fuel usage reduction. Furthermore, ensuring compliance with reliability and safety standards is essential.

An important design constrain is that unlike conventional aircraft, where overall weight decreases as fuel is consumed, electric aircraft maintain a constant weight, leading to heavier payloads over extended durations. This is translated into shorter flight ranges. There is a direct correlation between weight and lift-dependent drag, which contributes approximately 40-50% of the total drag [37]. Heavier aircraft, indicated by larger maximum take-off weight (MTOW), needs a higher angle of attack

to generate sufficient lift for take-off. Consequently, this results in increased induced drag, leading to higher energy consumption during flight or shorter flying ranges, as mentioned. Moreover, additional weight demands faster cruising speeds to maintain optimum aerodynamic efficiency, thereby increasing profile drag. Therefore, reducing the weight of every single element comprising the EPS of MEA and AEA/HEA is one of the primary research objectives.

As a matter of example, the 9-passenger Eviation Alice electric aircraft [34] has a MTOW nearly double that of the similarly-sized kerosene-fueled PC-12 [38]. This disparity explains why the targeted range of AEA Alice aircraft is 463 km, whereas the PC-12 has a range of 2803 km. This illustrates why enhancing efficiency and integrating lighter components become critical imperatives. High power density energy storage systems, electric motors/generators, wiring, and power converters are of utmost importance.

The following sections delve into key technological development areas of the power train, outlining research lines, achievements, and challenges in each domain. Four developing areas have been identified: power sources, power conversion, distribution and propulsion. Additionally, Electromagnetic Compatibility (EMC) and power density are established as transversal research topics, because of their overall influence.

1.4.1.1 Power sources

The energy storage technology must fulfil the dual requirements of steady-state and dynamic power delivery. This entails being capable of handling high peak currents, particularly during engine starting, and leading to significant continuous power demand. Moreover, adherence to aerospace safety standards mandates that the energy

storage system is sized to provide an additional 30 minutes of flight power in emergencies [39]. Consequently, specific energy and power are critical parameters defining the size of any energy storage system for aerospace applications.

Currently, SoA energy storage systems predominantly rely on Li-ion batteries. Despite a groundbreaking announcement of a lithium-ion battery achieving an energy density of 700 Wh/kg in 2023 [40], this still falls far from the specific energy of the fuel, which stands at 12,000 Wh/kg. This poses a significant hurdle for large-scale all electric aircraft. Alternative options such as Li–air batteries, boasting higher specific energy, have been proposed, although facing challenges like fast decomposing electrolytes. Li–S batteries represent another avenue, targeting specific power exceeding 500 Wh/kg [41]. Complicating matters further are the working conditions, where temperature fluctuations impact the power rate and capability of available batteries technologies. Notably, decreasing temperatures can elevate the internal resistance of batteries, potentially constraining maximum power delivery.

Due to the high energy density of liquid hydrogen, some research effort are directed towards the application of solid oxide fuel cells (SOFC) [42]. Some studies have reported a 70% reduction in fuel requirements owing to the high efficiency of SOFC and the integration within hybrid propulsion systems [43]. However, SOFC also present drawbacks such as the requirement for high operating temperatures and extended start-up times. Additionally, LH_2 storage tank design adds further complexity to this alternative. The main target is to achieve a storage tank that can guarantee safety levels and which volume is low enough to no penalised excessively the aircraft payload. Additionally, conventional fuel storage tanks are placed in the wings of the aircraft but their shape is unsuitable for holding LH_2 tanks. In [44], key design challenges related to LH_2 are addressed, and numerous projects are presently

underway to develop tank designs suitable for commercial aviation [45, 46].

Regarding generators, wound-rotor synchronous machines (WSRSM) are currently used as starter-generator (S/G) in commercial aircraft because of the control simplicity, large generation capacity and fail-safe inherit characteristic. In the new concepts of AEA/HEA there are two possible scenarios in which generators would be required. In all the propulsion concepts where turboshafts are used (i.e. series hybrid, series/parallel hybrid or turboelectric),generators are the main power source. As mentioned before, high power is expected and high efficiency and specific power become a desired target. WSRSM has reported recent efficiency and power density improvements [47], but it is not clear that they can suit the requirements of series hybrid, series/parallel hybrid or turboelectric propulsion architectures. In the rest of AEA/HEA propulsion architectures, generators only appear as S/G that only supply power in emergency or very specific cases, and similar specifications than the current S/G can be accepted. Nevertheless, S/G should perform high torque at low speed and constant power at high speed, difficult to achieve without oversizing or overloading, so there is room for improvement.

The limitations of the mentioned energy storage systems, which both industry and academia are facing are driving the pursuit of lower hybridisation ratios and alternative power sources for large-scale aircraft, such as Sustainable Aviation Fuel (SAF) or liquid hydrogen (LH_2). Nevertheless, this solution face the same challenge than fuel cells, the LH_2 storage tank design.

1.4.1.2 Power Conversion

Regarding power converters, the technology gap of the SoA power semiconductors constrain the development of high efficiency and high power density solutions. One strategy for increasing power density involves raising the switching frequency to reduce the weight of magnetics and targeting efficiencies over 95% to decrease the weight of the thermal management system. Additionally, the power rating of currently available semiconductors constrain the power converter design at high voltage MW EPS, forcing the use of multi-level topologies. In addition, EMC adds in general further challenges to the design of new EPS.

1.4.1.2.1 Semiconductor technologies. There are four main semiconductor technologies: IGBT, Si, SiC and GaN. IGBT switches can reach breakdown voltages of up to 4.5 kV with continuous conduction capabilities of up to 1.8 kA [48] and are well-used switches in other high power applications. However, IGBT technology lacks the necessary switching performance to achieve the required frequency with a typically recommended maximum switching frequency of 20 kHz for high-power devices. New 4th-gen field stop IGBTs further enhance power ratings and provide dynamic improvements, such as reducing turn-off losses resulting from tail current. However, despite those advancements, which enhance power ratings and provide dynamic improvements like turn-on energy loss reduction [49], they lack necessary switching speed for aerospace applications.

WBG semiconductor technologies, such as SiC seems to be one of the favourite candidates for the design of power converters for the propulsion EPS [50]. WBG increases efficiency at high switching frequencies. SiC MOSFETs offer promising

opportunities for enhancing operating frequency, efficiency, and power density. They can achieve relatively low on-resistances (e.g., 0.013 Ohms for a 750 V/80 A device [51]), enabling high frequency switching. Currently, the highest blocking voltage of SiC devices available in the market is 3.3 kV [52], which might required multilevel converter topologies selection. On the other hand of WBG, GaN exhibits a higher maximum switching frequency compared to SiC MOSFETs due to the two-dimensional electron gas effect, as well as higher energy gap electron-volt (eV) ranges, resulting in smaller packages for similar breakdown voltages (i.e. beneficial for pursuing high power density). Furthermore, GaN devices have lower on-resistance and parasitic capacitances, which could help increase efficiency and reduce EMI noise. However, the thermal conductivity of GaN technology is much lower than Si and SiC, requiring additional cooling efforts to prevent thermal runaway and making this technology difficult to be applied at the power levels expected at the aircraft propulsion EPS. It can be concluded that regarding semiconductor technology there still exists a certain technology gap in power modules that some researchers are attempting to overcome, for instance, by exploring hybrid switch solutions [53].

1.4.1.2.2 Magnetics design. Another component of power converters with a big influence on achieving high efficiency and high power density solutions are the magnetic components. Exploration of unconventional magnetic materials, such as nanocrystalline cores, which exhibit higher permeability than conventional ferrites cores, has been undertaken to reduce the size of magnetics. However, their use in applications like EMI filters has diminished due to higher losses at high frequencies. Furthermore, planar magnetics have emerged as a prominent solution for achieving high power density and performance in converters. The primary advantages include

the ability to achieve very compact designs and homogeneous temperature distribution [54, 55]. Nevertheless, planar magnetics face certain limitations. They require large footprints due to the reduction in profile, which might become a drawback at PCB design optimization level. Multi-layer PCB designs are necessary to address the low copper fill factor, but stacking windings may increase winding capacitance, potentially exacerbating EMI conduction noise [56].

1.4.1.2.3 EMC. MEA and AEA/HEA introduces higher number of power converters, which turns into more severe EMI levels while the EMC regulation keeps the same noise limitations. Two types of EMI are studied: conducted and radiated emissions. Excessive EMI can provoke failures in critical loads of the airplane, such as avionic systems, communication, navigation, surveillance equipment and sensors. Consequently, ensuring EMC is an important task. Additionally, a propulsion system is expected to generate high levels of electric and magnetic fields, which is a new source of concern regarding human safety, with World Health Organization (WHO) suggesting specific human exposure limits. It could be stated that the main challenge regarding EMC is the lack of knowledge about how EMI phenomena will manifest in the EPS of new electric aircraft. Consequently, a well understanding of the EMI generated by the power converters is quite important during the converter design. This is exemplified by projects such as EASIER [57], which closely examines EMI generation in hybrid propulsion systems to gain sufficient insights for providing optimized EMI filter solutions in terms of weight.

1.4.1.2.4 Power converter topologies. In the context of electrified aircraft there are several power converter topologies that are highlighted in all the power

review studies as potential solutions [58–60]. The converter topologies found are: 2-level voltage source converters (2L-VSC) or inverters (2L-VSI), multi-level voltage source inverters (ML-VSI) and modular solutions such as Cascaded H-bridge (CHB) or Modular Multilever Converters (MMC). Additionally, in recent papers it can be found other converter alternatives that try to excel the used of GaN power devices in the future electric aircraft application [61, 62]. In both cases, a two level current source inverter (2L-CSI) operating at cryogenic temperature is proposed. The most recent literature is analysed in the following lines in order to provide an overview of what is the current SoA of power converters for electric aircraft propulsion. Table 1.3 summarizes the main FoM of the presented solutions in the literature.

TABLE 1.3. Summary of the main characteristics of the SoA references with experimental verification

Ref	**Topology**	**DC bus**	**Tested power**	**Switch technology**	**Specific Power**	**Efficiency**
[63]	ANPC	2.4 kV	1 MW	SiC + Si	12kVA/kg	99%
[64]	FC	1 kV	18.9 kW	GaN	38.4 kW/kg	98.95%
[65]	NPC	3kV	1 MW	IGBT	20.8 kVA/kg	93%
[62]	2L-CSI	400 V	20 kVA	GaN	-	-
[66]	T-Type	740 V	422 kW	SiC	19.5 kW/kg	99%
[67]	2L-VSI	2 kV	1MVA	SiC	51.38 kW/kg	-
[68]	2L-VSI	450 V	11 kW	SiC	13 kW/kg	97%

2L-VSC and 2l-VSI are used in multi-phase electric motor drive applications [67, 69,70]. This configurations aim to be integrated with the motor and target to provide an integrated modular motor drive (IMMD) high power density solution. In [67], 2L-VSI are connected in parallel at a 1 kV DC bus, maximum achievable voltage level considering 1.7 kV SiC power modules. The specific power is claimed to be higher than 60 kW/kg for a 40 kHz switching frequency by following a electric-thermal co-design. The power rating of the motor is 250 kW, much lower than the twin-engine aircraft power rating requirement, but they can be a feasible study case for

distributed propulsion schemes. Another alternative, presented in [69], overcomes the voltage limitations of 2L-VSI due to the available power devices. The DC bus voltage is increased up to 2 kV by connecting in series the input of three 2L-VSI. By parallelizing H-bridge modules and using multiple three-phase systems, 1 MW power is achieved. The configuration is presented as a IMMD, achieving a power density of 35.36 kW/kg and a peak efficiency of 99%. Furthermore, the design considers partial discharge phenomena, additional challenge inherit in IMMD because of the low pressure operation condition.

Among the ML-VSI topologies expounded upon in the literature, Neutral-Point Clamped (NPC) or Active Neutral- Point Clamped (ANPC), T-type and Flying Capacitor topologies are the most recurrent. In [63], an ANPC inverter is proposed for a 1 MW motor driver with a 2.4 kV DC bus. 99% efficiency and a specific power of 12 kVA/kg are achieved while using Si IGBT for the clamping power devices to reduce the overall cost. An special modulation scheme which makes the Si IGBT switch only at fundamental frequency and perform soft-witching mitigates the under-performance characteristics of this switch device technology (as it was highlighted in Chapter 1). Furthermore, special attention is given to commutation loops, inherit challenge of this topology that can suffer from overshoot deterioration. Following the research line around multiple three-phase systems, in [65] the full design and implementation of a 4 MV rectifier stage connected to a multiple-phases generator is shown. This power rectifier builds two independent 3 kV DC buses. The solution consists of two identical units, each of them formed by a series/parallel combination of three-pase NPC modules. The total number of modules in each unit is 4, where the output of two three-phase NPC are connected in series to provide 3kV and this configuration is repeated and connected in parallel to reach 2 MW per unit. Each of the three-phase

NPC module is connected to one of the eight start-connected three-phase windings of the generator [71]. The implemented solution reports efficiencies under 93% and a specific power of 20.8 kVA/kg. Another example of three-level power converters is shown in [66]. It follows a similar multi-winding scheme, which has not such a high power rating but higher efficiency result. In this case, a dual configuration of two T-Type three level converters is used. The work shows a high level of integration, both input and output EMI filter are integrated with the power converter stage and busbar achieving a specific power of 19.5 kW/kg. EMI filters are a common bulky and voluminous part of every power converter, so achieving this level of density is a significant milestone. Regarding power inverters with higher number of voltage levels, multi level Flying Capacitor (ML-FC) topology is proposed in [64, 72–74] as a disruptive solution. The mentioned papers described the development of a 10-Level ML-FC inverter based on GanFET power devices to drive an electric motor in an aircraft application. The solution presents three 10-Level ML-FC modules [73] interleaving to supply a peak power of 18.9 kW with an output fundamental frequency of 1 MHz (i.e. high specific power electric motors projection [75]). The overall specific power of the inverter approach is 38.4 kW/kg and the peak efficiency claimed is 98.9%.

High specific power and efficiency are the main design goals of the power converter solutions displayed, however reliability is a major requirement in future EPS. Therefore it has to be considered that even though the previous solutions can cover the power rating specifications, analysis of their reliability is needed to identify redundancy requirements. When redundancy is considered in the design case, the other two FoM (i.e., efficiency and specific power) are affected [76].

1.4.1.3 Distribution

In the context of power distribution, MW applications demand high voltages, reaching kV levels, to mitigate otherwise excessively high current levels. The adoption of high voltages is imperative for weight reduction in the system. High current levels would require huge conductor sections in order to not generate massive power losses, which turns into a prohibitive cable weight. Current industry trends explore high-voltage operation in aircraft, with study voltages exceeding 1 kV, and a potential new standard of 3 kV, as indicated by the E-FANX project [31]. However, concerns arise in aerospace applications when implementing high voltage levels, as they elevate the risk of electric discharge, serial arcs, or space charge within the power system. Specifically in power conversion devices, electrical machines, connectors, and cabling/wiring [77]. Full comprehension of electrical discharges, particularly in terms of their initiation and severity within the aircraft environment, is paramount for ensuring safe and reliable operation [78]. For MEA, SAE AIR6127 investigates arcs and electric discharge up to 1.5 kV, offering guidance for safety implementation. However, AEA EPS will operate beyond the voltage levels studied in this reference [79].

To assess the risk of experiencing electric discharge within the system, Paschen's Law is of essence. This empirical equation, discovered by Friedrich Paschen, examines voltage behaviour across short distances between electrons in a static gas medium [80]. This law is vastly used to understand the altitude influence on the partial discharge, which is fundamental in a aviation application. Essentially, the equation indicates that, for a given gas medium, distance or insulation thickness must increase as pressure decreases. Numerous studies have investigated the voltage

levels at which future electric aircraft EPS can operate without encountering partial discharge by using this law [81, 82]. Conclusions suggest that conductors and power electronics, in general, will require significantly larger insulation, leading to additional unwanted weight and volume that offset the benefits of reducing conductor size by increasing voltage levels. A significant research effort is focused on developing new cable solutions due to their impact on the overall weight of the aircraft. In a large transport aircraft, such as the Airbus A380-800, the total length of the wiring system is approximately 470 km, resulting in a total weight exceeding 5 tons [83]. In [78], recent advancements in insulation technologies are reviewed, including micro-layered insulation structures and the incorporation of micro or nano fillers.

Fault-management is an important aspect at the distribution network too. As investigated in [84] the definition of the DC bus architecture and isolation strategy impacts in the final system weight due to the use of excessive number of circuit breakers (CBs) and oversizing of components to guarantee continuous operation of the propulsion system. Adoption of DC distribution systems adds an additional challenge, this is the protection device technology. Solid State Circuit Breaker CB seems to be the most desirable solutions. Due to low impedance of the high voltage system big di/dt are expected. Transitional SSCB design result in heavy solutions because of the liming current inductor used [85]. New alternatives that could suit better the aviation application requirements are explored in [86].

Finally, in addition to power converters as a source of EMI, cables and wires are crucial aspects regarding EMI of the overall on-board system. Cables are part of the propagation path, emitting noise/interference from connected sources. This primarily concerns conducted emissions, where cables serve as the medium through which interference can leave the equipment. Such cables can radiate interference to the

equipment connected to them. A critical aspect of cabling is the connector, as it might form a weak spot, for instance, for crosstalk. In cables and connectors, a conversion of common-mode (CM) to differential mode (DM) conducted EMI or vice versa can occur.

1.4.1.4 Propulsion

The main types of electric machines highlighted as potentially utilized in electric aircraft are: permanent magnet synchronous machine (PMSM), induction machines (IM) and switched reluctance machines (SRM) [47]. PMSM are highlighted as a promising alternative as they can achieve higher power densities (i.e., from 3.3 to 8 kVA/kg) [87]. In [88] PMSM with internal magnets and with Halbach array are identified as the best options in terms of high specific power. The paper exposes a detailed motor design with specific power maximization target. Regarding SRMs, this technology has been used in the Lockheed Martin F-22, but have never been applied in commercial aviation yet. SRMs provide a more robust and reliable solution compared with PMSMs but lower power, torque density and efficiency than PMSMs. Similarly, IMs are an attractive solution because of they high-speed operation thanks to flux weaking capabilities but present lower torque density than PMSM [89]. Finally, HTS research has already reported impressive results that demonstrate this technology can meet the strict power density and efficiency requirements of AEA/HEA [90]. However, HTS machines required a cryogenic cooling system to operate at cryogenic temperatures, which are bulky and have very low efficiency [91]. A broad review of current SoA and potential future electric machines for the use in the future aircraft is presented in [87] and in [92] the existing motor

technologies used in the recent AEA/HEA demostrators is provided.

One important aspect to take into account for any of the cited types is that the pursuit of high-power small machines design hinder the thermal capability of the electric machines, being more critical in the case of PMSM because they can reach irreversible demagnetization. Additionally, high thermal operation can compromise the winding insulation lifetime, which would be already constrained by the high voltage and possible partial discharge discussed. Furthermore, motor directly coupled with the propeller is preferred to avoid the presence of a gearbox. This imply a restriction of the motor rotational speed to match the propeller speed. This challenge the power density optimization as this parameter is directly related to the power density of the motor [93]. Table 1.4 [87] draft the power density requirements according to aircraft type and potential EPS architecture.

TABLE 1.4. Electric machines power density requirements

Aircraft type	Aircraft architecture	Power density [kW/kg]
Narrow body	Parallel hybrid	>3.0
	Turboelectric	>6.5
Regional	Parallel hybrid	>3.0
	Turboelectric	>6.5
Wide body	Turboelectric	>10

1.4.2 Regulation and certification

On top of the identified technological development challenges, that could be defined as necessary to obtain EPS solutions for AEA/HEA that will have a rationale flight range, there are extra challenges in terms of safety levels that are necessary to fulfil for certifying the EPS.

Conventional aircraft EPS design is strongly regulated and there are many standards and certification guides that ensure any design will achieve safety and quality needs. The main challenge with new aircraft concepts is that the current regulation and certification are not currently prepared for them, such as hybrid or full electric solution, due to the disparity of power, voltage and current levels. For these reason, certification agencies, original equipment manufactures (OEMs) and equipment manufacturers are constantly working to achieve regulation and certification standards for greener aircraft. For instance, one topic of discussion is the possibility of design the EPS separated from the secondary distribution network. This would imply less restrictive EMI limits at the EPS due to absence of sensitive equipment and consequently potential smaller and lighter EMI filters that compare with designs based on the actual regulation. The application of actual EMI limits to EMI filters at such power level might constrain the size/weight optimization of EMI filters, significantly reducing the power density improvement due to their high contribution to the overall power converter weight [94]. Furthermore, DO-160 does not provide regulation limits under 150 kHz. If needed other standards such as MIL-STD-461 could be used as a reference. However, caution should be taken when combining limits from different standards. The test methods and setups are not always the same in different standards, and therefore the limits might not always be comparable. For instance, in MIL-STD-461, conducted emissions are measured as voltages by a LISN, while in DO-160, they can be measured by a current probe.

Several safety regulation and certification requirements are defined by EUROCAE, the RTCA, which DO-160G belongs to, the FAA, ATM International International, EASA and military standards. A big effort is still needed to reach such levels in the context of AEA/HEA. EUROCAE has created a working group, the WG-113, with

the aim to work towards the creation of standardisation needs for hybrid propulsion and recently has published guidance material [95]. Other working groups are: SAE-E-40 Electric Aircraft Steering group, the AE-4 Electromagnetic Compatibility committee and the AE-8D Wire and cable committee. Additionally, some EU-funded projects, such as CONCERTO [96], are working to construct novel certification methods and means of compliance for disruptive technology for aviation.

Chapter 2

Electric propulsion system architectures for commercial aviation

In Chapter 1, the main technology challenges to overtake for the implementation of EPS have been discussed, key technology gaps have been identified, and research lines for disruptive technologies have been presented. This Chapter is focused on the top level electric system analysis, crucial to set the requirements of the different building blocks, which guide the technology development effort.

Top level requirements are dependent on the type of aircraft, and the study of the aircraft as a synergy of all components and disciplines is needed to define them. The EPS architecture definition requires understanding the interaction of the electric system with other aircraft systems, fuselage wings, aerodynamics, etc. Full analy-

sis process has high complexity and proper study of all the aircraft systems would require Model-Based System Engineering (MBSE) and Multidisciplinary Design Optimization [97–99]. But MBSE is out of the scope of this thesis and this chapter will focus on the impact of the EPS alone. Nevertheless, the analysis of the EPS architecture alone can provide useful information which helps to identify the propulsion architecture that would be the most suitable for each aircraft type. For instance, a measure of the EPS Key Performance Indicator (KPIs) such as weight, volume and efficiency.

Distributed propulsion is highly regarded in some future electric aircraft proposals to enhance the fuselage aerodynamics [100], [101]. However, other studies report that distributed propulsion negatively impacts power, weight, and volumetric requirements for the electric system [102]. It is concluded that a proper evaluation would require the use of MBSE and consequently this is not covered in this document. From now on, the analyses are focused on the electrical architecture of a twin-engine A320-based aircraft,see Figure 2-1.

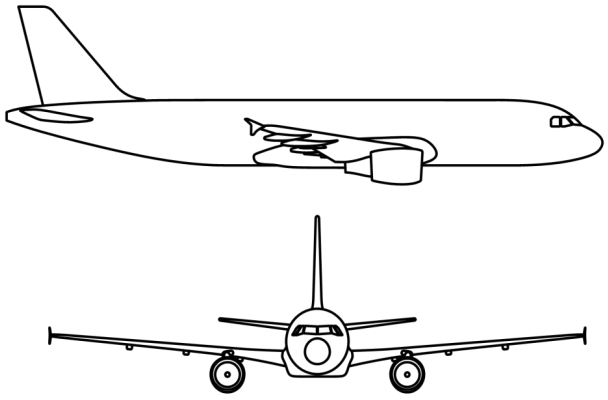

A320 specifications	
Range	6100 km
Seating	150-180 seats
Max Payload	16.6 tonnes

Figure 2-1. A320 aircraft appearance and main specifications.

In this chapter an analysis methodology to study and trade-off different EPS ar-

chitecture options is proposed. Numerous EPS cases are compared with the used of several figures of merit (FoM). Previously, the main building blocks forming each propulsion architecture EPS are identified and the principal assumptions at system level in which the study cases are based on. Additionally, in this introduction aerospace safety regulation considered during the analysis is covered.

2.1 Introduction

In this section, a brief introduction to the main components present in any AEA/HEA EPS is provided. Following, the main regulation requirements applicable to the study, as well as, a brief reviewing of reliability engineering modelling are discussed.

2.1.1 Main building blocks of AEA/HEA EPS

The conventional aircraft EPS architecture of a twin-engine airplane has been presented in Figure 1-3, section 1.3.1. The main elements of the electric network are: two generators, an APU, two 115 VAC buses, one 28 VDC bus, a 28V battery, unidirectional ac-dc conversion units, connection cables and several CBs which will help on the reconfiguration of the distribution network to guarantee supply continuity in case of any unit fails. Figure 2-2 and Figure 2-2 illustrate simplified diagrams where the main building blocks expected in all the propulsion cases , see Figure 2-2. Figure 2-2 cases are based on DC distribution and Figure 2-2 ones, in AC distribution.

The main elements of each of the propulsion architectures is briefly presented for each of the distribution type. In any of the cases, circuit breakers have been placed

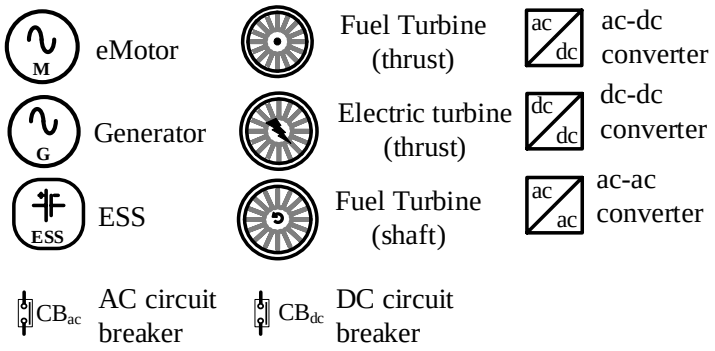

Figure 2-2. Symbol representation of the main building blocks.

following a fault-isolation strategy similar to the one used in ship microgrids [103].

Figure 2-2.a and Figure 2-2.a represent a parallel hybrid scheme with DC and AC distribution, respectively. ESS units are the main electrical source, which will be sized depending of the hybridization degree. A dc-dc power converter controls the power extraction from the battery and the voltage level of the main DC bus. Electric motors are mechanically attached to the turbines and support them on the peak thrust periods. The electric motors are driven by a dc-ac power converter which controls their speed and torque. With regards the case with AC distribution, the main difference is that a double power conversion stage is needed to connect the battery to the power bus. Assuming a conventional two stage power conversion scheme, a dc-dc converter is followed by a dc-ac, which synchronises to the AC distribution voltage signal.

Series hybrid concept is illustrated in Figure 2-2.b and Figure 2-2.b. The turbines are fully driven by an electric motor, which is controlled by an ac-dc at DC distribution case, and by a ac-ac power converter from the AC bus. A generator attached to a gas turbine, turboshaft, and a ESS are the main two electrical sources. The

ESS follows the same connection to the DC bus that was explained for the parallel hybrid case. The generator is interfaced with the rest of the network by a ac-dc power converter, or rectifier, in the case of DC distribution and with a ac-ac power converter with AC transmission. The ac-ac and dc-ac power conversion units allow to operate both generator and motor at different frequencies and to have a variable frequency AC bus.

In a series/parallel scheme, Figure 2-2.c and Figure 2-2.c, the previous concepts are mixed. Therefore, the system presents some fuel driven turbines which are attached to a generator and also electric motors driving other turbines. In the schemes represented in this document, it is assumed that the two turbines of the twin-engine aircraft move two generators. The power produce by them and a ESS unit feeds an electric motor that drives a third turbine. In the AC distribution variant, if both generators supplied the electric motor, both AC buses must operate with the same frequency. Otherwise, one must keep disconnected in a idle mode. Partial turboelectric system, Figure 2-2.e and Figure 2-2.e, is similar to the series/parallel architecture presented but without a ESS unit.

Figure 2-2.d and Figure 2-2.d illustrates full turboelectric schemes. The fuel driven turbines present in the system are turboshhafts, whose aim is to provide shaft power to drive a generator. Thus, the generator power is adapted by a ac-dc power conversion unit, DC distribution, or by a ac-ac power conversion unit, AC distribution, and deliver to the bus. Electric motors are the responsible of provide the needed thrust. The motor drive follows the same configuration explain in other cases.

Finally, the last case is the all electric propulsion configuration, see Figure 2-2.f and Figure 2-2.f. The full propulsion power is provide by the ESS unit and thrust

is produced by turbines driven by electric motors. With AC distribution, the ESS is split into two smaller units, each of them feeding one of the motors through one of the two AC buses. Two AC buses are assumed as in conventional twin-engine aircraft electric distribution. In this particular case, it can be seen AC distribution requires a double conversion to connect the ESS to the bus, this clearly penalize this approach.

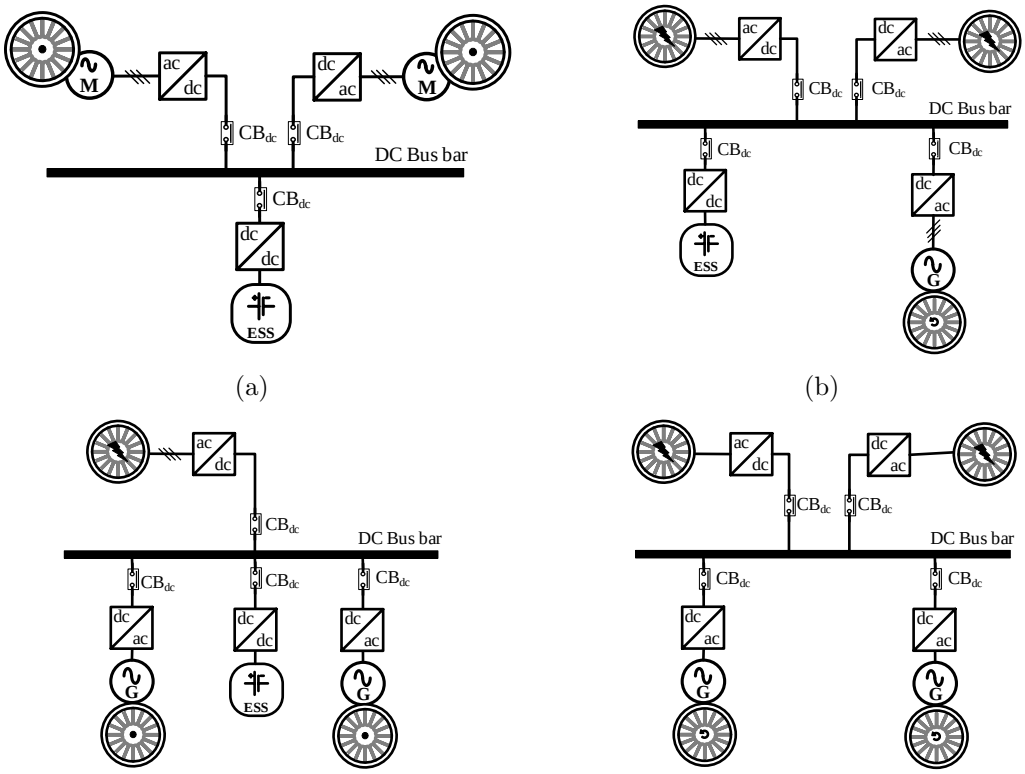

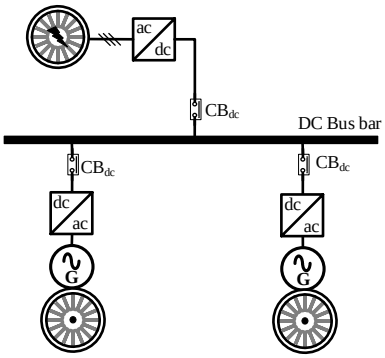

(e)

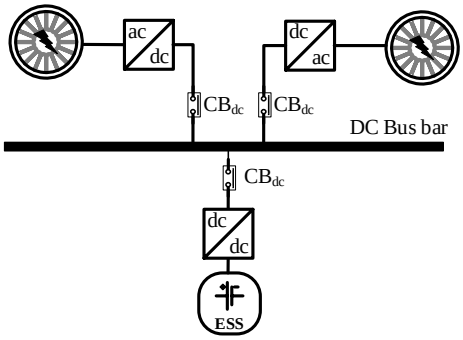

(f)

Figure 2-2. Simplified schemes of the future aircraft EPS with DC distribution. (a) Parallel hybrid. (b) Series hybrid. (c) Series/parallel hybrid. (d) All turboelectric. (e) Partial turboelectric. (d) All electric

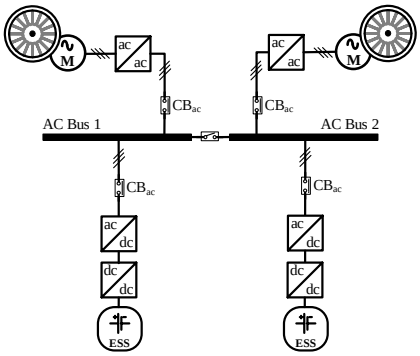

(g)

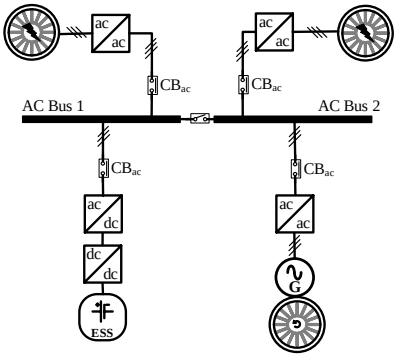

(h)

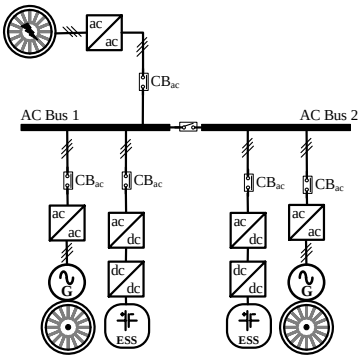

(i)

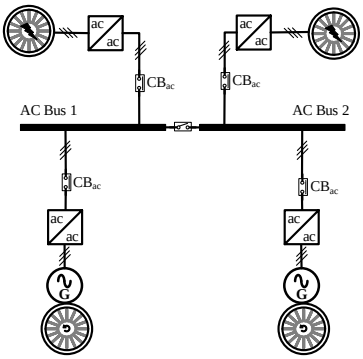

(j)

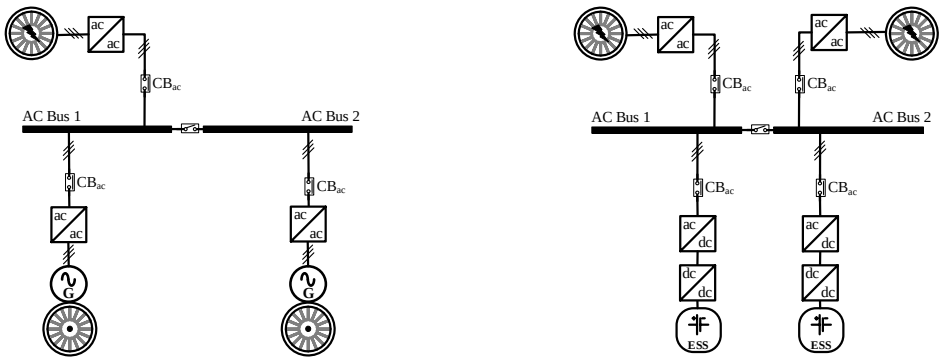

Figure 2-2. Simplified schemes of the future aircraft EPS with AC distribution. (a) Parallel hybrid. (b) Series hybrid. (c) Series/parallel hybrid. (d) All turboelectric. (e) Partial turboelectric. (d) All electric

From the identification of the different elements involved in the EPS and comparing between similar propulsion architectures with DC, Figure 2-2, or AC, Figure 2-2, distribution schemes, it can be appreciated the first scenario seems to provide easier integration of all the elements. It seems to imply lower number and power conversion units overall. This reinforce the main trend in adopting DC distribution because of cable weight reduction that has been discussed in Chapter 1. AC approaches with higher number of power conversions or series connection of power converter units might tend to achieve lower efficiency than DC distribution ones. Nevertheless, in this PhD thesis both distribution options are considered of interest. And the requirements AC distribution building blocks need to become a competitive solution when compare with DC approaches has been evaluated.

2.1.2 Aerospace safety regulation applicable to EPS system level analysis

On top of any design of the EPS, there is certain safety requirements that should be strictly guaranteed. The EPS system can be characterised under the safety requirements defined in the DO-254, Design guidance for Airborne Electronic Hardware. The DO-254 is defined as a requirement-driven process-oriented safety standard used on commercial electronics that go into the aircraft [104]. It provides guidance of what should be the target system failure rate. Five Design Assurance Levels (DAL) or categories are defined depending of the criticality of equipment and the level of compliance, they are summarised in Table 2.1. EPS as a whole system can be allocated in the most stringent category, as the total failure of the system may derive into the crash of the plane.

TABLE 2.1. DO-254 Design Assurance Levels (DALs)

DAL	**Description**	**Target System Failure Rate (failure/flight-hr)**	**Example system**
Level A (Catastrophic)	Failure causes crash, deaths.	10^{-9}	Flight controls
Level B (Hazardous)	Failure might cause crash, deaths.	10^{-7}	Braking systems
Level C (Major)	Failure might cause stress,injuries	10^{-5}	Backup systems
Level D (Minor)	Failure may cause inconvenience.	No safety metric.	Ground navigation systems
Level E (No effect)	No safety effect on passengers or cew	No safety metric.	Passenger entertainment

DO-254 is more complex than the definition of hardware reliability targets as it defines an entire requirement-based design flow with strict process assurance that would need of longer explanation but would not be of interest in the context of this

thesis. In this document only the DAL definition is taking into account as a reliability target guidance for the trade-off of the different EPS types. Aircraft systems reliability is a complex endeavour from the initial design stage until the final implementation. SAE ARP4761A provide recommended practice guidance to conduct safety assessment process on civil aircraft. For the sake of simplicity, it has been followed in the later explained analysis [105]. Figure 2-3 shows a block diagram summarizing the process.

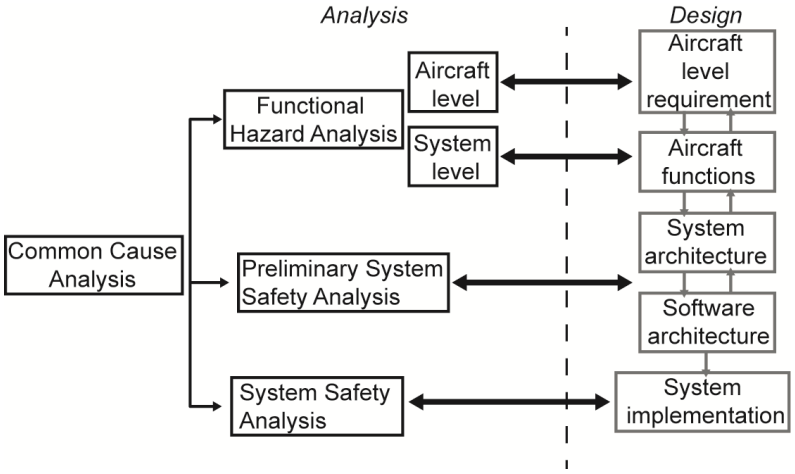

Figure 2-3. SAE ARP4761A general flow of the safety life cycle

As it can be seen, several safety analysis are recommended during the different stages of the aircraft design. In the architecture evaluation presented later in Section 2.2.2, Functional Hazard Analysis (FHA) and Preliminary System Safety Analysis (PSSA) are applied. FHA is performed in early stage of the aircraft design and is mainly focus on identification of the possible failure conditions, effects and hazard categorization following for instance DO-254 DALs. FHA results feed into the PSSA in which each hazard identified is analysed in a more qualitative way by performing,

for instance, fault tree analysis (FTA). In addition to the mentioned reliability requirements, other airworthiness standards applicable for certification of the airplane can be considered to enrich the EPS analysis. Some additional safety requirement considered in the architecture evaluation performed in this work is the contingency fuel requirements defied in [106]. Also, NASA establishes the reserve fuel requirements to be able to continue flying additional 200 nm to the regular route [107]. Thus, in the analysis it has also been contemplated that all the requirements mentioned must be fulfilled in absence of one engine. This is explained in the pilot guides [108].

2.1.2.1 Reliability modelling

In this thesis, part of the architecture analysis is focused on reliability prediction. When performing reliability modelling and failure studies of any system is very important to first accurately define the failure is aimed to analyse. In this case, the failure is defined as the total failure of the propulsion system. The common metric used to provide qualitative data to perform an analysis is the observed failure rate, or also called just failure rate [109]. The failure rate of a device varies along its life cycle. This is commonly represented by the bathub distribution, which is formed by the addition of three Weibull distributions [110], Figure 2-4.

In PSSA commonly the constant failure rate of the useful life period is used for simplicity. Several basic probability rules involved in reliability prediction analysis to model systems relations [109]. They have been summarize in Table 2.2.

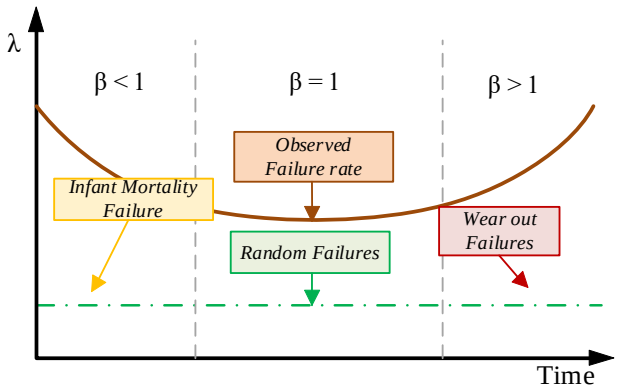

Figure 2-4. Bathub distribution

TABLE 2.2. Basic reliability prediction rules

Probability rule	Description	Equations
Multiplication	It expresses the probability of two events happening simultaneously. It is used with series connection of systems, where the failure of one of them will interrupt operation.	$R = Ra * Rb$
Addition	It defines the probability that event A, or event B or both occurring. It is used with active redundancy cases, when two identical systems are connected in parallel but only one is necessary to operate. This is also known as active redundancy.	$R = 1 - (1 - Ra) * (1 - Rb)$
Binomial	It defines the possibility that more than "r" out of "n" succeed. This is used with partial redundancy cases, where "r" systems are needed to operate but there are a total of "n" identical systems.	$R = \sum_{i=r}^{n} \binom{n}{i} \cdot R^i \cdot (1 - R)^{n-i}$
Poisson	It defines the succeed probability of "n" paralled connected elements where one is active and the rest are in stand-by mode. This is used in stand-by redundancy, where there are back-up units connected to the main system.	$R = \sum_{i=1}^{n} \left(e^{-\lambda \cdot t} \cdot \frac{\lambda \cdot t^{i-1}}{(i-1)!} \right)$

Furthermore, to quantify the reliability of the EPS or power electronics, there are several reliability calculation methodologies that can be used. They can be categorized based on the model used in three categories, sorted from more to less simplicity, they are: Part-count model, combinational model and Markov Model [111]. A combination model has been chosen to perform the reliability analysis of the architectures trade off in the study proposed in this thesis. Combinational models define the relations of the sub-parts of the system, it is, they describe the combination of events leading to a defined system. The most used tool from this family is the

FTA. This graphical method provides a deductive calculation of the effect of the malfunction of any component and has been extensively used in the field of power electronics at different levels [112, 113]. Figure 2-5 offers an example of a fault tree reliability analysis.

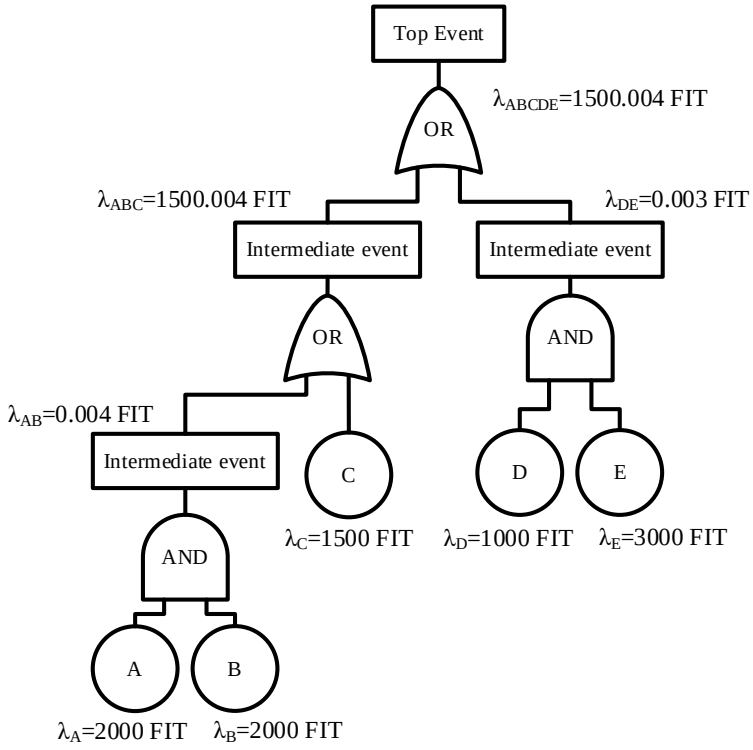

Figure 2-5. FTA illustrative example

From bottom to top, it is represented the different components of the system. Then, the relation among them is represented by using logic gates, where the gate "AND" illustrate a active redundancy dependency and the "OR" gate a series connection. Intermediate event, can refer to a subsystem or a sub-event. The top event represent the failure that is studied.

As previously mentioned, Poisson rule stand for stand-by redundancy, and this can be included in the FTA by defining a gate that stands for this rule. However, it is worth noting that this calculation method ignores the failure of the standby element before running, FTR and the failure during the connection, FTS. In order to include that, a "Priority AND " gate has been used, which imposes and AND gate condition with specific execution order among its inputs. The spare unit reliability is defined with an OR gate whose inputs are the following three events: 1) automatic switch fails to switch on demand to start standby component; 2) standby element FTS given successful operation of the automatic switch; and 3) standby element FTR after successfully substituting the failed element.

To identify where the redundancy should be applied in the system in order to lower the failure rate, the weakest-link technique has been applied. This consists in identifying the element or subsystem with the highest failure rate and to apply redundancy to it. An example that illustrates all explained above is displayed in Figure 2-5.

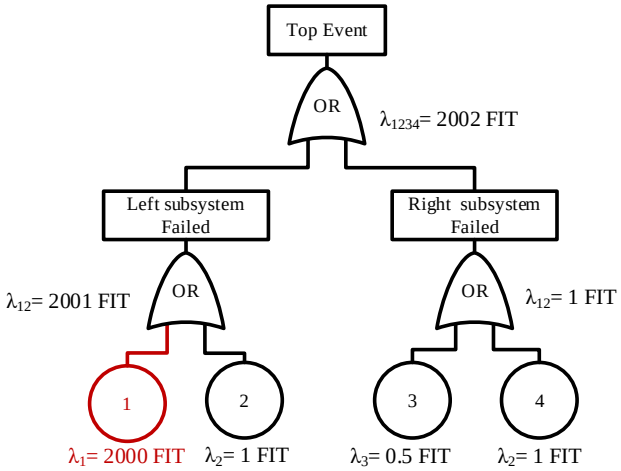
Top Event
OR
λ1234= 2002 FIT
Left subsystem Failed
Right subsystem Failed
λ12= 2001 FIT
OR
OR
λ12= 1 FIT
1
2
3
4
λ1= 2000 FIT
λ2= 1 FIT
λ3= 0.5 FIT
λ2= 1 FIT

(a)

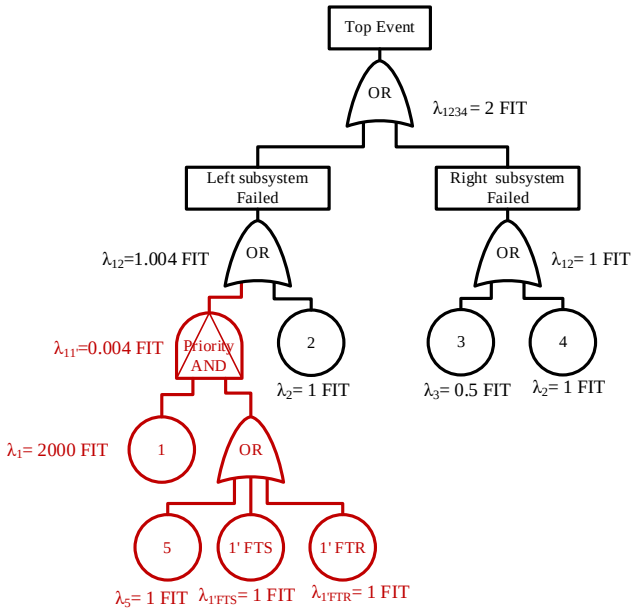

(b)

Figure 2-5. Highlighted in red: (a) Application of the weakest-link. (b) Standby component represented by a logical "priority AND" gate.

In the context of power electronics it is require reliability research on failure rate models of the key components. They are power semiconductors, capacitors, gate drivers and magnetic devices, being the first three the most vulnerable ones [114]. Empirical-based model, is widely used as failure rate model for electronics devices. Although there are several available, the most used one might be the Military-Handbook-217. However, it should be used wisely, taking into account it has certain limitations, such as, constant failure rate assumption and often pessimistic data [115]. In the particular case of aviation application, cosmic ray intensity should be taken into account in the reliability studies as it has been reported in [116]. At high altitudes the higher cosmic radiation can derive into an increase of the random failure rate of semiconductors, being the blocking voltage and the radiation particules flux

intensity the main influencing factors. Analysis in [117] gives an example of how to consider this phenomena within the reliability analysis. In this thesis the failure rate of the different components has been defined from internal company technology studies and SoA reviewing.

2.2 Proposed propulsion systems evaluation for commercial aviation

As it has previously introduced, due to the power rating of the AEA EPS, the design is not trivial as several technologies challenges have to be tracked for each of the different building blocks of the EPS. At the same time, definition of system level requirements are essential to handle the technology challenges in an efficient way. This is the reason there is a big research effort to identify building blocks projection characteristics and aircraft architecture requirements.

For instance, based on the results obtained from some projects, such as DRAGON EU project, runned by Onera the Aerospace lab [118], researches are trying to defined the criteria to classify the building blocks so the current trend in the state of the art technology can be materialized in mainly those three FoMs: reliability, efficiency and specific power or power density. Table 2.3, shows the specific power and efficiency for the most significant technology evolution scenario toward 2035.

Authors in [119] have developed an extensive historical data base study to identify the efficiency and specific power projections of electric machines. The results claim that by 2050 an efficiency of 98.9% and 50kW/kg is achievable. In [120], the type of

power converter presence in the conventional aircraft versus those needed in future electric ones is evaluated. Some FoM of different converters are presented for power converters greater than 5 kW based on supplier data. The power density of any converter type is not higher than 1.5 kg/kW. In [87] it is highlighted some power density targets at system level of the future electric aircraft that have been set by various organizations in long-term plans. NASA seeks power densities of 13 and 16 kW/kg in 10- and 15-year plans, respectively. The U.S. Air Force requires 5 kW/kg in a 20-year plan, whereas Airbus targets 10–15 kW/kg in a 15-year plan.

TABLE 2.3. Onera building blocks specifications

Building Blocks	**Specific Power [kW/kg]**	**Efficiency [%]**
Generator	19	98
Motor	25	99
Inverter	25	99
Cable	0.5 kg/m	99.6
CBs	100	

Some other works in the literature have aimed to define as well the future electric aircraft design specifications. An example is published in [121]. This work presents a preliminary study of a commercial aircraft based on a narrowbody airplane type, A320. The work presents a comparative evaluation of two propulsion architectures where cryogenic-fuels for alternatives Jet-A fuels and distributed propulsion are explored for identifying their benefits and limitations in the context of AEA/HEA. However, only an all turboelectric propulsion architecture and DC distribution are explored in this analysis. A more extended system level analysis which covers the most common AEA/HEA propulsion architectures and both DC and AC distribution approaches is proposed in this thesis. The aim is to define system specifications in terms of specific power and efficiency and estimate the best solution achievable with the expected technology improvement in 10 years term.

With the aim to contribute on the architecture requirements definition challenge, this section presents a high-level study of the different EPS architectures to estimate the most promising configuration for future electric aircraft in the context of a twin-engine aircraft type, it is equivalent to an Airbus A320. The comparison among all the cases is done based on three different FoMs: reliability, efficiency and specific power or power density. All the study cases designed for the analysis include redundant elements needed to satisfy the maximum failure rate imposed in DO-254. The study case definition, assumptions taken, calculation methodology and final results are presented in the following subsections.

2.2.1 Definition of the study case and assumptions.

The analysis is oriented to narrowbody passenger aircraft class architectures, which is the main contributor of CO_2 emissions related to commercial aircraft, as has been explained in Chapter 1. Based on the current power required, from previous studies, it is considered that the estimated maximum power of the propulsion system would be around 20 MW [121]. In Figure 2-6, the main dimensions of the aircraft, Figure 2-1, that has been taken into account for the calculation of the cable weight are displayed.

Current trends on high-voltage operation of aircraft study voltages above 1 kV. For example in the case of [121], 5 kV was considered and in the case of the project E-FANX, 3 kV [122]. The E-FANX project explores a series hybrid architecture in a BAe 146-110 framework, narrowbody regional airplane. One of the conventional turbofan is replaced by a combined 2.5MW turbofan connected to a power generator which supplies 3kV to the aircraft electric distribution line ac-dc converter. Because of the similarities of the aircraft type to be studied in this analysis with the one used in

the E-FANX project, 3kV is selected as the dc distributed voltage, and ac distribution voltage is established as the equivalent RMS line-to-line 3kV rectified voltage under space vector pulse width modulation (SVPWM) and maximum modulation index, it is $\frac{V_{dc}}{\sqrt{2}}$.

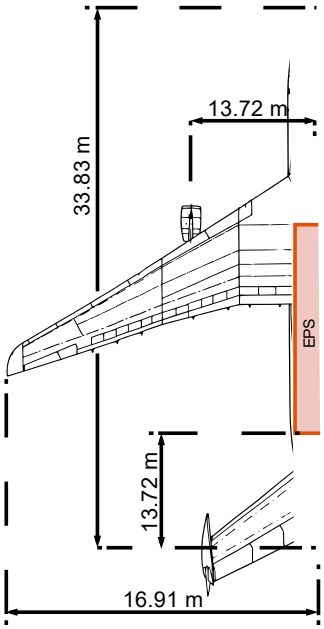

Figure 2-6. Main aircraft dimensions considered for the study

During the preliminary state of the study, two potential location options were identified for the main building blocks, see Figure 2-7. These two alternatives, are evaluated in terms of weight, and therefore are more focused on DC distribution as there will not be a big difference in the case of AC distribution. But in the case of DC distribution the integration of power electronics with electric motors and generators is considered as a promising approach to decrease system weight, see Figure 2-7.b. From the definition of conductor mass given and explained in Section 2.2.2, it can

be deduced that even assuming unity power factor (i.e., the most beneficial situation for ac cable), ac transmission line mass is approximately 20% higher than a dc transmission line, assuming the same cable material and length. Nevertheless, power electronics integration with electric machines leads to a trade-off between power electronic design complexity (i.e., safety design) and weight reduction. Power electronics design complexity is dramatically increased because of the tough environmental conditions [123] (i.e.,noise, unpressurised/pressurized operation, dirt,vibrations,etc.).

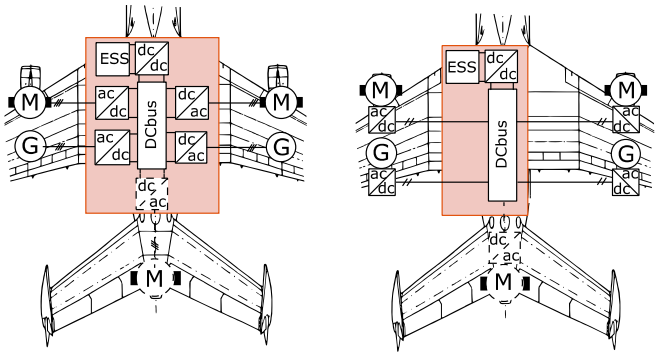

(a) (b)

Figure 2-7. Potential EP building blocks location in the aircraft for power electronics. (a) Installed in the pressurized cabin. (b) Integrated within the electric machines in the nacelle.

Some of the individual EPS architecture building blocks FoMs have been estimated in an internal company study with a ten-year horizon based on expected technology progression. Power converters, cables and circuit breakers are based on the technology analysis of different topologies and materials. In the case of the ESS, it is fuel cells and batteries, the data has been extracted from the state of the art [124–126]. A summary of the technology evaluated is presented bellow.

In the case of electric machines, noncryogenic solutions, such as PMSM and HTS

machines, were considered. Proton exchange membrane (PEM) fuel cells, as a mature technology option, and also SOFC, as a more disruptive technology, were contemplated. It is worthy to notice here that in none of the cases the LH_2tank design has been considered. Metal air and lithium-air technology are the most promising battery solutions in terms of power density and therefore of interest for their implementation in aircraft applications. Regarding protection devices, SSPCs are considered a clear candidate to substitute conventional circuit breakers in MW applications [127]. From SoA technology, such as [128], technical specifications could be extrapolated. Power electronics analysis was carried out by considering three-level inverters/rectifiers and three-level bidirectional boost/buck converters using next generation SiC for the switches [129]. A summary of the estimated data is shown in Table 2.4. This data are presented as the average of all the results obtained for a range of operation conditions (i.e.,range of voltages and currents). The information related to the specific power includes packaging and cooling penalization factors. This information serves to enhance the data previously shown in introduction, Table 2.3.

TABLE 2.4. EPS building blocks specifications

Failure rate [FITs]		**Specific Power [kW/kg]**	**Efficiency [%]**
Motor	30000	21	96.0
Inverter	1100	37	99.5
Cable	60	(*)	(*)
Generator	30000	21	96
Rectifier	1100	49	60.0
Fuel Cell	45000	5	60.0
Battery	45000	(**)	60.0
dc-dc	3000	62.5	99.0
CBs	1	31	99.5

(*) Cable specific power and efficiency are calculated based on a conductor model presented later in the document.
(**) Assumed 700 W.h/kg energy density

Additionally several assumptions have been taken into account during the FoM

calculation presented in the next section. They are listed below:

- None of the EPS cases are assumed to have reconfiguration capability, neither fault-tolerance is considered for the power converter units (i.e., elements only have one active stage, for instance, power converters have not a degradation mode, which allows them to continue working if they lose a leg).
- Propellers, turboshafts or turbofan are not included in the calculation of any of the FoM, thus only the electric components are evaluated during the analysis. Additionally, for the sake of simplicity the ESS are excluded in the efficiency calculation.
- In terms of power rating, it has been estimated that the minimum power to fulfil the abnormal operation requirement define in the regulation and pilot guides, see Section 2.1.2, is 1/3 of the total power (i.e. 6.67 MW). In case there are "n" power sources, it is considered that all of them are designed for giving that minimum power.
- During the reliability analysis, only "open stage" failure mode is evaluated. Additionally, only standby redundancy is assumed. Spare unit idle failure is considered for the switch, as well as FTR and FTS.

2.2.2 Analysis methodology and FoM calculation

The EPS analysis has been divided in two sections, DC distribution EPSs and AC distribution EPSs have been evaluated separately. In both analysis the main FoM studied are reliability, specific power and efficiency. In the case of DC distribution

fuel dependency has been added as a third FoM to help on the comparison. This is defined as the percentage of the total power that directly (i.e., by conventional propellers) or indirectly (i.e., by turboshaft) is produced by fuel burn.

2.2.2.1 DC distribution EPS analysis

The EPS trade-off analysis methodology for DC distribution cases is explained with the help of the flowchart displayed in Figure 2-8.

Firstly, the PSSA of each of the architectures defined in Figure 2-2 has been performed to identify the compliance with the DO-254. FTA is the calculation method chosen and the building block failures rates of Table 2.4 are considered. In those cases, in which the reliability target is not achieved, the weak-link technique is applied. From the two redundancy options, presented in Section 2.1.2.1 the "priority AND" gate was chosen as it is considered more accurate to reality. The failure rate of the switch to allow the spare unit to operate is assumed to be low, it is 20 FITs. Additionally, it has been assumed that the FTS of the component is 10 times lower than the failure under operation conditions. The safety level requirement during the study of EPS architectures is DAL Level A, as the main hardware failure is allocated in the most stringent category. This part of the methodology correspond with an iterative process until the system failure rate estimation become lower than 1 FIT. Once the safety target is achieved, the real number of components needed is known and the system specific power and efficiency can be calculated.

Specific power of the whole EPS is calculated by,

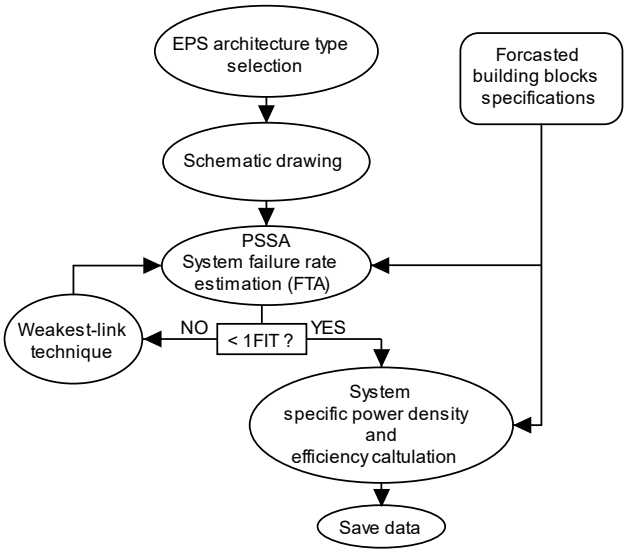

Figure 2-8. EPS trade-off analysis flowchart

$$\gamma_{system} = \frac{P_{total}}{W_c + \sum_{x=1}^{n} W_x}, \tag{2.1}$$

where, P_{total} is the EPS system total power, W_n is the the weight of each EPS architecture building block except the transmission cable, which is represented by W_c. W_x is computed by assuming Table III specific power (γ_x) times the building block power rate (P_x),

$$W_x = \gamma_x \cdot P_x. \tag{2.2}$$

The cable weight comes from the addition of the conductor and the insulation

weight,

$$W_c = W_{cond} + W_{insul}. \tag{2.3}$$

The conductor is sized following the model presented in [130], where the conductor diameter is computed based on thermal limitations. That model yields to equation (2.4) for a DC line and equation (2.5) for a three phase ac line. P_{cond} is the power flowing through the transmission line, V_{DC} the dc voltage level, J_{cab} the maximum current density for a maximum operation temperature, ρ the specific gravity of the conductor material and a multiplication factor that is equal to 2 in the case of DC distribution and $\frac{\sqrt{6}}{\cos\phi}$ for ac systems (being $\cos\phi$ the power factor). L_{cond} is the cable length.

$$W_{cond,dc} = \frac{P_{cond}}{V_{DC} \cdot J_{cab}} \cdot \rho \cdot L_{cond} \cdot 2 \tag{2.4}$$

$$W_{cond,dc} = \frac{P_{cond}}{V_{DC} \cdot J_{cab}} \cdot \rho \cdot L_{cond} \cdot \frac{\sqrt{6}}{\cos\phi} \tag{2.5}$$

Insulation weight (W_{insul}) is given by the insulation thickness needed and the length of the cable. As have been aforementioned in Chapter 1,the high altitude conditions make it a unique application when compared to other installations of similar voltage or power levels. In fact, current space high voltage cable technology may not be suitable. For instance, GORE High voltage cables [131] cover up to 36 kV but their design is focused on spaceflight applications and therefore they are mainly designed for vacuum conditions. For these reasons, the insulation is going

to be calculated based on extrapolating aerospace cables specifications, by using the insulation thickness of terrestrial cables as a baseline. From these analyses an empirical relation between the thickness and the voltage level is yielded as,

$$\delta_{insul} = 0.25 \cdot V_{DC} + 1.3. \tag{2.6}$$

W_{insul} is calculated based on the insulation volume and an insulation material density, ρ_{insul}, equal to 1400 kg/m3,

$$W_{insul} = A_{insul} \cdot \rho_{insul} \tag{2.7}$$

Efficiency of the system is defined as the ratio between the power consumed by the loads (P_{total}) and the generated power,

$$\eta_{system} = \frac{P_{total}}{P_{total} + L_{total}}, \tag{2.8}$$

where L_{total} is the total system losses. To calculate L_{total}, cable losses (L_c) and building block losses (L_x) are calculated separately and added up,

$$L_{total} = L_c + \sum_{x=1}^{n} L_x \tag{2.9}$$

L_c are defined as the total EPS conductor joule losses,

$$L_c = L_{DC} + L_{AC} = \sum (R_{DC} \cdot I_{DC}^2) + \sum (3 \cdot R_{1\phi} \cdot I_{1\phi}^2) \tag{2.10}$$

where AC and DC cable resistance are obtained from [130] transmission line model and the cable lengths estimated from Figure 2-6 dimensions.

L_x are calculated with the estimated average efficiency, given by Table 2.4, assuming it remains constant for the whole power range,

$$L_x = (1 - \eta_x) \cdot P_x. \tag{2.11}$$

2.2.2.2 AC distribution EPS analysis

The second part of the analysis focuses on the AC EPS architectures, Figure 2-2 . In this kind of EPS, ac-ac converters become a key piece. The main functions of ac-ac converters are to drive the electric motors and to interconnect two different AC networks. However, ac-ac converters, such as matrix or back to back converters, were not analyzed in the building block study presented in Table 2.4.

The specific power and efficiency requirements of ac-ac converters for ac EPS architectures has been studied firstly. To compute them it has been considered the same EPS building block specifications for the rest of the elements in the system, Table 2.4. Equally, the FoMs calculations presented in Section 2.2.2.1 have been followed. From there, a system of equations was solved for each the cases studied imposing the best achievable system requirements (i.e., boundary conditions that provide a valid system solution), it means, the highest possible system efficiency and specific power density. The objective was to get ac-ac converter needed requirements. The most demanding scenario is considered, the possibility of having redundancy of any building block is not assumed to achieve the system level failure rate.

2.2.3 Analysis results

17 DC EPS architectures have been analysed. They follow the EPS schemes displayed in Figure 2-2, Table 2.5 describes all the cases considered in the study. All of the cases have been designed ensuring the reliability requirement is fulfilled at system level. In Table 2.5, it is specified if redundancy has been applied and where. Within the all electric architectures an additional case has been considered where the DC bus is split into two buses to reduce the failure rate, see Figure 2-9.Furthermore, references of inspiring EPS studied in the literature have been added.

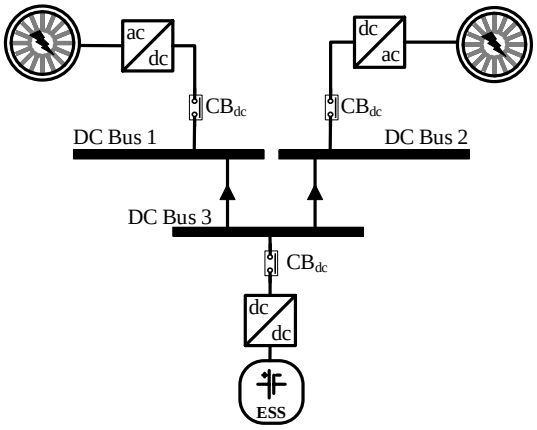

Figure 2-9. Special case of all electric EPS architecture, corresponding with the F1 study case.

The study has been performed for a generic flight profile for a CS-25 aircraft operating during 1.5 h, considering climb, cruise, and descent phase for a full power operation of 20 MW reaching an altitude at cruise of 25 000 ft. Target requirements have been set based on the study presented in [121]. For a 20 MW AEA/HEA the system level requirements are 7.5 kW/kg specific power and 93% efficiency. Efficiency (red), fuel dependence (blue), and specific power (green) results of all the DC EPS cases have been represented in Figure 2-10. From left to right, it can be seen the data

obtained for parallel hybrid, series hybrid, series/parallel hybrid, all turboelectric, partial turboelectric, and all electric cases. Table 2.6 summarizes the data included in the diagram. In addition, Table 2.7 presents the details about the weight and losses calculations for B1 series hybrid study case as a matter of example. In this case, by performing the FTA, redundancy in the DC bus has been identified as a key fact to reach the reliability requirement. This affects the total weight of the system. The resulted total weight and losses are 6339.33 kg and 1496.73 kW, respectively.

Looking at the specific power FoM (green), hybrid parallel systems A3 and A4 and series/parallel hybrid systems C3 and C4 are the heaviest EPS architecture solutions. Those cases have been designed assuming future Li-Air battery technology with an energy power density of 700 Wh/kg and an energy capability to supply 20 MW during 1.5 hours. It has been concluded that even with the future expected battery technology improvement, the specific power is significantly penalized.

In terms of efficiency, depicted in red in Figure 2-10, the all electric EPS architectures cases with fuel cells exhibit the highest efficiency (i.e. less conversion stages from generation to motors reduce the losses) and a zero-fuel dependency. However, they are the next heavier cases with an average estimated specific power density of 2.3 kW/kg. It is worth noting that the all electric cases are expected to use future fuel cell technologies, which include a small battery for stability and fast transient reaction, as ESS and that this value would be lower if only batteries would have been used instead (i.e., lower than 1 kW/kg). However, it has to be considered that fuel cell technology has its own design and implementation constrains that challenge their use, and has not been contemplated here. For instance, the operating temperature and start-up time, the high temperature exhaust and the weight and volume of the LH_2 tank [132].

It can be concluded that even though the ideal solution, in terms of CO_2 emissions, would be full electric propulsion, ESS technologies, even fuel cells, will not be prepared in a short-medium term to make all electric EPS architectures a reality in narrowbody aircrafts. Instead, hybrid systems using fuel cells or turboelectric EPS architectures seems to be more suitable candidates. Partial turbo-electric system (E2) achieves a high specific power density. However, system efficiency drops under 91% and the fuel dependency is total. The turboelectric concept is based on the idea of reducing the fuel consumption, by improving the aircraft efficiency, and could be a potential solution during the transition from MEA to AEA/HEA or other aircrafts types, such as future widebody aircrafts, which perform longer missions.

Consequently, the most promising EPS architectures are those that reach a good trade off among the three FoMs. Parallel hybrid and series hybrid EPS architectures, using fuel cell as ESS are the four cases with best performance (i.e., A1, A2, B1 and B2). They present high efficiency, that is in most of the cases above the minimum target of 93%, and a reduction of at least a 50% on the use of fuel. But, it should be noted that the achievable specific power drops far from the set target of 7.5 kW/kg indicating the necessity of a major technological challenge to happen in the next 10 years.

TABLE 2.5. Brief description fo the DC EPS cases studied

Type	ID	Description	Redundancy	Refs.
A	**A1**	Electric propulsion system is rated at 2/3 of the total power. Fuel cell is used as ESS. *Figure 2-2.(a)*	No	[30, 133]
	A2	Electric propulsion system is rated at 5/6 of the total power. Fuel cell is used as ESS. *Figure 2-2.(a)*	No	
	A3	Electric propulsion system is rated at 2/3 of the total power. Li-Ion battery is used as ESS. *Figure 2-2.(a)*	No	
	A4	Electric propulsion system is rated at 5/6 of the total power. Li-Ion battery is used as ESS. *Figure 2-2.(a)*	No	
B	**B1**	One turboshaft moves one generator. Two independent fuel cells are used to assist peak power demands. *Figure 2-2.(b)*	DC bus	[31]
C	**B2**	One turboshaft moves one generator. Three independent fuel cells are used to assist peak power demands. Main DC bus is split in two, the fuel cells can supply power to either or both of them but power flow from one to another is forbidden. *Figure 2-2.(b)*	No	
	C1	STARC-ABL concept plus fuel cell as ESS. 1/3 of the propulsion is provided by tail propeller. *Figure 2-2.(c)*	No	[33]
	C2	STARC-ABL concept plus fuel cell as ESS. 2/3 of the propulsion is provided by the tail electric propeller. *Figure 2-2.(c)*	No	
	C3	STARC-ABL concept plus battery as ESS. 1/3 of the propulsion is provided by the tail electric propeller. *Figure 2-2.(c)*	No	
	C4	STARC-ABL concept plus battery as ESS. 1/3 of the propulsion is provided by the tail electric propeller. *Figure 2-2.(c)*	No	
D	**D1**	Two turboshafts drive two generators. *Figure 2-2.(d)*	DC bus	[32]
	D2	Two turboshafts, each one drives two independent generators (1/3 and 1/6 rated power). *Figure 2-2.(e)*	DC bus	
E	**E1**	STARC-ABL concept. 1/3 of the propulsion is provided by the tail electric propeller. *Figure 2-2.(e)*	No	[33]
	E2	STARC-ABL concept. 2/3 of the propulsion is provided by the tail electric propeller. *Figure 2-2.(e)*	No	
F	**F1**	Three independent fuel cells supply the power. Main DC bus is split in two, the fuel cells can supply power to either or both of them but power flow from one to another is forbidden. *See Figure 2-9*	No	[34, 35]
	F2	Two independent fuel cells supply the power to two electric fans. *Figure 2-2.(f)*	DC bus	
	F3	Three independent fuel cells supply the power to two electric fans. *Figure 2-9.(f)*	DC bus	

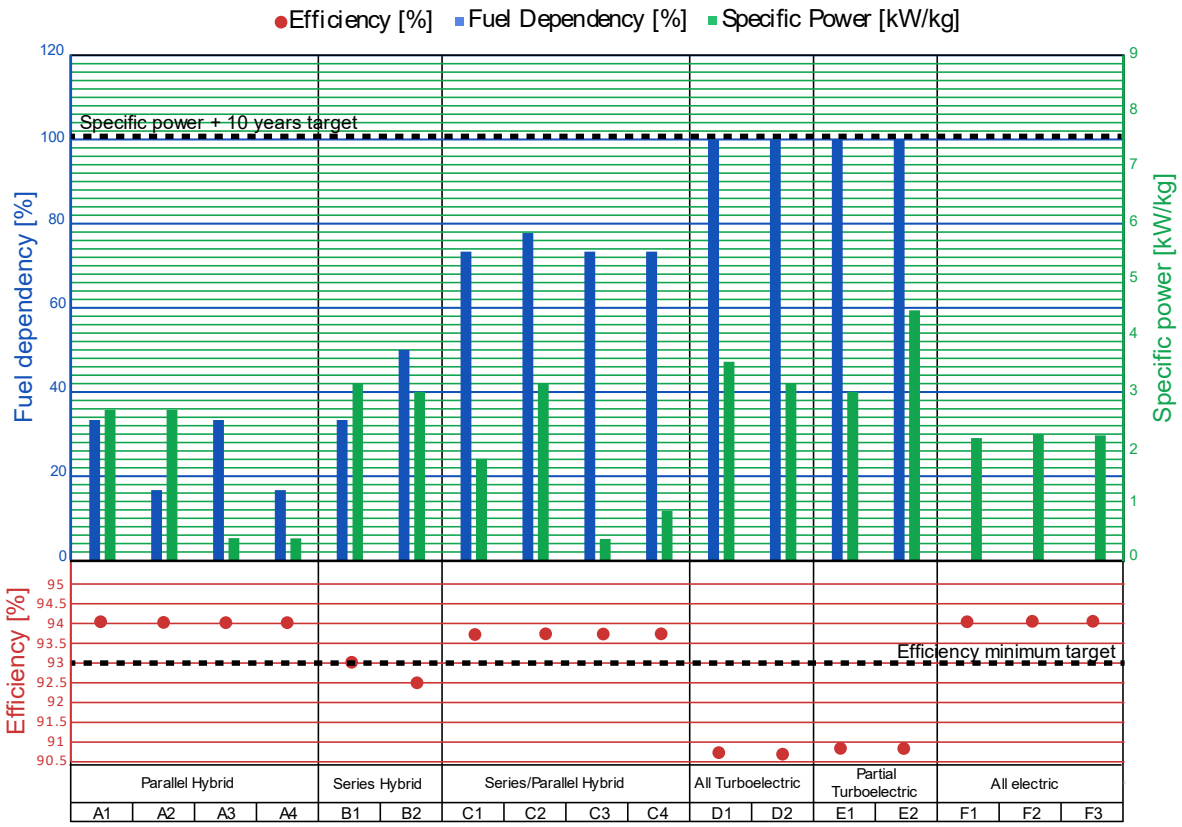

Figure 2-10. Specific power density, efficiency, and fuel dependence results for all the DC study cases.

TABLE 2.6. DC EPS Analysis FoM Results

Type	ID	Specific Power [kW/kg]	Efficiency [%]	Fuel Dependency [%]
A	A1	2.71	94.16	33.33
	A2	2.71	94.16	16.67
	A3	0.43	94.16	33.33
	A4	0.43	94.16	16.67
B	B1	3.02	93.04	33.33
	B2	3.15	92.45	50.00
C	C1	5.37	93.62	73.33
	C2	3.14	93.62	77.78
	C3	0.4	93.62	73.33
	C4	0.78	93.62	73.33
D	D1	3.36	90.60	100.00
	D2	3.08	90.57	100.00
E	E1	3.05	90.68	100.00
	E2	4.41	90.68	100.00
F	F1	2.56	94.14	0.00
	F2	2.30	94.15	0.00
	F3	2.29	94.14	0.00

There are further benefits identified for series and parallel hybrid EPS architecture. They have a low fuel dependency due to the introduction of batteries and fuel cells. In the case of parallel hybrid, the electric motors powered by the ESS will provide most part of the thrust reducing the size of conventional turbines. In series hybrid, the battery will provide most part of the power so the fuel utilized to power up the generator will be reduced. A lower size turboshaft can be translated into lower fuel dependency of the EPS architecture. Furthermore, those turboshafts can be operated more efficiently in the case of series hybrid. In parallel hybrid systems the turbofans only operate during peaks of power demand (e.g.,take off or transitions) [133].

TABLE 2.7. Calculation data example. B1, Series hybrid study case.

		Specific Power [kW/kg]	Efficiency [%]	Total Power [kW]	Total length [m]	Total weight [kg]	Power Losses [kW]
		Table 2.4		Table 2.5	Figure 2-6	Eqs. (2.2)-(2.7)	Eqs. (2.9)-(2.11)
Building Blocks	**Motor**	21	96.00	20000	-	952.38	800
	Inverter	37	99.5	20000	-	540.54	100
	Generator	21	96.00	6667	-	317.46	266.67
	Rectifier	49	99.00	6667	-	136.05	66.67
	Fuel Cell	5	60.00	13333	-	2666.67	Not considered
	dc-dc converter	62.5	99.00	13333	-	213.33	133.33
	CB	31	99.50	20000	-	1290.32	100
	DC cable	-	-	-	47.16	199.00	30
	AC cable	-	-	-	3	23.48	30
Subsystems	**Propulsion**					1492.92	-
	Power Source					3333.51	
	Distribution					222.58	
	Protection					1290.32	
	Total					6339.33	1496.73

Regarding AC distribution, Figure 2-11 displays the simplified schemes of the most relevant AC dsitribution EPS analysed. Figure 2-11.(a) is taken as a baseline; it is designed following a full turboelectric propulsion configuration with three generators. The power flow is controlled by ac–ac converters from ac bus 3 to the other two buses avoiding the power flow between buses 1 and 2. From PSSA, it has been deduced that three generators increase the reliability of the power source subsystem to the target requirement. For designing Figure 2-11.(b), Figure 2-11.(c) has been derived into a series hybrid EPS architecture by replacing the third generator with two ESS units. It is assumed that each ESS is rated to 1/3 of the propulsion power. In normal operation, AC buses are working independently, but both buses can be connected in case of failure. Figure 2-11.(d) is similar to Figure 2-11.(c), but ESS is connected to the electric motor terminals with the aim of reducing the ac–ac requirements by decreasing the power managed. Finally, Figure 2-11.(d) explores the influence of buses interconnection elimination considered in architecture of Figure 2-11.(b).

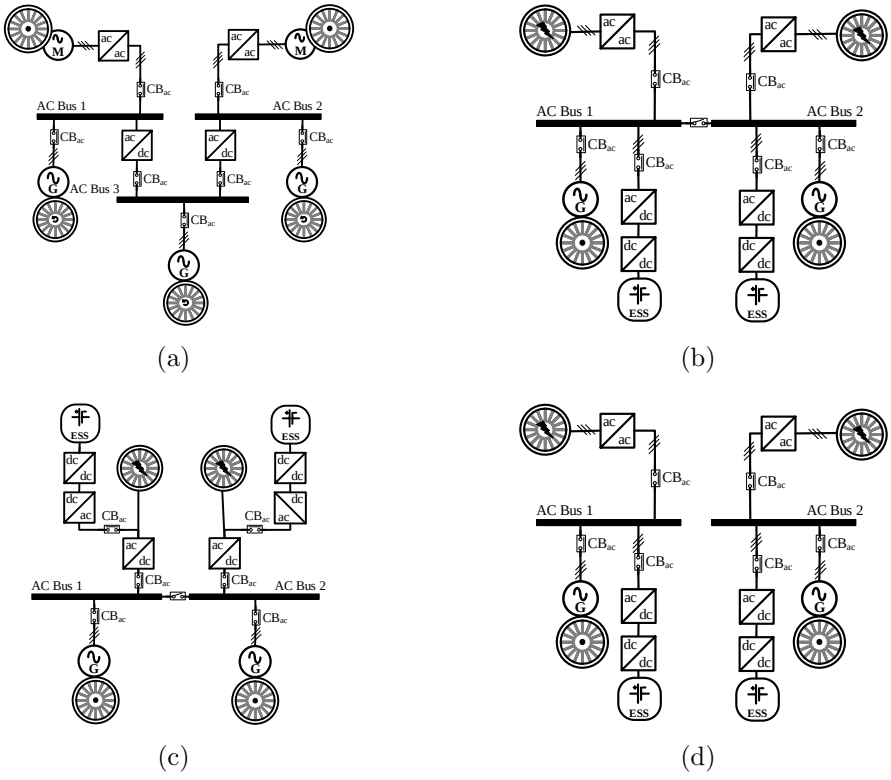

Figure 2-11. Diagrams of ac EPS architecture. (a) Case G, full turboelectric, baseline case. (b) Case H, ESS merged with generators and interconnected buses. (c) Case I, direct ESS assistance to motor, ac–dc converter can drive the motor in case of emergency. (d) Case J, separated buses with merged ESS.

Table VII summarizes the results of the ac-ac specifications needed to achieve system requirements (i.e., boundary conditions that provide a valid system solution and specified in the same table).

The study concludes that ac-ac converters failure rate should be below 1500 FITs to fulfil DO-254 reliability requirement. It is worth noting that in Case I, Figure 2-11.(c), the reliability of the ac-ac is not critical (labeled as no restricted) because the

TABLE 2.8. Estimated FoM required to fulfil system target numbers

Case		G	H	I	J
System	**Failure rate [FIT]**	1	1	1	1
	Specific Power [kW/kg]	4.5	2.75	2.7	2.7
	Efficiency [%]	92	93	93	93
ac-ac	**Failure rate [FIT]**	1502	1503	*No restricted*	1501
	Specific Power [kW/kg]	48.47	67.65	43.25	38.23
	Efficiency [%]	99.90	99.61	99.61	99.61

motor can be driven from the ac-dc converter in case of ac-ac failure. In addition, Figure 2-11.(d) reports the most restrictive ac-ac reliability requirement because there is only one possible power flow path from power sources to motor. Additionally, ac-ac converters should achieve a very high efficiency (i.e., higher than 99%) to allow system efficiency to be over the 90%. The double conversion stage needed to integrate ESS in the ac EPS system is the main efficiency penalization. In terms of specific power, the average of all the results, it is 50 kW/kg specific power density, can be set as the target value.

Once the ac-ac converter specifications were estimated, a similar analysis to the one performed for DC EPS architecture has been carried out. The most promising DC EPS architecture cases have been compared with the AC EPS architecture cases in terms of efficiency, weight, and fuel dependency. The comparison in weight has been divided in subsystems: propulsions system (i.e., motors and drives), power supply (i.e., generators, ESS and required power conversion stages), distribution network, (i.e., cable and buses) and protections (i.e., breakers). Thus, the building blocks involved into the most significant penalizations in terms of weight for both EPS architecture types can be identified. Particularly, the target value 50 kW/kg ac-ac converter specific power has been used for the comparative study. Figure 2-12

presents the three FoMs data, where A1, A2, B1 and B2 are the dc EPS architecture cases and G, H, I and J are the ac EPS architecture cases.

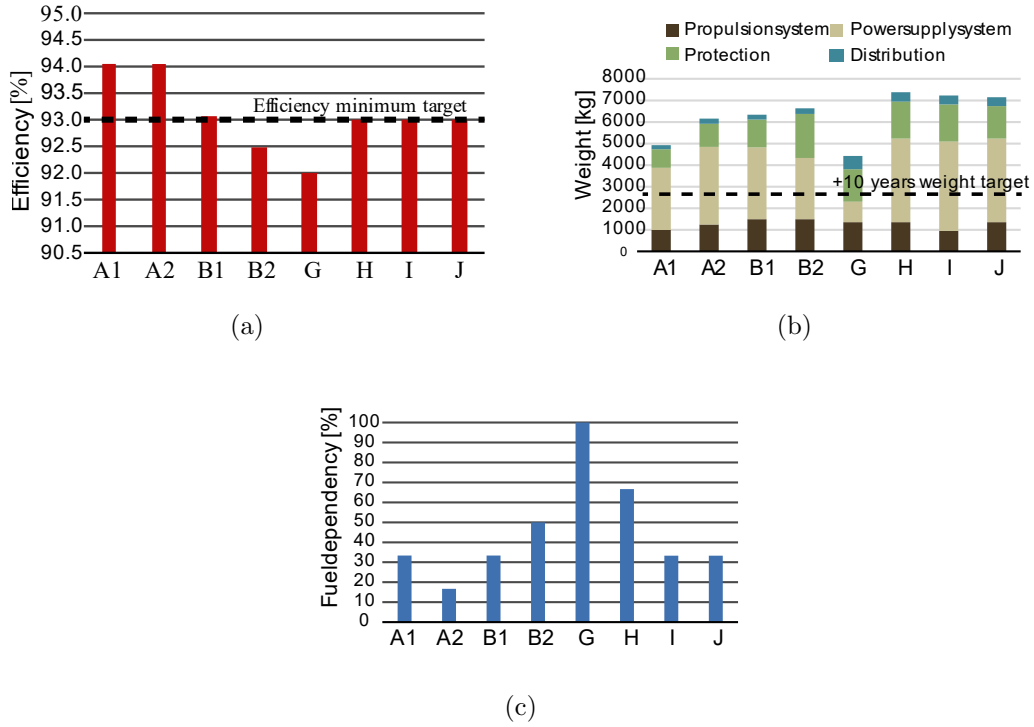

Figure 2-12. FoMs comparison between most promising dc cases and ac cases. (a) Efficiency. (b) Weight. (c) Fuel dependency.

Figure 2-12.(a) shows that DC EPS architecture systems can achieve higher efficiency values than AC EPS architecture systems. In terms of weight, from Figure 2-12.(b) it can be observed that AC distribution weight is higher than DC distribution weight due to cable mass as has been aforementioned. AC distribution architectures also present heavier power systems (i.e., generators, ESS and needed power converters) when comparing them to DC distribution. One of the biggest drawbacks is the difficulty or the extra power stages required to include ESS making AC distribu-

tion not of particular interest for hybrid approaches but particularly interesting for turboelectric architectures. In general, AC EPS systems are heavier than DC EPS systems, the only exception is G because the ESS is not considered. DC distribution demonstrate a more useful case for either of the distribution cases depicted in Chapter 1 that leverage an ESS.

2.3 Conclusions

A comparative analysis on AEA/HEA state of art architectures has been presented in this chapter and has yielded a set of promising EPS architectures that have been compared using three FoMs (i.e., reliability, efficiency and specific power density), and covering both DC and AC distribution systems.

In the case of DC EPS architectures, it has been highlighted the benefits regarding the reduction of cable weight and the ease of implementation for both turboelectric and hybrid propulsion systems. From the analysis, it has been concluded that the parallel hybrid and the series hybrid configurations can be considered promising future aircraft EPS architectures in the medium-term for CO_2 emissions reduction. However, the resultant specific power for those EPS architectures conclude that the 10-year horizon FoM building block estimations do not achieve the fixed target objectives of specific power for narrowbody aircrafts requiring a technological breakthrough in some technologies. Although the main limiting factors is the ESS additional weight, progression of all building blocks technology is needed. Furthermore, circuit breakers lead the system specific power down and are identified as elemental parts in the EPS architecture target achievement. Table 2.9 displays an

estimation of the building blocks specific power values needed to achieve the system design requirements (i.e., 7.5 kW/kg specific power and 93% efficiency) for the cases A2 and B2.

The conclusion is that a new paradigm of power electronics, insulation conductors and electric machines technologies needs to be explored. Technology development will reduce the fuel dependency for these hybrid architectures achieving higher specific power densities and eventually transitioning into a full green electrical system. Insulation requirements can be highlighted as critical with power density requirements. Nowadays, the effort of many AEA/HEA designers is focused on the pursuit of insulation technologies that address high voltage phenomena without penalizing size or weight. It can be done by adapting terrestrial insulation materials or with alternative solutions such as, micromultilayer insulation technology [134].

TABLE 2.9. Estimation of building block requirements to fulfil system targets

Case A2	**Specific power [kW/kg]**		**Efficiency [%]**	
	Old	*New*	*Old*	*New*
Motor	21	50	96	96
dc-ac	37	60	99.5	99.5
Generator	-	-	96	96
Fuel Cell	-	-	99	99
dc-dc	5	18	100	100
CBs	62.5	75	99	99
System	2.71	7.52	94.16	94.16

Case B2	**Specific power [kW/kg]**		**Efficiency [%]**	
	Old	*New*	*Old*	*New*
Motor	21	50	96	97
dc-ac	37	55	99.5	99.5
Generator	21	50	96	96
Fuel Cell	5	14.5	100	100
dc-dc	62.5	80	99	99
CBs	31	150	99.5	99.5
System	2.71	7.58	92.45	93.31

The challenge for electric machines design is to achieve high specific power solutions

with high efficiency. The study presented in [135] analyses electric machines design for AEA application. The impact of several design parameters on the power density and the efficiency is explored for nonsuperconducting and superconducting machines. This study demonstrated that superconductivity materials allow to go beyond non-superconducting achievable specific power ratings but at the same time it introduces extra complexity to the design. Thermal management becomes an important concern for achieving the power density requirements needed in new aircraft propulsion concepts. The main reason is the number of heat loads increases, so optimizing the design of the thermal management systems become important [136]. Some authors propose cryogenic cooling and thermal management system integration [137] or the integration of power converters within the propulsion motors to use the bypass flow in the duct to cool the power modules [138].

The significant weight addition of battery ESS as a main source, such as Li-Air (i.e., expected battery technology used in 2030) demotivates their application as a primary source in the future narrowbody AEA unless a breakthrough technology is discovered to improve their energy density for the power levels discussed in this work. Nevertheless, the use of batteries will be always necessary in certain extend. Lighter aircrafts pertaining to EASA CS-23 classification may still benefit from battery use on the lower power end [139, 140]. For instance, over the last years several projects around light aircrafts that propose all electric EPS architectures have been presented [34], [35]. As regards ac EPS architectures, it has been assumed that ac-ac converters must achieve a high performance (i.e., very high reliability, over 99% efficiency and high specific power density). These requirements stress the design of this component making it extremely difficult to achieve the requirements and thus falling short in comparison to simple dc EPS architectures.

Note that the conclusions expounded above are based on an analysis focused on narrowbody aircrafts, and in the hybrid schemes on the hybridization level. Similar analysis could be applied to other types of aircrafts, although the conclusions expounded may differ due to the characteristics of flight profiles, altitude, distances, or flight time. Several projects around widebody aircrafts can be found, which focus on turboelectric propulsion architectures, such as N3-X prototype [141]. In that case, the fuselage aerodynamic performances become more important, benefiting from distributed propulsion architectures. The EPS architecture presented in [141] combined with innovative superconducting electrical systems can supposed around a 70% of fuel burn reduction. One of the most recent projects that has reported results in regards this topic are Chyla and Siena Clean Aviation projects [142]. In both projects they have focused on studying the different propulsion options in order to identify to which aircraft categories and market they suit the best.

The benefits of using dc architecture for either hybrid or fuel electric have been concluded in this work. Nonetheless, in terms of the required building blocks there are several technological gaps such as: understanding of high altitude and high voltage operation, achieving fast and power density dc breakers, or increasing the overall efficiency of the system. Currently efforts in superconductive systems, special insulation materials and hydrogen fuel cells will be key for the future of greener and electrical aircraft.

Conclusions regarding power converter topologies requires a through study and more thoughts around this are covered in Chapter 3. In this thesis we focused on modular or multilevel topologies, which can reduce the power semiconductor requirements and bring AEA/HEA EPS power converters requirements closer to state of the art technology. Furthermore, assuming some modifications this kind of

power converter topologies could be suitable to AC distribution cases, which are not extensively study in the literature.

Chapter 3

Evaluation of modular multilevel converters for the future electric aircraft.

The emerging concepts of AEA/HEA introduce new application scenarios characterized by high power, high voltage operational prerequisites, and demanding environmental conditions. These requirements often surpass the capabilities of existing power converter solutions, requiring the development of new solutions. While traditional power topologies, such as dc-dc boost converters or dc-ac two-level inverters, suffice for electric vehicle applications, the future electric aircraft EPS might need multi-level topologies or parallel and/or series connections of the mentioned power converters. It is noteworthy that the adoption of electrified propulsion schemes not only impacts the power converters within the power train but also influences the components within the distribution network [143].

Concerning power converter requirements, the selection between uni-directional or bi-directional converters is contingent upon the specific application. For instance, bi-directionality is needed when connecting a battery to the distribution bus, whereas a uni-directional converter may be sufficient for connecting a fuel cell. In cases involving power converters for connecting different voltage level distribution buses, the necessity of bi-directionality hinges upon the EPS architecture definition and the management strategy devised. The use of isolated power converter topologies to limit the failure propagation throughout the EPS might be required to enhance the safety levels. But, at the same time, it is possible that the safety requirements can be guaranteed with the use of protection devices, such as CBs. Note that the inclusion of transformers in isolated converters results in heavier solutions, potentially leading to weight penalties.

This chapter presents a modified MMC, which has being investigated to enhance MMC features by reducing the weight of cell capacitors used. Fault tolerance capability is demonstrated to be improved as well.

3.1 Modular multilevel converters for on-board aircraft electric power system

Modular multilevel converter can be considered also candidate topology in the aircraft power train, as this is a suitable solution for medium/high power applications with high voltage levels. In addition, its modularity provides scalability, which helps to achieve an adaptable solution to different aircraft platforms. CHB and MMC are reported as high efficiency solutions as well, and allow the used of lower voltage

power devices [144]. The MMC has become a popular solution in applications such as high voltage direct current (HVDC) transmissions lines and industrial variable-speed drivers, integration of low/medium voltage batteries to the grid, power electronic transformers, railway electric traction systems, and ship electric propulsion systems [145, 146]. The high number of components could be a concern because of the potential lower reliability. In [147] a modular converter based on a solid state transformer (SST) is proposed as a high reliability solution reaching 6 kV DC bus level. Furthermore, there are several references in the literature of MMCs supplied from multi-three phase systems of a MW scale electric machine. For instance in [148] a the CHB cells are supplied from a multiwinding generators and in [149] and ac-dc MMC solutions for high voltage and high power gas turbine driven generators is proposed. Similarly, in [150] and [151], a multiport transformer is used in an industrial application.

Its modularity provides scalability and fault resilience [152, 153]. Not having a physical element connecting the positive and negative terminals reduces the probability of having a fault in the DC link, which may have severe consequences. Current state of the art is looking into improving fault management, volume reduction [154] and cooling size optimization [155].

3.2 Proposal of a modified MMC based on multiple three phase winding generators

In [60], the MMC is compared with the previously cited topologies, concluding that one of its main disadvantage is the potential higher weight due to the cells capaci-

tances and arm inductances. This fact in addition with the lack of research around this topology for the specific application in future electric aircraft have prompted the evaluation of MMC variations that could reduce the size of the capacitors used at cell level. As a result, the distributed input modular multilevel converter (DIMMC) topology is proposed in this thesis [156–158], see Figure 3-1.

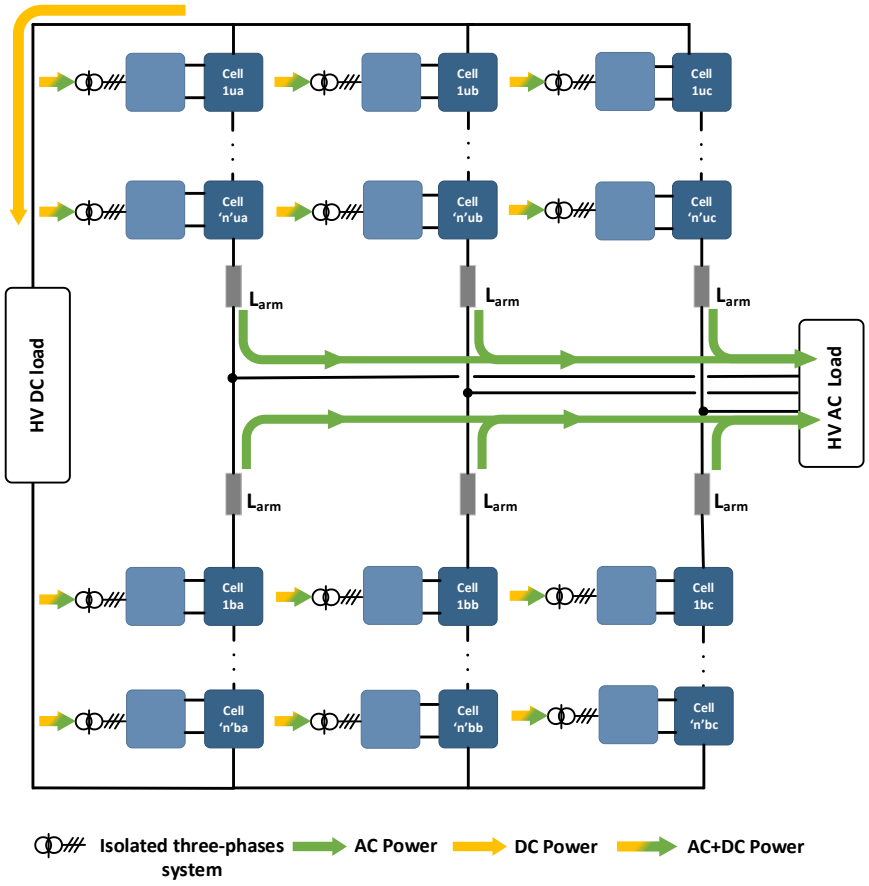

(a)

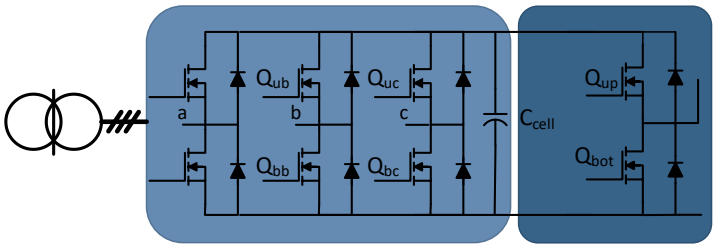

(b)

Figure 3-1. DIMMC topology. (a) General topology scheme. (b) Details of the DIMMC cell structure.

The DIMMC topology explores the possibility of feeding the capacitor of each of the total number of half-bridge cells (N_{cells}) of a MMC by an ac-dc rectifier with high power factor (PF). Similarly to the solution explained in [159] or [150], the idea is that each of the rectifier is connected to one of the multiple three-phase systems, Figure 3-1. In this chapter, a preliminary analysis of the DIMMC features is presented, putting more emphasis on the cell capacitance reduction that implies a potential weight reduction. The proposed topology follows a multiport configuration with one HV DC port and one HV AC port, Figure 3-1.(a). Each phase is comprised of two arms and each arm is comprised by several cells and an inductor connected in series (L_{arm}). The cells proposed are based on a half-bridge and a capacitor, but they could potentially be exchanged for any other [160]. In this thesis, it is described the operation for the half-bridge due to its simplicity. The cell capacitor (C_{cell}) voltage is regulated by one of the multiple three-phase systems through an active rectifier, Figure 3-1.(b). The inherit isolation, provided at the input by the generator or transformer, between the multiple three-phase systems eliminates the

requirement of using isolated cells as in the case of MMC based power electronics transformers [161]. The active rectifier can be implemented with any non-isolated topology, but in this case a simple two-level rectifier has been chosen for the sake of simplicity. This is controlled to drain ac power with unity PF and to maintain a constant C_{cell} voltage level [158].

3.2.1 Basic operating principle of the DIMMC

Figure 3-2 illustrates a simplified scheme of the topology and the main voltage waveforms. Similarly to the MMC, the DIMMC is controlled to generate an unipolar arm voltage. The homopolar component of the upper and bottom arm voltage, v_{x1} and v_{x2}, respectively, determines the HV DC port voltage level (V_{dc}) as defined in

$$V_{x1} = \frac{V_{dc}}{2} - V_x, \tag{3.1}$$

$$V_{x2} = \frac{V_{dc}}{2} + V_x, \tag{3.2}$$

$$V_{dc} = V_{x1} + V_{x2}, \tag{3.3}$$

where V_x is the phase output voltage, given by

$$V_x = \frac{V_{x1} - V_{x2}}{2}. \tag{3.4}$$

The AC output current is split between the upper and the lower arm, each of them carrying half of it,

$$i_x = i_{x1} + i_{x2}. \tag{3.5}$$

A unique feature of the MMC is the circulating current (i_c) and is defined as

$$i_c = \frac{i_{x1} - i_{x2}}{2}. \tag{3.6}$$

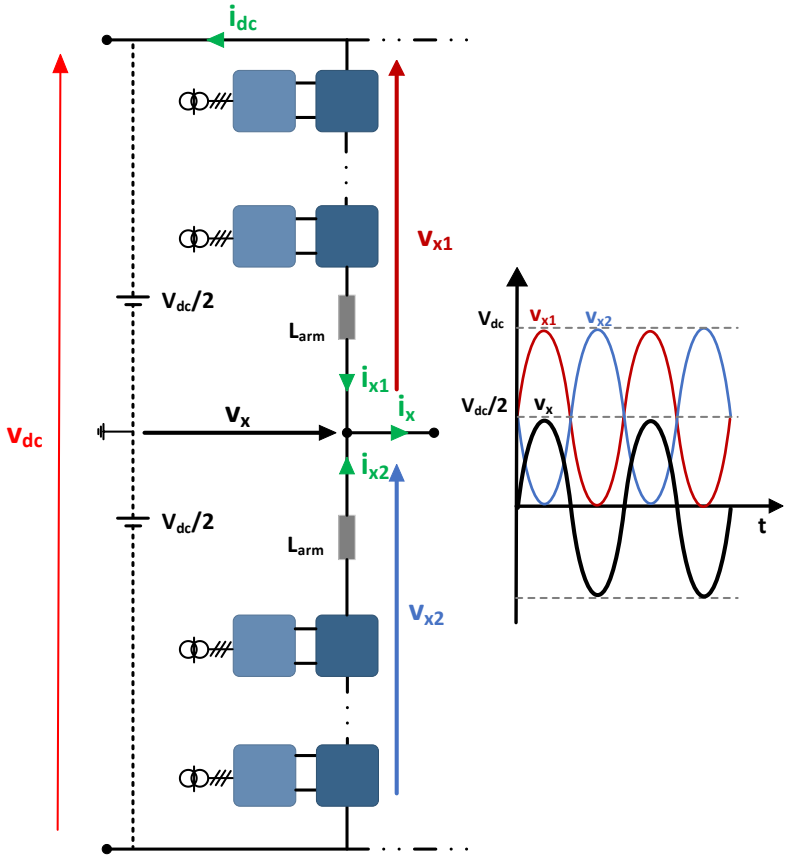

Figure 3-2. Simplified representation of the main DIMMC signals. Only one phase represented for the sake of simplicity

In the DIMMC this circulating current per leg will be equal to 1/3 of the demanding current by the DC Load. Conventionally, the arm inductances are designed in the MMC to limit the i_c but in the DIMMC a different design approach might be needed. The optimization of the size of the arm inductors will be considered as future work

and it is not part of the current document.

Assuming both HV DC and HV AC ports are connected to loads, the power flow direction displayed in Figure 3-1 is expected. However, this multiport topology could manage other power flow directions. As the cell voltages are fixed by the local control of the active rectifier, the DIMMC central control will be only responsible of guarantee the power balance equation

$$P_{ac} = V_a \cdot i_a + V_b \cdot i_b + V_c \cdot i_c, \tag{3.7}$$

$$P_{dc} = V_{dc} \cdot i_{dc}, \tag{3.8}$$

$$\sum_{n=1}^{N} P_{n,j} = P_{ac} + P_{dc}, \tag{3.9}$$

where $P_{n,j}$ represents the active power provided by the cell n of the phase j, being N the total number of cells.

In an MMC, C_{cell} is designed to hold its voltage over a minimum value when the cell is activated. This normally yields a high capacitance value, which penalizes the overall specific power of the converter. In the particular case of being used in variable-speed machine drivers, a challenge exists at low motor speed when the C_{cell} voltage ripple become significant higher [162]. Additionally, cell voltage balancing algorithms are necessary to ensure all cells stay at a similar voltage level. An example of this is the sorting algorithm, which measures all the cell voltages and depending on the arm current direction it inserts first those cells with higher or lower voltage [68]. One of the targets that is aimed with the DIMMC is the necessary capacitance reduction for similar voltage level fluctuation, this has been explored in [158] and is explained in the following lines. This is achieved by regulating the C_{cell} voltage with an active

rectifier.

3.2.2 Analysis of the cell capacitance reduction with a distributed input modular multilevel converter

To evaluate the capacitance reduction feature of the DIMMC the study case displayed in Figure 3-3 is analysed. The study case consists on a three phase input source, two level power factor correction six-switch voltage source rectifier (PFCVSR), an output capacitor, representing the DIMMC C_{cell} and a current source. When connected, each cell of the DIMMC supplies the current circulating through the converter arm, this can be modelled as a current source. For the study, this current is simplified as a pulsating current source connected to the output capacitor with a long period (i.e., the connection period of the cell, which is on the order of milliseconds) when compared to the switching period of the power converter.

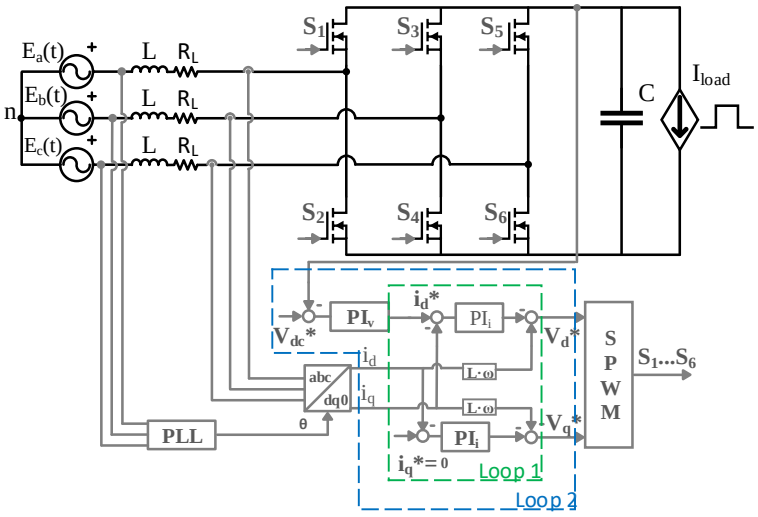

Figure 3-3. Study case scheme.

The capacitance reduction is attained with the design of the control for the rectifier. The control design process includes the digital time delay introduced by digital implementation (T_d). This is normally expressed in terms of sampling periods, which in this case are related with the switching period (T_{sw}). The analysis trades-off the control effort (i.e., control loop required bandwidth and phase margin), the switching frequency, the output voltage ripple and the required capacitance, yielding as a result a mapping of the minimum capacitive values required to achieve the desired performance. The switching frequency range under study is limited for practical reasons, Table 3.1. The input filter design is not studied in this thesis, the minimum switching frequency is fixed over 40 times the mains frequency not to penalize its design [123]. It should be noted, the current power devices technology allows to manage high voltage (i.e. hundreds of volts) and medium current level (i.e. tens of amps) up to MHz range, switching frequency has been set 10 times lower to work in a more conservative range.

Table 3.1 shows the data of the system under study. A DIMMC with seven cells per arm is considered, assuming that the DC bus voltage is 3 kV and operating at 1MW. Each C_{cell} nominal voltage is 430 V, labelled here as V_C. If a staircase operation without sorting algorithm is applied, this means that in the worst scenario one cell is connected almost the whole period. For an output frequency of 400 Hz this means 2.5 ms, it has been simplified to 2 ms. Furthermore, as detailed in (3.5) the arm current (i_{x1}) will be half the output current. The most demanding scenario in terms of control design is the connection of the cell when the arm current is maximum. Assuming no circulating current, it is no DC load, this is half the peak output current. For a 1 MW operation case, it yields to 220A. Consequently, the amplitude of the pulse current is set to that value.

TABLE 3.1. Specifications of the study case

Variable	Value
AC frequency	400Hz
Nominal Cell voltage (Vn)	430 V
Maximum voltage variation	10 %
Minimum switching frequency	32 kHz
Maximum switching frequency	100 kHz
Pulse load amplitude (Iload)	220 A
Pulse load period (Tload)	2 ms
Modulation index (Mp)	0.85
Td	Tsw

It should be noted that the methodology procedure can be applied to other system specifications if the system is correctly modelled. For example, this is potentially useful for adapting the converter power rating. But if higher frequencies are considered, parasitic elements may start playing an important role. The PFCVSR control design presented is based on d-q synchronous reference frame converter average model assuming a sinusoidal PWM modulation [163]. A classic dual-loop control structure is used, where the outer control loop is responsible for maintaining a constant output capacitor voltage and the inner control loop is designed to control the boost inductor currents. Feedforward compensation is also implemented in the current control loop to eliminate the inherent d-q phases cross coupling, see Figure 3-3. Therefore, the current control loop dynamics can be reduced to the input boost inductor, which can be simply modelled as a first order plant [164]. The stability requirements can be established in terms of phase margin (PM) by studying the control loop in the frequency domain. The minimum acceptable PM is set to 45 deg in both control loops. Mathematical expressions are derived from both current and voltage open loop gain (OL) to define the PI controller parameters as function of the phase margin (PM) and the crossover frequency (ω). At ω conditions (3.10) and (3.11) are imposed.

$$|OL(\omega_c)| = 1 \tag{3.10}$$

$$\angle OL(\omega_c) = -180^\circ + PM \tag{3.11}$$

The current control loop, control loop 1 in Figure 3-3, generates the PWM modulation index required to reproduce a sinusoidal input current in phase with the input voltage and with the required amplitude. The current OL expression is given by:

$$OL_i(s) = Kp_1 \cdot \frac{Ti_1 \cdot s + 1}{Ti_1 \cdot s} \cdot \frac{1}{T_d \cdot s + 1} \cdot \frac{1}{L \cdot s + R_L}. \tag{3.12}$$

Although more complex and detailed approaches can be used to model the effect of T_d , the approach detailed in [164] is used to model it as a first-order system helping on reducing the complexity of the analysis. Substituting the conditions defined by 3.10 and 3.11 in 3.12, yields the next mathematical expressions,

$$Ki_1 = \frac{1}{Ti_1} = \frac{\omega_c}{\tan(-90^\circ + PM + \tan^{-1}(T_d \cdot \omega_c) + \tan^{-1}(L/R_L \cdot \omega_c)}, \tag{3.13}$$

$$Kp_1 = \frac{Ti_1 \cdot \omega_c}{\sqrt{(Ti_1 \cdot \omega_c)^2 + 1}} \cdot \sqrt{(T_d \cdot \omega_c)^2 + 1} \cdot R_L \cdot \sqrt{(L/R_L)^2 + 1}, \tag{3.14}$$

$$PI_i = Kp_1 \cdot \frac{s + Ki_1}{s}. \tag{3.15}$$

Equations (3.13), (3.14) and (3.15) determine the current controller parameters:

Kp_1 that is the PI proportional gain and Ki_1, the PI integral action. They are defined in function of the design constraints, such as PM, ω_c, the inductor time constant defined by the ratio of L, the inductance value, and R_L, which is its series resistance, and T_d represents the PI control time constant and it is the inverse of Ki_1 and the PI current controller is defined by a PI series form (PI_i). Note that T_d and the inductor time constant ($^L/_{R_L}$) degrade the loop stability which will be compensated by the PI integral action.

The control loop stability can be studied by evaluating (3.13). The theoretical maximum for the crossover frequency ω_{climt}, can be obtained by equating Ti_1 to zero. T_d can be easily estimated by taking into account the sampling and updating rating [165]. It is normally expressed in terms of sampling periods, which in this case is related with the switching period. For example, T_d can be 1 or 0.5 sampling cycles. Evaluating (3.13) for $Ti_1 > 0$ the minimun $^L/_{R_L}$, it is, $^L/_{R_{min}}$, for different combinations of ω_c, switching frequency and PM are obtained, Figure 3-4. These limits indicate the dynamic constraint of the inductor design for a certain PM and ω_c. That is, there are $^L/_{R_L}$ that will turn the system unstable and control compensation is not possible. Those limits are used to stablish constraints to the capacitance reduction study meaning that the attained solution will always be a feasible solution from a stability perspective.

The control loop 2, voltage control loop,in Figure 3-3, is designed to regulate a constant voltage level. Load changes are seen as voltage disturbances by the control loop, so the design is focused on disturbance rejection. The effect of the control loop 1 dynamics has been approximated by a first order transfer function defined by this time constant response T_{CL}. This can be done if the inner control loop, in this case control loop 1, dynamics are significantly higher than the outer control loop, the

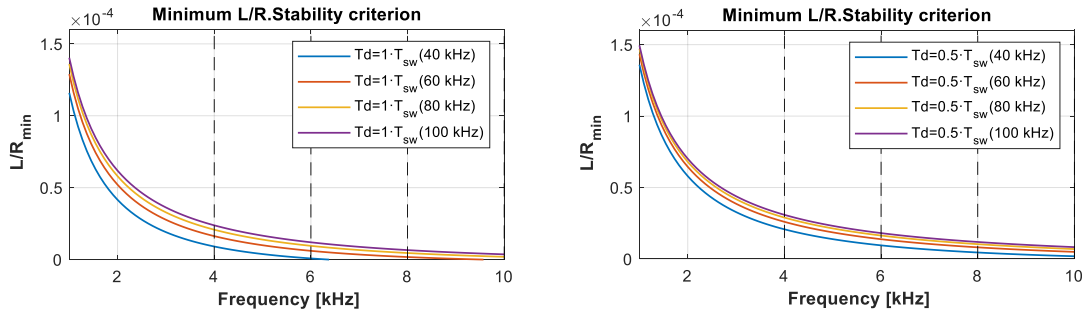

(a) (b)

Figure 3-4. Current control loop stability minimum boundaries when the PM is 45º and updating occurs at: (a) sampling time, (b) half the sampling time

control loop 2 in this work. Voltage OL expression is given by,

$$OL_v(s) = Kp_2 \cdot \frac{Ti_2 \cdot s + 1}{Ti_2 \cdot s} \frac{1}{T_{CL} \cdot s + 1} \cdot \frac{3}{4} \cdot M_d \cdot \frac{ESR \cdot C \cdot s + 1}{C \cdot s}. \tag{3.16}$$

Where, ESR stands for the equivalent series resistance of the capacitor.

Substituting the conditions (3.10) and (3.11) in (3.16), the following mathematical expressions are derived,

$$Ki_2 = \frac{1}{Ti_2} = \frac{\omega_c}{\tan(PM + \tan^{-1}(T_{CL} \cdot \omega_c) - \tan^{-1}(C \cdot ESR \cdot \omega_c))}, \tag{3.17}$$

$$Kp_2 = \frac{Ti_2 \cdot \omega_c}{\sqrt{(Ti_2 \cdot \omega_c)^2 + 1}} \cdot \frac{\sqrt{(T_{CL} \cdot \omega_c)^2 + 1} \cdot C \cdot \omega_c}{\sqrt{(C \cdot ESR \cdot \omega_c)^2 + 1}} \cdot \frac{4}{3 \cdot M_d}. \tag{3.18}$$

They determined the current controller parameters: Kp_2 that is the PI proportional action and Ki_2, the PI integral action. The voltage controller is defined by a PI series (PI_v). As can be seen, the OL gain depends on the modulation index (M_d), which decreases when load current increases. The voltage control loop is designed for the

worst case (i.e. for the peak pulse amplitude). For simplicity, in the study presented in this work ESR effect has been neglected considering the expectation of very low equivalent series resistance (ESR) value. Nonetheless, it is important to take it into account otherwise.

Figure 3-5 illustrates the different design steps followed to determine the capacitance reduction.

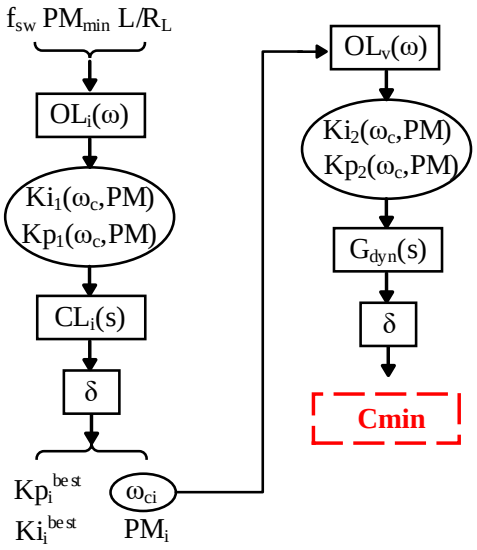

Figure 3-5. Flowchart of the proposes output capacitance methodology.

The solution with the best performance is selected based on (3.13)-(3.18) analysis. Best performance selection is evaluated with a performance factor (σ) that is defined in terms of the main close loop ($CL(s)$) time step response characteristics: the rise time (T_{rise}), the settling time ($T_{settling}$) and the overshoot percentage($Overshoot(\%)$). For simplicity, in this work σ has been defined as the multiplication of all these

characteristics:

$$\sigma = T_{settling} \cdot T_{rise} \cdot Overshoot(\%) \tag{3.19}$$

To perform the minimum capacitance identification, the control loop 1 and control loop 2 transfer function expressions that determines the reference tracking and disturbance rejection respectively have been rearranged to more general expressions,

$$\frac{id(s)}{id_{ref}(s)} = \frac{Kp_1' \cdot \frac{Ti_1 \cdot s+1}{Ti_1 \cdot s} \cdot \frac{1}{T_d \cdot s+1} \cdot \frac{1}{L/R_L \cdot s+1}}{1 + Kp_1' \cdot \frac{Ti_1 \cdot s+1}{Ti_1 \cdot s} \cdot \frac{1}{T_d \cdot +1} \cdot \frac{1}{L/R_L \cdot s+1}} \tag{3.20}$$

$$\frac{V_o(s)}{i_o(s)} = \frac{1}{C} \cdot \frac{s \cdot (T_{CL} \cdot s + 1)}{T_{CL} \cdot s^3 + s^2 + Kp_2' \cdot s + \frac{Kp_2'}{Ti_v}} = \frac{1}{C} \cdot G_{dyn} \tag{3.21}$$

$$Kp_1' = \frac{Kp_1}{R_L} \tag{3.22}$$

$$Kp_2' = Kp_2 \cdot \frac{3 \cdot M_d}{4 \cdot C} \tag{3.23}$$

It can be deduced from (3.21) that the value of the capacitor does not affect the dynamics (i.e., in terms of poles and zeros position). It only affects to the gain of the transfer function. Therefore, analysing G_{dyn} in terms of performance factor σ, the best disturbance rejection dynamics can be identified independently of the capacitance value and the operating point. The best disturbance rejection response that can be expected under f_{sw}, PM and L/R_L ratio constraints can be obtained for a normalized case where I_{load} and the nominal voltage are set to unity. This yields a

normalized voltage variation, ΔV_{pu}. From ΔV_{pu}, the minimum capacitance for any voltage variation ($\Delta V_{required}$, expressed as an absolute value) and any certain current level demand (I_{load}) can be deduced with,

$$C_{min} = \Delta V_{pu} \cdot \frac{I_{load}}{\Delta V_{required}} \tag{3.24}$$

3.2.2.1 Capacitance reduction results and simulation validation

The main contribution of this study is the derivation of the limits of the output capacitance reduction by the action of the classic dual control loop. The capacitance reduction ratio in terms of the base case can be calculated. The base case has been set as the cell capacitance design for traditional MMC operating under the same conditions. The design of the cell capacitance to limit the voltage variation to a 10% is 0.67 mF for a 1 MW output power [166].

The obtained data can be also used for proving the effectiveness of more complex control algorithms proposed for capacitance reduction. Table 3.1 specifications and a $^{L}/_{R_L}$ ratio equal to $0.5 \cdot 10^3$ (i.e., as matter of example and based on a preliminary inductor design) have been used for the evaluation of the results in Figure 3-6. Figure 3-6.(a) shows the results obtained using (3.24) for an example in which $\Delta V_{required}$ and I_{load} are set to 1. This data can be easily extrapolated to any operation point by multiplying by the load current and dividing by the nominal voltage. Thus, the minimum capacitance values for the study case described in Table 3.1 are displayed in Figure 3-6.(b).

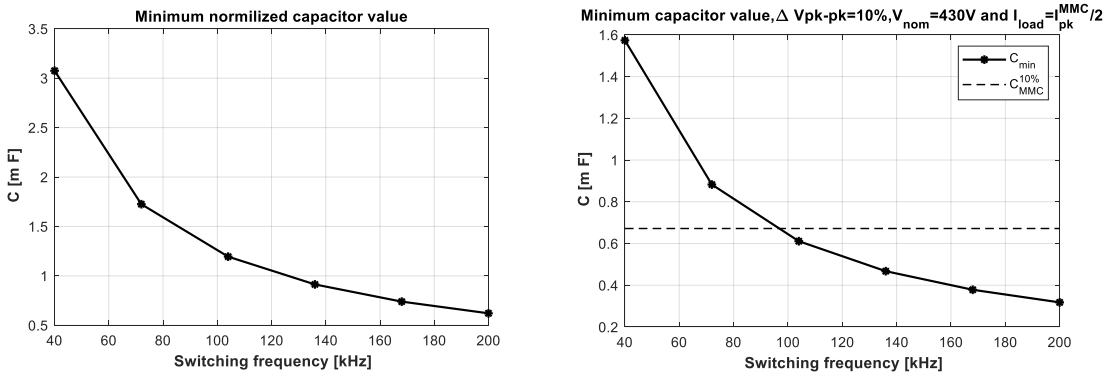

(a) (b)

Figure 3-6. Capacitance reduction study results. (a) Case where I_{load} and $\Delta V_{required}$ are set to 1 (Normalized case) (b) Results particularization for a given operating point (Table 3.1).

TABLE 3.2. Reduction ratio estimation.

fsw [kHz]	**Cmin [mF] @430 V, 220 A**	**Reduction ratio [%] ($C_{MMC}^{10\%}$ = 0.67 mF)**
104	0.61	9
136	0.47	31
168	0.37	44
200	0.32	53

To validate the theoretical study results, a simulation has been performed. The simulation has been developed in MATLAB/Simulink software and a good approximation to the real control implementation in a DSP platform was achieved, Figure 3-7. Figure 3-8 shows the voltage variation of an equivalent linear system when a current of a unit pulse is demanded and Fig. 6.b displays the voltage variation of the switching model simulation of Figure 3-7 for a 220 A pulse current.It can be concluded that it is possible to reduce the C_{cell} capacitance if the control loop has the enough bandwidth. As it has been described, the way of defining the control loop bandwidth has been proportionally related to the switching frequency. Thus, it can be appreciated that a switching frequency higher than 100 kHz is required in order

to get benefit of this solution. Table 3.2 illustrates the capacitor reduction ratios for those valid switching frequencies when comparing with the MMC capacitance (C_{MMC}) under the specifications described in Table 3.1.

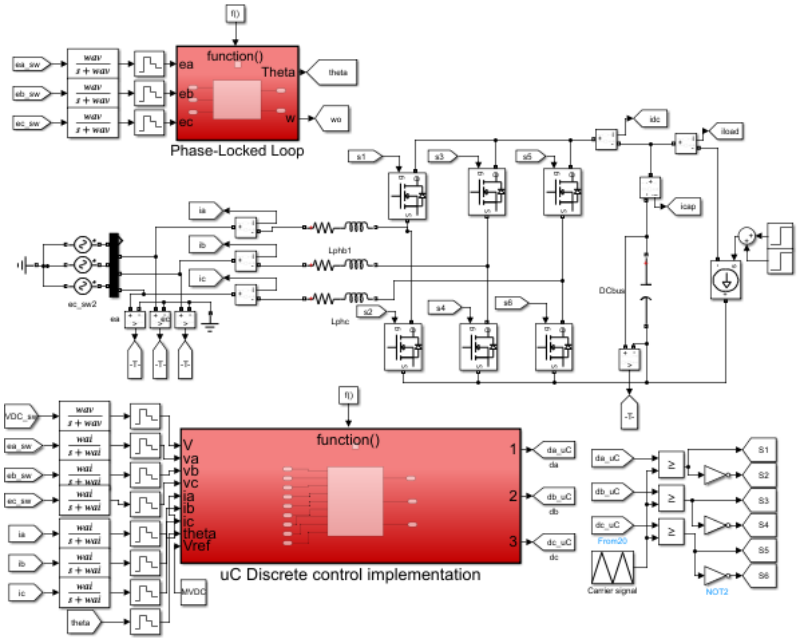

Figure 3-7. MATLAB/Simulink discrete system simulation with C-code based control loop implementation

Details of the designed PFCVR prototype are shown in Annex A, although experimental test finalization is postpone to future work.

3.2.3 Additional topology features

The main claims of this new topology are expounded in [156]. The DIMMC has been identified as a promising candidate to be used in AC to AC conversion systems with accessible HV DC bus, in which commonly two conversion stages are implemented, see Figure 3-9. The main advantage of the DIMMC over the back to back MMC is

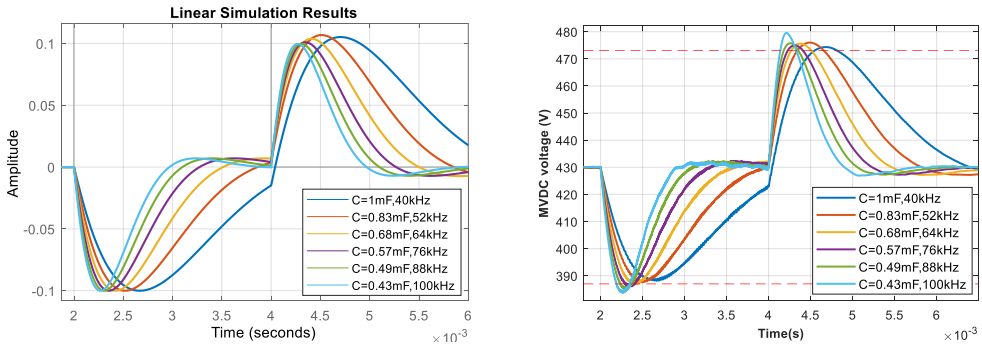

(a) (b)

Figure 3-8. Step response evaluation with the minimum capacitance calculated. Red dashed lines indicate the allowable voltage variation band (a) Theoretical time response. (b) PFCVR switching model simulation implemented in MATLAB/Simulink

that in the DIMMC, one MMC stage can be eliminated, and the number of arms inductors and capacitors is halved. Duplication of switches is the price to pay for reducing the volume and weight of the topology as passive elements are the main drivers. This fact, in addition to the capacitance reduction, presented previously, result into a more compact topology providing a higher specific power for applications related to transportation electrification under the aforementioned architecture conditions. Therefore, the DIMMC can be of high interest for high power electric mobility applications such as aerospace, where the weight reduction is one of the main targets when designing power converters [157].

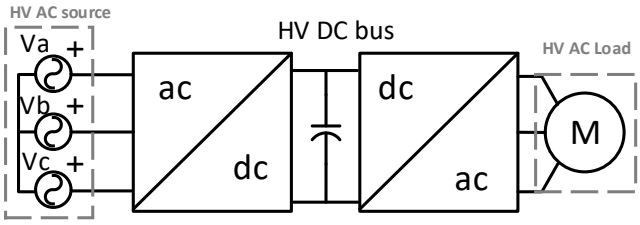

Figure 3-9. Back-to-back ac to ac conversion scheme.

The C_{cell} capacitance reduction has been explored with detail. But the fact of controlling the C_{cell} voltage level has and additional feature, the requirement of cell balancing techniques is suppressed. Consequently, the number of commutations per cycle of the half-bridge and the switching losses are reduced when comparing with balancing techniques as the sorting method. The cells are connected sequentially following an staircase modulation and remain connected the entire level cycle without swapping with another one to balance the voltage.

Another feature of the proposed DIMMC topology is its better short-circuit capability in comparison with the traditional MMC in a back-to-back configuration. Short-circuit capability has been evaluated based on the topology effectiveness in blocking the fault current when the modulation is disabled. No extra fault current control is considered. Two types of short-circuits are analyzed: AC side and DC side short-circuit. In the situation of suffering a short-circuit at the HV AC load side, both topologies feature a similar performance. The path followed by the fault current from the source to the faulty point is illustrated in Figure 3-10.(a) and Figure 3-11.(a). After disabling the modulation, the fault current will naturally fade when the cell capacitor voltage is higher than the phase peak voltage and the freewheeling diode is reverse biased [167]. When a short-circuit happen in the HV DC bus, the MMC converter that is connected to the HV AC source will further contribute to the fault, the free-wheeling diodes of the switches will provide a path for the current from the HV AC source to contribute to the short-circuit current [168]. The expected current path is displayed in Figure 3-10.(b). With the DIMMC, in case of having a fault in the HV dc port, after disabling the modulation, the fault current will flow through C_{cell} until this is charged to the input phase peak voltage and the current is blocked by the freewheeling diode (similar to the case of the

short-circuit at the HV ac load side). The current path in this case is illustrated in Figure 3-11 .(b). Only the contribution of one of the ac phases is shown for simplicity.

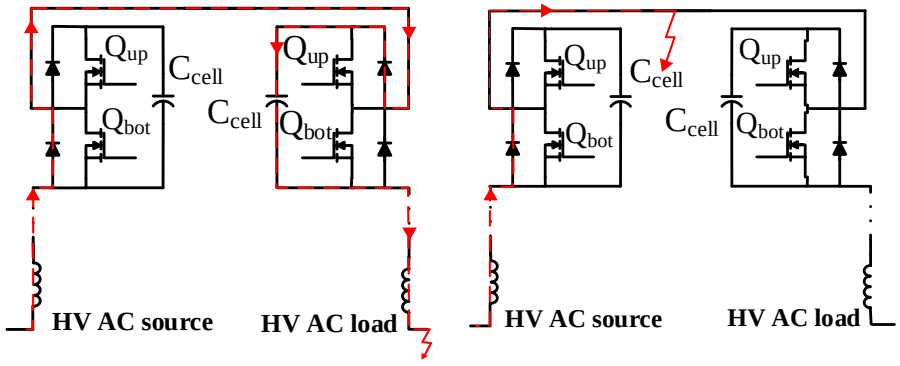

(a) (b)

Figure 3-10. MMC fault current paths. (a) AC side output short-circuit. (b) DC ports short-circuits

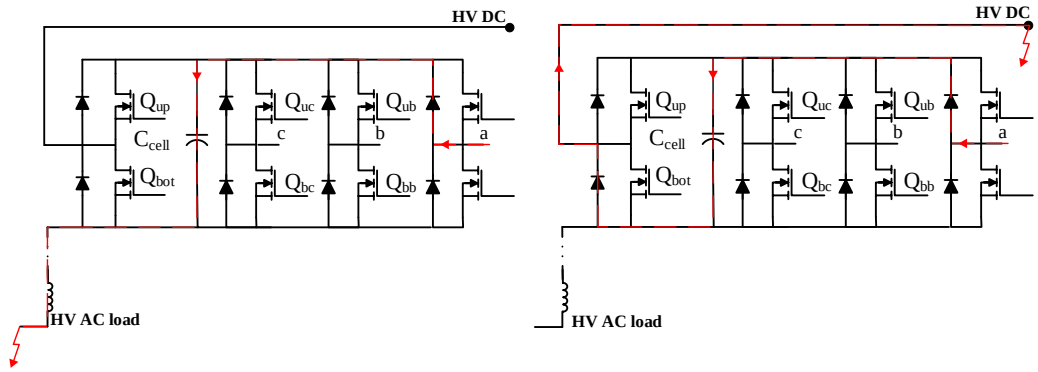

(a) (b)

Figure 3-11. DIMMC fault current paths. (a) AC side output short circuit. (b) DC ports short-circuits

It can be concluded that in terms of short-circuit handling capability the DIMMC topology is superior to a conventional MMC.

3.2.4 DIMMC simulation results

All the claimed features has been validated by simulation, a model has been developed in MATLAB/Simulink. The DIMMC model is formed by 7 cells per arm (N_{arm}), which is translated into 15 voltage levels (N_{levels}). The arm inductances have been designed to reduce the second harmonic component of the circulating current. The MMC conventional design method described in [169] has been followed. Each cell is formed by a half bridge and the chosen C_{cell} value is 0.47 mF, which correspond to the design case of 136 kHz switching frequency. The half bridge switches are model with an ideal switch model, only considering the on resistance (Rds_{on}). The PFCVSR has been simplified by the voltage control loop and a current source. The control signal of the voltage control loop is the reference direct component current of the PFCVR input ac current (i_d), assuming an ideal current control loop, this would be the current injected to correct the voltage deviation of the C_{cell}. This can be deduced from the average model equation in steady state and assuming power factor correction,

$$C_{cell} \cdot \frac{\partial V_{cell}}{\partial t} = \frac{3}{4} \cdot i_d \cdot M_d - i_{cell}. \tag{3.25}$$

Where i_{cell} is the load demanded by the cell.

The main simulation parameters are summarized in Table 3.3. The steady state operation of the new topology has been tested running the model under the following specifications: seven cells per arm, DC cell voltage of 430 V which is translated into 3000 V DC voltage (i.e. DC bus voltage level value expected for a AEA/HEA), three-phase AC voltage peak of 1500 V, AC power of 1 MW, and DC power of 50 kW. These specifications have been chosen as matter of example of a feasible application

for this topology in the context of aircraft electrification.

In Figure 3-12, it can be seen that the HV AC voltage and currents are similar to those in a equivalent MMC. If the system is balanced, the DC current through each phase will be 1/3 of the demanded current by the HV DC load. Figure 3-12 also displays the HV DC voltage and current, both AC and DC loads are supply simultaneously. At 30 ms a HV DC load step is performed, HV AC output signals remain invariable. Additionally, at 40 ms the HV ac voltage frequency changes from 400 to 300 Hz, the HV DC port signals are not affected. Consequently, this verify the system multiport feature, which makes the topology to be able to provide DC and AC current simultaneously.

TABLE 3.3. DIMMC simulation main parameters.

DIMMC design		**Operation point**	
Parameter	**Value**	**Parameter**	**Value**
N_{arm}	7	V_{HVDC}	3 kV
N_{levels}	15	V_{cell}	430 V
L_{arm}	1.2 mH	$freq$	400 Hz
R_{Larm}	1 $\mu\Omega$	P_{ac}	1 MW
C_{cell}	0.47 mF	PF	1
Rds_{on}	0.65 $m\Omega$	P_{dc}	50 kW

In addition to the steady state operation of the topology, it has been also verified by simulation the capacitance reduction, main feature analyzed in [158]. Thanks to the regulation of the cell voltage, the required capacitance at the cell can be significantly reduced, and therefore, the overall volume and weight of the converter. In the bottom figures of Figure 3-13, the voltage level of the cell labelled as "1ua" of a conventional MMC and the DIMMC are shown. In both cases, the converter is operating in steady state at the same operating point. But, in the case of the DIMMC the capacitance value of the cell capacitor is 30% lower. The MMC cell capacitance has

been designed following [166], the resulted value is 0.67 mF (0.47 mF in the DIMMC). It is appreciated that in Figure 3-13.(b) the voltage is kept within the limits even the C_{cell} value has been reduced by a 30%. However, it has been detected that the modulation and control algorithm chosen does not allow to reverse the current flow in a controllable way, but the current demanded when inserting the cell in the DIMMC arm can demand negative current (i.e. current flowing in the PFCVSR). The data showed in Figure 3-13.(b) correspond to a simplified scenario in which this constrain is not taken into account as the purpose was to verify the capacitance reduction capability of the DIMMC. Further research needs to be performed in regards this, which has been postponed as future work.

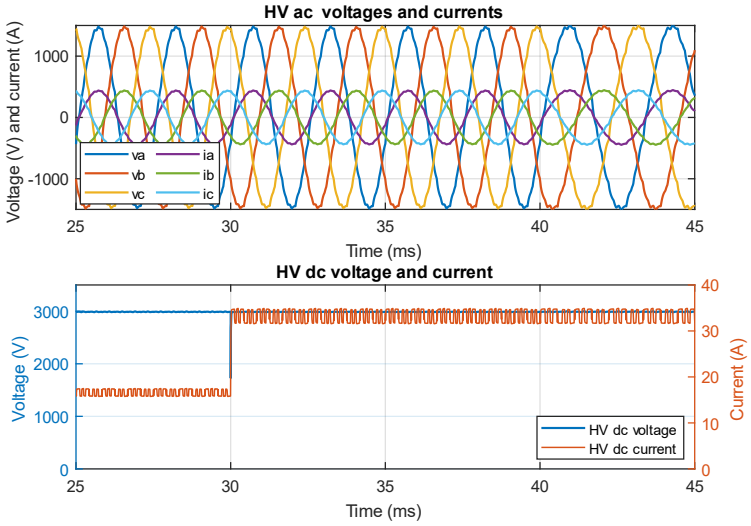

Figure 3-12. Steady state output HV ac phase voltages and currents (upper) and steady state output HV dc voltage and current (bottom).

As has been mentioned and can be seen in in Figure 3-13, the number of commutations of each cell per grid cycle is significantly lower in the DIMMC. In Figure 3-13.(a), the insertion state of one cell is illustrated when a sorting algorithm is used

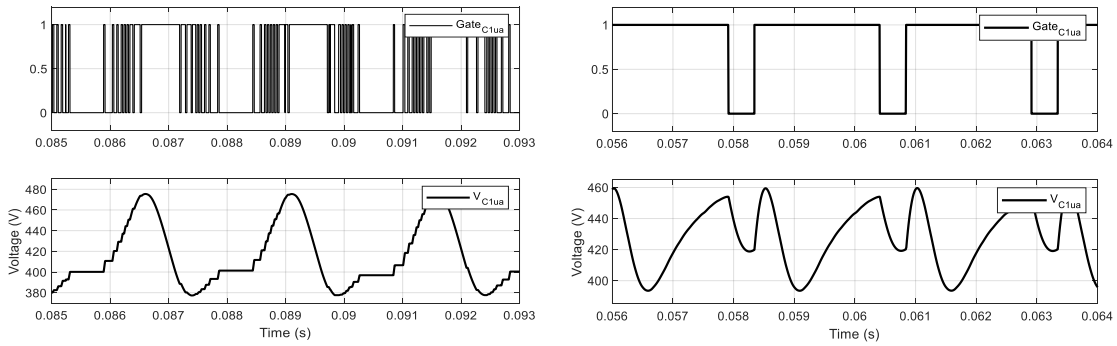

Figure 3-13. Cell *1ua* activation signal and C_{cell} voltage level. (a) MMC topology with sorting algorithm implemented for cell's voltage balancing. (b) DIMMC (sorting is not needed)

for maintaining the cell voltages balanced in a conventional MMC [170]. The sorting algorithm measures the cell voltage and depending on the arm current direction it inserts first the cells with higher or lower voltage so at the end of the output AC voltage cycle the average voltage of every single cell is the same. Figure 3-13.(b) illustrates the insertion state of the same cell in the DIMMC. It is clear that the number of state commutations is significantly reduced when comparing Figure 3-13.(a) and Figure 3-13.(b), which potentially would reduce the switching losses of the cell at the DIMMC.

Similarly, the short-circuit fault handling capability of the DIMMC has been tested by simulating a short-circuit at the HV DC port. Figure 3-14 illustrates a short-circuit at t = 50 ms, it can be seen how the HV DC voltage decreases to zero. The modulation is disabled at t = 50.1 ms (i.e. reasonable high current detection time) and the short-circuit current intermediately after disappears. The fault peak current depends on the L_{arm} value and the fault detection time. In this specific case the peak fault current value is significantly high and further re-design is possible to reduce it.

HV side current and voltages are shown in Figure 3-15. As expected, the HV AC output turns zero when the modulation is disabled.

Additionally, Figure 3-16 illustrates what happens at one of the C_{cell}. In normal operation, C_{cell} voltage is higher than the input phase peak voltage. Therefore, if the modulation is disabled the freewheeling diode is reversed bias. In Figure 3-16, the voltage of the C_{cell} drops initially, this is because the fault occurs at t = 50 ms and the modulation is disabled at t = 50.1 ms. Once the rectifier switches are open, as the C_{cell} voltage remains higher than the input phase peak voltage the diode blocks the current and the voltage remains constant.

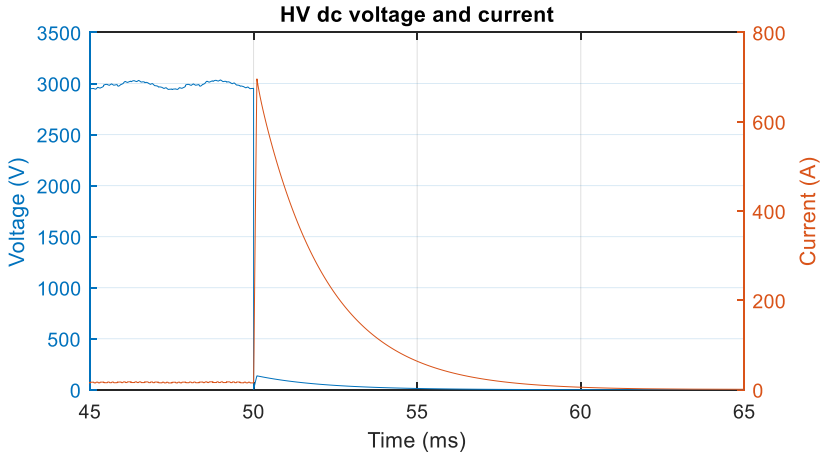

Figure 3-14. HV DC port fault simulation. At t = 50 ms a short-circuit occurs and at t = 50.1 ms the modulation is disabled.

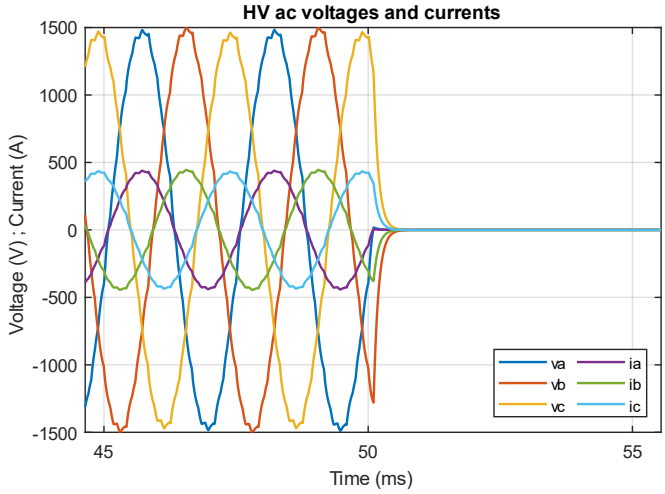

Figure 3-15. HV AC output voltages and currents. At t = 50 ms a short-circuit occurs and at t = 50.1 ms the modulation is disable

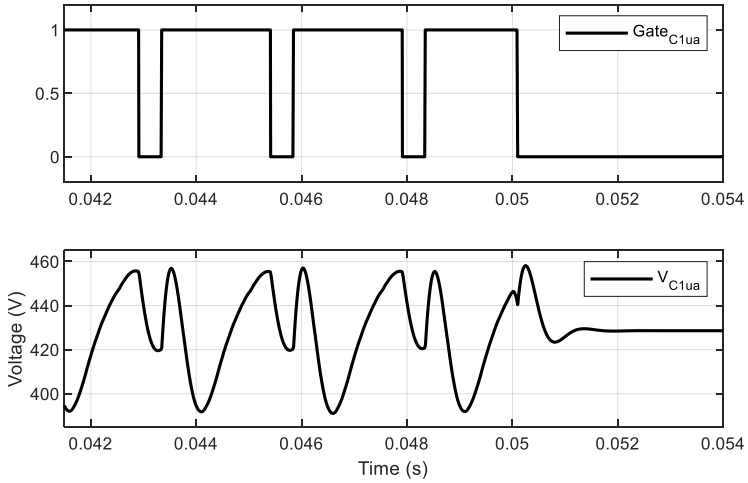

Figure 3-16. C_{cell} voltage of one cell. At t = 50 ms a short-circuit occurs and at t = 50.1 ms the modulation is disabled

3.3 Conclusions

The analysis presented in subsection 3.2.2 has shown the potential reduction of the capacitance to achieve a more compact solution for the DIMMC. The DIMMC provides modularity and scalability features, cells capacitor volume and weight reduction and better short-circuit current handling capability when comparing with a conventional MMC. It has been shown, how with the DIMMC the cells capacitance value can be reduced for a similar voltage fluctuation in the cell. Additionally,a sorting method for balancing the voltage cells is not needed, providing a significant reduction of the half bridge commutations, therefore, potential switching losses. Furthermore, its better short-circuit handling capability with respect to a common MMC makes possible to fade the short-circuit current caused by a HV DC port fault by opening all the switches.

Nevertheless, further investigation is needed to consolidate the potential of this solution. A deeper study of the control and modulation methodology of the PFCVSR needs to be done, as during the DIMMC evaluation certain limitations has been detected that deteriorate the expected results. Furthermore, a combination of the results obtained with the study of the system losses can give a better understanding of the advantages of this solution to be implemented in the any HEA.

In addition to the DIMMC, the methodology to estimate and reduce the size of output capacitor is considered as other contribution on its own. The reduction ratio depends in a non-linear way to the switching frequency of the PFCVR and depending of the operation point a different minimum switching frequency is required to obtain advantages. Further analysis to select the optimum switching frequency should need

to take into account the losses calculations of the proposed topology. Experimental validation of the presented simulation results has been postponed as future work due to limitation of time.

Chapter 4

EMI mitigation.

In previous chapters the reader has been able to explore from architecture level the technology gaps and challenges of an aircraft electrical power train. Afterwards, this document has expounded the particular issues of power converter design in this application and a new power converter idea that could be of interest in aircraft electrical propulsion.In this chapter the thesis focuses on the third major concern faced when working on the design of new EPS for the future aircraft, EMI compliance.

The EMI mitigation in future electric planes presents serious challenges due to the high voltage and power levels, the lack of scalability to this new scenario of the existed regulation and the high specific power enabled by designs with high dv/dt and di/dt, which bring new EMI filtering requirements. Regarding power density reduction, passive EMI filters (PEFs) are limited by the material technology available, being the magnetic material used for the core and the winding technique the main limiting factors for reducing the inductor size. In [171], the impact of core saturations issues

in the inductor volume is covered. The shape factor is studied and a picture of the difficulty of getting an optimized inductor design for minimizing its volume can be concluded.

It is for the aforementioned reasons that EMI is a major topic in the aerospace industry. An example of this, is the project EASIER [57], where this thesis has contributed. The propulsion architecture covered in this project is the hybrid parallel propulsion, which has been highlighted as the most promising one in Chapter 2 for regional plane application.

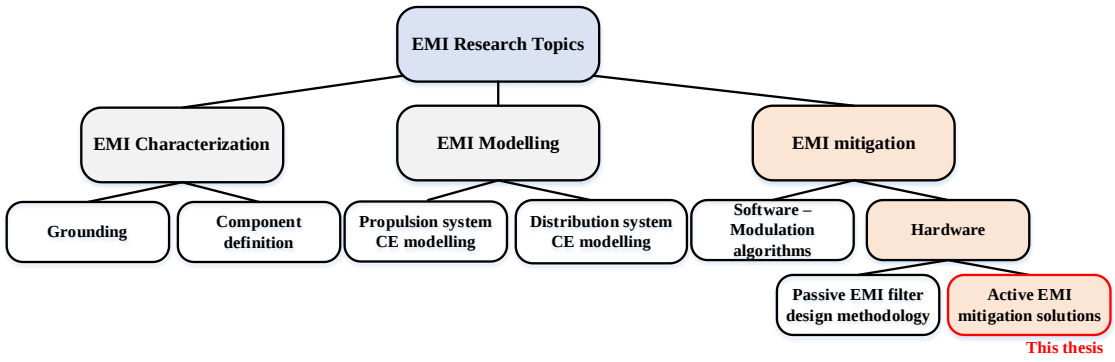

Figure 4-1. Main research topics in conducted EMI found in the literature.

The project covers both radiated and conduction emissions. Figure 4-1 displays the main research lines covered by the project: EMI Characterization, modelling and mitigation research lines. A thorough investigation has been conducted on software and hardware mitigation of conduction emissions. The work of this thesis has contributed in this last topic by focusing on the development Active EMI filter (AEF) solutions for helping on the optimization of the hardware mitigation designs. Possible AEF implementation is shown in Figure 4-2. Figure 4-2.b illustrates a typical implementation where the AEF is installed and combined with a PEF [172,173], and

Figure 4-2.c a specific case where the AEF is used to modify the impedance of any element of the PEF. The thesis has focused on this specific case and this is named as Hybrid EMI filter (HEF) in the document for now and on. The aim is to allow the reduction of the size of the passive elements involved in the filter.

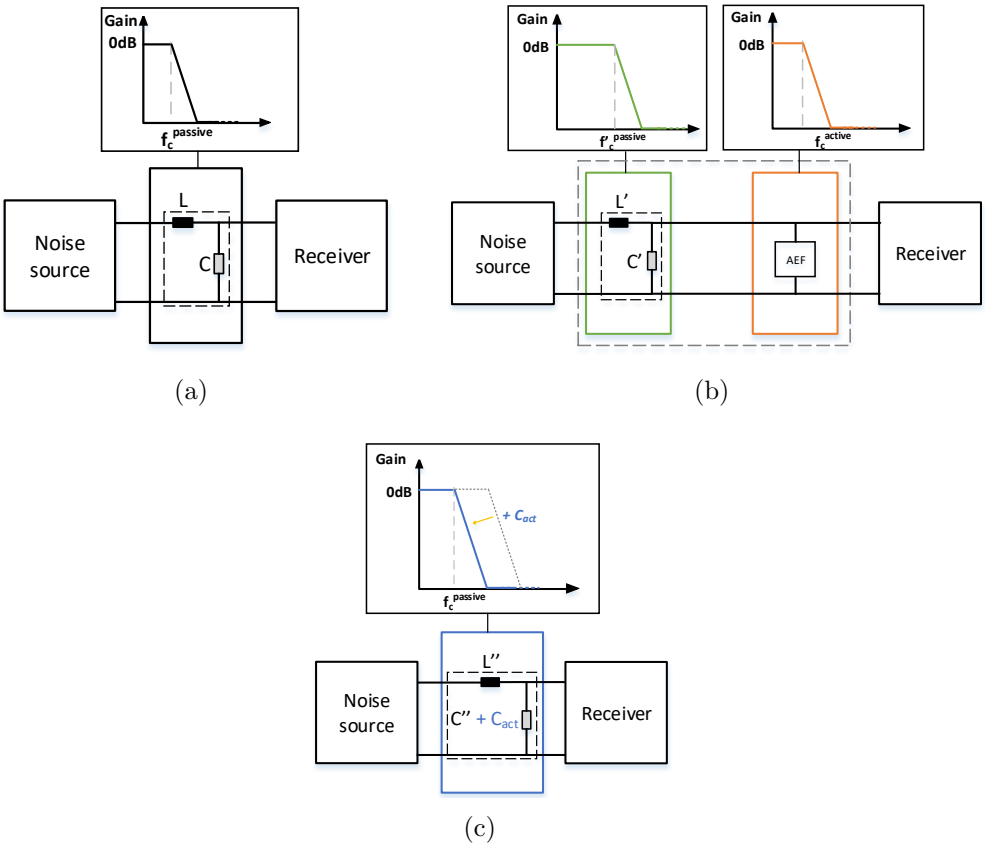

Figure 4-2. Possible AEF implementation to improve the EMI filter design. a) Original PEF. b) AEF used in combination of a PEF. c) AEF particular used to active impedance modification.

The chapter is organised as follow. Firstly, it presents a brief introduction of the scenario under study and the main EMI and safety constraints. Basic theory of

EMI and filter design theory is explained after that. After, the AEF state of the art is extensively introduced,in which the main AEF topologies, implementation and characteristics are presented. The two last parts of this section focus on two novel active solutions that allow volume and weight improvements of the CM filter stage.

4.1 Introduction

4.1.1 Scenario and requirements.

The EMI filter stage or stages presence in the system needs to provide the required attenuation without penalising the power converter volume and weight. The main concern of electronics and EMI engineers is achieving compliance with EMC standards. Current accepted EMI standards like DO-160 will be taken into account for the development of this work although they do not cover the magnitude range that a hybrid electric propulsion requires. The main EMI magnitude constraints assumed at the power connection with the dc source and the interconnection bundle of the inverter with the motor are illustrated in Figure 4-3.

Additionally, Figure 4-3 illustrates three potential locations for EMI filters although the actual presence of input, output filter or both will depend on each case. The interaction between input and output filter makes difficult to know before design and verification what is the ideal filter stage combination. The main reason is the effect they produce over the conduction mode noise loops. For instance, output filter modifies the impedance seen by the noises sources presence in the inverter and consequently certain CM noise can be redirected to the input, increasing the level

of EMI noise. The idea behind the across filter solution is to offer the possibility of a combined attenuation action [174]. An example case is measuring the input CM noise and attenuating at the output. An example can be seen in [175], where the common mode current at the input is measured and a compensating current is injected in the ground connection of the motor (i.e. system load).

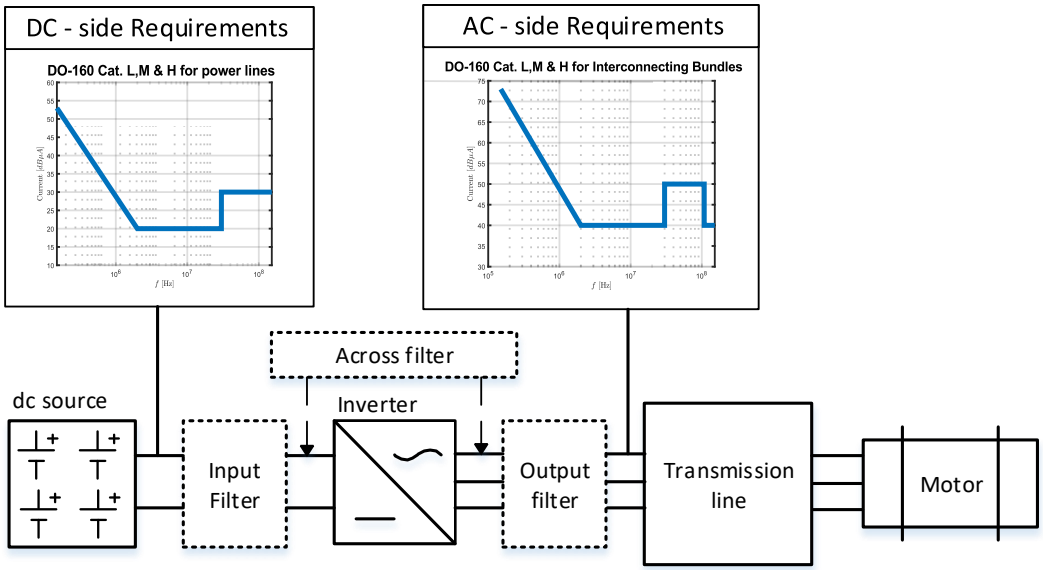

Figure 4-3. Simplified scheme of the potential EMI filter deploy within the overall propulsion system. Regulated DO-160 requirements.

In the particular scenario of aerospace, OEMs lighting strikes safety requirements imposed certain constraints to the EMI filter design. In order to limit the propagation of the current generated by the lightning strike the minimum impedance between any conductor and the chassis of the equipment is limited to a value specified in the ABD100 (i.e.,Environmental Conditions And Test Requirements Associated With Qualification defined by Airbus). Indirectly, this impacts the minimization of weight and losses of conventional EMI filter design as the shunt capacitor value that can

be used is constrained. This has led the filter design optimization to look for new alternatives that can help on the reduction of volume of the overall PEF. One of these topics is the AEF that can be integrated , as it has been illustrated in Figure 4-2, in combination with the PEF to help to reduce the size.

4.1.2 Passive EMI filters, the classic design procedure.

The start point of any EMI filter is the examination of the study case and identification of potential noise sources and propagation paths. A noise source is identify as any element that can generate a disturbance ,identified as EMI, that through any coupling method (i.e. radiative, inductive, conducted or capacitive) can reach reach an electrical system and degrade its performance and even stop it. Power electronics are identify as noise sources due to they intrinsic di/dt and dv/dt that can propagate over-voltage and leakage currents along the system that can provoke malfunction and failures.

A clear picture of the grounding scheme of the system and the interconnection among multiple grounds, if applied, is important in order to identify the propagation paths of the conducted noise. Additionally, it is vital to identify parasitic elements present in the different parts of the system. Identification of the regulation measure requirements must be part of the initial steps too. This provides the details of the LISN network to be used in the measurements and the noise type that is limited. In the specific case of the DO-160 the EMI limits are defined as $dB\mu A$ and the LISN network to be used is illustrated in Figure 4-4. L_1, R_1, C_1 and C_2 values are defined in the regulation while R_{load} is the impedance we charge the circuit with, usually the EUT is charged with 50 Ωs .

The consecutive step is the measurement of the noise to be able to identify the required attenuation needed, it is the level of noise to be reduced. The respective CM and DM attenuation levels are defined by,

$$A_{CM} = I_{CM} - I_{CM}^{DO-160},$$
$$A_{DM} = I_{DM} - I_{DM}^{DO-160}. \tag{4.1}$$

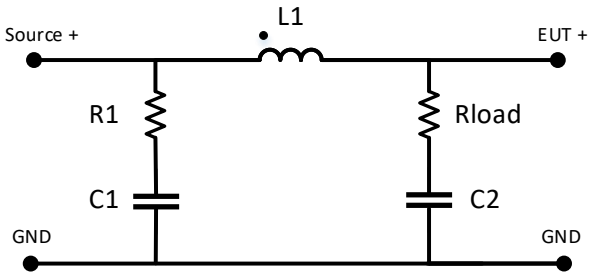

Figure 4-4. DO-160 LISN Network

Although the attenuation is used as the design metric it is of valued for the reader to know that EMI Filters are commonly characterized by their Insertion Loss (IL). IL can be described as the capability of create the maximum mismatch impedance between input and output at undesired frequencies while providing maximum matching at desired ones. As can be deduced this can be seen as a complementary metric of the attenuation. It is expressed as the ratio between the noise magnitude before and after connecting a EMI filter,

$$IL = 20 \cdot \log_{10}\left(\frac{Unfilteredsignalamplitude}{Filteredsignalamplitude}\right). \tag{4.2}$$

Both metrics (i.e. Attenuation and IL) can be expressed in terms of voltage or

current, however as established by the DO-160 the second one is used along the document. For the study case presented in the previous subsection the conducted noise measured at the LISN, Figure 4-5.a and the required attenuation, Figure 4-5.b are presented as matter of example. The DO-160 limit is also illustrated, it regulates the conducted emissions current level of airborne equipment from 150 kHz up to 152 MHz. A good practice is to add a 6dB margin to the calculated attenuation.

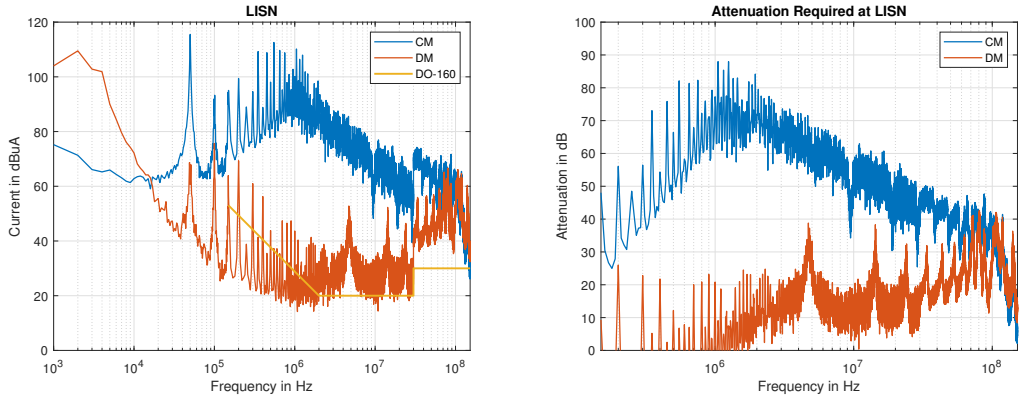

(a) (b)

Figure 4-5. Example of attenuation calculation. a) CM and DM noise measured at the LISN. b) Calculated Attenuation..

The following step in the EMI filter design procedure is to identify the design frequency, f_d. This is the first frequency, within the frequency range regulated, in which the noise exceeds the limit, with the assumption that for all higher frequencies the required attenuation does not exceed the asymptote formed by:

$$A_d < A_d + 20 \cdot n, \tag{4.3}$$

being n the order of the filter. Table 4.1 illustrates the order of the common EMI

filter topologies. If higher order filters are needed, a common practice is to stack stages. This is done for both CM and DM.

The theoretical cutt-off frequency of the filter based on te design frequency and the filter order is defined as:

$$f_c = f_d \cdot 10^{\frac{-A_d}{20 \cdot n}}. \tag{4.4}$$

One important comment to make at this point is that apart from the design considerations regarding attenuation, impedance mismatching is an important design requirement when defining the filter topology. Noise source and load impedances have a big impact on the EMI filter performance. This impacts the reflection loss of the filter, that can be translated into ratio of noise reflected back towards the source. Therefore, EMI filters need to be designed for both insertion (i.e. attenuation) and reflection [176].

TABLE 4.1. Attenuation slope of the most common EMI Filter topologies.

Filter Type	Filter order (n)
LC filter	2
CL filter	2
T type	3
π type	3

Commonly, the CM filter is designed first because of two reasons: the leakage inductance of the CM choke could impact the DM filter design and the CM filter shunt capacitors (C_y) will contribute to the total effective DM capacitance. Once the filter type is selected and the attenuation requirements are met, the next step is to determined the filter components. Following the equation,

$$L_{CM} = \frac{1}{(2\pi f_c)^2 \cdot C_y}, \tag{4.5}$$

the effective inductance and capacitance value of the CM filter can be calculated. Note here that the equation described in 4.5 have infinite solutions, additional design requirements as volume or impedance to ground limitations will lead to the final solution. Being L_{CM} the filter choke for LC, CL and π or the parallel equivalent for the T-type or multi-stage filters.

Regarding the DM filter design, the process is similar to the one described for the CM choke. The design frequency is chosen analysing the DM noise spectrum and the theoretical cut-off frequency is determined. Leakage inductance of 1-2% of L_{CM} can be assumed during the design of the DM filter. A damping network can be necessary to avoid the amplification of harmonics components at the resonance frequency of the filter of either or both filters. Commonly, a damping network consisting on a series connection of a resistance and a capacitance (RC branch) is implemented in parallel to C_y [177].

The EMI filter design is an iterative process. For the topology selection, it is important to take into account how this will interact with the rest of parasitic elements of the system, even after conducted path identification preliminary study. For instance, the attenuation can be lower than the expected because one element of the filter is bypassed caused by the interaction with rest of the system. Moreover, the parasitic elements present in the capacitors and chokes (i.e. ESR, EPC and EPR and ESL) can produce a filter deterioration of the response because of the non-idealities present in the frequency characteristic of its elements. Figure 4-6 illustrates this phenomena. Frequency modelling of the filter is need to guarantee an accurate theoretical result.

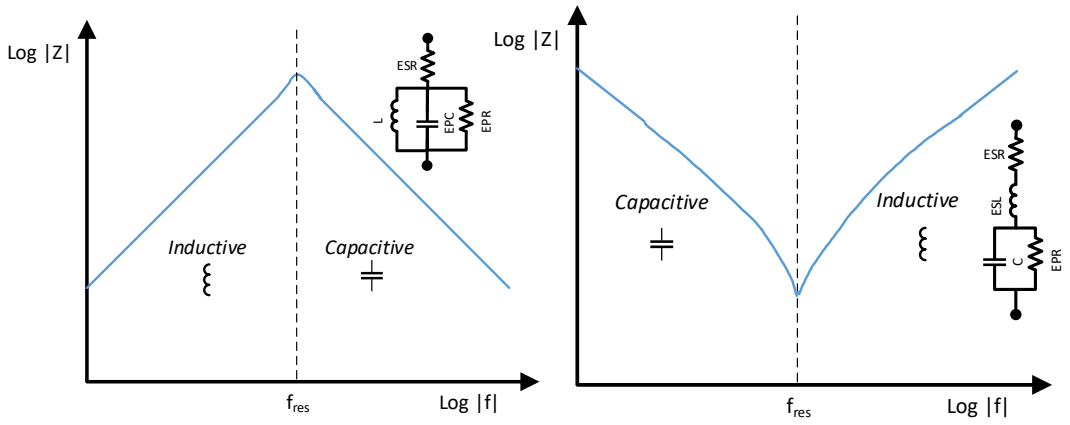

Figure 4-6. Non-ideal frequency characteristic of: (a) Real capacitor, (b) Real inductor

4.1.3 State of the art of active filters.

Active filtering gives numerous implementation options in terms of position, sensing and injection. Therefore mapping all the possibilities can become complex. The review presented in [178–180] can be used as the starting point. In [178, 179], AEFs are classified based on the compensation signal used (i.e. voltage or current injection), on the sensing method (i.e. noise measured as voltage or current signal) and the compensation method (i.e. feedforward or feedback compensation). The analysis presented helps on the configuration selection as it is focused on defining requirements and limitations of each of the AEF configurations explained . Figure 4-7 illustrates all possible sensing-injection combinations that are covered. They are: current sensing-voltage compensation (CSVC), voltage sensing–voltage compensation (VSVC), voltage sensing–current compensation (VSCC) and current sensing–current compensation (CSCC). I_s and u_s refer to the current and voltage sensed

signal, I_c and u_c are the current and voltage compensation signals.

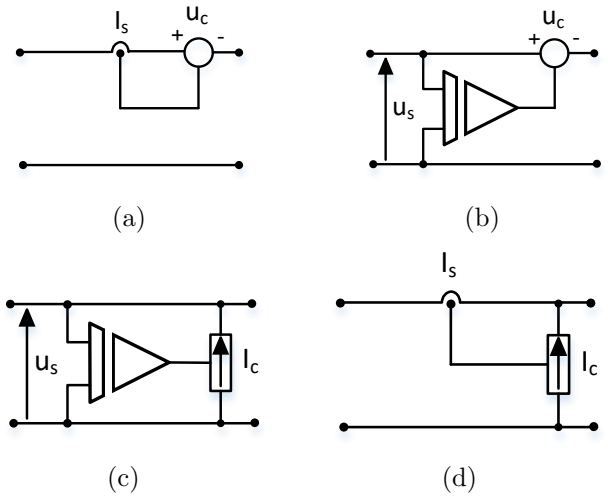

Figure 4-7. AEF types regarding measured and compensation signal. a) CSVC, b) VSCV, c) VSCC, d) CSCC

Depending on the compensation method, the noise mitigation nature of the filter is different. Voltage compensation will create a high impedance path in series with the noise source to attenuate the noise current. Therefore, it can be comparable to an inductor. On the other hand, current compensation creates a low impedance path in parallel with the noise source though where the current is recirculated. Thus, it would behave similarly to a capacitor.

Looking into how the noise measured is processed to generate the compensation signal, AEFs can be classified as feedback or feedforward compensation. Working under feedback compensation mode, the noise signal is measured at the receiver and the AEF output is generated by a close-loop response. In contrast, an AEF with feedforward compensation mode measures the noise at the source and generates a cancellation signal to mitigate the noise before reaching the receiver. Commonly, the

sensing and injection signals share the same nature. Thus, from the classification displayed in figure 4-7, only CSCC and VSVC AEF types can work with a feedforward mode. Figure 4-8, illustrates CSCC and VSVC feedback, and forward versions. u_n and z_n are the noise voltage source and impedance, respectively. Z_{load} illustrates the load seen by the filter.

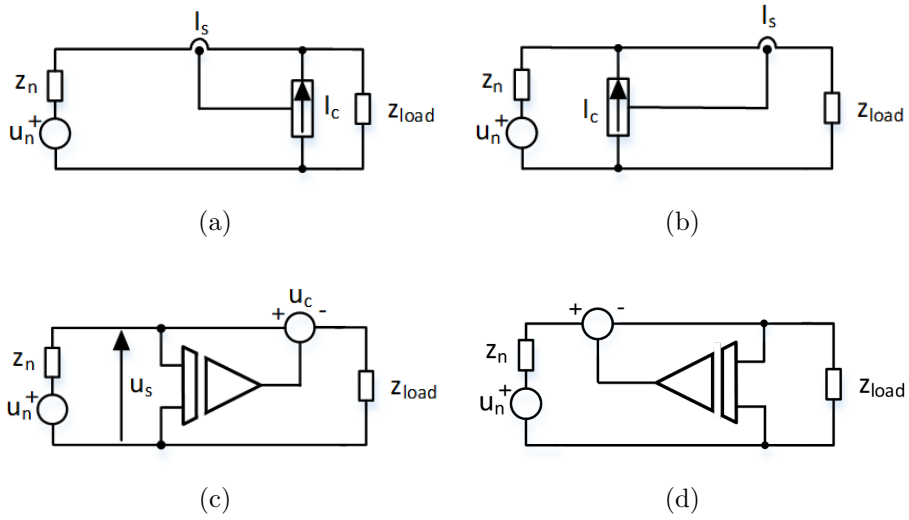

Figure 4-8. VSVC and CSCC AEF configurations depending on the compensation method. a) CSCC feed-forward , b) CSCC feedback. c) VSVC feedforward, d) VSVC feedback

Similarly to PEF, AEF filter performance can be evaluated based on IL. In [171] all the AEF types are evaluated based on this metric. Table 4.2 summarized the basic analytical expressions of all the AEF classes discussed up to now. Compensation equations describe the general operation of the AEF, where A_{type} defines the compensation gain. This must be equal or higher than 1 for any case. IL expressions are derived from the circuits shown in Figure 4-7 and Figure 4-8.

Analysing the IL expressions some operation particularities can be deduced which

TABLE 4.2. AEF compensation equation and IL

AEF Type	**Compensation**	**IL**
CSVC	$u_c = -A_{CSVC} \cdot i_s$	$1 + \frac{A_{CSCV}}{Z_{load}+z_n}$
CSCC feedback	$i_c = -A_{cscc} \cdot i_s$	$1 + \frac{z_n}{Z_{load}+z_n} \cdot A_{cscc}$
VSCC	$i_c = -A_{vscc} \cdot u_s$	$1 + \frac{A_{vscc}}{\frac{1}{Z_{load}}+\frac{1}{z_n}}$
VSVC feedback	$u_c = -A_{vsvc} \cdot u_s$	$1 + \frac{Z_{load}}{Z_{load}+z_n} \cdot A_{vsvc}$
CSCC feed-forward	$i_c = -A_{vscc} \cdot i_s$	$\frac{1}{1-A_{cscc}} \cdot \left(1 - \frac{A_{cscc} \cdot Z_{load}}{Z_{load}+z_n}\right)$
VSVC feed-forward	$u_c = -A_{vsvc} \cdot u_s$	$\frac{1}{1-A_{vsvc}} \cdot \left(1 - \frac{A_{vsvc} \cdot z_n}{Z_{load}+z_n}\right)$

help on identifying the best application cases. The IL capability of CSVC and the VSCC AEFs depends significantly on the noise source and load impedances. In both cases, the amplifier gain must be higher than the addition of both impedances to produce sufficient attenuation. Therefore, these types are recommended to cases in which the mentioned impedances are known. If they cannot be identified, CSCC and VSVC feedback compensation method would be preferable. Additionally, In all feed-forward compensation AEFs the compensation gain must be ideally unity, which makes the IL infinite based on the equations of Table 4.2. Furthermore, CSCC is recommended for the case in which the noise source is close to an ideal current source, it is $z_n \gg z_s$. VSVC feed-forward type is suggested to be used in systems with noise source close to an ideal voltage source, it is $z_n \ll z_s$. Thus, the IL would be determined mainly by A_{type}. From the literature, it can be deduced that feedback method gives more flexibility in terms of design. The reason is that feedforward compensation requires deeper information of the system in order to guarantee unity gain and therefore a good attenuation. That can be translated into a higher dependency on component value accuracy with a feedforward control method.

The survey presented in [179] gives a extensive AEFs classification focusing in the implementation. A humongous literature collection is displayed covering the main three parts of the AEF: noise measurement, noise processing and compensation signal injection. After reviewing the literature it seems the most common AEF solutions use current sensing and voltage injection, for instance [181–183]. However, in the context of the application case described previously in Figure 4-3, the use of measuring coils or transformers is avoid. One of the main two reasons is that those solutions tend to be more voluminous, costly and required higher cooling effort [184]. The second reason is scope based, as in this thesis the research has been oriented to AEF solutions to be implemented under the scenario displayed in Figure 4-2(c), where, from the point of view of the author, voltage sensing solutions are more suitable.

Theoretically speaking voltage sensing and current injection implementation only employ capacitance coupling, which must be rated for the operating voltage but has not to be designed to support the nominal current (i.e. potential light and small capacitors can be used). In practice, gain adaptation or high-pass filter connection stages in the sensing branch might be needed, for instance [172] CM voltage noise is detected by using Y-connected resistors and a high-voltage isolation amplifier.

Because of all the previous arguments the pre-selected AEF topology to be explored in the chapter of this thesis is the VSCC.

4.1.4 Hybrid EMI Filter introduction and conceptual design

In the literature and this thesis, the particular used of AEFs to modify the impedance of any element of a PEF is labelled as HEF, see Figure 4-2 (c). The objetive is to

increase the attenuation of the original filter in a certain frequency range or to reach a similar response of the filter using smaller passive elements (i.e. mainly focused in reducing the choke size). If the AEF acts as an active capacitor, the resultant HEF is labelled as Type I, and if the AEF acts as an inductor instead, it is a HEF Type II. Figure 4-9, illustrates the mentioned cases. Active capacitors are usually implement with current compensation AEFs and active inductors with voltage compensation AEFs.

As mentioned previously, this thesis is focused in VSCC AEF topology, therefore a HEF type II is explored. This HEF type is specially interesting for bypassing the shunt capacitance limitation imposed by airframes but keeping lighting strike safety requirements. The conceptual idea is that a passive capacitor can be designed to be under the maximum allowed capacitance defined by the ABD100 and an AEF working as an active capacitor can increase the effective capacitance along a certain frequency range. Therefore, the size of the entire filter can be reduced, as for the same attenuation the required chokes can be reduced. Furthermore, the safety ABD requirements regarding lighting strike can be guarantee, if an strike occurs the AEF can be disconnected and only the passive capacitance remains. Additionally, feedback compensation method is preferred as propulsions systems will be complex what makes difficult to have a good estimation of the noise source and load impedance, needed for the feedforward.

The design of a HEF can follow the same methodology introduced in section 4.1.2. Where the AEF is seen in the HEF as an active admittance defined by the compen-

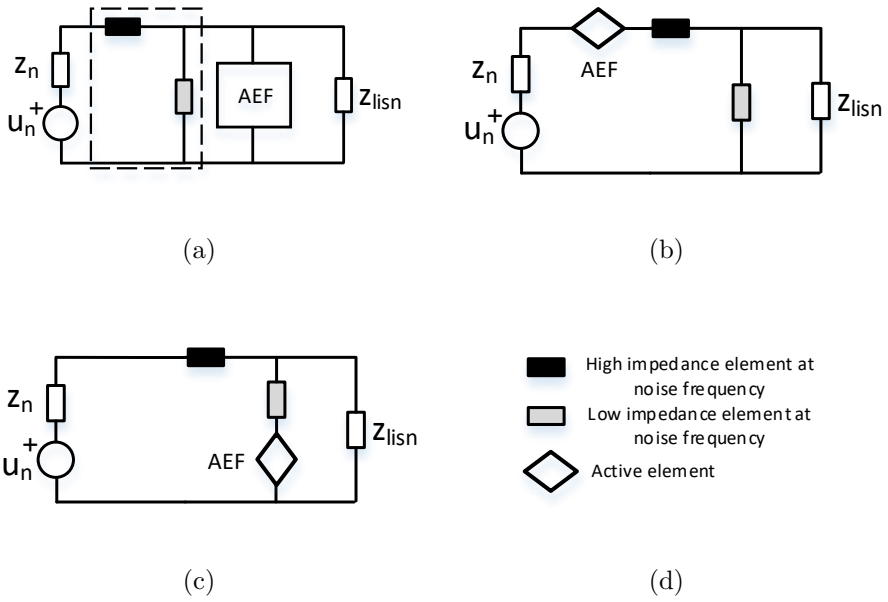

Figure 4-9. HEF used with or in PEF. a)PEF and AEF cascaded,b) HEF Type I,c) HEF Type II and c) Symbology Legend

sating current, I_c, and the noise voltage, u_s. ,

$$Y_{VSCC} = \frac{I_c}{u_s}. \tag{4.6}$$

HEF type II versions of the most common PEF (i.e.inverse gamma, gamma and T-type) filter topologies are illustrated in Figure 4-10. Where Z_{lcm} is the common mode choke impedance and Z_c is the shunt capacitor impedance. Notice in the illustrations Z_c is replaced completely by the AEF, although as mentioned before keeping it in connected in parallel with a passive capacitor is of interest.

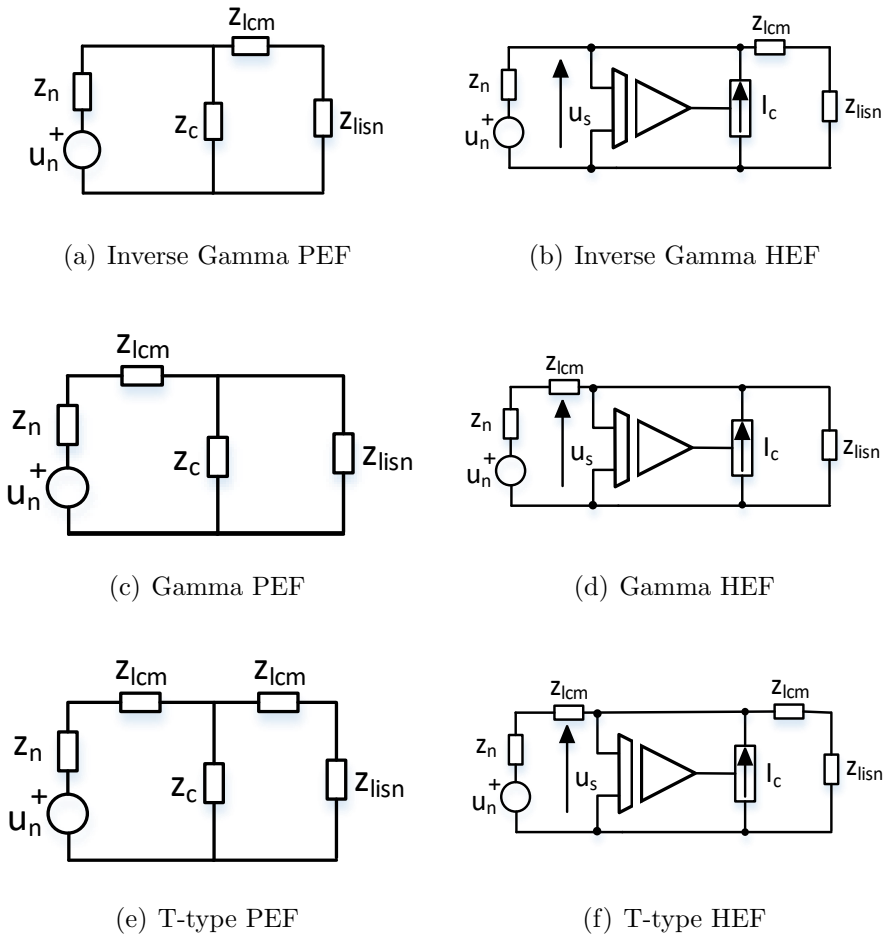

(a) Inverse Gamma PEF

(b) Inverse Gamma HEF

(c) Gamma PEF

(d) Gamma HEF

(e) T-type PEF

(f) T-type HEF

Figure 4-10. Examples of HEF using a VSCC AEF type

In table 4.2 the IL of each AEF type has been presented. The influence of the AEF in the original PEF IL characteristic is studied. The IL of the HEF examples illustrated in Figure 4-10 are displayed in Table 4.3. Ideally, the active VSCC AEF will act as a shunt path at the selected actuation frequency range. This is expressed as an admittance, Y_{VSCC}, and replace the original term $1/Z_c$ in the IL equations. The aim of the AEF is to emulate the behaviour of an equivalent passive capacitor

along the actuation frequency range. Increasing Y_{VSCC} it can see the IL will increase by analysing the equation. The actuation frequency range selected in the context of this thesis is from 150 kHz to 10 MHz.

TABLE 4.3. Main filter type IL expression

Filter Type	**IL**
Inverse Gamma	$IL_{IG} = 1 + \frac{Z_{lcm}}{Z_{lisn}+Z_n} + \frac{1}{Z_c} + Y_{VSCC} \cdot \frac{Z_n \cdot (Z_{lcm}+Z_{lisn})}{Z_{lisn}+Z_n}$
Gamma	$IL_G = 1 + \frac{Z_{lcm}}{Z_{lisn}+Z_n} + Y_{VSCC} \cdot \frac{Z_{lisn} \cdot (Z_{lcm}+Z_n)}{Z_{lisn}+Z_n}$
T-type	$IL_T = 1 + \frac{2 \cdot Z_{lcm}}{Z_{lisn}+Z_n} + Y_{VSCC} \cdot \frac{(Z_{lcm}+Z_{lisn}) \cdot (Z_{lcm}+Z_n)}{Z_{lisn}+Z_n}$

Although examples of VSCC AEF solutions can be found in the literature, none of the explored papers present a VSCC AEF design focused on obtained the Y_{VSCC} frequency response to validate the HEF Type II idea. Therefore, the present document main contribution are two novel VSCC AEF solutions that fill this gap.

4.2 Active EMI mitigation solutions.

Active filtering has become an attractive solution for achieving high power density converters, required in the future electric transport scheme, where the EMI filter entails a big percentage of the total weight. Most common implementation ideas has been presented in Figure 4-2.

In this section two novel AEF solutions that allow to modify the shunt capacitor impedance along the actuation frequency range of any EMI filter are presented. Circuitry design of each solution and analytical study of both designs are presented,

where mathematical expressions to model and design both are obtained. The non ideal characteristics of the analog elements used are taken into account, analysing their influence over the desired frequency response of the circuitry. Compensation techniques are included in each design in order to minimize their impact. The first design is based on operational amplifiers (OPAs) and it is able to emulate the impedance behaviour of a capacitor up to 10 MHz. A second design which incorporates a Linear Power Amplifier (LPA) at the output has been theoretically studied. This second design has potentially a higher power management capability. In the following lines, the theoretical analysis and design of both solutions is explained.

4.2.1 Design I: AEF based on Operational amplifiers

The first implementation idea is based on an analog circuit based on OPAs. Some technological requirements has been identified. The active system needs a wide-band frequency operation capability. Some radio frequency OPAs offer regulation bandwidth up to several GHzs, therefore they can be considered to be suitable candidates for implementing the AEF. Some AEF solutions using OPAs in the active system can be found in the literature [178, 184–187]. However, only a few focus on VSCC [175, 184, 188].

Two main types of OPAs exist, the Voltage feedback (VFB) and the current feedback (CFB) OPAs. Taking a look into the cited literature it can be seen the most used one is the VFB, except in [186, 187, 189]. To decide which type of OPA is used for the development of the AEF proposals the close loop gain of both is studied. The main claim for using a CFB OPA is they usually have wider bandwidths and higher slew rates than the VFB operational amplifiers, what could be translated in faster

responses. CFB does not have a Gain Bandwidth Product (GBP), that means that the close-loop bandwidth does not decrease with the gain, f_t. This is illustrated in Figure 4-11, where the close-loop gain under different dc gains values is displayed. It can be appreciated how in the case of VFB OPAs the close-loop response (red lines) decreases its bandwidth as the dc gain is increased.

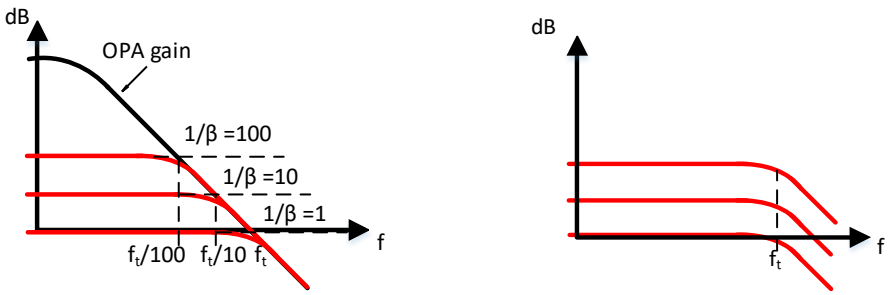

(a) Voltage Feedback OPA (b) Current Feedback OPA

Figure 4-11. Close loop gain

Even though the constant bandwidth feature makes CFB OPA attractive, the close-loop bandwidth is determined by an internal capacitor and the external feedback resistor. The latter, must be fixed for optimum stability, stray capacitance across the feedback will cause instability. Consequently, the degree of freedom in the design is reduced.This is the main reason why the design presented here is based purely in VFB OPAs.

The general scheme of the operational amplifier-based AEF integrated in a T-type filter (i.e the topology chosen to implement the HEF) is displayed in Figure 4-12 . The approach introduced here has mainly three different stages: the shaping stage, a boosting stage, and the decoupling stage. In the following lines we will go into

detail of each of them.

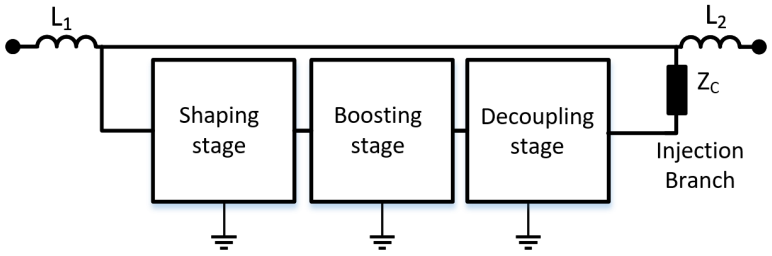

Figure 4-12. General scheme of the VSCC approach

4.2.1.1 Shaping stage

The aim of the VSCC active element is to control the injected current based on the input voltage measurement so the behaviour seen from outside looks like a shunt capacitor. The admittance of the system displayed in should be equal to the one of an equivalent capacitor of value C_{eq}. It is,

$$Y_{VSCC} = \frac{I_c}{u_s} = C_{eq} \cdot s. \tag{4.7}$$

Where, s is the Laplace operator.

The study of the system is oriented to impedance analysis. The shaping stage is designed focus on shaping the frequency response of the circuit so the voltage-current correlation is similar to a capacitor. The shaping stage together with the injection

branch defines the active system impedance. In Figure 4-13, it can be seen a general scheme of the shaping stage and the injection branch. This stage is implemented with an inverting OPA configuration where Z_i and Z_f define the inverting gain of the OPA and the injection branch can be seen as a load.

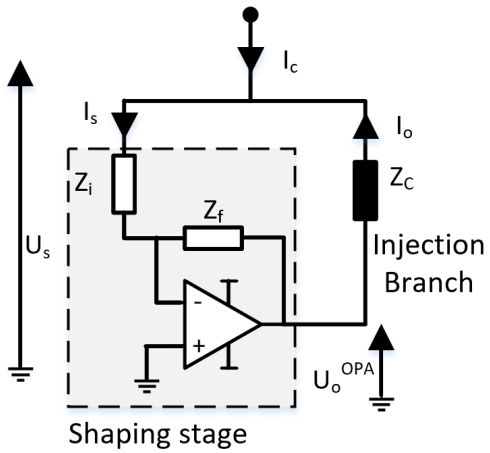

Figure 4-13. Shaping stage plus injection branch scheme.

The analysis of the input admittance of the filter yields,

$$Y^I_{VSCC} = \frac{1}{Z_i} + \frac{1}{Z_c} \cdot (1 + \frac{Z_f}{Z_i}). \tag{4.8}$$

RC branches are used for implementing the three main impedances,

$$Z_i = \frac{s \cdot C_i \cdot R_i + 1}{s \cdot C_i} \tag{4.9}$$

$$Z_f = \frac{s \cdot C_f \cdot R_f + 1}{s \cdot C_f} \tag{4.10}$$

$$Z_c = \frac{s \cdot C_c \cdot R_c + 1}{s \cdot C_c}. \tag{4.11}$$

Thus, equation (4.8) turns into,

$$Y^I_{VSCC} = \frac{R_c + R_i \cdot G_1}{R_i \cdot R_c} \cdot s \cdot \frac{s + \frac{1+C_c/C_i \cdot G_1}{C_c \cdot (R_c + R_i \cdot G_1)}}{(s + \frac{1}{C_i \cdot R_i})(s + \frac{1}{C_c \cdot R_c})}, \tag{4.12}$$

where G_1 is

$$G_1 = \frac{C_i \cdot (s \cdot C_f \cdot R_f + 1)}{C_f \cdot (s \cdot C_i \cdot R_1 + 1)}. \tag{4.13}$$

From (4.12) and (4.13) it can be deduced that if the term G_1 is a scalar, then the admittance of the system is defined by two zeroes and two poles. One of the zeroes is in the origin and another one at a position defined by the input and output impedances. One pole is defined by the impedance connected to the negative input of the OPA and the second one by the injection branch.

An initial design requirement is set for the feedback impedance. As mentioned is wanted to make that G_1 remains constant at all frequencies. Therefore,

$$C_f \cdot R_f = C_i \cdot R_i \tag{4.14}$$

Once this is applied, the rest of elements can be designed to keep a capacitive admittance behaviour along all the frequency range of interest. The applied methodology was based on locating the poles defined by the Z_i and Z_c branches out of the actuation frequency range (i.e at frequencies higher than 10 MHz). Figure 4-14 shows the admittance frequency response of the system shown in Figure 4-13. Two variants of the AEF Desing I are shown, Design A and B. In the Design A, the Z_i and Z_c

elements selection comply with equation (4.14), in contrast Design B illustrates the effect of not taking that design requirement into account in the design. The values of RC branches elements for both cases are displayed in Table 4.4.

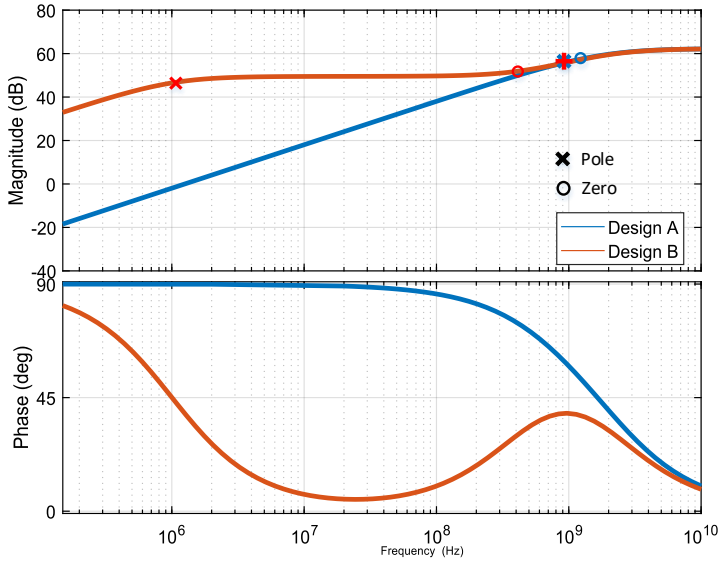

Figure 4-14. Admittance frequency response of the active system.

As it has been mentioned before, the AEF is required to provide adequate attenuation in the range from 150 kHz up to 10 MHz. By appropriately selecting the impedances, it can be seen how the active element admittance would behave as a capacitance among the full range.

TABLE 4.4. RC branches data for two study cases of Design I

Variable	**Value**	
	Design A	**Design B**
R_i	1 $m\Omega$	1 $m\Omega$
C_i	79.6 nF	79.6 nF
R_f	0.79 $m\Omega$	0.79 $m\Omega$
C_f	100 nF	100 nF
R_c	0.01 Ω	0.01 Ω
C_c	15.9 nF	15.9 μF

The capacitor value emulated by the active solution can be attained from equations (4.7) and (4.12), yielding,

$$C_{eq} = \frac{C_i}{\sqrt{(R_i \cdot C_i \cdot 2 \cdot \pi \cdot \omega)^2 + 1}} + \frac{C_c}{\sqrt{(R_c \cdot C_c \cdot 2 \cdot \pi \cdot \omega)^2 + 1}} \cdot G_1. \tag{4.15}$$

The calculated equivalent capacitance value for Design A and B are 0.1 μF and 24.3 μF, respectively.

4.2.1.2 Boosting stage

The first stage could work alone, however it has be seen in Figure 4-11 that the close-loop bandwidth of the VFB OPA is reduces when increasing the dc gains. Thus, although the capacitance could be increased by increasing the gain G_1, it is preferable to add an additional stage to boost it by increasing the value of the term G_1. Figure 4-15 shows the AEF system with the shaping and boosting stage.

A straightforward way of implement the boosting stage is to use a non-inverting

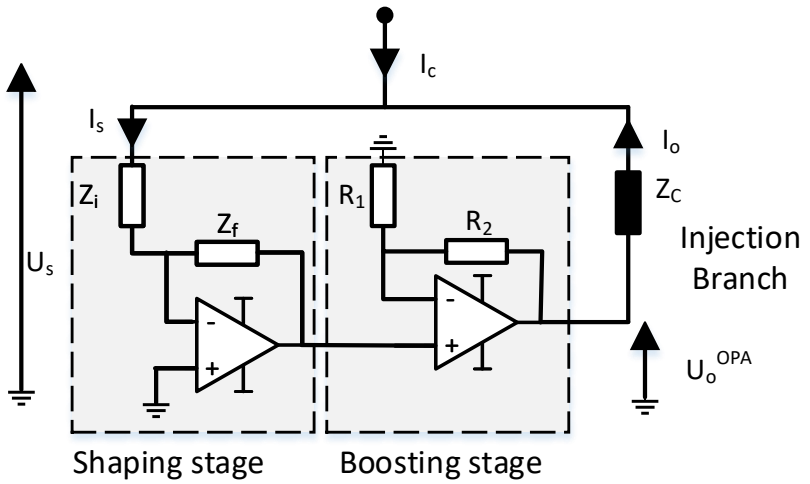

Figure 4-15. Active impedance circuit with a shaping stage and a boosting stage.

OPA to increase the gain by connected it to the output of the first stage. The impedance equation 4.12 and capacitor value (4.15) does not change but the term G_1 will turn into G_1',

$$G_1' = \left(1 + \frac{Z_f}{Z_i} \cdot \left(1 + \frac{R_2}{R_1}\right)\right). \tag{4.16}$$

The theoretical admittance shown in Figure 4-16 compares the new design ,Design C with the Design A presented before. Design C illustrates a two stage configuration. As can be seen, the admittance magnitude along the actuation frequency range increases equally. None frequency response change is observed.

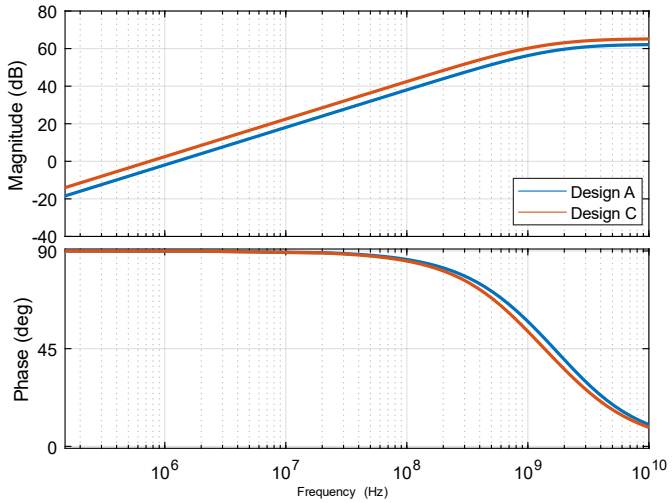

Figure 4-16. Admittance frequency response of the active system. Design A, only shaping stage. Design C, Design A with an additional second stage with gain of 3

However, in a practical implementation the attenuation of high frequency noise is needed to avoid oscillations in the AEF. The EPC at a certain frequency bypasses the inductor resulting in a loss of attenuation. Therefore, the active system can amplify any non-desired noise component, thus a recommended design practice is to implement a low pass filter in the AEF loop to avoid noise components above the cut-off frequency from harming the AEF operation.

Consequently, a low pass filter is implemented in the second stage with a Sallen-Key filter, which provides both amplification feature and high frequencies attenuation. The final implementation of the boosting stage will be the one shown in Figure 4-17, even if the previous non-inverting version is valid for theoretical analysis. A common design cut-off frequency for the Sallen-key filter can be 5 MHz.

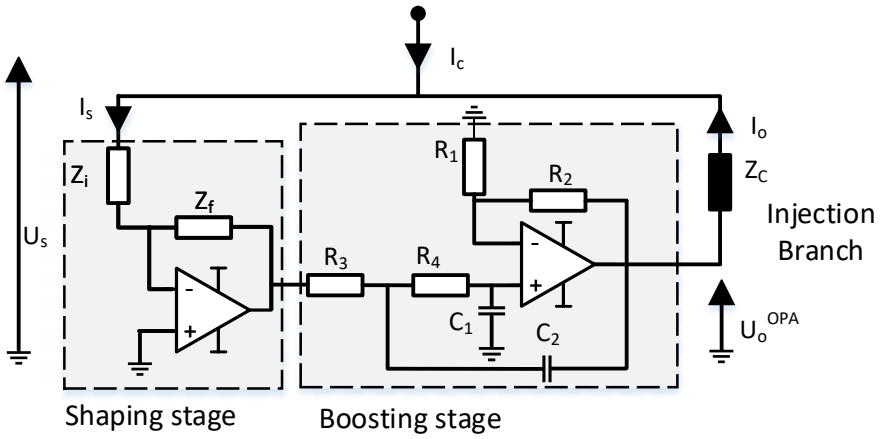

Figure 4-17. Alternative boosting stage with Sallen-Key filter.

4.2.1.3 Decoupling stage

From a theoretical point of view, the approach shown in Figure 4-15 would allow to control the capacitance as needed. Nonetheless, there are non-ideal properties of OPAs which need to be considered to achieve proper performance of the AEF.

In real OPA it is expected to have an inherent output resistance, R_o. If a capacitive load is connected to the output, the stability of the system is penalised. This happens because R_o in conjunction with the capacitance C_L form an additional pole in the amplifier loop gain transfer function. Real OPAs have a loop gain with a dominant pole at low frequencies (τ_1) and another one at high frequencies (τ_2), normally higher than the GBP. The additional pole is potentially placed at frequencies lower than the GBP, which contributes with -20 dB/dec and 90 lag. The stability of the OPA can be studied based on the open loop gain ($A\beta$). It can be seen in Figure 4-18 (b) how the phase margin is drastically reduced when a capacitor is connected

at the output, which makes the system unstable o making the system unstable.

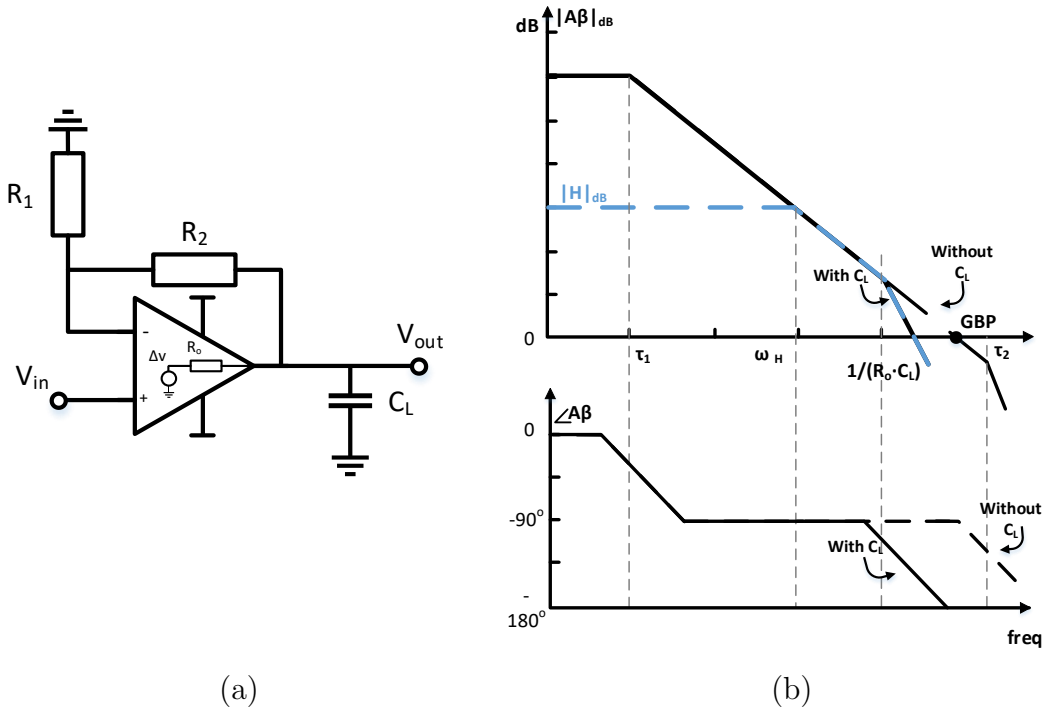

(a) (b)

Figure 4-18. Open loop gain when a capacitive load is connected. (a) System scheme, (b) Loop gain bode.

For both the non-inverting and inverting OPA configuration $A\beta$ is defined by equation,

$$A\beta = \frac{K}{(s+\tau_1)\cdot(s+\tau_2)} \cdot \frac{Z_G}{Z_F + Z_G} \cdot \frac{1}{R_o \cdot C_L \cdot s + 1}. \tag{4.17}$$

Where the first term is the OPA gain (A), K is the DC OPA gain, and the second term is feedback gain (β_{opa}).

There are several techniques for compensating the effect of a capacitive load. The simplest way is gain compensation by changing the close-loop gain parameters (i.e.,

input (Z_G) and feedback impedance (Z_F)). In this way the open-loop gain can be modified to attain a configuration with sufficient phase margin. For VFB the capacitive load capability increases proportionally with the close-loop gain.

External compensation methods consist of adding extra resistors and capacitors. For instance, adding a small output resistor (R_x) in the compensation loop to decouple the capacitive load and a small capacitor (C_x) in the feedback loop that provides high frequency bypass around the output capacitance.

Apart of stability reasons, the capacitive load will have a negative effect on the close-loop gain. If the OPA is studied as a feedback system, it can be conclude that the close-loop response ($HCL(s)$) is given by,

$$HCL(s) = H_o \cdot \frac{A\beta}{1 + A\beta}, \tag{4.18}$$

where H_o is the low frequency gain that will match the feedback loop gain. If $A\beta \gg 1$ for the case of an inverting OPA the close-loop gain can be simplified by,

$$HCL(s) = H_o \frac{1/\beta_{opa}}{1 + s/\omega_H}, \tag{4.19}$$

where,

$$\omega_H = \beta_{opa} \cdot \omega_{GBP}, \tag{4.20}$$

and where $\omega_{GBP} = 2 \cdot \pi \cdot f_{GBP}$, being f_{GBP} the GBP frequency of the close-loop gain. The terms β_{opa} can be defined by

$$Z_G/(Z_F + Z_G). \tag{4.21}$$

When there is not a capacitive load connected. By design $Z_F > Z_G$, therefore $\omega_H < \omega_{GBP}$. However, when the capacitive load is connected, as seen in Figure 4-18, there is an extra pole before GPB that will introduce an extra -20 dB/dec. This affects ω which will decrease rapidly after $R_O \cdot C_L \cdot s > 1$. It has been identified that when the close-loop gain of the system starts decreasing the impedance behaviour of the active system degrades. Additionally, the close-loop cut-off frequency reduces when the feedback gain is increased. This is illustrated in Figure 4-19 , where the close loop gain of a non-inverting OPA is shown for different feedback gains. Thus, is has been concluded that the capacitive load effect should be decoupled from the second stage.

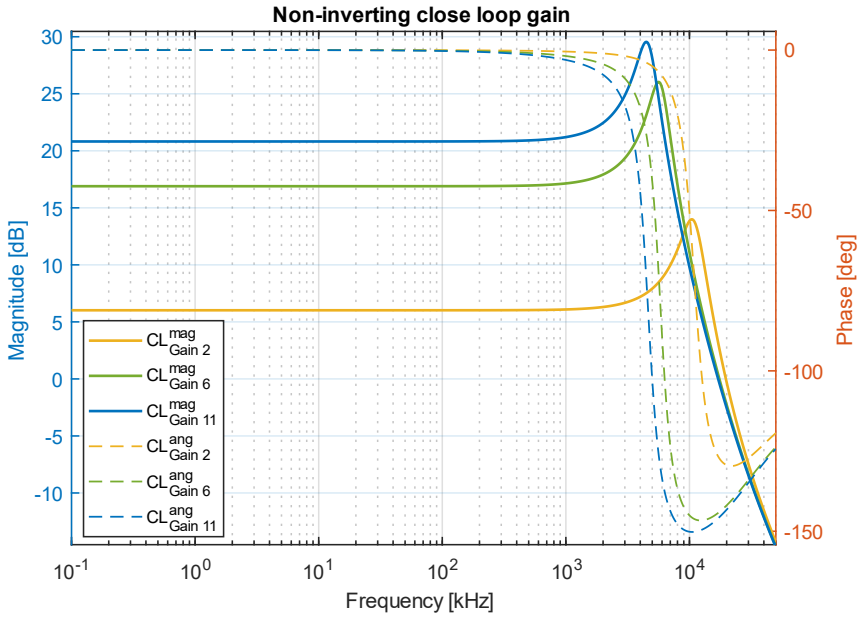

Figure 4-19. Close loops gain of the non – inverting OPA for different feedback gains.

The decoupling stage consists of an operational amplifier working as a buffer to

provide a high impedance at the output of the second stage. The open loop gain of the buffer matches the OPA gain and can be disregarded. It has, therefore, been concluded that choosing an operational amplifier with a high capacitance loading capability will help the system to decouple the injection branch from the previous stages without introducing modifications on the admittance definition. The scheme of the full Design I AEF is shown in Figure 4-20.

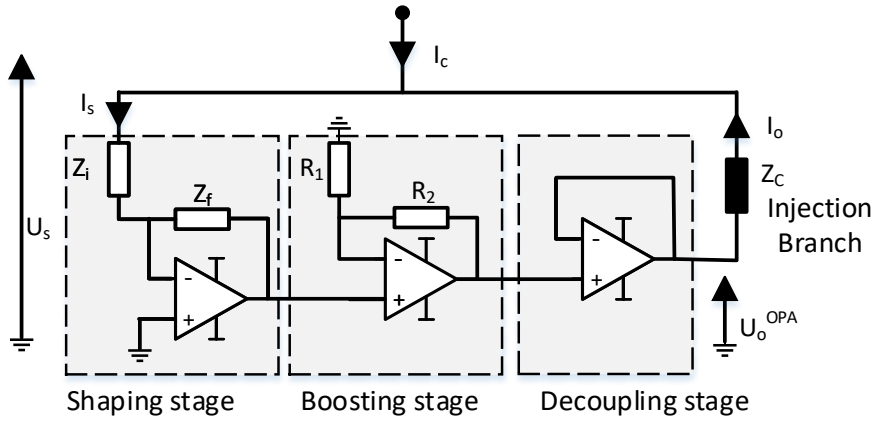

Figure 4-20. Scheme of the AEF configuration with a shaping and a decoupling stage.

The influence of the decoupling stage has been verified in simulation using the SPICE model of a real operational amplifier (i.e. macromodel). In Figure 4-21 it can be seen the impedance frequency response for a system with only the shaping stage, and the system described in Figure 4-20. The close-loop gain of the non-inverting stage is also shown. It can be seen how the admittance behaviour is extended to higher frequencies and the relation with the close loop gain of the non-inverting OPA. The high frequency peak around 40MHz is due to first stage internal resonances.

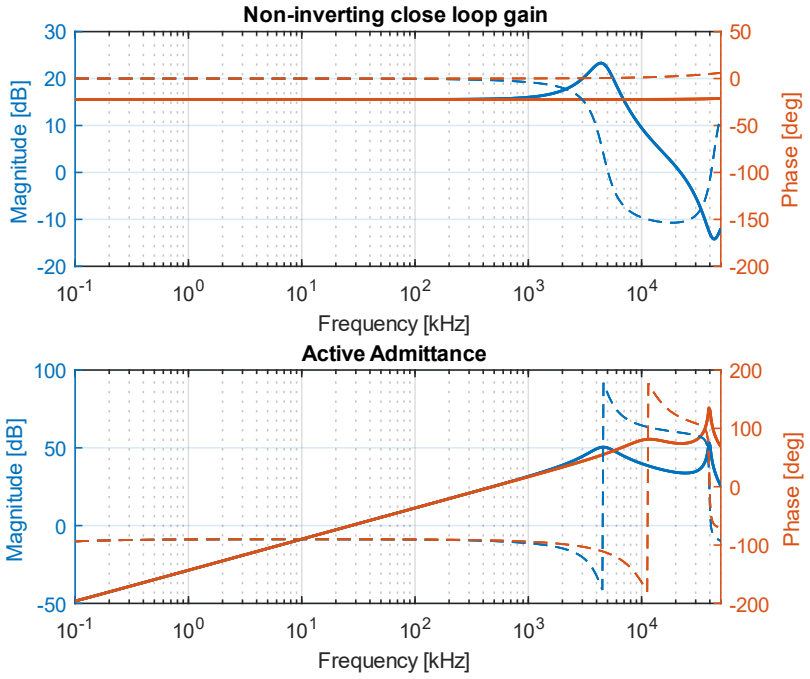

Figure 4-21. Admittance frequency response of a spice model of two stages system (blue) and three stages (red) of the Design I.

4.2.2 Design II: Power amplifier output for current injection increase

The main constrains of the previously presented active impedance solution based on OPA are related to the power rating of the available VFB OPA technology which constrain the mitigation capability of the solution. This will be further explored in Section 4.3.1.4. To address this limitation some authors has already explored the use of LPAs [190–192]. LPA provides higher compensation current levels but lower design flexibility than a purely OPA based design. The impedance behaviour that is shown for example in [192] does not covered the entire desired operation frequency range (i.e., from 100kHz up to 150 MHz). Other approaches consist of combining a

first pre-amplifier stage based on OPAs with an output LPA [193, 194]. In the line of the solutions seen in the literature it has been investigated how to modify the the previous approach, Section 4.2.1, to incorporate a LPA in the output.

LPAs can be classified as A, B, AB and C based on the conduction angle of the device. A Class A LPA is conducting all the signal period, it is 360 deg, in Class B LPA the device is active half of the period, it is 180 deg and the Class C , less than half a period. Class AB LPA is a intermediate state between Class A and B where the device is never totally turn off, where during half a period the total current is conducted while at the other half period the device is slightly bias conducting a small current value. Class B and Class AB are commonly presented in a push-pull configuration where the full period of and alternating signal is amplified.

In a first trade-off, Class A and C LPAs has been discarded because of low efficiency and high signal distortion, respectively. Both Class B and AB have been identified as potential candidates although Class AB LPA is finally chosen as it provides a good trade-off between efficiency and linearity and minimizes the cross-over distortion [195]. The proposed active circuit scheme is displayed in Figure 4-22. The impedance behaviour of the solution has been analysed paying attention to the LPA high frequency elements introduced by the bipolar transistors and explain in the next subsection.

4.2.2.1 LPA high frequency model

In order to define the new admittance expression of AEF Design II, it is important to analyse the high frequency behaviour of bipolar transistors. Hybrid π model or also called Giacoletto model is a well-known circuit model used for analysing small signal

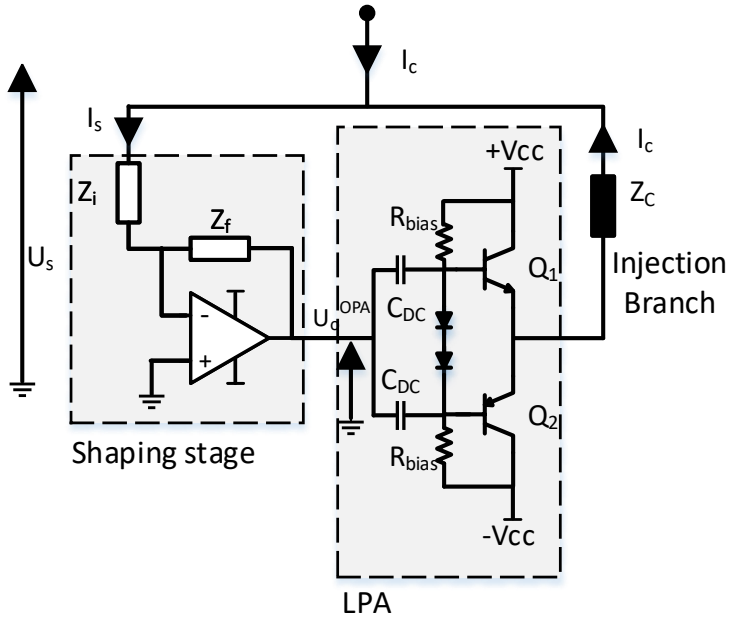

Figure 4-22. AEF approach II. General scheme.

behaviour of bipolar junction and field effect transistors. This can also be adapted to high frequency study introducing the inter-electrode capacitances and other parasitic elements. The Hybrid π model of a bipolar transistor looks like Figure 4-23 . Where the main connection points are "c" collector, "b" base, "e" emitter.

In the Hybrid π model the main model elements are listed below:

- C_μ : It represents the early effect. The charge gradient is increased across the base and consequently, the current of minority carriers injected across the collector-base junction increases. This is in the range of pF.
- C_π : Diffusion capacitance, minority carrier storage in the base. This is in the range of pF.
- R_b : Base connection contact resistance, base to active region contact.

- R_π : Ac input resistance associated with the base current. Resistance between base and emitter. It is associated with the dynamic resistance (Re), $R\pi = \beta R_e$.
- R_μ : This is the resistance between the base and collector terminal, normally it is neglected as this is in the range of $M\Omega$.
- R_o : Output resistance, between the collector and the emitter terminal.
- β : Bipolar transistor current gain (i.e. $\beta = {}^{i_c}/_{i_b}$).
- g_m : This is the transconductance of the bipolar transistor.

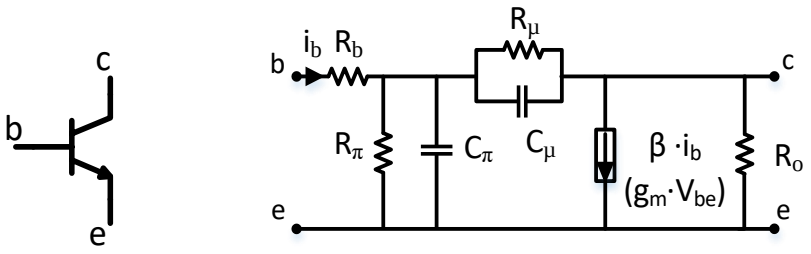

(a) (b)

Figure 4-23. Hybrid π model of a bipolar transistor. (a) NPN bipolar transistor. (b) High frequency adapted hybrid π model.

4.2.2.2 Impedance modelling

The impedance described by (4.7) presented previously in Section 4.2.1 cannot be used in this case as this has been calculated under the premise that the OPA behaves

as a voltage source, while the LPA behaves as a current source. The new impedance expression can be analytically calculated from the circuit displayed in Figure 4-22. The symmetry property of the Class AB LPA allows to simplify the circuit analysis by studying only half conduction period. Thus, only half push-pull circuitry needs to be analysed to obtain the impedance expression. The system can be seen as a common-emitter amplifier. After simplification and substituting bipolar transistor by the Hybrid π model, the simplified circuit is the one in Figure 4-24. Parasitic capacitances have been neglected for simplicity.

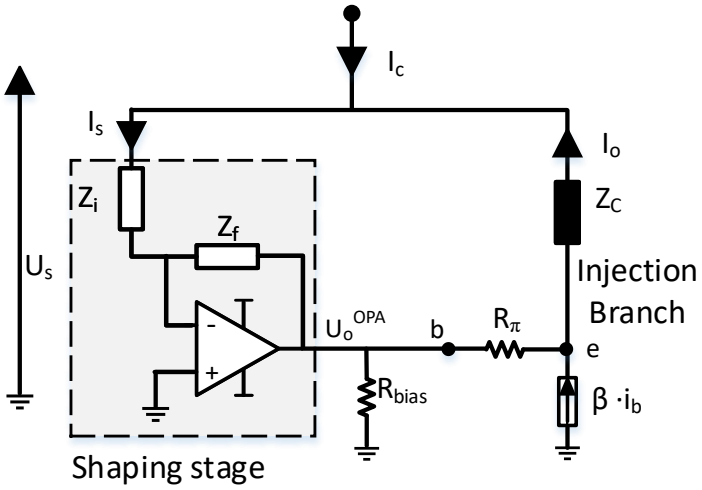

Figure 4-24. AEF approach II. Simplified scheme.

From the circuit in Figure 4-24 the following expression of the input admittance is derived,

$$Y_{AEF}^{II} = \frac{1}{Z_i} + \frac{1}{Z_c} \cdot \left(1 + \frac{Z_f}{Z_i}\right) \cdot \frac{1+\beta}{R_\pi / Z_c + (1+\beta)} \tag{4.22}$$

The new admittance expression depends on β and the R_π bipolar transistor components. R_π is the diffusion resistance, and it determines the the slope of the input characteristic between the base current and the base to emitter voltage (V_{be}) at the

quiescent point Q, see Figure 4-25. Therefore, R_π can be calculated with the equation,

$$R_\pi = \frac{V_{be}}{i_b} = \frac{V_T}{I_{BQ}} = \frac{\beta \cdot V_T}{I_{CQ}} = \frac{\beta}{g_m} \tag{4.23}$$

where V_T is the thermal voltage, it is the voltage in the depletion region due to temperature, and I_{BQ} and I_{CQ} the base and collector current at the quiescent point.

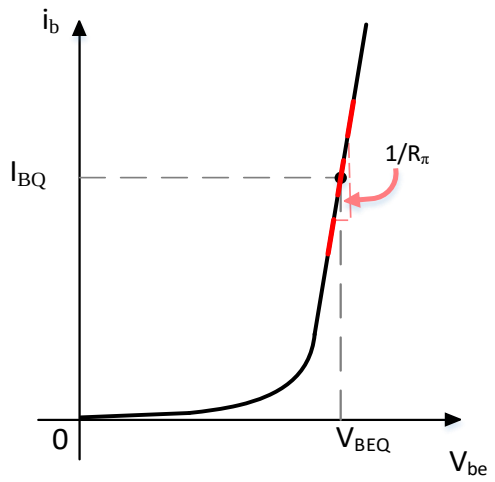

Figure 4-25. Input bipolar transistor characteristic relation with the diffusion resistance R_μ

The expression (4.22), can also be presented as impedance form,

$$Z_{AEF}^{II} = \frac{Z_i \cdot (R_\pi + (1+\beta) \cdot Z_c)}{R_\pi + (1+\beta) \cdot Z_c + (1+\beta) \cdot (Z_f + Z_i)} \tag{4.24}$$

Substituting the impedances by their expressions (4.9), (4.10) and (4.11), the impedance expression for the Design II yields,

$$Z_{AEF}^{II} = \frac{C_f \cdot (s \cdot C_i R_i + 1) \cdot (s \cdot (C_c \cdot R_\pi + (1+\beta) \cdot C_c R_c) + (1+\beta))}{s} \cdot$$
$$\cdot \frac{1}{(C_p \cdot R_\pi + (1+\beta) C_p (R_c + R_f + R_i)) + (1+\beta) \cdot (C_f \cdot C_i + C_c \cdot C_i + C_c \cdot C_f)} \tag{4.25}$$

being $C_p = C_c \cdot C_f \cdot C_i$. In (4.25) two poles ($p_1$ and p_2) and two zeros (z_1 and z_2) can be identified. They are defined as,

$$p_1 = 0 \tag{4.26}$$

$$p_2 = \frac{1}{C_p} \cdot \frac{(1+\beta) \cdot (C_f \cdot C_i + C_c \cdot C_i + C_c \cdot C_f)}{R_\pi + (1+\beta)(R_c + R_f + R_i)} \tag{4.27}$$

$$z_1 = \frac{1}{C_i \cdot R_i} \tag{4.28}$$

$$z_2 = \frac{1}{C_c} \cdot \frac{1+\beta}{R_\pi + (1+\beta) R_c} \tag{4.29}$$

The resistance values R_c, R_f and R_i are expected to be small, in the order of $m\Omega s$. Under this assumption, the p_2 and the z_2 expressions can be simplified. In p_2, $R_\pi \gg (1+\beta) \cdot (R_c + R_i + R_f)$ so the denominator can be simplified by R_π. Considering (4.23), equation (4.27) turns into,

$$p_2 = g_m \left(\frac{1}{C_c} + \frac{1}{C_f} + \frac{1}{C_i} \right). \tag{4.30}$$

Similarly in (4.29), $R_\pi \gg (1+\beta) \cdot R_c$ and $(1+\beta) \approx \beta$. Considering (4.23) the

position of z_2 can be simplified to

$$z_2 = \frac{1}{C_c} \cdot g_m \tag{4.31}$$

The mathematical expression of the impedance obtained is verified with a LTSpice simulation where actual models of the bipolar transistor are used. The main parameter values of the study case are summarized in Table 4.5. The frequency response of the theoretical and the LTSpice model are shown in Figure 4-26. The theoretical impedance expression matches quite accurately the simulation result. The slight differences can be caused by the parasitic capacitances that have not been considered.

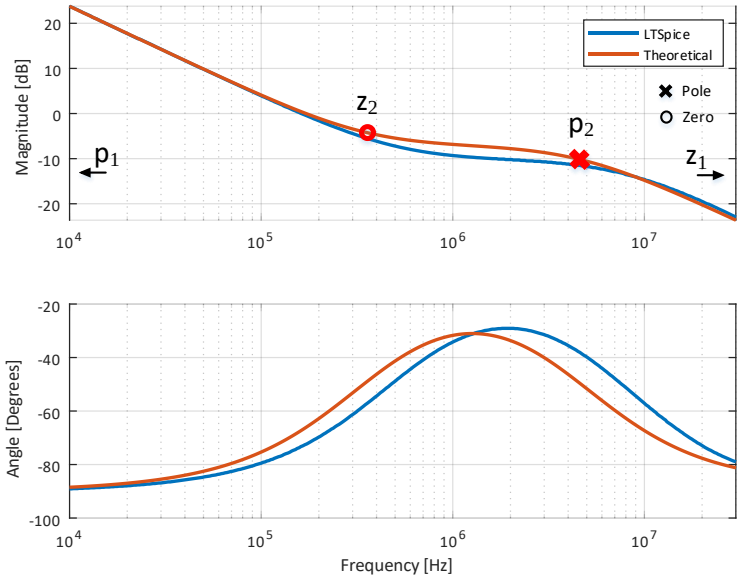

Figure 4-26. Impedance frequency response comparison with a LTspice simulation using spice models of bipolar transistors.

TABLE 4.5. Design II. Study case data

	Variable	Value
Transistor	V_{bias}	0.75 V
	β_{DC}	177
	g_m	1.17 S
	R_{pi}	150 Ohms
OPA elements	C_i	79 nF
	R_i	1 $m\Omega$
	C_f	100 nF
	R_f	0.79 $m\Omega$
	C_c	0.53 μF
	R_c	10 m $m\Omega$

From the previous expression it can be seen that z_2 at such low frequency is the main culprit of the capacitive behaviour degradation in Design II. This is directly related to the injection branch capacitance and g_m of each of the bipolar devices that comprise the LPA. This fact reduces the capability of extending the capacitive behaviour without reducing the injection capacitor. Therefore, the capacitive behaviour could be extended by operating the LPA in a more linear operation point, such as Class A. This means, g_m increases. However, a relevant drawback is that the efficiency will decrease. Table 4.6 shows the main parameters of a Class AB and a Class A LPA. Basically, by changing the VBE_Q the position of z_2 changes.

TABLE 4.6. Parameters used in the comparison of a Class AB and a Class A LPA operation

Class AB	V_{BEQ}	0.75 V	Class A	V_{BEQ}	1 V
	β_{DC}	177		β_{DC}	50
	g_m	1.17 S		g_m	20.7 S
	R_π	150 Ωs		R_π	8.5 Ωs
	z_2	350 kHz		z_2	1.7 MHz

An alternative solution for extending the capacitive behaviour operating the LPA as a Class AB is explored. The solution proposed consists on compensating the z_2. To do so, the approach explored in here is to design the feedback impedance of the first stage in such a way the effect of z_2 on the impedance behaviour is cancelled. Admittance expression is used because the cancellation is identified clearer. If we extend the expression (4.22) we can reach the following equation,

$$\begin{aligned} Y_{AEF}^{II} = \frac{1}{Z_{sen}} + \frac{1}{Z_o} \cdot \frac{R_i + R_f}{R_i} \cdot \frac{R_o}{R_\pi + (1+\beta) \cdot R_o} \\ \cdot (1+\beta) \cdot \frac{s + \frac{C_f + C_i}{C_i \cdot C_f (R_i + R_f)}}{s + \frac{1}{C_i \cdot R_i}} \cdot \frac{s + \frac{1}{C_o \cdot R_o}}{s + \frac{(1+\beta)}{C_o \cdot (R_\pi + (1+\beta) \cdot R_o)}}. \end{aligned} \tag{4.32}$$

Where the z_2 effect is defined here by the term,

$$p_{z2} = s + \frac{(1+\beta)}{C_o \cdot (R_\pi + (1+\beta) \cdot R_o)} \tag{4.33}$$

As it can be observed the p_{z2} term can be cancelled if the input and feedback impedances are selected carefully as follow,

$$s + \frac{C_f + C_i}{(C_i C_f (R_i + R_f)} = s + \frac{(1+\beta)}{C_o \cdot (R_\pi + (1+\beta) \cdot R_o)}. \tag{4.34}$$

Considering the initial values displayed in Table 4.5, the new feedback impedance parameters that satisfied (4.34) are,

$$\begin{aligned} C_f &= 10\,\mu F \\ R_f &= 5\,\Omega. \end{aligned} \tag{4.35}$$

The admittance expression after applying (4.34) and arranging the terms yields

$$Y = \left(\frac{1}{R_i} + \frac{K_a}{R_o}\right) \cdot \frac{s}{s + \frac{1}{C_i \cdot R_i}}, \tag{4.36}$$

where K_a is a constant term which varies with the resistance values and the bipolar transistor parameters

$$K_a = \frac{R_i + R_f}{R_i} \cdot \frac{R_o}{R_\pi + (1+\beta) \cdot R_o} \cdot (1+\beta). \tag{4.37}$$

Figure 4.34 illustrates the frequency impedance response after applying the proposed compensation. It has been verified that the active solution shows an extended capacitive behaviour along all the frequency range. However, it has been noticed that even though the capacitive behaviour is extended the actual active capacitance is equal to the injection capacitance (C_c). Therefore, the next step is to explore how to amplify the equivalent capacitance.

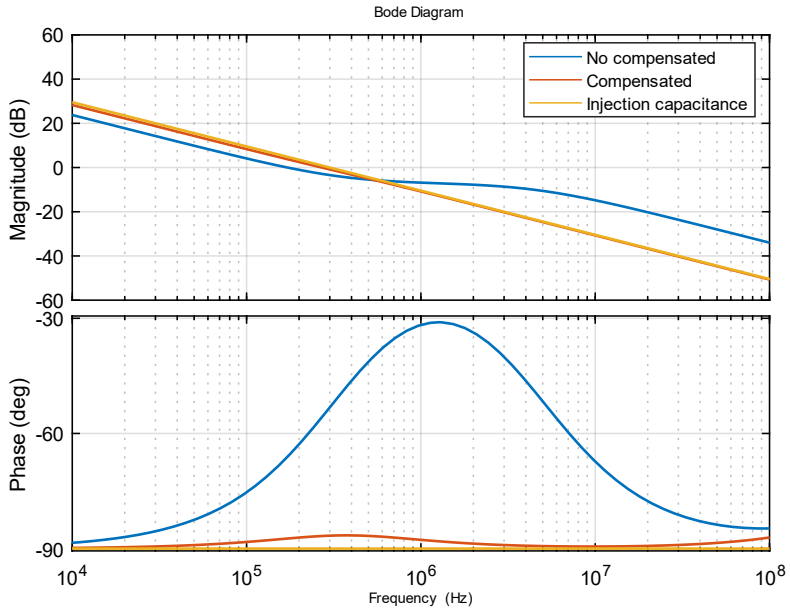

Figure 4-27. Approach II impedance response after applying the compensation of z_2

4.2.2.3 Amplification of the effective capacitance

Following a similar strategy to Design I, an additional non-inverting OPA stage has been added. Figure 4-28 shows the scheme of the final proposed Design II. The admittance expression is slightly modified, the "Boosting stage" gains (G_2) is included,

$$Y = \frac{1}{R_i} \cdot \frac{1}{s + \frac{1}{C_i \cdot R_i}} + \frac{R_i + R_f \cdot G_2}{R_i} \cdot \frac{R_o}{R_\pi + (1+\beta) \cdot R_o} \cdot$$
$$(1+\beta) \cdot \frac{s + \frac{C_f + C_i \cdot G_2}{C_i \cdot C_f (R_i + R_f \cdot G_2)}}{s + \frac{1}{C_i \cdot R_i}} \cdot \frac{1}{s + \frac{(1+\beta)}{C_o \cdot (R_\pi + (1+\beta) \cdot R_o)}}, \tag{4.38}$$

where,

$$G_2 = 1 + \frac{R_2}{R_1}. \tag{4.39}$$

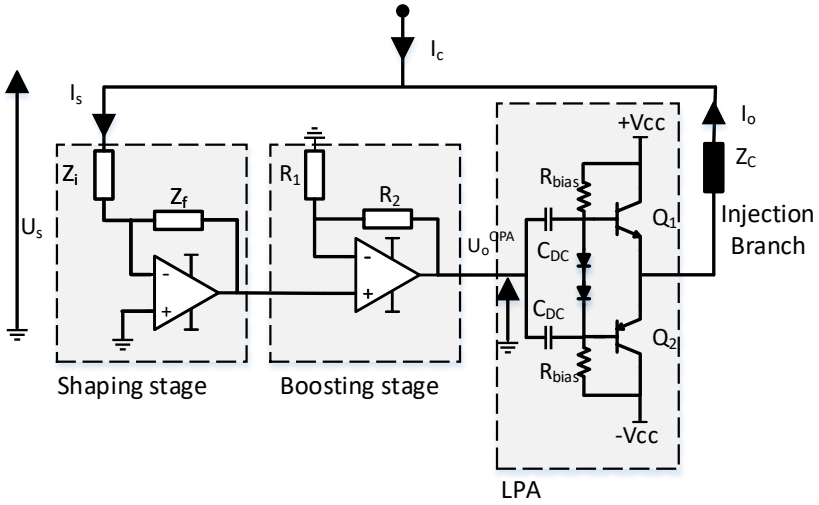

Figure 4-28. AEF Design II with a boosting stage

However, the impedance amplification is not direct and some considerations have to be considered. Two design conditions have been identified to influence the amplification through circuit elements. The first condition is,

$$R_i < R_f \cdot G_2. \tag{4.40}$$

This condition simplifies the position of the compensation pole (p_c), helping to predict its variation with G_2.

$$p_c = \frac{C_f + C_i \cdot G_2}{C_i \cdot C_f \cdot R_f \cdot G_2} \tag{4.41}$$

Additionally, based on (4.40), it is possible to simplify the term that provides the

gain variation (K_{var}) to the admittance impedance as follows,

$$K_{var} = \frac{R_i + R_f \cdot G_2}{R_i} \rightarrow \frac{R_f \cdot G_2}{R_i} \tag{4.42}$$

However, under this design condition it can be see that if $C_f > C_i \cdot G_2$ then the pole position yields,

$$p_c = \frac{1}{C_i \cdot R_f \cdot G_2}. \tag{4.43}$$

This means that for keeping the pole position, R_f needs to be inversely proportional to G_2. Furthermore, observing (4.42), it can be seen that K_{var} it will not change. For achieving a variable gain a second design condition is required,

$$C_f < C_i \cdot G_2. \tag{4.44}$$

Based on the condition set in (4.44), the position of the pole is only determined by the feedback OPA branch impedance and the K_{var} is proportional to the boosting stage gain. In conclusion, if design conditions (4.40) and (4.44) are applied, Design II will provide active variable capacitive impedance in the frequency range of interest.

Figure 4-29 displays the frequency response of the no compensated and the compensated plus gain amplification active circuit. The boosting operation amplifier is set to have a gain of 10 and the equivalent emulated capacitance is 5.3 μF (i.e. 10 times C_c).

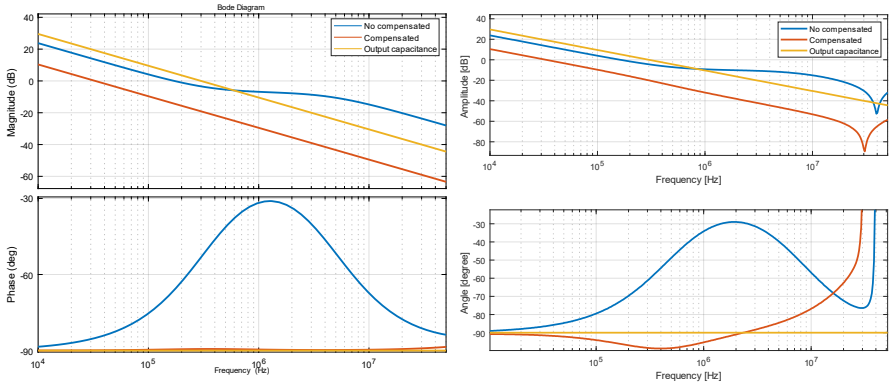

(a) (b)

Figure 4-29. Frequency response of the approach II. (a) Analytical result. (b) LTspice simulation using OPA858 and 2N222/2N2907 BJTs

4.3 Active filtering experimental validation

The Design I presented in the section 4.2.1 has been experimentally evaluated in a lab environment. In this section, it is shown the experimental validation of the solution implemented in a T-Type filter. The HEF filter response has been verified with an Virtual Network Analyser (VNA) and compare with an equivalent passive solution. Additionally, the solution operation boundaries have been identified by performing an analysis of the maximum power it would need to manage along the frequency range of operation. A preliminary comparison of weight and volume has been carried on to rise awareness of the advantages of the active solutions versus their passive counterpart.

4.3.1 Design I, experimental verification

To select the OPA technology for the implementation several Radio Frequency (RF) OPA response have been evaluated with the help of manufacture SPICE macromodels. In a first step, from the bunch of pre-selected OPAs only the ones with higher closed-loop bandwidth have been chosen as candidates. Secondly, various combinations of OPA types have been tested by analysing the frequency response of Design I solution. Finally, the combination defined in Figure 4-30 resulted to be the one with broader frequency operation range, presenting a good impedance behaviour up to 10 MHz with proper tuning of the parameters.

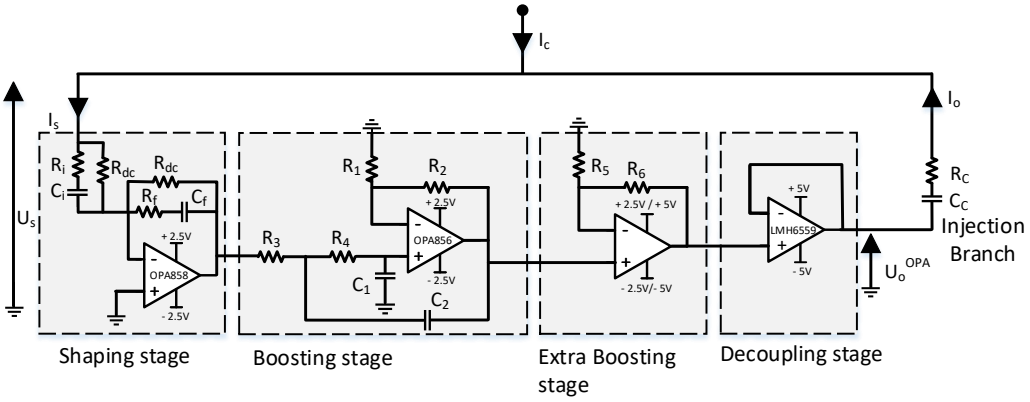

Figure 4-30. Schematic of the prototype tested based on Design I.

4.3.1.1 Prototype characteristics.

The final appearance of the prototype is displayed in Figure 4-31. As it can be observed in both the schematic, Figure 4-30, and the prototype photo, the three stages have been implemented. A brief description of the main elements is given in the following lines.

The prototype board main input supply connector is plugged to an external 12 V power supply (P_1). In the board it can be seen that a coaxial port is used to connect the AEF between the measuring point, M, and ground (P_2). A jumper (P_3) is installed to make able testing the circuitry in open- or close-loop. DETN02M-05N isolate dc-dc converter and, ADP122AUJZ and MIC5271YM5 linear regulators provide the supply voltage to the different OPAs. The "Shaping stage" has been implemented with a OPA858 because it was the one reporting the best closed-loop bandwidth during the evaluation done with the SPICE macromodels. In the case of the "Boosting stage", compensated OPA856 has been selected. This OPA belongs to same family than the OPA858, and both have an excellent high frequency performance. The reason of using it instead of the OPA858 at this stage is that its minimum gain is 1 V/V instead of 7 V/V. A high minimum gain at this stage would constrain the design flexibility. Minimum gain is common in decompensated OPAs [ref]. Additional options for this second stage has been explored such as the AD8067 OPA. This OPA has much lower GPB but higher supply voltage what provides wider output voltage range and then potential higher amplification. For the "Decoupling stage" an embedded closed loop buffer specific for high frequency signals, LMH6559, has been chosen.

4.3.1.2 Impedance behaviour testing

In order to verify the impedance response of the Design I, frequency response measurements have been done. In Table 4.7, two study cases designs to emulate an 300 nF equivalent capacitor are shown. The equivalent capacitance has been calculated using a numerical integration of the active impedance over the frequency range.

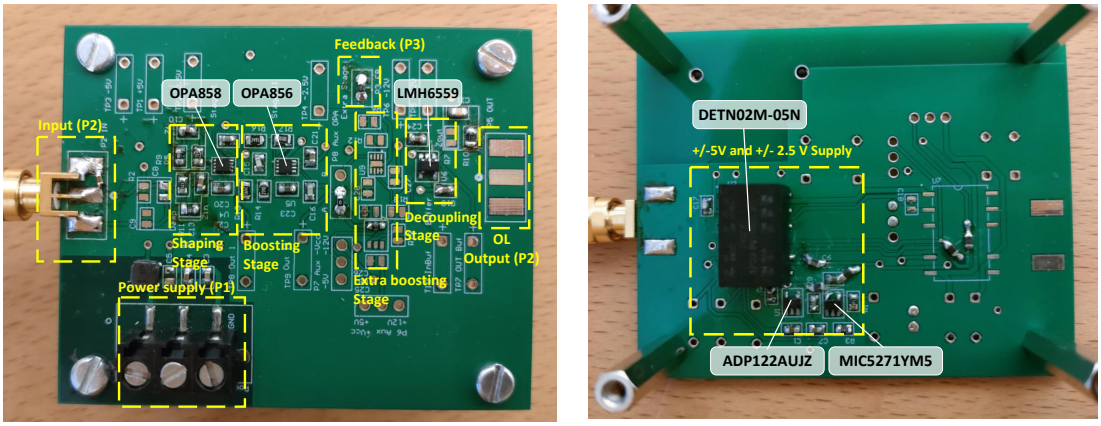

(a) (b)

Figure 4-31. Prototype photo. (a) Top view. (b)Bottom view.

As matter of example, the frequency response of the 300 nF capacitance with the frequency response results of *Case 1* design are displayed in Figure 4-33.

In both cases, the Sallen-Key filter was design with a cut-off frequency of 5 MHz. *Case 1* represents a design with high impedance injection RC branch and *Case 2* is a design that provides a good frequency response up to 10 MHz, which injection impedance is considerably lower. The measured input impedance magnitude of both cases has been compared with the result obtained from the LTSpice simulation and theoretical results. This is displayed in Figure 4-33. During the testing of these study cases, some extra empirical correction measures had to be applied. Noisy grounding was detected at the higher frequencies when testing *Case 1*. As a first action, ferrite beads were added at the OPA power supply pads, as this is considered as a good practice in power electronics for high speed PCB circuities to mitigate the high frequency components that could loop into the OPA supply. Additionally, it was identified that *Case 1* presents a low impedance injection branch and that the noisy response of the circuit happens only under feedback operation. A solution

found is to design the AEF so the impedance of the injection branch is high enough to avoid the high frequency looping phenomena.

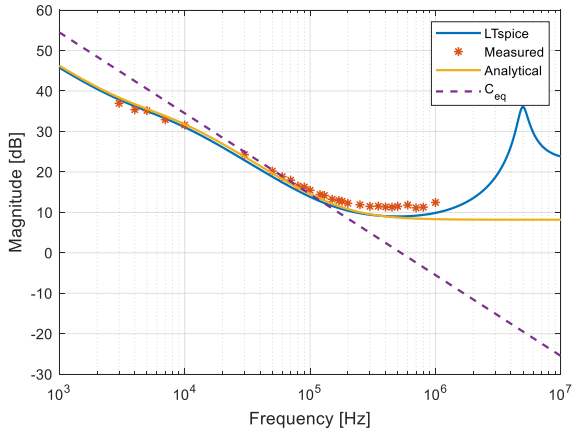

Figure 4-32. Frequency response of the equivalent capacitance of the passive solution with the expected response of the *Case 1*

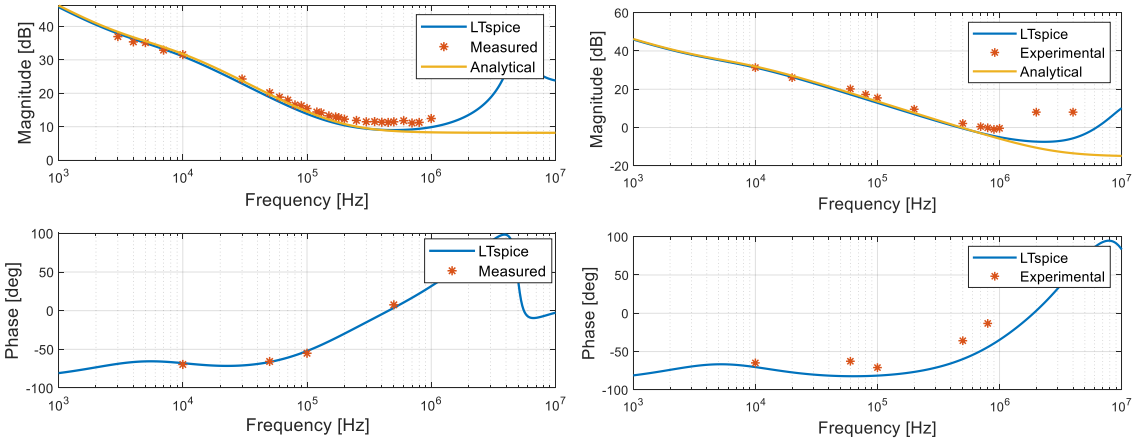

Figure 4-33. Impedance frequency response. (a) Case 1. (b)Case 2.

As it can be appreciated at Figure 4-33 the magnitude of the impedance response

has been measured with higher detail as it was easier to calculate it based in the data obtain from the oscilloscope than the phase. Nevertheless, enough points have been calculated of both magnitude and phase to verify the high accuracy of the theoretical results with the experimental ones. It can be observe that the design *Case 1* response does not achieve totally the target frequency operation range. The capacitive behaviour starts to degrade around 200kHz, but in contrast this design solves the noisy grounding problem that appears in *Case 2* at frequencies higher than 100 kHz. For the latter, despite the noise in the response, the magnitude impedance measurement was obtained for the whole frequency range by filtering this high frequency ripple. It can be seen that the design provides a good frequency response overall. However, practically speaking the noise injected in the ground should be avoid . The phase data mismatch with the theoretical one it is a consequence of the filtering and measurement errors.

TABLE 4.7. 300 nF prototype design.

	Component	Case 1	Case 2
Stage I	Ci	470nF	470nF
	Ri	100 Ω	100 Ω
	Cf	100nF	100nF
	Rf	470 Ω	470Ω
Stage II	R1	2.5kΩ	2.5kΩ
	R2	301 Ω	301 Ω
	R3	2.5k Ω	2.5kΩ
	R4	2.73kΩ	2.73kΩ
	C1	10pF	10pF
	C2	16.2pF	16.2pF
Stage III	Co	58nF	58nF
	Ro	15Ω	1 Ω

4.3.1.3 Implementation of the solution in a T-type filter

After validating of the impedance behaviour of the active solution, the AEF design *Case 1* has been incorporated in a CM EMI filter. The scheme of the resultant HEF under study is represented in Figure 4-34, the CM T-type filter prototype is shown in Figure 4-35 and the components values are displayed in Table 4.8.

TABLE 4.8. Component values of the scheme seen in Figure 4-34

Component	Value
L_1 & L_2	600 uH
Cp_{y1} & Cp_{y2}	33 nF

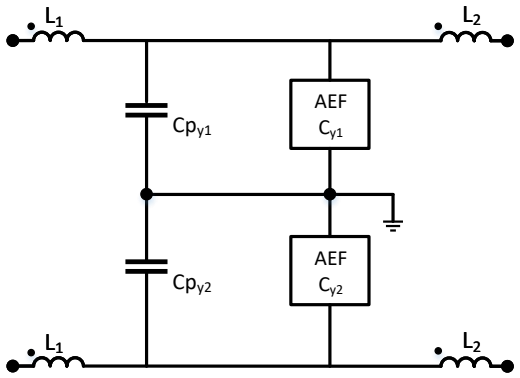

Figure 4-34. CM filter configuration of the HEF prototype

The attenuation response of the HEF is compared with an equivalent pure passive solution, it is, a PEF with identical passive capacitance than the one generated actively (i.e, 300 nF). The frequency response of the two cases are displayed in Figure 4-36. An additional case with the active filter disconnected has been also evaluated. Thus it can be seen what it would be the HEF response if the AEF should be shut-down because of the reasons described previously in this chapter. As

can be seen the active attenuation response of the HEF solution is quite similar to its passive counterpart.

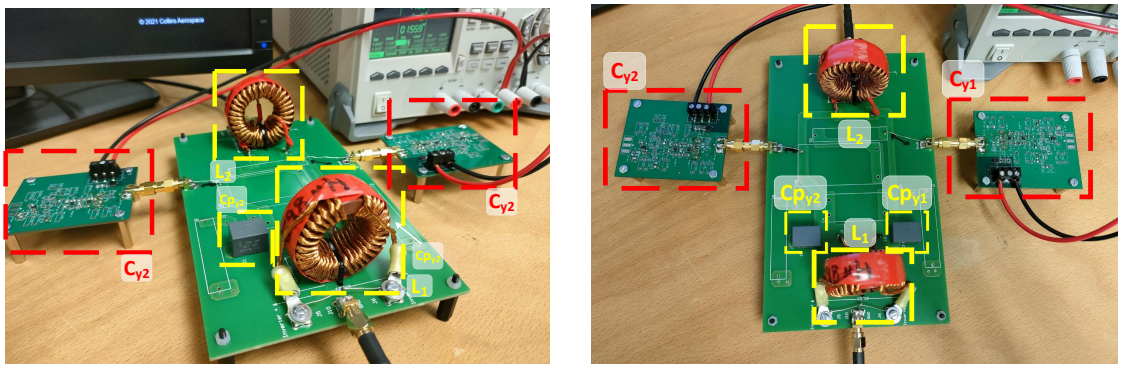

(a) (b)

Figure 4-35. Photos of the CM T-type prototype. (a) Side view, and (b) Top view.

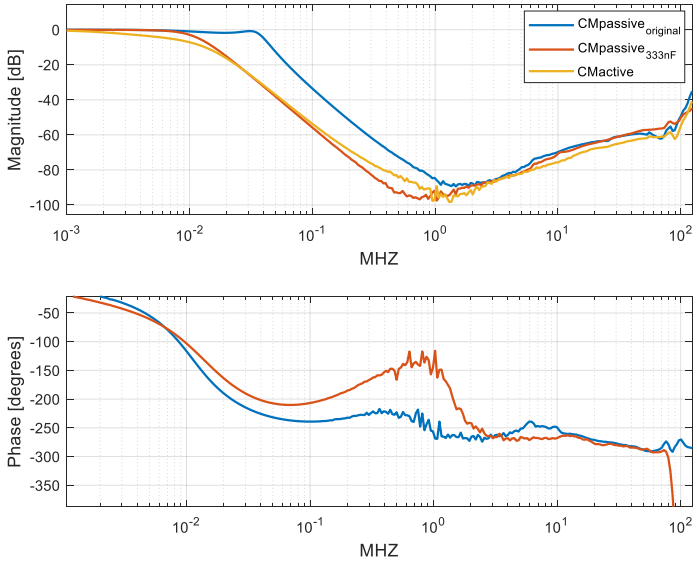

Figure 4-36. T-Type filter frequency response of the HEF and the PEF with equivalent passive capacitance

4.3.1.4 Evaluation of the design limitations

After validating the proper frequency behaviour of the Design I, the next step has been to identify the operation limits. The aim is to generate an useful mask to understand in a preliminary evaluation if the solution fits the noise attenuation of the application. This mask will be defined based on the maximum power capability among the frequency range, this would be label as peak power spectrum envelope (PPSE). This is directly related with the OPA electric ratings. To compute the PPSE of the active circuit, the maximum voltage swing of the first and second stage, as well as, the maximum output current of the buffer are evaluated.

Table 4.9 summarizes the main absolute maximum electric ratings of the three OPA technology used in the prototype. Because of the characteristics of the OPA used and the role inside the active circuit OPA858 (Shaping stage) and OPA856 (Boosting stage) limiting electric feature is the maximum swing voltage. While in the case of LMH6559 (Decoupling stage), it is the maximum output current. Considering those absolute values, it is possible to get the maximum input voltage and output current envelopes of operation of the system explored.

TABLE 4.9. Main maximum absolute ratings

OPA Type	Parameter	Value
OPA858	Vout [V]	[-1.45,1.6]
OPA856		
LMH6559	Ioutmax [mA]	75

At low frequencies the impedance is higher and therefore the current to compensate is smaller. Consequently, at low frequencies the limiting rating that will determined the PPSE of the circuit is the maximum input voltage that the system can proceed

without saturating the two first stages output. Saturation would produce a non-linear behaviour that degraded the compensation capability. Therefore, the maximum input voltage envelope to be applied to the circuit has to be calculated. Based on the shaping and boosting stages, this can be defined as,

$$U_s^{max} = \frac{V_{out}^{max}}{G_{OPA}^{total}} \tag{4.45}$$

where V_{out}^{max} indicates the maximum absolute swing voltage of the last OPA in the chain (i.e the boosting stage) and G_{OPA}^{total} is the product of all OPA stages gains.

At medium and high frequencies, the PPSE is no longer limited by the maximum voltage but the maximum output current of the decoupling OPA. The reason is that the injection impedance decreases with the frequency causing the output current to increase. Therefore, the voltage imposed over the injection branch should be limited to prevent the injection branch from imposing an overcurrent on the buffer.Figure 4-37 shows the calculated envelope limits for U_s^{max} and I_c^{max} along the frequency range from 2 kHz up to 30 MHz. Based on them the PPS is calculated, see Figure 4-38.

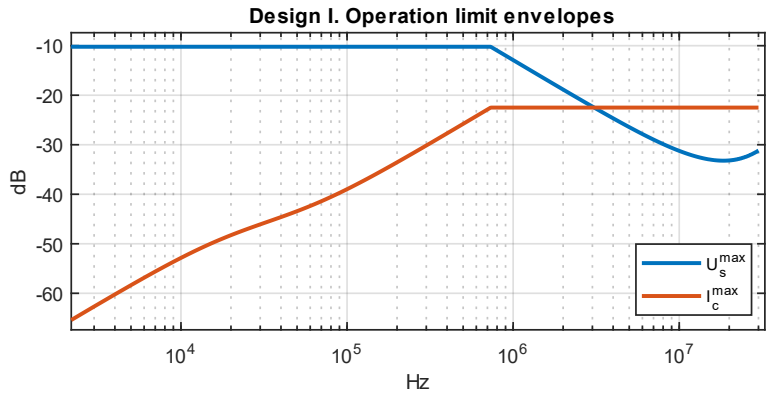

Figure 4-37. Maximum voltage and current masks of Design I.

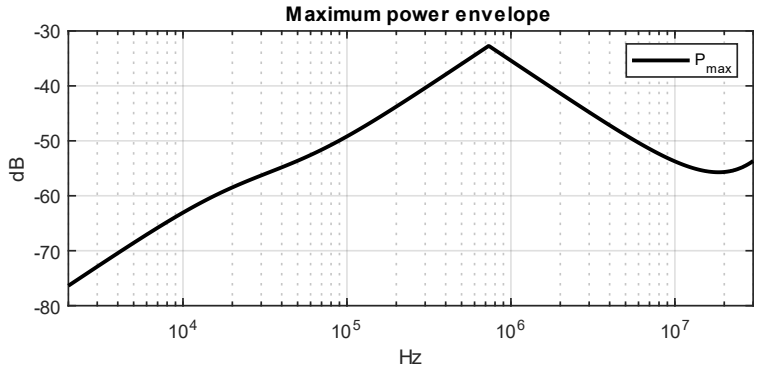

Figure 4-38. PPSE mask of Design I.

The operation envelopes calculation has been verified with the simulation of a 5 KW propulsion system scenario, Figure 4-39. To integrate the active solution displayed in Figure 4-30. A high-pass filter had to be added at the connection nodes of the active capacitance. The reason is the active solution cannot be connected directly to the positive rail to the ground connection as the Cp_{yx} will be charged to a DC

voltage equal to half of the DC bus voltage. The active solution is design to process only the EMI noise, this means ac variations.

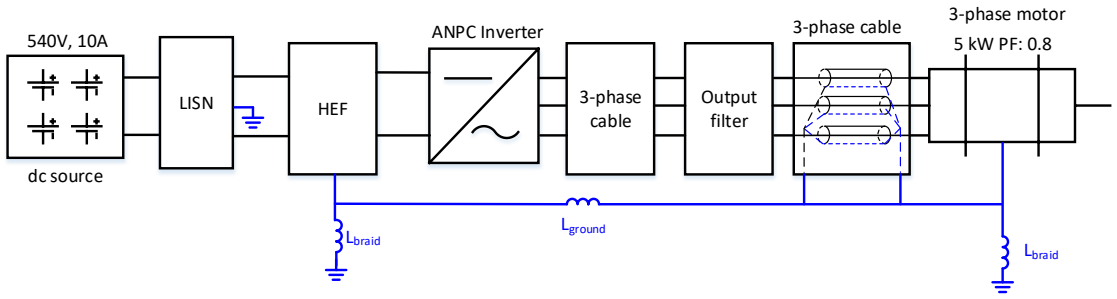

Figure 4-39. 5 kW scaled propulsion system. General scheme of the simulation case used for validation

The spectrum of the voltage and current manage by the HEF solution implemented in the T-Type input EMI filter are superimposed with the previous theoretical envelopes, see Figure 4-39 . It can be appreciated that they well define the expected response of the active capacitance. Additionally, the power managed by the equivalent passive solution and the active proposal are calculated and compared. Based on the previous maximum envelope graphs the maximum peak power that the solution can manage is 0.0231 W. This peak power might limit the performance at certain frequencies, but the filter might be able to perform and provide attenuation for much higher power systems. Ultimately, the consideration for design may be related to maximum peak power and thermal performance of the OPAs.

From Figure 4-39 , it can be seen the main power difference of the active solution with a passive equivalent occurs at the switching frequency. However, as has been mentioned before, the solution is intended for the frequency range from 150 kHz to

10 MHz. If we compared both options at this range the behaviour is quite similar.

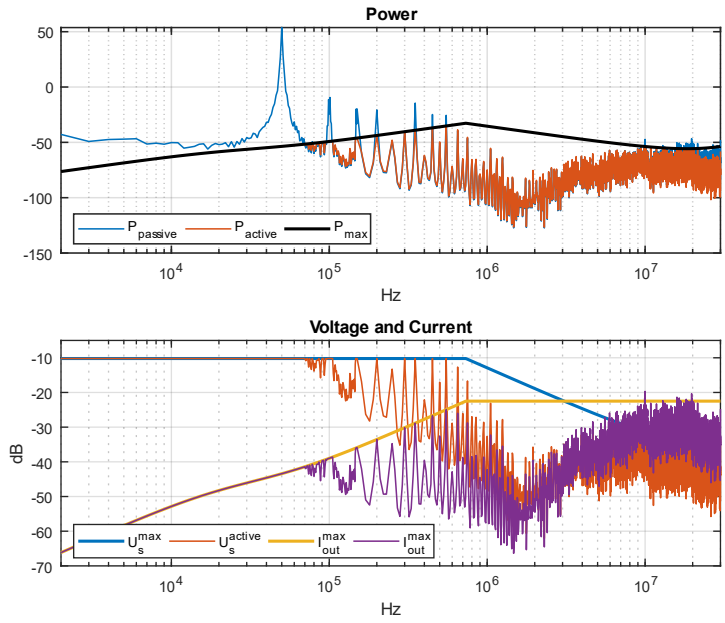

Figure 4-40. Operation limitation analysis of the design I for the 5kW scaled system model.

4.3.1.5 Weight/Volume comparison with a passive equivalent solution.

Apart of the feature of bypassing the limitations of maximum impedance connected tot he ground imposed by airframes regulations, another claims of the active impedance solution here presented is the reduction of wight and volume when comparing with an equivalent passive alternative.

Using the expected voltage spectrum at the connection node of the C_y, see Figure 4-39, a passive 330 nF (i.e., the equivalent active capacitance) capacitor has been selected. The idea is to compare the weight and the volume of the passive technology available with the Design I done. In Table 4.10, passive capacitor FKP1T023306D

and active circuit weight and volume are compared. Please note that the data displayed here is for one element. It can be concluded that the proposed active solution provides a lighter and smaller solutions.

TABLE 4.10

Manufacture numbers	Votlage Rating (VDC)	Dimensions WxHxL (mm)			Volunme (cm3)	Weight (g)
FKP1T023306D	1600	31	46	41.5	59.179	62.5
Active Circuit	-	50.8	48.9	1.15	2.8	20

However, in terms of power managed, the active solution will have certain limitations mentioned previously . The Design II, where the buffer is replaced by a LPA can help to take over the current injection limitation. As it was explored previously in the document, the design add certain level of complexity though. How to take over those operation constraints to improve the performance of the approach is future work objectives.

4.4 Conclusions

Active EMI mitigation solutions, which enable to overcome the PEF size reduction limitations, have been explored in this chapter. An overview of the current SoA of AEF and HEF has been provided. Based on a study case scenario of a future electric aircraft propulsion system, the main EMI limits has been presented identifying the key EMI filter locations.

Two active solutions, based on VSCC AEF configuration, have been proposed for being implemented in a HEF. Design methodology has been provided for both proposals, Design I and Design II. The aim of the design method proposed consists on

the replication of the behaviour of a passive shunt capacitor. Design I, which is an analog electronic circuit base on VFB OPAs, has demonstrated to be able to guarantee an active amplification of the C_y capacitance of a CM filter up to 10 MHz. A study case, in which the C_y is amplified nearly 10 times has been successfully experimentally verified. Limitations on the maximum compensation current and EMI voltage magnitude processing capabilities have been detecting. Design II, has been proposed to overcome the maximum compensation current constrains identified, a LPA increase the magnitude of the current injection of the solution. Special indications to compensate the effect of the high frequency parasitic components of the BJTs has been explained. Design II, has been only verified analytically scheduling the experimental verification as future work.

Weight and volume comparison of the Design I prototype with an equivalent passive capacitor has been provided. The active solution achieves lower volume and weight, being an additional benefit the PCB integration flexibility versus a passive capacitor.

Chapter 5

Conclusions and future work

This last chapter of this PhD thesis provides a summary of the main outcome and proposes several ideas to further research the concepts developed in the document. At the end, the publications and patents resulted from the research are listed.

5.1 Conclusions

The development of MEA or AEA/HEA to replace the current aviation fleet will require a multi-disciplinary research effort to advance the required disruptive technologies. Chapter 1 contributes on the understanding of the aircraft electrification challenge nature, providing the main insights into the conventional aircraft electric power system and the main challenges to upgrade it to the new aircraft concepts, while keeping weight and safety requirements. A full redesign is needed to scale the conventional EPS to a tends of MWs system with voltages levels in the range of

kV. Furthermore, the operation environment mainly influenced by the high altitude, adds additional constrains in terms of weight and safety. One of the main obstacles detected is the technological immaturity. High power and energy density ESS, high specific power converters and electric machines and light distribution cables and shot-circuit breakers are some of the EPS elements where technological development is needed. Consequently, technology such as fuel cells, weight and efficiency optimized multi-level power converters and EMI filters, optimized PMSM or HTS machines and DC SSCB are currently investigated as enablers of AEA/HEA.

The technological development effort of the mention elements needs a clear definition of the EPS architecture and deep analysis of the system requirements. In Chapter 2, EPS trade-off analysis and identification of the most promising propulsion architectures for commercial aviation is covered. In depth-analysis of all the main AEA propulsion architectures to identify the most promising architecture configuration for future electrical aircraft in the context of a twin-propeller 20 MW plane is proposed. The analysis is based on the study of three FoM, reliability, efficiency and specific power density. One of the main outputs of the analysis is the general higher achievable specific power of EPS architectures based on DC distribution. Additionally, the following conclusion is resulted from the analysis. In terms of propulsion configurations, parallel hybrid, series hybrid and turboelectric solutions report the highest specific power. However, the last two are penalised by extra conversion stages which lower the efficiency. Additionally, it has been concluded that in any of the cases, an important limiting factor to achieve desired specific power values is the ESS technology available. Being DC circuit breakers the second main element leading the system specific power down. At commercial aircraft level, the prediction is that hybrid propulsion systems, with a limiting hybridization degree,

will be selected for medium-term electric aircraft solutions.

In Chapter 3 the thesis contributes to the pursuit of power converters that aims high voltage compatibility and weight reduction. A distributed input multiport topology is proposed based on the use of a MMC. The DIMMC is based on the application of an MMC to multiphases systems, such as multiport generators or multiport transformers. The chapter provides a methodology to study the C_{cell} reduction capability for a study case in which a PFVSR is connected to each cells of the modular configuration. Up to 50% of reduction on the C_{cell} value is achieved, being the cell voltage variation constrain to a 10% band. This demonstrates that there is a weigh reduction opportunity for this type of converters. Nevertheless, certain limitations on the control algorithm design has been detected and further analysis of the real reduction weight efficiency and EMI of the proposed solutions are pending to explore. For instance, taking into account the additional elements implications. Additionally, short-circuit handling capability result reported advantages with respect the conventional MMC.

As a rule of thumb, it can be said that EMI filters can contribute to the 30% of the total volume and weight of a power converter. Consequently, their size optimization is of big importance. In Chapter 4 new active EMI mitigation solutions with potential to reduce the EMI filter weight are explored. The study has resulted in the proposal of two novel approaches based on analog circuits. A step-by-step design procedure is described in order to reach an actuation frequency range which covers from 150 kHz up to 10 MHz. Both solutions has demonstrated active enhancing of the shunt capacitance value of a CM EMI filter (e.g. 10 times in the study case presented). Concluding that the use of this type of approaches could give an additional degree of freedom in the EMI filter design optimization. The first approach, based on OPAs, has been prototyped, resulting in a smaller and lighter alternative to an

equivalent PEF. It is, 30% weight reduction and 95% volume reduction. However, power processing limitations has been detected during the study of the integration of the hybrid AEF in the power train of an electrified aircraft. The second solution is proposed to increase the current injection capability of the circuit by integrating a LPA in the last stage. Volume and weight reduction advantages of this approach has not been explored and are pending for future work.

As a general conclusion, it can be said that the development of advanced power converters for the electrification of the future aircraft involves more aspects than the converter design itself. The current research effort is focused on exploring potential power converters solutions while the power system architecture characteristics are not definitely defined yet and the requirements are not clear and vary with the aircraft platform. All constrained by the very demanding operation conditions of aviation application. It is, due to the high altitude working conditions, safety requirements and weight and volume constrains. Making the EPS design for MEA or AEA/HEA aviation concepts result in a problem with many synergies.

5.1.1 Publications and patents related with the work presented

Some of the mentioned outcomes of this work has ben translated into publications and intellectual property disclosure (IPD). They are listed below:

- T. C. Cano et al., "Future of Electrical Aircraft Energy Power Systems: An Architecture Review," in IEEE Transactions on Transportation Electrification, vol. 7, no. 3, pp. 1915-1929, Sept. 2021, doi: 10.1109/TTE.2021.3052106.

- T. C. Cano, D. Pedroso, A. Rodríguez, I. Castro and D. G. Lamar, "On the reduction of output capacitance in two-level three phase PFC boost rectifier for pulsating loads," 2022 24th European Conference on Power Electronics and Applications (EPE'22 ECCE Europe), Hanover, Germany, 2022, pp. 1-9.

- T. C. Cano, A. Rodriguez, I. Castro and D. G. Lamar, "Distributed Input Multiport MMC Based Power Converter for AC and DC Loads," in IEEE Transactions on Power Electronics, vol. 38, no. 7, pp. 7971-7975, July 2023, doi: 10.1109/TPEL.2023.3260719.

- I. Castro, T. C. Cano, "Power converter" U.S. Patent US20220209680A1, June 30, 2022.

- T. C. Cano, "EMI Active Filter" U.S. Patent US20230421134A1, Dec 28, 2023.

5.2 Future work

Several potential research ideas to extend and improve the work develop here presented are proposed:

- Extension of the trade-off analysis proposed to different aircraft platforms and different hybridization levels to study the influence on the outcome. Additionally, a potential improvement could be performing the integration of of flight profiles in the analysis, which defines the power consumed along the operation of the aircraft, and simulating the EPS within an MBSE to characterise the efficiency of the system.

- Further experimental validation of the capacitance reduction estimation methodology. Additionally, this would bring additional information of the detected limitations in the control algorithm.

- Evaluation of different control algorithms to implement in the PFVSR that might provide high-power density achievements at lower switching frequencies. They could overcome the implementation difficulties experience during the testing with GaN modules.

- Enhancement of the DIMMC study by evaluating the topology from a dynamic perspective and evaluation of the EMI implications involved on the faster variations on the C_{cell} voltage. Being interesting to perform the evaluation of the converter with a flight profile. Re-definition of the design of the L_{arm} to achieve a minimized inductor size.

- Proposal of novel insertion methodologies for the DIMMC to provide thermal improvements.

- Further validation of Design II of the hybrid EMI filter proposal, based on LPAs.

- Integration of the Desing IIof the hybrid EMI filter solution on the application test setup to achieve higher technology readiness levels (TRLs).

Capítulo 6

Conclusiones y trabajo futuro

Este último capítulo de tesis proporciona un resumen de los principales resultados y propone varias ideas para continuar investigando los conceptos desarrollados. En último lugar, se enumeran las publicaciones y patentes resultado de la investigación.

6.1 Conclusiones

El desarrollo de "MEA" o "AEA/HEA" para reemplazar la flota actual de aviación requerirá un esfuerzo de investigación multidisciplinario para alcanzar las tecnologías disruptivas necesarias. El Capítulo 1 contribuye a la comprensión de la naturaleza del desafío de la electrificación de aeronaves, presentando las principales característics del sistema eléctrico de los aviones convencionales y explicando los principales desafíos para su adaptación a los nuevos conceptos de aeronaves, mientras se mantienen requisitos de peso y seguridad. Se necesita un rediseño completo para escalar el sistema

"EPS" convencional a un sistema que maneje decenas de MW con niveles de tensión en el rango de kV. Además, el entorno de operación añade severas restricciones adicionales en cuanto a peso y seguridad. Uno de los principales obstáculos detectados es la inmadurez tecnológica actual. Sistemas de almacenamiento de energía con alta densidad de potencia y energía, convertidores de potencia y máquinas eléctricas compactas, y cables de distribución y disyuntores de cortocircuito ligeros son algunos de los elementos del "EPS" donde se necesita más desarrollo tecnológico. En consecuencia, tecnologías como las pilas de combustible, los convertidores multinivel y filtros "EMI" optimizados en peso y eficiencia, así como, máquinas "PMSM" o "HTS" optimizadas y "SSCB"de DC están siendo investigadas como habilitadores de "AEA/HEA".

El esfuerzo tecnológico de los elementos mencionados necesita una definición clara de la arquitectura "EPS" y un análisis profundo de los requisitos del sistema. En el Capítulo 2, se presenta un análisis comparativo de sistemas de distribución. Su objetivo es la identificación de las arquitecturas de propulsión más prometedoras para un avión de tipo comercial. Se propone un análisis de todas las principales arquitecturas de propulsión "AEA/HEA", con el fin de identificar la arquitectura más prometedora en el contexto de un avión bimotor de 20 MW. El análisis se basa en el estudio de tres "FoM": fiabilidad, eficiencia y potencia específica. Uno de los principales resultados del análisis es la mayor potencia específica alcanzable de las arquitecturas "EPS" basadas en distribución de DC. Además, el análisis concluye lo siguiente: en cuanto a configuraciones de propulsión, las soluciones híbrido paralelo, híbrido serie y turbo-propulsión eléctrica proporcionan la mayor densidad de potencia específica. Sin embargo, estas dos últimas se encuentran penalizadas por etapas de conversión adicionales que reducen la eficiencia global. Además, se ha concluido que,

en cualquiera de los casos, un factor limitante importante para alcanzar los valores deseados de potencia específica del sistema es la tecnología "ESS" disponible. Siendo los disyuntores de cortocircuito, el segundo elemento que más reduce la potencia específica del sistema. A nivel de aviones comerciales, se predice que los sistemas de propulsión híbridos, con un grado de hibridación limitado, serán la alternativa preferida a implementar a medio plazo.

En el Capítulo 3, la tesis contribuye a la búsqueda de convertidores de potencia que apunten a la compatibilidad de alto voltaje y la reducción de peso. Se propone una topología de entrada distribuida multipuerto basada en el uso de un "MMC". El "DIMMC" se basa en la aplicación de un "MMC" a sistemas multifásicos, como generadores o transformadores multipuerto. El capítulo proporciona una metodología de estudio de la capacidad de reducción del valor de C_{cell}, para un caso de estudio en el que un "PFVSR" está conectado a cada celda de la configuración modular. Se ha logrado demostrar una reducción de hasta el 50 % en el valor de C_{cell}, restringiendo la variación de tensión de la celda a una banda del 10 %. Esto demuestra que existe una oportunidad de reducción de peso para este tipo de convertidores. Sin embargo, se han detectado ciertas limitaciones en el diseño del algoritmo de control y se necesita un análisis adicional de la capacidad real de reducción del peso. En el que se tenga en cuenta las implicaciones de los elementos adicionales. Además, la capacidad de manejo de cortocircuitos reporta ventajas respecto a un "MMC" convencional.

Como regla general, se puede decir que los filtros "EMI" pueden contribuir al 30 % del volumen y peso total de un convertidor de potencia. En consecuencia, la optimización de su tamaño es de gran importancia. En el Capítulo 4, se exploran nuevas soluciones activas para la supresión de ruido, con potencial para reducir el peso del filtro "EMI". El estudio ha resultado en la propuesta de dos nuevas soluciones

basados en circuitos analógicos. Se describe un procedimiento de diseño paso a paso para alcanzar un rango de frecuencia de actuación que cubra desde 150 kHz hasta 10 MHz. Ambas soluciones han demostrado amplificar activamente el valor de la capacidad conectada a tierra de un filtro "EMI" de modo común (por ejemplo, 10 veces en el caso de estudio presentado). Se concluye que el uso de este tipo de enfoques podría dar un grado adicional de libertad en la optimización del diseño del filtro "EMI". El primer enfoque, basado en OPAs, ha sido prototipado, resultando en una alternativa más pequeña y ligera que un "PEF" equivalente. La solución presenta una redución de peso del 30 % y una redución de volumen del 95 %. Sin embargo, se han detectado limitaciones en la máxima potencia procesada durante el estudio de su integración en el tren de potencia de un avión con propulsión electrificada. La segunda solución, se propone para aumentar la capacidad de inyección de corriente del circuito. Para ello se integra un "LPA" en la última etapa. Las ventajas de reducción de volumen y peso de este enfoque no han sido exploradas y están pendientes para futuros trabajos.

Como conclusión general, se puede decir que el desarrollo de convertidores de potencia avanzados para la electrificación de aeronaves futuras implica más aspectos que el diseño del convertidor en sí. El esfuerzo de investigación actual se centra en explorar soluciones de convertidores de potencia, mientras se definen las características de la arquitectura del sistema de potencia y se comprueba el cumplimiento de los requisitos. Estudios que varían con el tipo de plataforma de aeronave. Todo esto, restringido por las muy exigentes condiciones de operación en aviación (altitud, los requisitos de seguridad y las restricciones de peso y volumen). Lo que hace que el diseño del "EPS"para conceptos como el "MEA.º "AEA/HEAresulte en un problema con muchas sinergias.

6.1.1 Publicaciones y patentes relacionadas con el trabajo presentado

Algunos de los resultados mencionados en este trabajo han dado lugar a una serie de publicaciones y patentes. Estas, se enumeran a continuación:

- T. C. Cano et al., "Future of Electrical Aircraft Energy Power Systems: An Architecture Review,.[en] IEEE Transactions on Transportation Electrification, vol. 7, no. 3, pp. 1915-1929, Sept. 2021, doi: 10.1109/TTE.2021.3052106.
- T. C. Cano, D. Pedroso, A. Rodríguez, I. Castro y D. G. Lamar, .[o]n the reduction of output capacitance in two-level three phase PFC boost rectifier for pulsating loads,"2022 24th European Conference on Power Electronics and Applications (EPE'22 ECCE Europe), Hanover, Germany, 2022, pp. 1-9.
- T. C. Cano, A. Rodriguez, I. Castro y D. G. Lamar, "Distributed Input Multiport MMC Based Power Converter for AC and DC Loads,.[en] IEEE Transactions on Power Electronics, vol. 38, no. 7, pp. 7971-7975, July 2023, doi: 10.1109/TPEL.2023.3260719.
- I. Castro, T. C. Cano, "Power converter" Patente de EE. UU. US20220209680A1, 30 de junio de 2022.
- T. C. Cano, "EMI Active Filter" Patente de EE. UU. US20230421134A1, 28 de diciembre de 2023.

6.2 Trabajo futuro

Se proponen varias ideas para extender el trabajo de investigación y mejorar el trabajo desarrollado:

- Ampliación del análisis comparativo de arquitecturas de propulsión con la incorporación de diferentes tipos de aeronaves y la consideración de diferentes niveles de hibridación. Esto permitiría detectar su influencia en los resultados del estudio. Además, otra posible mejora podría ser la integración de perfiles de vuelo en el análisis, que definan la potencia consumida durante la operación del avión, así como, el estudio del EPS en un MBSE que permita caracterizar la eficiencia todos los sitemas presentes en la aeronave.

- Validación experimental adicional de la metodología de reducción del valor de condensador de celda. Esto permitiría obtener información adicional sobre las limitaciones detectadas en el diseño del algoritmo de control.

- Evaluación de diferentes algoritmos de control para el PFVSR que puedan lograr una redución de peso similar con frecuencias de conmutación más bajas. Esto podría evitar las dificultades de implementación experimentadas durante las pruebas con módulos GaN.

- Mejora del estudio del DIMMC mediante la evaluación de la topología desde una perspectiva dinámica y la evaluación de las implicaciones de EMI involucradas en las variaciones más rápidas de la tensión de C_{cell}. Además, se considera interesante realizar la evaluación del convertidor con un perfil de vuelo y el rediseño de la inductancia de rama, L_{arm}, para minimizar el su tamaño.

- Propuesta de una metodologías de inserción de celdas nueva para el DIMMC que proporcione mejoras térmicas.
- Validación adicional del Diseño II de la propuesta del filtro EMI híbrido, basado en LPAs.
- Integración del Diseño I de la solución del filtro EMI híbrido en un sistema escalado experimental de la aplicación para lograr niveles de preparación tecnológica (TRLs, en inglés) más altos.

Appendix A

Two-level voltage source rectifier prototype

During the development of this PhD thesis work a test prototype of a 10kW scaled version of the PFCVSR presented in Chapter 3 was built. The aim was to demostrate experimentally the capacitance reduction results explained and verified by simulation in Section 3.2.2.1. Figure A-1, shows a general picture of the prototype. It has been designed as three independent PCB boards: a sensing board, a power stage and a signal adaptation board. The details of the three main parts are explained in the following lines. The fully test of the prototype could not be completed during the process of the PhD due to contingencies but it is though to be of interest to show the work developed.

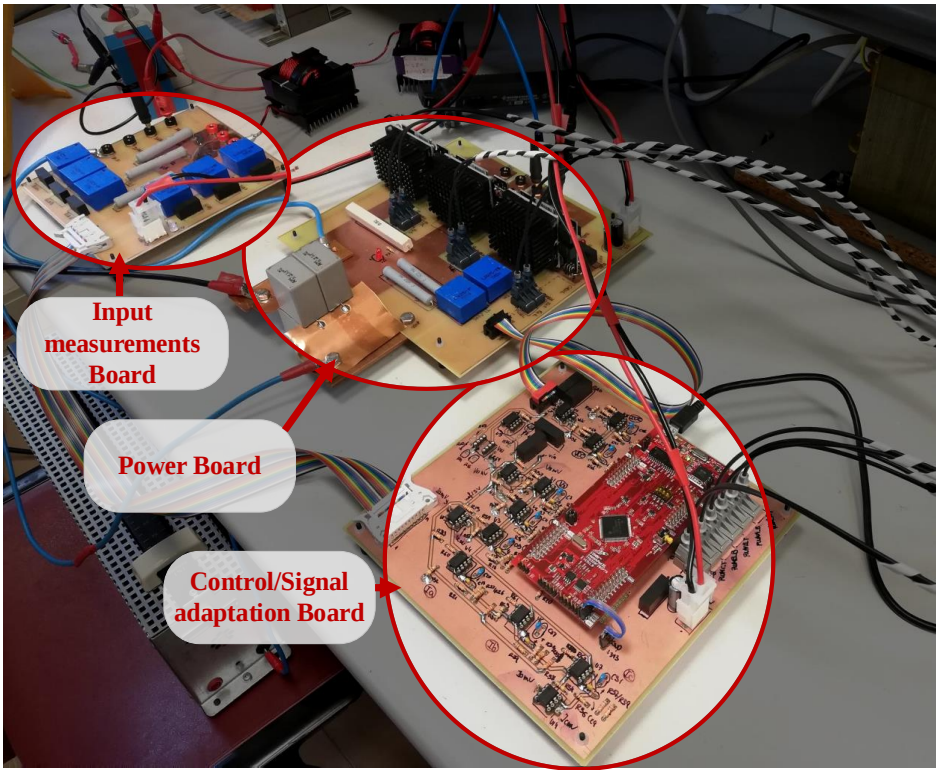

Figure A-1. General picture of the PFCVSR prototype

A.1 Input measurement board

The input AC voltage and currents are measured at the source connection, Figure A-2. Voltage AC signals are used by the phase-locked loop (PLL) in order to synchronize the PFCVSR system with the phase of the input voltage signal. This synchronization is essential to perform the d-q transformation of the voltage and current signals, needed in the control loop algorithm. AC currents are measured to be transformed in the DSP into their d-q components and then be used in the current control loop (Loop 2) , Figure 3-3.

Close loop Hall effect sensors have been used to measured both voltage and current

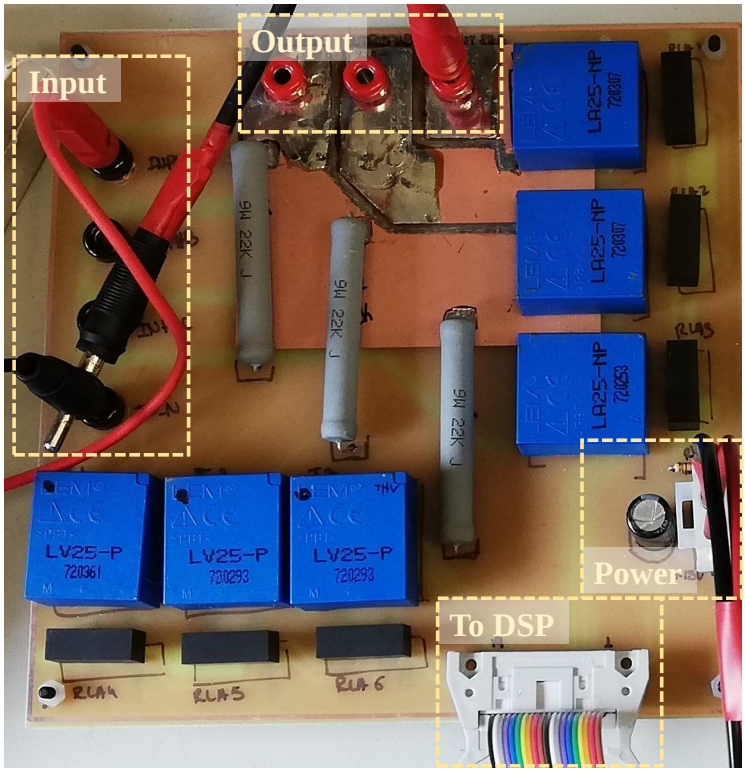

Figure A-2. Input Measuremnts board details

signals. Part number and main data of the sensors used are displayed in Table A.1. Figure A-3, shows simplify schemes of the LV25-P and the LA25-NP sensors. For the current sensor, Figure A-3.a, the connection of the pins have been performed for a nominal primary current of 25 A., resulting in a turn ratio (Np/Ns) 1/1000. The current to voltage measurement resistor (R_{Mv}) is not included in this board, instead the current signal Is, is sent to the control/ signal adaptation board. Voltage sensor, Figure A-3.a, R_1 resistor is design to limit the maximum input power to 10 mA at the maximum input peak voltage. Similarly to the current sensor, the measurement current signal is sent to the control/signal adaptation board.

The sensor voltage supply is provided by an independent 1W dc-dc isolated con-

TABLE A.1. Voltage and current sensors general data

Signal	Part number	Data	
Van,Vbn,Vcn	LV25-P	I_1 *RMS current*	10 mA
		I_{sV} *RMS current*	25 mA
		Np/Ns	2500/1000
		Supply voltage (V_s)	+/- 12-15V
		t_{delay}	40 us @ R1 25 $k\Omega s$
Ia, Ib, Ic	LA25-NP	I_{in} *RMS current*	25 A
		I_{sI} *RMS current*	25 mA
		Np/Ns	1...5/1000
		Supply voltage (V_s)	+/- 15 V
		t_{delay}	$1\mu s$

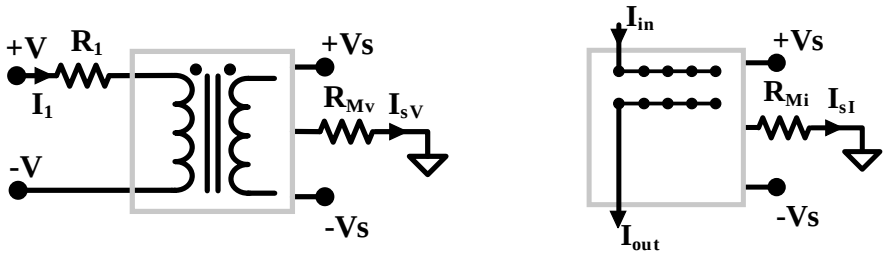

(a) (b)

Figure A-3. Close loop hall effect sensor configuration. (a) LV25-P and (b) LA25-NP

verter with a dual +/- 15 V output (TMA1515D).

A.2 Power board

The power board consist of three GaN power modules, a current and voltage sensor similar to the ones presented before and a DC bus connection. The gate signals are transmitted through optical fiber, optical receivers are placed close to the power modules. Figure A-4 shows a picture of the power board, where the mentioned elements are identified. The input inductances present at the input of the 2-level

three phase bridge have been connected externally to the power board at the input power connections.

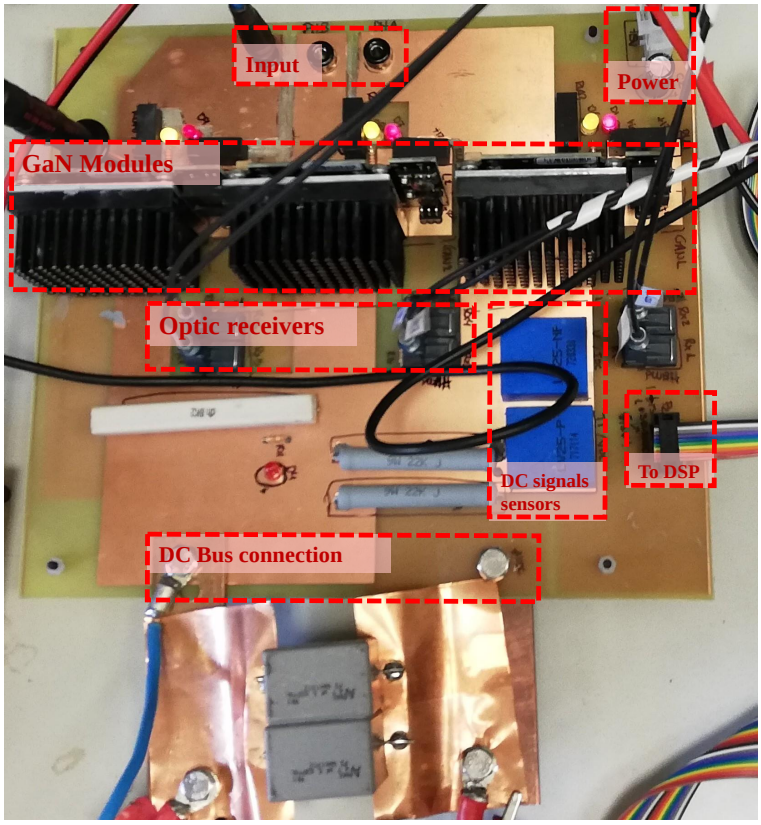

Figure A-4. Power board board details

Two evaluation board have been considered to build each the three half-bridge modules of the PFCVSR, the GS66508B-EVBDB1 and the GSP65R13HB-EVB. To evaluate the behaviour of each module, a dc-dc boost converter was build with each of them. Each module was operated until continuous conduction mode up to 1 kW. The board temperature has been observed during the process, as is well known one of the main weakness of GaN devices is the heat evacuation, which causes many times the destruction of the device. Figure A-5 shows a photo of the modules evaluation

set-up.

Figure A-5. GaN modules evaluation set-up

During the evaluation the GS66508B-EVBDB1 board has shown noise problems at the gate to source signal of the GaN devices, which cause the failure of few modules. Additionally, GSP65R13HB-EVB has reported better thermal behaviour during the testing. Consequently, GSP65R13HB-EVB is selected to build the power stage shown in FigureA-4. Figure A-6, display thermal pictures taken under the operation conditions described in Table A.2.

TABLE A.2. GaN modules test data operating as a dc-dc boost converter.

Variable	**Value**
Vin	200 V
Vout	400 V
fsw	100 kHz
L	2 mH
Rload	238 Ohms

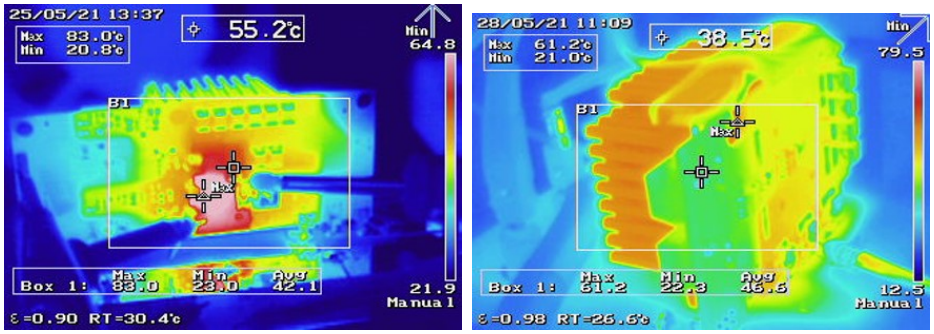

(a) (b)

Figure A-6. GaN power modules evaluation, thermal photo. (a) GS66508B-EVBDB1 and (b) GSP65R13HB-EVB

GSP65R13HB-EVB evaluation boards are equipped with a Insulated Substrate (IMS) PCB which increases the heat transfer from the GaN devices to the heatsink. The module combined two GS66516B GaN transistors in parallel. Figure XXX displays a closer picture.

A.3 Control/signal adaptation board

The control/signal adaptation board contains the Digital signal processor (DSP), which is responsible of the PWM signals generation,analog-to-digital (ADC) transformation of the sensor signals, and control algorithm execution. The PWM signals that govern the GaN drivers are sent through optic fiber to the power board.

The control adaptation board receives the AC and DC sensors signals which needs to be adapted and processed before inputting them in the ADC. Figure A-8, illustrates the adaptation and processing circuitry used for the AC signals, Figure A-8 .(a), and DC signals, Figure A-8 .(b).

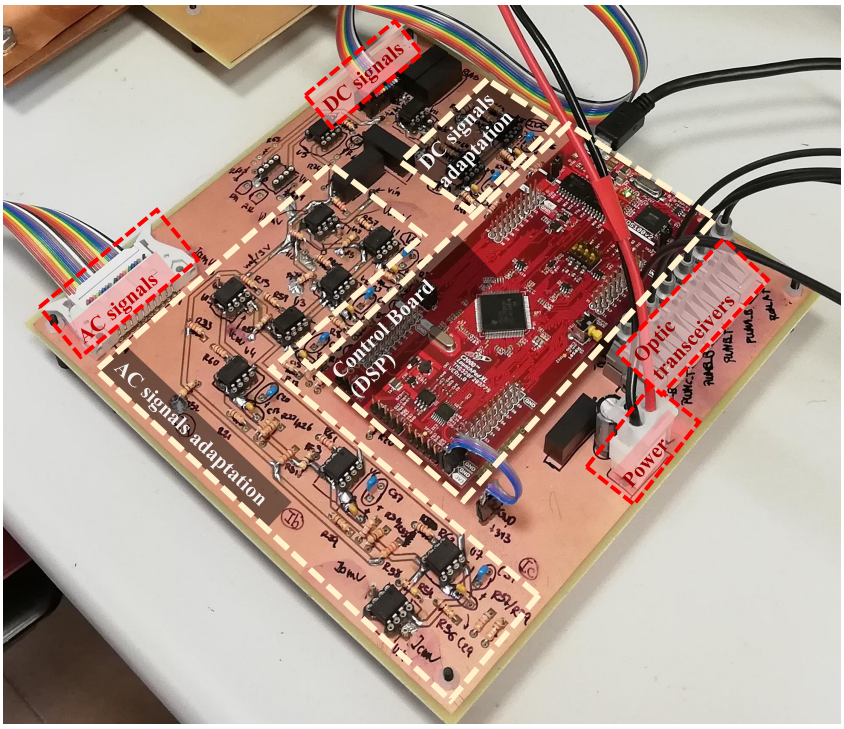

Figure A-7. Control/Signal adaptation board

The adaptation stage is responsible of converting the sensor signal, which is a curren, into a voltage signal within the range [0V,3V]. Firstly, the current signal is transformed into a voltage signal which absolute maximum value is 1V. It is, RM is designed so the AC sensor signal received is converted into a voltage level between -1V and 1V, and the DC sensor signal received is translated in a voltage from 0 V to 1V. afterwards, a non-inverting OPA is used to adapt the voltage signals into the [0V,3V]. This is designed following the equation,

$$V_z = (1 + \frac{R_2}{R_1}) \cdot V_x - \frac{R_2}{R_1} \cdot V_{ref}. \tag{A.1}$$

In the next stage an anti-aliasing filter is place to attenuate any undesired frequency

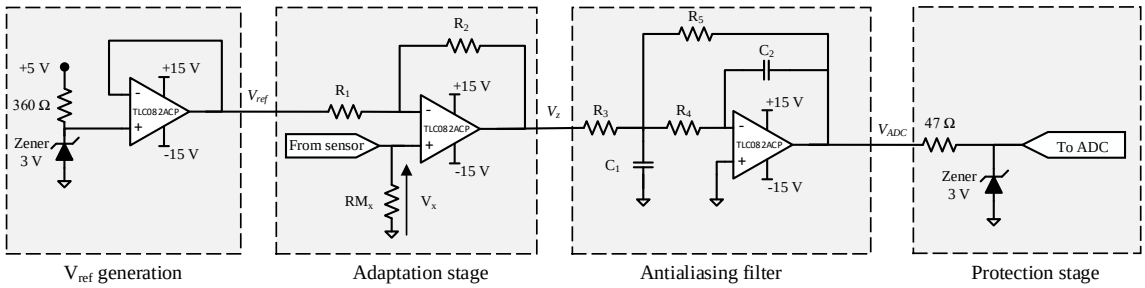

(a)

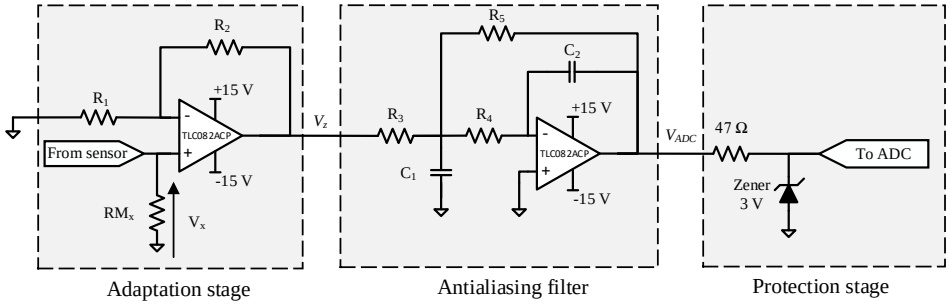

(b)

Figure A-8. Adaptation and processing signal circuit. (a) AC signals and (b) DC signals

component that can caused errors in the ADC conversion. A Bessel filter topology has ben chosen with a cut-off frequency set to the Nyquist frequency, which is equal to half the sampling frequency. In this case, the sampling frequency selected is equal to the switching frequency.

The board has been designed with an isolated ground from the power an measurement boards, the OPAS, DSP and optic transceivers are supplied by dc-dc isolated converters which transform a input 15V power supply into The voltage levels needed. Two TMA1515D are used to supply the OPAs, the optic transceivers are supplied with 5 V by a dedicated TMA1505S. The DSP used is the F28377S LaunchPad and can be supplied by a 3.3V port, a TMA1505S is combined with a linear regulator to

generated this voltage level. Additionally, the TMA1515D used to supply the DC voltage and current sensor is placed in this board.

The correct operation of the adaptation and processing signal has been verified comparing the theoretical value expected at the ADC register with the values measured by the sensors. Figure A-9 displays the three input AC voltage magnitudes obtained. After, the PLL functionality is tested. A three phase 400 Hz voltage has been applied at the input of the measurement board. Figure A-10 shows a screenshot of the DSP software interface. It can be seen the correct identification of the input AC signals frequency, f_o. Furthermore, to test the PWM the three phase AC 400 Hz is measured and used as the modulated signal. The PWM generated is compared with the modulated signal. An example is seen in Figure A-11.

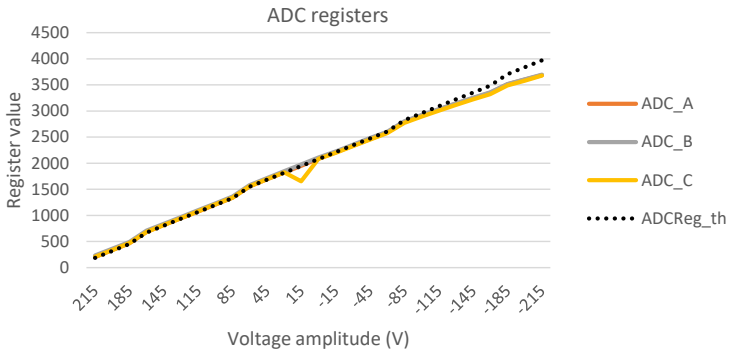

Figure A-9. ADC registers values of the input AC voltage during a sweep of the magnitude.

spll	struct spll1	{v_q=[-0.0170296431,-0.0157966...	0x0000AB26@Data
v_q	float[2]	[-0.035194397,-0.005530186]	0x0000AB26@Data
ylf	float[2]	[-6.93362904,8.15054131]	0x0000AB2A@Data
fo	float	399.393433	0x0000AB2E@Data
fn	float	400.0	0x0000AB30@Data
theta	float[2]	[0.18610917,0.466258556]	0x0000AB32@Data
delta_t	float	9.99999975e-05	0x0000AB36@Data
lpf_coeff	struct <unnamed>	{b1=-234.920593,b0=237.079407}	0x0000AB38@Data
fo_array	int[60]	[395,394,402,409,398...]	0x0000AA80@Data

Figure A-10. PLL implementation test.

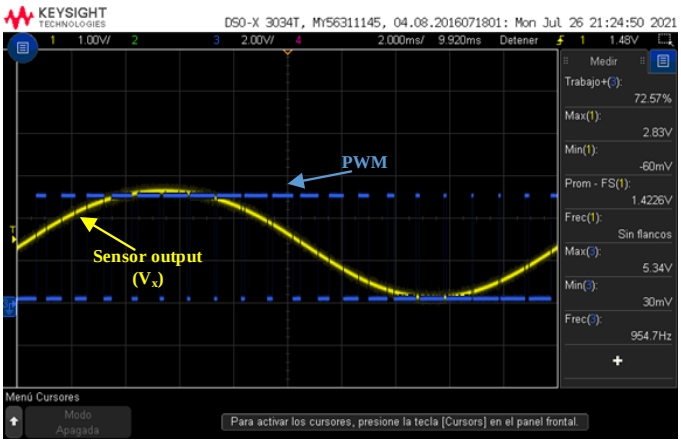

Figure A-11. PWM generation test

A.4 Prototype power testing

With the sensing, signal acquisition and processing and PWM generation tested, the next step is to verify the prototype under power conditions. As an intermediate test, it has been decided to test each phase independently first. In order to do so, each phase of the three phase rectifier is configured as a dc-dc boost converter and tested at nominal voltage and low power and finally a nominal voltage and 1 kW, see Figure A-12. Figure A-13 , shows the boost inductor current and the voltage at the bottom switch for each of the phases at 1 kW under the test conditions displayed in Table A.3.

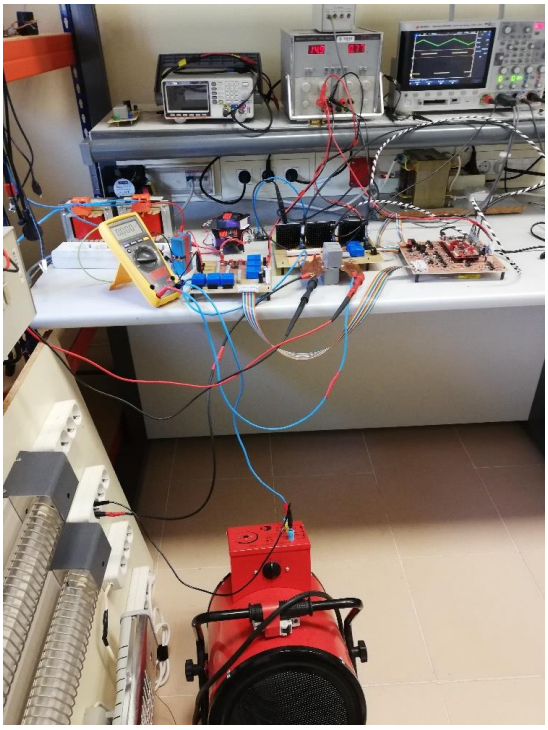

Figure A-12. Independent phase test under a dc-dc boost configuration.

TABLE A.3. Independent phase test waveforms.

Variable	**Value**
Vin	200 V
Vout	400 V
fsw	20 kHz
L	2 mH
Rload	128 Ohms

An open-loop tested has been performed for a low voltage case of the three phase rectifier. The input inductances are set to $550\mu F$, the input RMS voltage is set to 12.7 V in order to generate a 40 V DC bus. Initially the DC bus is charged witht he three phase rectifier operating as a passive rectifier, it is all the switches are kept

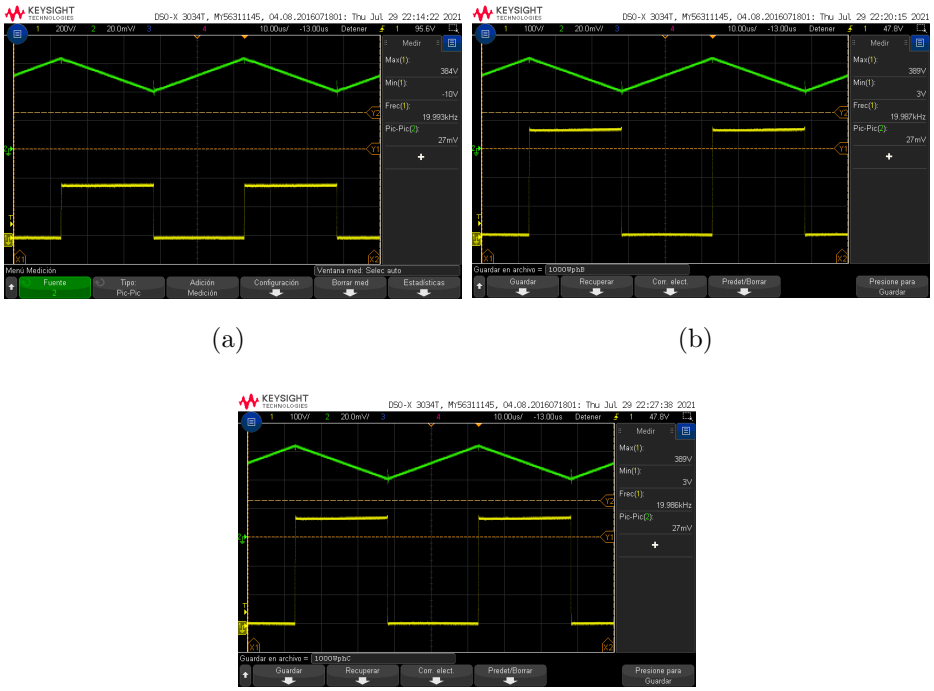

(a) (b)

(c)

Figure A-13. Individual rectifier phase testing. dc-dc boost configuration with an output power of 1 kW

open. Once the DC bus voltage reached the voltage value defined by,

$$V_{DC} = \frac{3 \cdot \sqrt{3}}{\pi} V_{ph}^{pk}. \tag{A.2}$$

The modulation is activating afterwards boosting the voltage to 40 V under a modulation $D_d = 0.9$ and a load equal to 148 Ωs. Unfortunately, waveforms records have not been saved and further testing has been interrupting due to the start of an internship in the company. Because of certain circumstances, that might not be relevant to describe in this document, the final close-loop test could not be performed.

Glossary

2L-CSI Two level current source inverter.

2L-VSC Two level Voltage Source Converter.

2L-VSI Two Level Voltage Source Inverter.

AC Alternating current distribution.

ACARE Advisory Council for Aeronautics Research in Europe.

AEA/HEA All-electric/hybrid-electric propulsion Aircraft.

AEF Active EMI Filter.

APU Auxiliary Power Unit.

ATM International American Society for Testing and Materials.

ATRU Auto-Transformer Unit.

ATU Auto-transformer..

BJT Bipolar Junction Transistor.

BLI Boundary Layer Injection.

CB Circuit Breaker.

CB Solid State Circuit Breaker.

CFB Current Feedback.

CHB Cascaded H-bridge.

CM Common-mode conducted EMI.

CONCERTO Construction of Novel Certification Methods and means of compliance for disruptive technologies.

COVID-19 CoronaVirus Disease.

CSCC Current Sensing - Current Compensation.

CSD Constant Speed Drive.

CSVC Current Sensing - Voltage Compensation.

DAL Design Assurance Levels.

DC Direct current distribution.

dc-ac Direct current - alternating current.

dc-dc Direct current - direct current.

DM Differential-mode conducted EMI.

DPCU Distributed Power Center Unit.

EAP NASA Glenn's research in Electrified Aircraft Propulsion.

EASA European Union Aviation Safety Agency.

EASIER Electric Aircraft System Integration Enabler.

ECS Environmental Control System.

EMC Electromagnetic Compatibility.

EMI Electromagnetic Interference.

EPC Equivalent Parallel Capacitance.

EPR Equivalent parallel Resistance.

EPS Electric power system.

ESL Equivalent Series Inductance.

ESR Equivalent series resistance.

ESS Energy Storage System.

EU European Union.

EVs Electric Vehicles.

FAA Federal Aviation Administration.

FHA Functional Hazard Analysis.

FIT Failure in Time.

FoM Figures of Merit.

FTA Fault Tree Analysis.

FTR Failure-to-run.

FTS Failure-to-start.

GaN Gallium Nitride.

GHG Greenhouse gases.

GPU Ground Power Unit.

HEF Hybrid EMI Filter.

HERA Hybrid Electric Regional Architecture.

HVDC High voltage direct current.

IGBT Insulated-gate Bipolar Transistor.

IM Induction Machine.

IMMD Integrated modular motor drive.

LISN Line Impedance Stabilization Network.

LPA Linear Power Amplifier.

MEA More-Electric Aircraft.

ML-FC Multi Level Flying Capacitor.

ML-VSI Multi-Level Voltage Source Inverter.

MMC Modular Multilever Converter.

MOSFET Metal Oxide Silicon Field Effect Transistor.

MTOW Maximum Take-off Weight.

NPN bipolar Negative-Positive-Negative bipolar transistor.

OEM Original Equipment Manufacturer.

OPA Operational Amplifiers.

PCB Printed Circuit Board.

PEF Passive EMI Filter.

PEM Proton exchange membrane Fuel Cell.

PFCVSR Two level power factor correction six-switch voltage source rectifier..

PMSM Permanent Magnet Synchronous Machine.

PPSE Peak Power Spectrum Envelope.

PSSA Preliminary System Safety Analysis.

RC branch Series connection of a resistance and a capacitance.

RF Radio Frequency.

RMS Root Mean Square.

RPDU Remote Power Distribution Units.

S/G Starter-Generator.

SAF Sustainable Aviation Fuel.

SMR ACAP Small/Medium Regional Aircraft architecture and technology integration Project.

SoA State of the Art.

SOFC Solid Oxide Fuel Cells.

SPICE Simulation Program with Integrated Circuit Emphasis.

SRIA Strategic Research and Innovation Agenda of Clean Aviation Joint Undertaking.

SRM Switched Reluctance Machine.

SSPC Solid-State Power Controllers.

SST Solid State Transformer.

STARC-ABL Single-aisle Turboelectric Aircraft with an Aft Boundary-Layer propulsor.

SVPWM Space Vector pulse width modulation.

TRU Transformer rectifier unit.

VFB Voltage Feedback.

VNA Virtual Network Analyser.

VSCC Voltage Sensing - Current Compensation.

VSVC Voltage Sensing - Voltage Compensation.

WAI Wing Anti-Icing.

WBG Wide band-gap.

WHO World Health Organization.

WSRSM Wound-Rotor Synchronous Machines.

Bibliography

[1] C. Programme, "Extreme heat, widespread drought typify european climate in 2022," Website, Apr. 2023. [Online]. Available: https://climate.copernicus.eu/extreme-heat-widespread-drought-typify-european-climate-2022

[2] E. E. Agency, "Global and eruopean temperatures," Website, Jun. 2023. [Online]. Available: https://www.eea.europa.eu/en/analysis/indicators/global-and-european-temperatures

[3] H. Ritchie, "How much does aviation contribute to climate change? how will this change in the future?" Sustainability by numbers, Tech. Rep., 2023. [Online]. Available: https://www.sustainabilitybynumbers.com/p/aviation-climate-part-one

[4] D. Hulst, "2021 commercial market outlook." The Boeing Company, 2021. [Online]. Available: https://www.boeing.com/content/dam/boeing/boeingdotcom/market/assets/downloads/CMO2021_presentation.pdf

[5] "Latest air traffic forecasts illustrate encouraging recovery and higher growth in global air travel," May 2022.

[6] R. Thomson, "Electrical propulsion ushers in new age of innovation in aerospace." Roland Berger LTD, Tech. Rep., Jul. 2018. [Online]. Available: https://www.rolandberger.com/en/Insights/Global-Topics/Electric-Propulsion/

[7] B. Graver, Z. Kevin, and D. Rutherford, "Co2 emissions from commercial aviation,2018," *The International council on clean transportation*, 2019.

[8] B. Kärcher, "The importance of contrail ice formation for mitigating the climate impact of aviation," *Journal of Geophysical Research: Atmospheres*, vol. 121, no. 7, pp. 3497–3505, 2016. [Online]. Available: https://agupubs.onlinelibrary.wiley.com/doi/abs/10.1002/2015JD024696

[9] J. Larsson, A. Kamb, J. Nässén, and J. Åkerman, "Measuring greenhouse gas emissions from international air travel of a country's residents methodological development and application for sweden," *Environmental Impact Assessment Review*, vol. 72, pp. 137–144, 2018. [Online]. Available: https://www.sciencedirect.com/science/article/pii/S0195925517303116

[10] E. Comission, "European green deal: new rules agreed on applying the eu emissions trading system in the aviation sector," Press Release, Dec. 2022. [Online]. Available: https://ec.europa.eu/commission/presscorner/detail/en/ip_22_7609

[11] A. T. A. G. (ATAG), "Commitment to fly net zero 2050," Oct. 2021. [Online]. Available: https://aviationbenefits.org/media/167501/atag-net-zero-2050-declaration.pdf

[12] "Waypoint 2050," Air Transport Action Group, Tech. Rep., 2021. [Online]. Available: https://aviationbenefits.org/media/167417/w2050_v2021_27sept_full.pdf

[13] E. Commission, D.-G. for Mobility, Transport, D.-G. for Research, and Innovation, *Flightpath 2050 – Europe's vision for aviation – Maintaining global leadership and serving society's needs*. Publications Office, 2011.

[14] E. Comission, "Reducing emissions from aviation," Website, Jul. 2021. [Online]. Available: https://climate.ec.europa.eu/eu-action/transport/reducing-emissions-aviation_en#:~:text=Inadditiontomarket-based,contributetoreducingaviationemissions

[15] "Strategic researcg and innovation agenda," Clean Aviation, Tech. Rep., 2021.

[16] "Nasa's electrified aircraft propulsion research and development efforts," NASA, Tech. Rep., 2023. [Online]. Available: https://oig.nasa.gov/docs/IG-23-014.pdf

[17] R. Thomson, "Aircraft electric propulsion - the next chapter of aviation." Roland Berger LTD., Tech. Rep., 2017. [Online]. Available: https://www.rolandberger.com/en/Insights/Global-Topics/Electric-Propulsion/

[18] L. Feiner, "Power electronics transforms aircraft systems," in *Proceedings of WESCON '94*, 1994, pp. 166–171.

[19] A. J. Lampe, "A discourse of the "bleedless" and "bleed air" gas turbine engines," *University of Colorado Boulder*, 2015. [Online]. Available: https://www.colorado.edu/faculty/kantha/sites/default/files/attached-files/

81079-116619_-_alexander_lampe_-_dec_17_2015_1159_am_-_acp_final_report_lampe.pdf

[20] V. Cavalcanti and C. Andrade, "A trade-off study of a bleedless and conventional air conditioning systems," 10 2008.

[21] G. Martínez, F. R. Lalanne, I. Sánchez-Guardamino, S. R. Benito, and J. M. Echeverría, "Novel modular device for a decentralised electric power system architecture for more electric aircraft," *IEEE Access*, vol. 10, pp. 19 356–19 364, 2022.

[22] G. Buticchi, S. Bozhko, M. Liserre, P. Wheeler, and K. Al-Haddad, "On-board microgrids for the more electric aircraft—technology review," *IEEE Transactions on Industrial Electronics*, vol. 66, no. 7, pp. 5588–5599, 2019.

[23] J. Chen, C. Wang, and J. Chen, "Investigation on the selection of electric power system architecture for future more electric aircraft," *IEEE Transactions on Transportation Electrification*, vol. 4, no. 2, pp. 563–576, 2018.

[24] M. Sinnett, "787 no-bleed systems: Saving fuel and enhancing operational efficiencies," *Aeromagazine*. [Online]. Available: http://www.boeing.ch/commercial/aeromagazine/articles/qtr_4_07/AERO_Q407_article2.pdf

[25] Q. Liu, T. Liang, Z. Huang, and V. Dinavahi, "Real-time fpga-based hardware neural network for fault detection and isolation in more electric aircraft," *IEEE Access*, vol. 7, pp. 159 831–159 841, 2019.

[26] C. L. Bowman, T. V. Marien, and J. L. Felder, *Turbo- and Hybrid-Electrified Aircraft Propulsion for Commercial Transport*. [Online]. Available: https://arc.aiaa.org/doi/abs/10.2514/6.2018-4984

[27] S. Adibhatla, S. Garg, S. Griffith, K. Karnofski, N. Payne, and B. Wood, *Propulsion Control Technology Development Roadmaps to Address NASA Aeronautics Research Mission Goals for Thrusts 3a and 4*. [Online]. Available: https://arc.aiaa.org/doi/abs/10.2514/6.2018-4732

[28] C. E. Lents, L. W. Hardin, J. Rheaume, and L. Kohlman, *Parallel Hybrid Gas-Electric Geared Turbofan Engine Conceptual Design and Benefits Analysis*. [Online]. Available: https://arc.aiaa.org/doi/abs/10.2514/6.2016-4610

[29] L. Dorn-Gomba, J. Ramoul, J. Reimers, and A. Emadi, "Power electronic converters in electric aircraft: Current status, challenges, and emerging technologies," *IEEE Transactions on Transportation Electrification*, vol. 6, no. 4, pp. 1648–1664, 2020.

[30] K. R. Antcliff and F. M. Capristan, *Conceptual Design of the Parallel Electric-Gas Architecture with Synergistic Utilization Scheme (PEGASUS) Concept*. [Online]. Available: https://arc.aiaa.org/doi/abs/10.2514/6.2017-4001

[31] L. Juvé, J. Fosse, E. Joubert, and N. Fouquet, *Airbus Group Electrical Aircraft Program, The E-Fan Project*. [Online]. Available: https://arc.aiaa.org/doi/abs/10.2514/6.2016-4613

[32] H. D. J. Felder, G. Brown and J. Chu, "Turboelectricdistributed propulsion in a hybrid wing body aircraft," *NTRS - NASA Technical Reports Server*, 2011.

[33] J. Welstead and J. L. Felder, *Conceptual Design of a Single-Aisle Turboelectric Commercial Transport with Fuselage Boundary Layer Ingestion*, 2016. [Online]. Available: https://arc.aiaa.org/doi/abs/10.2514/6.2016-1027

[34] "Eviation alice," accessed: Feb. 5, 2024. [Online]. Available: https://www.eviation.com/

[35] "Magnix," accessed: Feb. 5, 2024. [Online]. Available: https://www.magnix.aero/

[36] "Low-carbon aviation. introducing new technology to aerospace." https://www.airbus.com/en/innovation/low-carbon-aviation, accessed: 2024-04-7.

[37] R. Wilson, "Electric Aircraft - The Weight Challenge — rawavcon.com," https://www.rawavcon.com/single-post/electric-aircraft-the-weight-challenge, [Accessed 05-02-2024].

[38] "PC-12 NGX — The World's Greatest Single — Pilatus Aircraft Ltd — pilatus-aircraft.com," https://www.pilatus-aircraft.com/en/fly/pc-12#:~:text=Through%20clever%20aerodynamic%20refinements%2C%20it, nautical%20miles%20(3%2C269%20kilometres)., [Accessed 05-02-2024].

[39] U. D. of Transportation, *Airplane Flying Handbook*, F. A. Administration, Ed. Airman Testing Standards Branch.

[40] I. Dumé, "Lithium-ion batteries break energy density record," Apr. 2023, accessed: Feb. 5, 2024. [Online]. Available: https://physicsworld.com/a/lithium-ion-batteries-break-energy-density-record/

[41] J. C. H. Raza, S. Bai, "Li-s batteries: Challenges, achievements and opportunities." *Electrochem. Energy Rev. 6, 29*, 2023.

[42] A. Farsi and M. A. Rosen, "Performance analysis of a hybrid aircraft propulsion system using solid oxide fuel cell, lithium ion battery and gas

turbine," *Applied Energy*, vol. 329, p. 120280, 2023. [Online]. Available: https://www.sciencedirect.com/science/article/pii/S0306261922015379

[43] Z. Ji and M. M. Rokni, "Energy and configuration management strategy for battery/fuel cell/jet engine hybrid propulsion and power systems on aircraft," *Energy Conversion and Management*, vol. 225, p. 113393, 2020. [Online]. Available: https://www.sciencedirect.com/science/article/pii/S0196890420309298

[44] J. Z. G. Subodh K. Mital, "Review of current state of the art and key designissues with potential solutions for liquid hydrogencryogenic storage tank structures for aircraftapplications," 2016. [Online]. Available: https://ntrs.nasa.gov/api/citations/20060056194/downloads/20060056194.pdf

[45] "Flight demonstration of a Liquid HYdrogen load-bearing tank in an unmanned cargo platform — fLHYing tank Project — Fact Sheet — HORIZON — CORDIS — European Commission — cordis.europa.eu," https://cordis.europa.eu/project/id/101101946, [Accessed 05-02-2024].

[46] "Home — H2ELIOS — h2elios.eu," https://h2elios.eu/, [Accessed 05-02-2024].

[47] J. K. Nøland, M. Leandro, J. A. Suul, and M. Molinas, "High-power machines and starter-generator topologies for more electric aircraft: A technology outlook," *IEEE Access*, vol. 8, pp. 130 104–130 123, 2020.

[48] "IGBT Modules - Infineon Technologies — infineon.com," https://www.infineon.com/cms/en/product/power/igbt/igbt-modules/, [Accessed 05-02-2024].

[49] "4th Generation Field Stop IGBT - Fairchild — DigiKey — digikey.co.uk," https://www.digikey.co.uk/en/pdf/f/fairchild-semiconductor/4th-generation-field-stop-igbt, [Accessed 05-02-2024].

[50] M. Buffolo, D. Favero, A. Marcuzzi, C. D. Santi, G. Meneghesso, E. Zanoni, and M. Meneghini, "Review and outlook on gan and sic power devices: Industrial state-of-the-art, applications, and perspectives," *IEEE Transactions on Electron Devices*, pp. 1–12, 2024.

[51] "SCT4013DR - Data Sheet, Product Detail — ROHM.com — rohm.com," https://www.rohm.com/products/sic-power-devices/sic-mosfet/sct4013dr-product, [Accessed 05-02-2024].

[52] "Msc025sma330d/s 3300v, 25 mohm sic n-channel power mosfet die," https://www.microchip.com/en-us/product/msc025sma330, [Accessed 05-02-2024].

[53] A. Deshpande and F. Luo, "Practical design considerations for a si igbt + sic mosfet hybrid switch: Parasitic interconnect influences, cost, and current ratio optimization," *IEEE Transactions on Power Electronics*, vol. 34, no. 1, pp. 724–737, 2019.

[54] X. Zhao, J. Hu, L. Ravi, D. Dong, and R. Burgos, "Planar common-mode emi filter design and optimization in a 100-kw sic-based generator-rectifier system for high-altitude operation," in *2021 IEEE Energy Conversion Congress and Exposition (ECCE)*, 2021, pp. 3555–3562.

[55] M. I. Hassan, N. Keshmiri, A. D. Callegaro, M. F. Cruz, M. Narimani, and A. Emadi, "Design optimization methodology for planar transformers for more

electric aircraft," *IEEE Open Journal of the Industrial Electronics Society*, vol. 2, pp. 568–583, 2021.

[56] Z. Ouyang and M. A. E. Andersen, "Overview of planar magnetic technology—fundamental properties," *IEEE Transactions on Power Electronics*, vol. 29, no. 9, pp. 4888–4900, 2014.

[57] A. Factory, "EASIER : Electric Aircraft System Integration Enabler - Home — easier-h2020.eu," http://www.easier-h2020.eu/, [Accessed 05-02-2024].

[58] A. Barzkar and M. Ghassemi, "Electric power systems in more and all electric aircraft: A review," *Ieee Access*, vol. 8, pp. 169 314–169 332, 2020.

[59] B. Rahrovi and M. Ehsani, "A review of the more electric aircraft power electronics," in *2019 IEEE Texas Power and Energy Conference (TPEC)*. IEEE, 2019, pp. 1–6.

[60] J. Ebersberger, M. Hagedorn, M. Lorenz, and A. Mertens, "Potentials and comparison of inverter topologies for future all-electric aircraft propulsion," *IEEE Journal of Emerging and Selected Topics in Power Electronics*, vol. 10, no. 5, pp. 5264–5279, 2022.

[61] M. u. Hassan, A. I. Emon, F. Luo, and V. Solovyov, "Design and validation of a 20-kva, fully cryogenic, two-level gan-based current source inverter for full electric aircrafts," *IEEE Transactions on Transportation Electrification*, vol. 8, no. 4, pp. 4743–4759, 2022.

[62] M. ul Hassan, Y. Wu, A. I. Emon, Z. Yuan, and F. Luo, "Electrical-thermal-mechanical considerations for the design of a compact two-level current source

inverter using gan devices," in *2023 IEEE Applied Power Electronics Conference and Exposition (APEC)*, 2023, pp. 854–861.

[63] D. Zhang, J. He, and D. Pan, "A megawatt-scale medium-voltage high efficiency high power density "sic+si" hybrid three-level anpc inverter for aircraft hybrid-electric propulsion systems," in *2018 IEEE Energy Conversion Congress and Exposition (ECCE)*, 2018, pp. 806–813.

[64] R. S. Bayliss, R. K. Iyer, R. Liou, and R. C. Pilawa-Podgurski, "A segmented electric aircraft drivetrain employing 10-level flying capacitor multi-level dual-interleaved power modules," in *2023 IEEE Applied Power Electronics Conference and Exposition (APEC)*, 2023, pp. 225–230.

[65] A. Trentin, G. Sala, L. Tarisciotti, A. Galassini, M. Degano, P. H. Connor, D. Golovanov, D. Gerada, Z. Xu, A. La Rocca, C. N. Eastwick, S. J. Pickering, P. Wheeler, J. C. Clare, and C. Gerada, "Research and realization of high-power medium-voltage active rectifier concepts for future hybrid-electric aircraft generation," *IEEE Transactions on Industrial Electronics*, vol. 68, no. 12, pp. 11 684–11 695, 2021.

[66] X. Zhao, R. Phukan, C.-W. Chang, R. Burgos, D. Dong, and P. Asfaux, "Design and optimization of 2×211-kw sic-based aircraft propulsion inverter system with high power density and high efficiency," in *2023 IEEE Applied Power Electronics Conference and Exposition (APEC)*, 2023, pp. 1009–1016.

[67] O. Lopez, Z. Guo, J. Ordonez, H. Li, P. Masson, and T. Ananthanpillai, "A high power density sic motor drive for a 6-phase pmsm," in *2023 IEEE Applied Power Electronics Conference and Exposition (APEC)*, 2023, pp. 3182–3187.

[68] S. C. Susanah Kowalewski, David Avanesian and J. Terry, "X-57 high lift motor controller design and testing," in *AIAA/IEEE Electric Aircraft Technologies Symposium (EATS)*, Jun. 2023.

[69] Y. Cong, N. Adina, Z. Wei, H. You, R. Borjas, X. Lyu, P. Fu, B. Hu, and J. Wang, "Submodule design of a 2 kv 1 mw integrated modular motor drive for aviation applications," in *2021 IEEE 8th Workshop on Wide Bandgap Power Devices and Applications (WiPDA)*, 2021, pp. 345–350.

[70] H. Zeng, J. Swanke, T. M. Jahns, and B. Sarlioglu, "Modular modeling and distributed control of permanent-magnet modular motor drives (mmds) for electric aircraft propulsion," in *2021 IEEE Energy Conversion Congress and Exposition (ECCE)*, 2021, pp. 4598–4605.

[71] D. Golovanov, D. Gerada, G. Sala, M. Degano, A. Trentin, P. H. Connor, Z. Xu, A. L. Rocca, A. Galassini, L. Tarisciotti, C. N. Eastwick, S. J. Pickering, P. Wheeler, J. Clare, M. Filipenko, and C. Gerada, "4-mw class high-power-density generator for future hybrid-electric aircraft," *IEEE Transactions on Transportation Electrification*, vol. 7, no. 4, pp. 2952–2964, 2021.

[72] N. Pallo, T. Foulkes, T. Modeer, S. Coday, and R. Pilawa-Podgurski, "Power-dense multilevel inverter module using interleaved gan-based phases for electric aircraft propulsion," in *2018 IEEE Applied Power Electronics Conference and Exposition (APEC)*, 2018, pp. 1656–1661.

[73] N. Pallo, S. Coday, J. Schaadt, P. Assem, and R. C. N. Pilawa-Podgurski, "A 10-level flying capacitor multi-level dual-interleaved power module for scalable and power-dense electric drives," in *2020 IEEE Applied Power Electronics Conference and Exposition (APEC)*, 2020, pp. 893–898.

[74] L. Horowitz and R. C. Pilawa-Podgurski, "High power density flying capacitor multilevel inverter for electric aircraft with a stacked pcb interleaved hybrid commutation loop design," in *2023 IEEE Applied Power Electronics Conference and Exposition (APEC)*, 2023, pp. 1065–1069.

[75] A. D. Anderson, N. J. Renner, Y. Wang, S. Agrawal, S. Sirimanna, D. Lee, A. Banerjee, K. Haran, M. J. Starr, and J. L. Felder, "System weight comparison of electric machine topologies for electric aircraft propulsion," in *2018 AIAA/IEEE Electric Aircraft Technologies Symposium (EATS)*, 2018, pp. 1–16.

[76] L. Zhou, D. Wang, Y. Yang, C. Liu, G. Pietrini, and A. Emadi, "A comparative study of single- and multi-cell three- level anpc inverters for electric aircraft applications," in *2023 IEEE Applied Power Electronics Conference and Exposition (APEC)*, 2023, pp. 3119–3124.

[77] "Electrical breakdown of gases. by j. m. meek and j. d. craggs. oxford (clarendon press), 1953. pp. vii, 507; 320 figs., 82 tables. 60s," *Quarterly Journal of the Royal Meteorological Society*, vol. 80, no. 344, pp. 282–283, 1954. [Online]. Available: https://rmets.onlinelibrary.wiley.com/doi/abs/10.1002/qj.49708034425

[78] M. Lizcano, T. S. Williams, E.-S. E. Shin, D. Santiago, and B. Nguyen, "Aerospace environmental challenges for electrical insulation and recent developments for electrified aircraft," *Materials*, vol. 15, no. 22, 2022. [Online]. Available: https://www.mdpi.com/1996-1944/15/22/8121

[79] "AIR6127: Managing Higher Voltages in Aerospace Electrical Systems - SAE International — sae.org," https://www.sae.org/standards/content/air6127/, [Accessed 05-02-2024].

[80] G. Galli, H. Hamrita, C. Jammes, M. J. Kirkpatrick, E. Odic, P. Dessante, and P. Molinié, "Paschen's law in extreme pressure and temperature conditions," *IEEE Transactions on Plasma Science*, vol. 47, no. 3, pp. 1641–1647, 2019.

[81] I. Cotton, A. Nelms, and M. Husband, "Defining safe operating voltages for aerospace electrical systems," in *2007 Electrical Insulation Conference and Electrical Manufacturing Expo*, 2007, pp. 67–71.

[82] M. Morales, "An experimental v an experimental validation of a re alidation of a revised p vised paschen's law relating s law relatingto the esd of aerospace vehicle surfaces," Master's thesis, University of Central Florida, 2020.

[83] V. Madonna, P. Giangrande, and M. Galea, "Electrical power generation in aircraft: Review, challenges, and opportunities," *IEEE Transactions on Transportation Electrification*, vol. 4, no. 3, pp. 646–659, 2018.

[84] A. K. R. Siddavatam, K. RajaShekara, R. P. Reddy, H. Huang, H. S. Krishnamoorthy, Z. Dong, and F. Wang, "Fault-tolerant architectures with enhanced bus protection for electric/hybrid aircraft systems," *IEEE Transactions on Transportation Electrification*, vol. 9, no. 3, pp. 3564–3578, 2023.

[85] D. Zhang, Y. Xu, J. Brandt, Z. Zhang, D. Qin, and D. Dong, "A solid-state circuit breaker without current limiting inductor," *IEEE Transactions on Industry Applications*, vol. 59, no. 4, pp. 4640–4650, 2023.

[86] R. Rodrigues, Y. Du, A. Antoniazzi, and P. Cairoli, "A review of solid-state circuit breakers," *IEEE Transactions on Power Electronics*, vol. 36, no. 1, pp. 364–377, 2021.

[87] E. Sayed, M. Abdalmagid, G. Pietrini, N.-M. Sa'adeh, A. D. Callegaro, C. Goldstein, and A. Emadi, "Review of electric machines in more-/hybrid-/turbo-electric aircraft," *IEEE Transactions on Transportation Electrification*, vol. 7, no. 4, pp. 2976–3005, 2021.

[88] D. Golovanov, D. Gerada, Z. Xu, C. Gerada, A. Page, and T. Sawata, "Designing an advanced electrical motor for propulsion of electric aircraft," in *2019 AIAA/IEEE Electric Aircraft Technologies Symposium (EATS)*, 2019, pp. 1–12.

[89] P. E. Kakosimos, A. G. Sarigiannidis, M. E. Beniakar, A. G. Kladas, and C. Gerada, "Induction motors versus permanent-magnet actuators for aerospace applications," *IEEE Transactions on Industrial Electronics*, vol. 61, no. 8, pp. 4315–4325, 2014.

[90] C. A. Luongo, P. J. Masson, T. Nam, D. Mavris, H. D. Kim, G. V. Brown, M. Waters, and D. Hall, "Next generation more-electric aircraft: A potential application for hts superconductors," *IEEE Transactions on Applied Superconductivity*, vol. 19, no. 3, pp. 1055–1068, 2009.

[91] X. Y. P Song T.M. Qu L.F. Lai, M.S Wu and Z. Han, "Thermal analysis for the hts stator consisting of hts armature windings and an iron core for a 2.5 kw hts generator," *Superconductor Science and Technology,Volume 29,Number 5*, 2016.

[92] R. C. Bolam, Y. Vagapov, and A. Anuchin, "A review of electrical motor topologies for aircraft propulsion," in *2020 55th International Universities Power Engineering Conference (UPEC)*, 2020, pp. 1–6.

[93] R. J. Keuter, B. Kirsch, J. Friedrichs, and B. Ponick, "Design decisions for a powertrain combination of electric motor and propeller for an electric aircraft," *IEEE Access*, vol. 11, pp. 79 144–79 155, 2023.

[94] X. Zhang, D. Boroyevich, P. Mattavelli, J. Xue, and F. Wang, "Emi filter design and optimization for both ac and dc side in a dc-fed motor drive system," in *2013 Twenty-Eighth Annual IEEE Applied Power Electronics Conference and Exposition (APEC)*, 2013, pp. 597–603.

[95] "Eurocae publishes guidance material for easa hybrid electric propulsion compliance2013; Urban Air Mobility News — urbanairmobilitynews.com," https://www.urbanairmobilitynews.com/emerging-regulations/eurocae-publishes-guidance-material-for-easa-hybrid-electric-propulsion-compliance/, [Accessed 05-02-2024].

[96] "CONCERTO project — Clean Aviation — concertoproject.eu," https://www.concertoproject.eu/?_sm_nck=1, [Accessed 05-02-2024].

[97] P. Schmollgruber, D. Donjat, M. Ridel, I. Cafarelli, O. Atinault, C. François, and B. Paluch, *Multidisciplinary Design and performance of the ONERA Hybrid Electric Distributed Propulsion concept (DRAGON)*. [Online]. Available: https://arc.aiaa.org/doi/abs/10.2514/6.2020-0501

[98] I. Lind and H. Andersson, "Model based systems engineering for aircraft systems-how does modelica based tools fit?" in *Proceedings of the 8th Interna-*

tional Modelica Conference; March 20th-22nd; Technical Univeristy; Dresden; Germany, no. 063. Linköping University Electronic Press, 2011, pp. 856–864.

[99] A. K. Jeyaraj, "A model-based systems engineering approach for efficient system architecture representation in conceptual design: A case study for flight control systems," Ph.D. dissertation, Concordia University, 2019.

[100] J.-K. Mueller, A. Bensmann, B. Bensmann, T. Fischer, T. Kadyk, G. Narjes, F. Kauth, B. Ponick, J. Seume, U. Krewer *et al.*, "Design considerations for the electrical power supply of future civil aircraft with active high-lift systems," *Energies*, vol. 11, no. 1, p. 179, 2018.

[101] H. D. Kim, A. T. Perry, and P. J. Ansell, "A review of distributed electric propulsion concepts for air vehicle technology," in *2018 AIAA/IEEE Electric Aircraft Technologies Symposium (EATS)*. IEEE, 2018, pp. 1–21.

[102] J. Kim, K. Kwon, S. Roy, E. Garcia, and D. N. Mavris, "Megawatt-class turboelectric distributed propulsion, power, and thermal systems for aircraft," in *2018 AIAA Aerospace Sciences Meeting*, 2018, p. 2024.

[103] Z. Jin, G. Sulligoi, R. Cuzner, L. Meng, J. C. Vasquez, and J. M. Guerrero, "Next-generation shipboard dc power system: Introduction smart grid and dc microgrid technologies into maritime electrical netowrks," *IEEE Electrification Magazine*, vol. 4, no. 2, pp. 45–57, 2016.

[104] RTCA, "D0-254. design assurance guidance for airborne electronic hardware," https://my.rtca.org/productdetails?id=a1B36000001IcjTEAS, [Accessed 05-02-2024].

[105] *ARP4761A: Guidelines for Conducting the Safety Assessment Process on Civil Aircraft, Systems, and Equipment*, SAE International Std., 2023.

[106] ICAO, "Operation of aircraft, annex 6. part i." *International Standards and Recommended Practices*, 2001, [Accessed 17-02-2024].

[107] J. Laurence K Loftiun, "Quest for performance. the evolution of modern aircraft," *NASA*, 1985, [Accessed 17-02-2024].

[108] F. A. Administration, *Pilot's Handbook of Aeronautical knowledge*, U.S. Department of Transportation, 2023.

[109] D. J. Smith, *Reliability, maintainability and risk: practical methods for engineers*. Butterworth-Heinemann, 2021.

[110] J. I. McCool, *Using the Weibull distribution: reliability, modeling, and inference*. John Wiley & Sons, 2012, vol. 950.

[111] Y. Song and B. Wang, "Survey on reliability of power electronic systems," *IEEE Transactions on Power Electronics*, vol. 28, no. 1, pp. 591–604, 2013.

[112] Y. LOZANOV, "Reliability assessment of variable speed induction motor drive with fault tree analysis," in *2020 21st International Symposium on Electrical Apparatus and Technologies (SIELA)*, 2020.

[113] J.-H. Cha, J.-S. Jo, S.-J. Lim, F.-s. Kang, and T.-J. Kim, "Comparison of failure rates according to secondary circuit configurations of full-bridge converters using fault-tree analysis," in *IECON 2023- 49th Annual Conference of the IEEE Industrial Electronics Society*, 2023, pp. 1–6.

[114] S. Yang, A. Bryant, P. Mawby, D. Xiang, L. Ran, and P. Tavner, "An industry-based survey of reliability in power electronic converters," *IEEE Transactions on Industry Applications*, vol. 47, no. 3, pp. 1441–1451, 2011.

[115] M. Pecht and W.-C. Kang, "A critique of mil-hdbk-217e reliability prediction methods," *IEEE Transactions on Reliability*, vol. 37, no. 5, pp. 453–457, 1988.

[116] U. Scheuermann and M. Junghaenel, "Limitation of power module lifetime derived from active power cycling tests," in *CIPS 2018; 10th International Conference on Integrated Power Electronics Systems*, 2018, pp. 1–10.

[117] J. Harikumaran, G. Buticchi, G. Migliazza, V. Madonna, P. Giangrande, A. Costabeber, P. Wheeler, and M. Galea, "Failure modes and reliability oriented system design for aerospace power electronic converters," *IEEE Open Journal of the Industrial Electronics Society*, vol. 2, pp. 53–64, 2021.

[118] P. Schmollgruber, D. Donjat, M. Ridel, I. Cafarelli, O. Atinault, C. François, and B. Paluch, "Multidisciplinary design and performance of the onera hybrid electric distributed propulsion concept (dragon)," in *AIAA Scitech 2020 Forum*, 2020, p. 0501.

[119] C. L. Pastra, C. Hall, G. Cinar, J. Gladin, and D. N. Mavris, "Specific power and efficiency projections of electric machines and circuit protection exploration for aircraft applications," in *2022 IEEE Transportation Electrification Conference and Expo (ITEC)*, 2022, pp. 766–771.

[120] J. Brombach, T. Schröter, A. Lücken, and D. Schulz, "Optimized cabin power supply with a 270 v dc grid on a modern aircraft," in *2011 7th International*

Conference-Workshop Compatibility and Power Electronics (CPE), 2011, pp. 425–428.

[121] P. Kshirsagar, J. Ewanchuk, B. van Hassel, R. Taylor, S. Dwari, J. Rheaume, and C. Lents, "Anatomy of a 20 mw electrified aircraft: Metrics and technology drivers," in *2020 AIAA/IEEE Electric Aircraft Technologies Symposium (EATS)*, 2020, pp. 1–9.

[122] D. B. Jayme, "Evaluation of the hybrid-electric aircraft project airbus e-fan x," Master's thesis, Haw Hamburg, 2019.

[123] DO-160, Enviromental Conditions and Test Procedures for Airborne Equipement. Std.

[124] M. J. Armstrong, M. Blackwelder, A. Bollman, C. Ross, A. Campbell, C. Jones, and P. Norman, "Architecture, voltage, and components for a turboelectric distributed propulsion electric grid," Tech. Rep., 2015.

[125] K. Haran, "Electric/hybrid-electric drives for aircraft propulsion," in *Advanced Research Projects Agency-Energy (ARPA-E)*, 2019, p. 23.

[126] H. Gui, R. Chen, J. Niu, Z. Zhang, L. M. Tolbert, F. F. Wang, B. J. Blalock, D. Costinett, and B. B. Choi, "Review of power electronics components at cryogenic temperatures," *IEEE transactions on power electronics*, vol. 35, no. 5, pp. 5144–5156, 2019.

[127] C. Peng, X. Song, A. Q. Huang, and I. Husain, "A medium-voltage hybrid dc circuit breaker—part ii: Ultrafast mechanical switch," *IEEE Journal of Emerging and Selected Topics in Power Electronics*, vol. 5, no. 1, pp. 289–296, 2016.

[128] "Advanced electrical protections. electromechanics mechatronics electronics," https://www.crouzet.com/, [Accessed 25-02-2024].

[129] J. Wyss and J. Biela, "Optimal design of bidirectional pfc rectifiers and inverters considering 2l and 3l topologies with si, sic, and gan switches," *IEEJ Journal of Industry Applications*, vol. 8, no. 6, pp. 975–983, 2019.

[130] S. Teichel, M. Dörbaum, O. Misir, A. Merkert, A. Mertens, J. Seume, and B. Ponick, "Design considerations for the components of electrically powered active high-lift systems in civil aircraft," *CEAS Aeronautical Journal*, vol. 6, no. 1, pp. 49–67, 2015.

[131] "Gore space cables." [Online]. Available: https://www.gore.com/resources/space-cables-catalog-traditional-space

[132] S. Wu and Y. Li, "Fuel cell applications on more electrical aircraft," in *2014 17th International Conference on Electrical Machines and Systems (ICEMS)*, 2014, pp. 198–201.

[133] C. E. Lents, L. W. Hardin, J. Rheaume, and L. Kohlman, "Parallel hybrid gas-electric geared turbofan engine conceptual design and benefits analysis," in *52nd AIAA/SAE/ASEE joint propulsion conference*, 2016, p. 4610.

[134] E.-S. E. Shin, D. A. Scheiman, and M. Lizcano, "Lightweight, durable, and multifunctional electrical insulation material systems for high voltage applications," in *2018 AIAA/IEEE Electric Aircraft Technologies Symposium (EATS)*. IEEE, 2018, pp. 1–21.

[135] S. Du, J. Tangudu, and P. Kshirsagar, "Analytical model and design space studies for a non-superconducting and superconducting electric machine for

an aircraft application," in *2020 AIAA/IEEE Electric Aircraft Technologies Symposium (EATS)*. IEEE, 2020, pp. 1–10.

[136] E. Comission, "Thermal management for the hybrid electric regional aircraft," https://cordis.europa.eu/project/id/101102008, [Accessed 25-02-2024].

[137] P. Cheetham, B. Darbha, S. Telikapalli, C. H. Kim, M. Coleman, and S. Pamidi, "Superconducting dc power distribution networks for electric aircraft," in *2020 AIAA/IEEE Electric Aircraft Technologies Symposium (EATS)*. IEEE, 2020, pp. 1–7.

[138] R. Merkler, "D4.05. power plant integration concept for electric generator," CENTRELINE Project, Tech. Rep., 2020.

[139] *C-23 Normal, Utility,Aerobatic and Commuter Aeroplanes.*, EASA Std.

[140] E. Comission, "Size and weight reduction of cell and packaging of batteries system, integrating lightweight and functional materials, innovative thermal management and safe and sustainable by design approach (batt4eu partnership)," https://ec.europa.eu/info/funding-tenders/opportunities/portal/screen/opportunities/topic-details/horizon-cl5-2024-d2-02-03, 2024, [Accessed 11-05-2024].

[141] G. Brown, "Weights and efficiencies of electric components of a turboelectric aircraft propulsion system," in *49th AIAA aerospace sciences meeting including the new horizons forum and aerospace exposition*, 2011, p. 225.

[142] "Chyla and siena reveal scaling-up opportunities of hybrid-electric propulsion in aviation." Clean Aviation, Tech. Rep., 2024. [On-

line]. Available: https://www.clean-aviation.eu/clean-sky-2/results-stories/chyla-siena-reveal-scaling-up-opportunities-of-hybrid-electric-propulsion-in-aviation

[143] "Hybrid electric regional aircraft distribution technologies," 2023-2025. [Online]. Available: https://hecate-project.eu/

[144] D. Wang, S. Hemming, Y. Yang, A. Poorfakhraei, L. Zhou, C. Liu, and A. Emadi, "Multilevel inverters for electric aircraft applications: Current status and future trends," *IEEE Transactions on Transportation Electrification*, pp. 1–1, 2023.

[145] S. Debnath, J. Qin, B. Bahrani, M. Saeedifard, and P. Barbosa, "Operation, control, and applications of the modular multilevel converter: A review," *IEEE Transactions on Power Electronics*, vol. 30, no. 1, pp. 37–53, 2015.

[146] M. A. Perez, S. Bernet, J. Rodriguez, S. Kouro, and R. Lizana, "Circuit topologies, modeling, control schemes, and applications of modular multilevel converters," *IEEE Transactions on Power Electronics*, vol. 30, no. 1, pp. 4–17, 2015.

[147] H. Kamizuma, K. Furukawa, H. Morooka, Y. Mabuchi, R. Moteki, and K. Nakatsu, "High-reliability converter with silicone-coating insulation architecture for electric aircraft," in *2022 IEEE Energy Conversion Congress and Exposition (ECCE)*, 2022, pp. 1–6.

[148] T. W. M. Company, "Power converter for use with wind generator," World Intellectual property Organization Patent. Patent WO2 011 008 466A2, 2010.

[149] P. Huynh, P. Wang, and A. Banerjee, "An integrated permanent-magnet-synchronous-generator-rectifier architecture for limited-speed-range applica-

tions," in *2018 IEEE Energy Conversion Congress and Exposition (ECCE)*, 2018, pp. 3413–3420.

[150] E. Yamamoto, H. Hara, T. Uchino, M. Kawaji, T. J. Kume, J. K. Kang, and H.-p. Krug, "Development of mcs and its applications in industry [industry forum]," *IEEE Industrial Electronics Magazine*, vol. 5, no. 1, pp. 4–12, 2011.

[151] M. Hiller, D. Krug, R. Sommer, and S. Rohner, "A new highly modular medium voltage converter topology for industrial drive applications," in *2009 13th European Conference on Power Electronics and Applications*, 2009, pp. 1–10.

[152] J. V. M. Farias, A. F. Cupertino, H. A. Pereira, S. I. Seleme, and R. Teodorescu, "On converter fault tolerance in mmc-hvdc systems: A comprehensive survey," *IEEE Journal of Emerging and Selected Topics in Power Electronics*, vol. 9, no. 6, pp. 7459–7470, 2021.

[153] R. Marquardt, "Modular multilevel converter topologies with dc-short circuit current limitation," in *8th International Conference on Power Electronics - ECCE Asia*, 2011, pp. 1425–1431.

[154] T. Nakanishi and J.-I. Itoh, "High power density design for a modular multilevel converter with an h-bridge cell based on a volume evaluation of each component," *IEEE Transactions on Power Electronics*, vol. 33, no. 3, pp. 1967–1984, 2018.

[155] M. A. Perez, S. Ceballos, G. Konstantinou, J. Pou, and R. P. Aguilera, "Modular multilevel converters: Recent achievements and challenges," *IEEE Open Journal of the Industrial Electronics Society*, vol. 2, pp. 224–239, 2021.

[156] D. G. L. A. R. A. Ignacio Castro, Tania C. Cano, "Power converter," U.S. Patent US11 916 493B2, 2024. [Online]. Available: https://patents.google.com/patent/US11916493B2/en?oq=US11916493B2

[157] T. C. Cano, I. Castro, A. Rodríguez, D. G. Lamar, Y. F. Khalil, L. Albiol-Tendillo, and P. Kshirsagar, "Future of electrical aircraft energy power systems: An architecture review," *IEEE Transactions on Transportation Electrification*, vol. 7, no. 3, pp. 1915–1929, 2021.

[158] T. C. Cano, D. Pedroso, A. Rodríguez, I. Castro, and D. G. Lamar, "On the reduction of output capacitance in two-level three phase pfc boost rectifier for pulsating loads," in *2022 24th European Conference on Power Electronics and Applications (EPE'22 ECCE Europe)*, 2022, pp. 1–9.

[159] P. T. Huynh, P. J. Wang, and A. Banerjee, "An integrated permanent-magnet-synchronous generator–rectifier architecture for limited-speed-range applications," *IEEE Transactions on Power Electronics*, vol. 35, no. 5, pp. 4767–4779, 2020.

[160] G. P. Adam, I. Abdelsalam, J. E. Fletcher, G. M. Burt, D. Holliday, and S. J. Finney, "New efficient submodule for a modular multilevel converter in multiterminal hvdc networks," *IEEE Transactions on Power Electronics*, vol. 32, no. 6, pp. 4258–4278, 2017.

[161] F. Briz, M. Lopez, A. Rodriguez, and M. Arias, "Modular power electronic transformers: Modular multilevel converter versus cascaded h-bridge solutions," *IEEE Industrial Electronics Magazine*, vol. 10, no. 4, pp. 6–19, 2016.

[162] B. Li, J. Hu, S. Zhou, and D. Xu, "Hybrid back-to-back mmc system for variable speed ac machine drives," *CPSS Transactions on Power Electronics and Applications*, vol. 5, no. 2, pp. 114–125, 2020.

[163] D. Boroyevich, R. Burgos, I. Cvetkovic, and B. Wen, "Modeling and control of three-phase high-power high-frequency converters," in *IEEE Workshop on Control and Modeling for Power Electronics*, 2018.

[164] V. Blasko and V. Kaura, "A new mathematical model and control of a three-phase ac-dc voltage source converter," *IEEE transactions on Power Electronics*, vol. 12, no. 1, pp. 116–123, 1997.

[165] L. Xueyan and Y. Zheng, "Comparison of time delay processing methods in control system," in *2015 4th international conference on computer science and network technology (ICCSNT)*, vol. 1. IEEE, 2015, pp. 1502–1505.

[166] L. M. Cunico, G. Lambert, R. P. Dacol, S. V. G. Oliveira, and Y. R. de Novaes, "Parameters design for modular multilevel converter (mmc)," in *2013 Brazilian Power Electronics Conference*, 2013, pp. 264–270.

[167] P. Wang, X.-P. Zhang, P. F. Coventry, and Z. Li, "Control and protection strategy for mmc mtdc system under converter-side ac fault during converter blocking failure," *Journal of Modern Power Systems and Clean Energy*, vol. 2, no. 3, pp. 272–281, 2014.

[168] X. Yang, Y. Xue, P. Wen, and Z. Li, "Comprehensive understanding of dc pole-to-pole fault and its protection for modular multilevel converters," *High voltage*, vol. 3, no. 4, pp. 246–254, 2018.

[169] Q. Tu, Z. Xu, H. Huang, and J. Zhang, "Parameter design principle of the arm inductor in modular multilevel converter based hvdc," in *2010 International Conference on Power System Technology*, 2010, pp. 1–6.

[170] L.-P. Qu, Z. Lu, C.-J. Liu, and C.-L. He, "A sort method of balancing capacitor voltage of mmc," in *2019 18th International Symposium on Distributed Computing and Applications for Business Engineering and Science (DCABES)*, 2019, pp. 241–244.

[171] B. Zaidi, A. Videt, and N. Idir, "Optimization method of cm inductor volume taking into account the magnetic core saturation issues," *IEEE Transactions on Power Electronics*, vol. 34, no. 5, pp. 4279–4291, 2019.

[172] P. Pairodamonchai, S. Suwankawin, and S. Sangwongwanich, "Design and implementation of a hybrid output emi filter for high-frequency common-mode voltage compensation in pwm inverters," *IEEE Transactions on Industry Applications*, vol. 45, no. 5, pp. 1647–1659, 2009.

[173] S. Wang, Y. Y. Maillet, F. Wang, D. Boroyevich, and R. Burgos, "Investigation of hybrid emi filters for common-mode emi suppression in a motor drive system," *IEEE Transactions on Power Electronics*, vol. 25, no. 4, pp. 1034–1045, 2010.

[174] I. Takahashi, A. Ogata, H. Kanazawa, and A. Hiruma, "Active emi filter for switching noise of high frequency inverters," in *Proceedings of Power Conversion Conference - PCC '97*, vol. 1, 1997, pp. 331–334 vol.1.

[175] Y. Zhang, Q. Li, and D. Jiang, "A motor cm impedance based transformerless active emi filter for dc-side common-mode emi suppression in motor drive

system," *IEEE Transactions on Power Electronics*, vol. 35, no. 10, pp. 10 238–10 248, 2020.

[176] K. Z. WanJun Yin, LinNa Jiang and Y. Zhang, "Design of emi filter based on impedance matching," *International Journal of Electronics Letters*, vol. 10, no. 1, pp. 48–56, 2022. [Online]. Available: https://doi.org/10.1080/21681724.2020.1843714

[177] L. Xing, F. Feng, and J. Sun, "Optimal damping of emi filter input impedance," *IEEE Transactions on Industry Applications*, vol. 47, no. 3, pp. 1432–1440, 2011.

[178] Y.-C. Son and S.-K. Sul, "Generalization of active filters for emi reduction and harmonics compensation," *IEEE Transactions on Industry Applications*, vol. 42, pp. 545–551, 2006. [Online]. Available: https://api.semanticscholar.org/CorpusID:5723685

[179] W. Chen, X. Yang, and Z. Wang, "Analysis of insertion loss and impedance compatibility of hybrid emi filter based on equivalent circuit model," *IEEE Transactions on Industrial Electronics*, vol. 54, no. 4, pp. 2057–2064, 2007.

[180] B. Narayanasamy and F. Luo, "A survey of active emi filters for conducted emi noise reduction in power electronic converters," *IEEE Transactions on Electromagnetic Compatibility*, vol. 61, no. 6, pp. 2040–2049, 2019.

[181] W. Chen, X. Yang, and Z. Wang, "An active emi filtering technique for improving passive filter low-frequency performance," *IEEE Transactions on Electromagnetic Compatibility*, vol. 48, no. 1, pp. 172–177, 2006.

[182] ——, "An experimental study and comparison of common mode and differential mode noise compensation characteristic for active emi filter," in *2008 IEEE Power Electronics Specialists Conference*, 2008, pp. 4399–4404.

[183] S. Jeong, D. Shin, and J. Kim, "A transformer-isolated common-mode active emi filter without additional components on power lines," *IEEE Transactions on Power Electronics*, vol. 34, no. 3, pp. 2244–2257, 2019.

[184] B. Narayanasamy, F. Luo, and Y. Chu, "Modeling and stability analysis of voltage sensing based differential mode active emi filters for ac-dc power converters," in *2018 IEEE Symposium on Electromagnetic Compatibility, Signal Integrity and Power Integrity (EMC, SI and PI)*, 2018, pp. 322–328.

[185] S. Takahashi, S. Ogasawara, K. Orikawa, M. Takemoto, and M. Tamate, "An active common-mode filter for reducing radiated noise from power cables," in *2017 IEEE 3rd International Future Energy Electronics Conference and ECCE Asia (IFEEC 2017 - ECCE Asia)*, 2017, pp. 1753–1758.

[186] B. Nassurdine, P. Lévy, D. Labrousse, J. Schanen, X. Maynard, and S. Carcouet, "Design and experimental validation of a voltage sensing-current cancellation common mode linear active filter," in *2022 24th European Conference on Power Electronics and Applications (EPE'22 ECCE Europe)*, 2022, pp. P.1–P.11.

[187] L. Dai, W. Chen, R. Wang, Y. Yang, and Y. Zhou, "A new approach for improving stability of active cm emi filters for ac/dc power converters," in *2018 IEEE International Power Electronics and Application Conference and Exposition (PEAC)*, 2018, pp. 1–4.

[188] Y. Chu, "Active emi filters to reduce size and cost of emi filters in automotive systems," https://www.ti.com/lit/an/slyt812/slyt812.pdf?ts=1714854144905&ref_url=https%253A%252F%252Fwww.google.com%252F, [Accessed 05-02-2024].

[189] X. Chang, Y. Yang, W. Chen, and X. Yang, "Implementation of a novel active common-mode filter used in dc-dc converters," in *2014 XXXIth URSI General Assembly and Scientific Symposium (URSI GASS)*, 2014, pp. 1–4.

[190] M. C. Di Piazza, A. Ragusa, and G. Vitale, "Design of grid-side electromagnetic interference filters in ac motor drives with motor-side common mode active compensation," *IEEE Transactions on Electromagnetic Compatibility*, vol. 51, no. 3, pp. 673–682, 2009.

[191] M. L. Heldwein, H. Ertl, J. Biela, and J. W. Kolar, "Implementation of a transformerless common-mode active filter for offline converter systems," *IEEE Transactions on Industrial Electronics*, vol. 57, no. 5, pp. 1772–1786, 2010.

[192] D. Shin, J. Kim, C. Son, S. Jeon, B. Cho, and J. Han, "A simple low-cost common mode active emi filter using a push-pull amplifier," in *2016 IEEE Energy Conversion Congress and Exposition (ECCE)*, 2016, pp. 1–5.

[193] R. Goswami, S. Wang, E. Solodovnik, and K. J. Karimi, "Differential mode active emi filter design for a boost power factor correction ac/dc converter," *IEEE Journal of Emerging and Selected Topics in Power Electronics*, vol. 7, no. 1, pp. 576–590, 2019.

[194] M. Li, M. Shen, L. Xing, and W. Said, "Current feedback based hybrid common-mode emi filter for grid-tied inverter application," in *2012 IEEE Energy Conversion Congress and Exposition (ECCE)*, 2012, pp. 1394–1398.

[195] D. Self and a. O. M. C. Safari, *Audio Power Amplifier Design, 6th Edition*. Routledge, 2013. [Online]. Available: https://books.google.co.uk/books?id=rCp9zwEACAAJ